Structural and dynamical properties of inclusion complexes compounds and the solvents from first-principles investigations

Von der Fakultät für Naturwissenschaften
der Universität Duisburg-Essen
(Standort Duisburg)
zur Erlangung des akademischen Grades eines
Doktors der Naturwissenschaften (Dr. rer.nat.)
genehmigte Dissertation von

Waheed Adeniyi Adeagbo
aus
Ibadan, Oyo State, Nigeria

Referent: Prof. Dr. P. Entel
Korreferent: PD. Dr. A. Baumgärtner
Tag der mündlichen Prüfung: 20 April 2004

Abstract

In this work, a series of *ab-initio* calculations based on density functional theory is presented. We investigated the properties of water and the inclusion complexes of cyclodextrins with various guest compounds such as phenol, aspirin, pinacyanol chloride dye and binaphtyl molecules in the environment of water as solvent.
Our investigation of water includes the cluster units of water, the bulk properties of the liquid water and the crystalline ice structure. Some equilibrium structures of water clusters were prepared and their binding energies were calculated with the self-consistency density functional tight binding (SCC-DFTB) method. The global minimum water clusters of TIP4P classical modelled potential were also calculated using the DFTB method and Vienna Ab-initio Simulation Package (VASP). All results show a non-linear behaviour of the binding energy per water molecule against water cluster size with some anomalies found for the lower clusters between 4 and 8 molecules. We also calculated the melting temperatures of these water clusters having solid-like behaviour by heating. Though, the melting region of the heated structures is not well defined as a result of the pronounced fluctuations of the bonding network of the system giving rise to fluctuations in the observed properties, but nevertheless the range where the breakdown occurs was defined as the melting temperature of the clusters. The bulk properties of the liquid, such as radial distribution functions, calculated with the VASP method show good agreement with neutron diffraction scattering data with respect to positions and height of the peaks. The DFTB method gives good positions of the peaks but with too broad peaks due the approximations on which the method relies, which makes it less accurate. Due to the complexity of the hydrogen bonding network, it is difficult to obtain the real ice structure by mere cooling liquid water under normal condition without imposing external constraints such as extreme external pressure or electric field. A special rule of proton ordering was followed in order to prepare the real ice structure for our calculations. We succeeded in preparing a hexagonal tetrahedrally coordinated type of ice. The statical properties of this ice were calculated as well as the phonon spectra. The results were compared with neutron diffraction data and other available *ab-initio* calculations.
The molecular dynamics simulations of inclusion complexes of β-cyclodextrin with each of these guest molecules, phenol and aspirin show the encapsulation which are in good agreement with dichroism measurements. The inclusion complex of a dimer calculation of pinacyanol dye with some droplet of water inside γ-cyclodextrin shows structural properties which can be ascribed to the experimental observation of UV/CD spectra of the chromophores, in which there is a split of the excited states of the monomer units. The calculations on chiral molecules of binaphtyl-β-cyclodextrin complex shows a longitudinal axis as preferred axis of entry of the binaphtyl during the inclusion process rather than an axial propagation in agreement with circular dichroism measurements. The investigated chiral separation ability of β-cyclodextrin on the enantiomeric pair of this compound R and S, which differ in symmetry only by reflection, shows that the S-enantiomer has lower energy than the R-enantiomer as revealed by our *ab-initio* calculations.

Contents

List of Figures

List of Tables

1 Introduction

1.1 Biological and organic molecules

Biological research has helped to characterize the incredible diversity of species, ranging from huge mammals to microscopic bacteria that can survive far above the boiling point of water, not to mention the diversity of plants [1]. Talking of the components of complex compounds making up these living species, hydrogen (H), carbon (C), nitrogen (N), sulphur (S) and oxygen (O) are the major elements found in the compounds like the proteins and the carbohydrates. In addition, the most abundant inorganic liquid on earth is important for the reactivity of the latter compounds. The whole cell of living creatures is made up of 70 percent of water which influences the bimolecular structure of the cell. At home, when you open ice cream stored in the freezer for a long time, it is found that it doesn't taste as rich and creamy due to the formation of large ice crystals that cause a coarse texture altering the way the ice cream feels on your palate. During the winter period some parts of the earth surface are covered with cotton-wool-like structure called snows which are also the main product of water.
Most of the foods we eat are derived from plants, and the plants are composed of starch from which the carbohydrates are derived. Most of the drugs man consumes to cure a particular ailment also consist of these essential elements mentioned. To make and preserve these drugs also requires the same class of compounds like the cyclodextrins. Therefore, the study of compounds like cyclodextrins solvents, which provide the favourable medium for their complexation with various types of organic guest compounds, is very necessary to gain insight into their structural and dynamical behaviour.
Both chemistry and most experimental sciences usually rely on a top-down approach. That is, measurements are gradually refined to be able to observe smaller structures, and faster processes until technical limits are reached. Many force-field methods based on the classical approach have been used to study molecules like water clusters and bigger organic molecules like cyclodextrins and proteins in the solvent environment. With the advent of *ab-initio* simulation technique, it is possible to account for the electronic behaviour and binding energy at the quantum level and also to see the atomic motion on a level usually not accessible to experiments. The knowledge gained can be used to return to the drawing table and formulate better models for the phenomena observed, to be able to understand and perhaps manipulate the systems, e.g. melting of small clusters of water of various sizes, and the structural behaviour of the bulk water, in providing the driving force in the encapsulation of the guest compounds in the hydrophobic cavity of the cyclodextrins (see Fig. 1.2) or their derivatives of various diameters. When the simulations reach time and length scales where it is also possible to perform the experiments, the chemistry and physics of the molecules can be traced all the way from individual atoms up to "real-world" macroscopic systems.
Usually the experimental methods can resolve individual atoms, but they are usually not capable of directly quantifying complex collective motions. Indirect methods like the

nuclear magnetic resonance method or the circular dichroism method or spectroscopy can sometimes be applied in combination with theoretical methods to obtain informations of the motions, but these approaches are far from being generally applicable. As it can be noticed or will be noticed later, the most frequent occurring molecules in this thesis are however water molecules as solvent and its freezing form, ice, starting from its cluster units to the bulk, and the other hydrogen bonding organic solvents like linear chain aliphatic methanol, aromatic chain ring phenol and then the giant molecules obtained from these aromatic chains, cyclodextrins.

To the modern physical scientist water is a source of fascination on account of its unusual properties. It is the only chemical compound that occurs naturally in the solid, liquid and vapour phases, and the only naturally occurring inorganic liquid on earth. It displays a formidable array of unusual physical and chemical properties in its condensed phases. It is among the most studied of chemicals, owing, in part, to its ubiquity and its necessity for all life. In addition to these "natural" reasons, water is an interesting compound because it has unique physical properties and is a model hydrogen-bonded liquid [2, 3] and of continuing interest [4]. Much of this interest is due to the role it plays in not only physical chemistry but also biology and atmospheric science [5]. Water is the commonly used solvent in chemistry and yields strong solvent effects on reactions. It participates in most biochemical reactions, and one of the greatest challenges for the simulation of biological systems is to accurately, yet simply, include the microscopic effects of the surrounding H_2O molecules on the properties of complex organic molecules and their interactions [6]. Water also acts as a very efficient energy absorber in the relaxation processes of photochemical reactions. In oder to understand these and other solvents effects, a detailed knowledge of the statical and dynamical properties of water on the molecular level is required [7]. An understanding of small clusters in general and how their properties evolve with size will provide an insight into the bulk behaviour [8]. The bulk water provides a useful medium for any complex reaction. Also water in its freezing form, ice is now becoming popular in the area of physics and chemistry because of the intriguing features of its crystalline form.

Ice is a very interesting and long known solid. Its composition is that of the most abundant liquids on earth and it is the essential component of snow, rain, and the generation of thunderstorm electricity. Liquid water under normal conditions freezes into hexagonal ice. The hexagonal ice called Ice Ih, is one of the most thoroughly disordered crystalline materials and it is the most commonly known phase of ice. The "ordinary" ice Ih has a crystal structure, as far as the position of oxygen atoms are concerned, which can be considered as two inter-penetrating hexagonal closely packed structures. There is a cubic analogue of this structure [9], consisting of two inter-penetrating face-centered cubic lattices based on the points (0,0,0) and (1/4,1/4,1/4), which is a diamond-type structure. It is a metastable variant of ice Ih which can be produced by changing the condition of ice Ih such as lowering the temperature below 150 K. The stacking arrangement of this structure looks similar to that of ice Ih in Fig 1.1 (see Appendix A.2). Ice Ic is a very popular structure for theoretical modelling of ice because of its high symmetry simplifies calculations. It has been found recently from results of molecular dynamics simulation

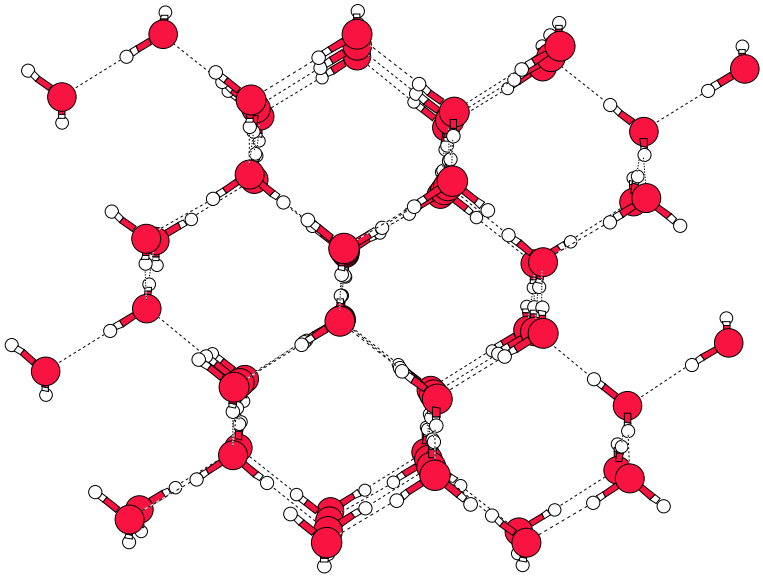

Figure 1.1: Crystal structure of ice showing its hexagonal geometry.

[10] that crystallisation of ice from super-cooled liquid water produces ice Ic when subject to a threshold electric field. The most useful crystallographic experiment on ice Ih is performed with neutron radiation. Neutrons interact strongly with hydrogen, deuterium and oxygen atoms. The scattering power in the neutron case is a constant as a function of the scattering angle and similar for all three elements, whereas in the X-ray case it is proportional to the number of electrons and decreases with increasing scattering angle. Therefore, X-ray experiments are less informative and provide useful data mainly on the lattice constants and the distribution of electrons in the vicinity of the oxygen atoms and between oxygen and hydrogen atoms. The *ab-initio* method has recently gained ground to study the behaviour of ice not only because of its reliability in the study of static and dynamical properties [11,12] but also some important features such as modelling ordered periodic ice structure [13], and also to probe the nature of hydrogen bond in different geometries [14].

One further intriguing aspect of water/ice, not treated in this thesis, should at least be mentioned, since it might be of fundamental importance for technologically exploiting natural gas resources in near future. This is connected with the ability of water to act as host and to form complexes too; here we think of the formation of natural gas hydrates, which are solid, non-stoichiometric compounds of small gas molecules and water with some similarities of the molecular structures with ice. For details we refer to two recent publications [15, 16].

Like water solvent, methanol belonging to the alcohol group compound, is another useful solvent used in many chemical reactions. Numerous efforts have been devoted to its study of small units and its bulk properties. For example, the study of mixed clusters, in which one species is in an excess of another, can provide a useful method of studying solute-solvent interactions [17, 18]. A class of this alcohol group has also been found useful in

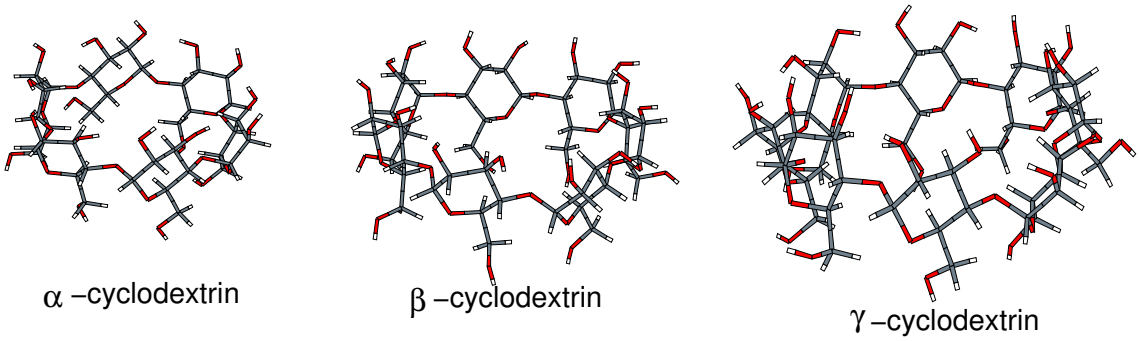

Figure 1.2: The first three family members of cyclodextrins (CDs). Oxygen (O) is in (red) colour, hydrogen (H) in white and carbon (C) in grey.

modifying the chemical nature of cyclodextrins when producing the native derivative of cyclodextrins in the enhancement of its encapsulation ability.
Cyclodextrins are in general truncated doughnut-shaped cyclic oligosaccharides molecules consisting of α-1,4 linked D-glucose units with a hydrophobic interior surface and a hydrophilic external surface. The most prominent and abundant of the cyclodextrins are α, β and γ cyclodextrins with six, seven and eight glucose units, respectively. The first three family members of cyclodextrins are shown in Fig. 1.2. They have the ability to form inclusion compounds, acting as hosts, by allowing other molecules (guests) into their hydrophobic cavity [19–21]. In various sizes and chemical characteristics they are being used in pharmaceutical chemistry as drug delivery systems, in chromatography as enzyme catalysis models or assistants in protein folding and other useful area of inclusion complexes [22]. Of particular interest of these mentioned applications discussed in this thesis are inclusion complexes with organic binaphty derivatives (2,2'-dihydroxy-1,1'-binaphthyl), which are chiral molecules, phenol, aspirin and pinacyanol dye. Most of these inclusion complexes are investigated in the water medium which provides the driving force for the complexation. Binaphtyl molecules are sources of the most important family of auxiliaries, ligands and catalysts employed in the enantioselective reactions [23]. The inclusion complex study of this compound is important to offer information about the stable adduct in the catalytic reaction. In particular, the pinacyanol chloride compound has received wide attention because of its application as a saturable absorber, mode-locker, and sensitizer in imaging technology [24]. Aspirin (acetylsalicylic acid, a phenolic acetate ester) is known to be unstable in aqueous solution. NMR studies show that this compound forms an inclusion complex in unionized form with β-cylcodextrin of various forms in ratio 1:1 [25]. The study of the structures and dynamics properties of these compounds offers more insight into their behaviour at ambient temperature.

1.2 Computer simulations

Computer simulation has proved to be an optimum numerical recipe applicable to problems with many degrees of freedom from quite different fields of science. Development

of the computers during the last decades has led to remarkable achievements in solid state physics as well as in other areas of the natural science. In the year 1953 Metropolis demonstrated that a classical problem of N particles can be solved by means of the Monte-Carlo methods by using computers [26]. Much more sophisticated Monte-Carlo method have been developed to date. They are used to solve a wide range of models describing structural transformations, different kinds of kinetics, etc. Not long after the work of Metropolis, first molecular dynamics (MD) simulation works appeared [27, 28]. In this method, the classical equations of motion are solved for each particle of the system using numerical procedures starting from a pre-specified initial state and subject to a set of boundary conditions appropriate to the problem. The knowledge of the energy or potential landscape of interacting particles, like electrons and atoms, enables one to calculate the forces acting on the particles and to study the evolution of the system with time. The MD methodology allows both equilibrium thermodynamic and dynamics properties of a system at finite temperature to be computed, while simultaneously providing a "window" for the macroscopic motion of individual atoms in the system. Simplicity of this method allows to simulate very big systems. One of the most challenging aspects of an MD calculation is the specification of the forces derived from suitable potentials. Different kinds of interatomic potentials can be used. The more realistic potentials are implemented, the better the comparison with experiment can be done and more physical phenomena can be predicted.
The molecular dynamics methods can be very effective when utilizing realistic model potentials taking into account electronic structure features of the materials. In many applications, these are computed from an empirical model or force *field*, in which simple mathematical forms are employed to describe bond, bend and dihedral angle potentials as well as van der Waals and electrostatic interactions between atoms; the model potential can be parametrized by fitting to experimental data or high level *ab-initio* calculations on small clusters or fragments [29]. Recent simulations using the Embedded-Atom Method (EAM) allowed to observe realistic phenomena of systems of about 10^6 atoms.
The growing power of computers allowed to develop new, so called, *ab-initio* calculation techniques that are of ultimate importance in modern physics. *Ab-initio* means calculation of the properties of a system from first principles with no parametrisation. The main goal of this kind of methods is to solve the Schrödinger equation as accurately as possible, that is in principle a perfect approach for obtaining any desired information on a given system. However, one has to invoke various approximations to solve this problem, while its direct solution is practically impossible. Among many successful approximate approaches that allow to solve *ab-initio* problems, Hartree-Fock and density-functional-based methods are the basis for almost all current electronic-structure methods. Presently, *ab-initio* calculations allow to simulate systems of the order of 100 atoms. Of course, there exists other methods that utilize more approximations and are not really *ab-initio* but allow to simulate systems of about 1000 heavy atoms with moderate precision. In total, the existing methods nearly cover the needs of the theoreticians, but the compromise between the required precision and the available resources must be chosen every time. In order to bridge the gap between the empirical methods (which are fast and efficient

but lack transferability) and *ab-initio* approaches (which are accurate and of excessive computational workload), *tight-binding* (TB) molecular dynamics has emerged as a powerful method for investigating the atomic-scale structure of materials, in particular, the interplay between structural and electronic properties [30–32]. *Tight-binding* retains the fundamental quantum mechanical aspects, as with *ab-initio* methods and in contrast to the empirical methods. It was proposed by Slater and Koster [33] in 1954 as modification of Bloch's Linear Combination of Atomic Orbitals (LCAO) method [34].

1.3 Objective of this work

The objective of this work is to understand the structure formation and thermodynamical properties of the mentioned organic solvents in Section 1.1 like water and its freezing form, ice from its fundamental units at cluster level and the bulk behaviour in the environment of a class of organic compounds such as cyclodextrins and the inclusion complex of these compounds with various guest molecules in the solvent, (water), with the aid of *ab-initio* molecular dynamics technique. Many molecular dynamics and Monte Carlo studies have been carried out on the structure and thermodynamics properties of small clusters of water using the simple Lennard-Jones (LJ) potential [35]. The present study is one of a series of MD simulations which are being undertaken to investigate the properties of small water clusters. Our first aim is to simulate the melting temperature of water clusters $(H_2O)_n$ of selected sizes and show how their properties evolve with size from *ab-initio* type of simulations for a meaningful comparison with calculations using model potentials. The simulation of water at the cluster level provides useful information to the bulk liquid properties.
Since the attention of most research in *ab-initio* field simulation is shifting to the calculation of complex molecules such as carbon nanotube and complex fullerene systems, it is worthwhile investigating the properties of cyclodextrins and its inclusion complexes with various types of guests molecules in the solvent with *ab-initio* and approximate density functional methods and comparing the results of the simulation with respect to the UV/Vis and circular dichroism (CD) spectra. The use of computational chemistry in the area of cyclodextrins has, until recently, been somewhat limited however. The reason for this is not a lack of interest from those studying this material but rather due to the fact that the cyclodextrins are relatively large, flexible molecules that are often studied experimentally in aqueous environments [20]. This makes the computation rather prohibitive and creates a major hurdle which most computational chemists were not willing to surmount, or, as often is the case, forces one to introduce so many assumptions/restrictions so as to become unrealistic. The present study using our *ab-initio* program (VASP) and ab-initio-like (TB) methods tends to provide some challenge to the study of this complex and also gives hope to provide vital information not being accessible experimentally.
In the first part of this work, basic calculations were done on the properties of the above mentioned molecules by using the *ab-initio* type of *density functional tight-binding code* (DFTB) [32] in order to compare the results with previous works known from the literature and to test its reliability. The ground state geometrical configurations of all

the molecules investigated are comparable with some of the existing calculations in the literature. We also tried to investigate the structural and dynamical properties of solvents like water and phenol, and solutes like the crystalline ice and cyclodextrins by MD simulations. Though, the positions of the nearest neighbours are well predicted and agrees with the experimental predictions, the height of the peaks are too high showing too much overstructure (DFTB results).
We also used another highly developed density functional theory code on the ground state properties obtained by DFTB calculations in order to verify some energy differences such as in chiral investigation of one of the chiral guest compounds forming complexes with cyclodextrin where it is difficult to identify such difference in the ground-state complexes formed using the DFTB method. This code, the *Vienna Ab-initio Simulation Package* (VASP) [36], has sophisticated implementations of the pseudo-potential methods but it is computational too expensive to investigate the dynamical properties of the complex molecules.
At the various stages of the calculations discussed in this thesis, we highlight, as far as possible, the similarities and the differences obtained by applying the density-functional related tight binding method (DFTB) and by using the *Vienna Ab-initio Simulation Package* (VASP). While the first method allows to deal with a sufficiently large number of molecules like the interaction of organic molecules in solvents, the later method is more accurate but allows to simulate a smaller number of atoms only. Thus, all our calculations reported here have to be understood to be a compromise between simulation of large system size, and the demand for accuracy simultaneously. The simulations also show which systems sizes are possible today to deal with on the basis of density-functional theory. Large system sizes require more approximate treatments.
We also like to mention that although the basic codes were not developed in Duisburg, we have nevertheless implemented additional features in the DFTB code enabling us to evaluate additional statistical information like distribution functions etc. at different temperatures. We have also founded the very interesting question in how far water changes its properties in the vicinity of organic molecules (for cyclodextrin inclusion complexes in solution) like developing glassy behaviour. Although those investigations are somewhat limited by the use of too small system sizes because of the density-functional methods used here, the first results corresponding to changes in the radial distribution functions look very promising and will certainly require further investigations.
The whole structure and organization of this thesis are as follows: In Chapter 1, we give an overview of the whole thesis. In Chapter 2, we present the basic formalism of density functional theory and various features of the two packages used in the work. The differences are also highlighted. Chapter 3 is devoted to the discussion of the *tight-binding* model which explains some basic implementations of the self-consistence density functional *tight-binding* code applied in this work. In Chapter 4, we present the general features of molecular dynamics simulation and some of the important equations used in the analysis of the structural and dynamical data obtained from the MD runs. In Chapter 5, we present the results of binding energy calculations and melting of some water clusters up to 36 molecules and compare the results to some classical modelled potential calculations.

In Chapter 6 we present the results of structural and dynamical properties of bulk liquid water based on MD simulations using the analysis discussed in Chapter 4. Also in this Chapter, the lattice dynamical properties of ice are investigated based on the lattice dynamical theory which can be found in Appendix under Section A.1. We end this Chapter by presenting a brief structural properties of another hydrogen bonded liquid, methanol, from the radial distribution functions calculated from the MD simulation data obtained. In Chapter 7, we present our results based on the applications of density functional theory and *ab-initio* molecular dynamics to the inclusion complexes of cyclodextrins with the various guest molecules. Following this Chapter is the Summary and concluding remarks. The Appendix contains the basic theory of lattice dynamics which is applied to study the dynamical properties of ice. Also presented are some well known phases of ice which are briefly discussed in the Appendix as well as the other intriguing properties exhibited by the ice structure when compared to other tetrahedrally bonded crystals.

2 The density functional theory formalism

2.1 Introduction and importance

In principle, all knowledge about a system can be obtained from the quantum mechanical wave function. This is obtained (non-relativistically) by solving the Schrödinger equation of the complete many-electron system. However, in practice solving such an N-body problem proves to be impossible. This Section will give a brief description of earlier approximations made to solve this many-body problem and a description of the important physical features omitted from these theories. For these reasons, it is necessary to use density functional theory developed by Kohn and Sham [37] based on the theory of Hohenberg and Kohn [38] which, in principle, is an exact ground state theory. Density Functional theory (DFT) is a powerful, formally exact theory [39–41]. It is a general approach to the *ab-initio* description of quantum many-particle systems, in which the original many-body problem is rigorously recast in the form of an auxiliary single-particle problem [37]. For the most simple case of (nondegenerate) stationary problems, DFT is based on the fact that any ground state observable is uniquely determined by the corresponding ground state density n, i.e., it can be understood as a functional of n. This statement applies in particular to the ground state energy, which allows to (indirectly) represent the effects of the particle-particle interaction as a density-dependent single-particle potential. In addition to the Hartree (direct) contribution this potential contains an exchange-correlation (xc) part, which is obtained from the so-called xc-energy functional. The exact density functional representation of this crucial quantity of DFT is not known, the derivation of suitable approximations being the major task in DFT. Extensions of this scheme to spin-dependent, relativistic or time-dependent systems, utilizing the spin-densities, the four current or the time-dependent density as basic variables, are also available. Recently, a DFT approach to quantum hydrodynamics (as a model for the relativistic description of nuclei) has been developed. The main areas for applications of DFT are condensed matter and cluster physics as well as quantum chemistry [39, 42].

2.1.1 General foundation

Within the scope of this work, only a brief introduction to the density functional method can be given. A comprehensive review of the theoretical basics, strengths, and limitations can be found for instance in [37–40, 42–44].
The general condensed matter (non-relativistic) Hamiltonian of a system of N nuclei described by coordinates R_I, momenta P_I and masses M_I ($I = 1, \ldots, N$) containing N_e electrons described by coordinates r_i, momenta p_i and spin variable s_i ($i = 1, \ldots, N_e$) is given by:

$$H = \sum_{I=1}^{N} \frac{\mathbf{P}_I^2}{2M_I} + \sum_{i=1}^{N_e} \frac{\mathbf{p}_i^2}{2m} + \sum_{i>j}^{N_e,N_e} \frac{e^2}{|\mathbf{r}_i - \mathbf{r}_j|} + \sum_{I>J}^{N,N} \frac{Z_I Z_J e^2}{|\mathbf{R}_I - \mathbf{R}_J|} + \sum_{i,I}^{N,N_e} \frac{Z_I e^2}{|\mathbf{R}_I - \mathbf{r}_i|}$$

$$\equiv T_N + T_e + V_{e-e}(\mathbf{r}) + V_{NN}(\mathbf{R}) + V_{eN}(\mathbf{r}, \mathbf{R}), \tag{2.1}$$

where m is the mass of the electron and $Z_I e$ is the charge on the Ith nucleus. In the second line, T_N, T_e, V_ee, T_{NN}, V_{eN} represent the nuclear and electron kinetic energy operators and electron-electron, nuclear-nuclear and electron-nuclear potential operators, respectively. In order to solve the complete quantum mechanical problem, we start by seeking the eigenfunctions and eigenvalues of this Hamiltonian, which will be given by the solution of the time-independent Schrödinger equation

$$\left[T_N + T_e + V_{e-e}(\mathbf{r}) + V_{NN}(\mathbf{R}) + V_{eN}(\mathbf{r}, \mathbf{R})\right] \Psi(\mathbf{x}, \mathbf{R}) = E\Psi(\mathbf{x}, \mathbf{R}), \tag{2.2}$$

where $\mathbf{x} \equiv (\mathbf{r}, s)$ denotes the full collection of electron position and spin variables, and $\Psi(\mathbf{x}, \mathbf{r})$ is an eigenfunction of H with eigenvalues E.

2.1.2 Born-Oppenheimer approximation

Clearly, an exact solution of Eq. (2.2) is not possible and approximations must be made. One of the most approximations used in materials science is the Born-Oppenheimer approximation [45] which is also used in our investigations. The essence of the approximation is that the nuclei, being so much heavier than the electrons move relatively slowly, and may be treated as stationary while the electrons move relative to them. This means, there is a strong separation of time scales between electronic and nuclear motions. Hence, the nuclei can be thought as being fixed, which makes it possible to solve the Schrödinger equation in Eq. (2.2) for the wavefunction of electrons alone. In terms of Eq. (2.2), this approximation can be exploited by assuming a quasi-separable ansatz of the form

$$\Psi(\mathbf{x}, \mathbf{R}) = \Phi(\mathbf{x}, \mathbf{R})\chi(\mathbf{R}), \tag{2.3}$$

where $\chi(\mathbf{R})$ is the nuclear wavefunction and $\Phi(\mathbf{x}, \mathbf{R})$ is an electronic wavefunction which depends parametrically on the nuclear positions (that is, electrons adiabatically follow the nuclei). We note, at this point, that alternative derivation using a fully separable ansatz to the time-dependent Schrödinger equation was presented by Marx and Hutter in [46]. Substitution of Eq. (2.3) into (2.2) and using the quantum definition of the momentum as $P_x = i\hbar\frac{\partial}{\partial x}$ or $P = i\hbar\nabla$, one obtains by re-arranging Eq. (2.2)

$$\begin{aligned}\left[T_e + V_{ee}(\mathbf{r}) + V_{eN}(\mathbf{r}, \mathbf{R})\right] \Phi(\mathbf{x}, \mathbf{R})\chi(\mathbf{R}) + \left[T_N + V_{NN}(\mathbf{R})\right] \Phi(\mathbf{x}, \mathbf{R})\chi(\mathbf{R}) - \\ \sum_I \frac{\hbar^2}{2M_I} \left(2\nabla_I \Phi(\mathbf{x}, \mathbf{R})\nabla_I \chi(\mathbf{R}) + \chi(\mathbf{R})\nabla_I^2 \Phi(\mathbf{x}, \mathbf{R})\right) = E\Phi(\mathbf{x}, \mathbf{R})\chi(\mathbf{R}).\end{aligned} \tag{2.4}$$

The third term in Eq. (2.4) is not zero, but it is very small compared to the sum of the first two terms of this equation on account of the appearance of the nuclei masses in the denominator. This implies, because of the large masses that the nuclear wavefunction $\chi(R)$ is more localized than electronic wavefunction, i.e. $\nabla_I \chi(\mathbf{r}) \gg \nabla_I \Phi(\mathbf{x}, \mathbf{R})$. So, the

essence of the Born-Oppenheimer approximation is to set this term from Eq. (2.4) to zero, .i.e.,

$$-\sum_I \frac{\hbar^2}{2M_I}\left(2\nabla_I\Phi(\mathbf{x},\mathbf{R})\nabla_I\chi(\mathbf{R})+\chi(\mathbf{R})\nabla_I^2\Phi(\mathbf{x},\mathbf{R})\right)=0, \tag{2.5}$$

so that it can reduce to

$$\frac{[T_e+V_{ee}(\mathbf{r})+V_{eN}(\mathbf{x},\mathbf{R})]\,\Phi(\mathbf{x},\mathbf{R})}{\Phi(\mathbf{x},\mathbf{R})}=E-\frac{[T_N+V_{NN}(\mathbf{R})]\,\chi(\mathbf{R})}{\chi(\mathbf{R})}. \tag{2.6}$$

From the above, it is clear that the left-hand side can only be a function of R alone. Let this function be denoted as $\epsilon(R)$, then

$$\begin{aligned}\frac{[T_e+V_{ee}(r)+V_{eN}(x,R)]\,\Phi(x,R)}{\Phi(x,R)}&=\epsilon(\mathbf{R}),\\ [T_e+V_{ee}(\mathbf{r})+V_{eN}(\mathbf{x},\mathbf{R})]\,\Phi(\mathbf{x},\mathbf{R})&=\epsilon(\mathbf{R})\Phi(\mathbf{x},\mathbf{R}).\end{aligned} \tag{2.7}$$

Eq. (2.6) is an electronic eigenvalue equation for an electronic Hamiltonian, $H_e(\mathbf{R}) = T_e + V_{ee}(\mathbf{r}) + V_{en}(\mathbf{r},\mathbf{R})$, which will yield a set of normalized eigenfunctions $\Phi_n(\mathbf{x},\mathbf{R})$ and eigenvalues $\epsilon(\mathbf{R})$, which depend parametrically on the nuclear positions, $\mathbf{R}$. For each solution, there will be a nuclear eigenvalue equation:

$$[T_N+V_{NN}(\mathbf{R})+\epsilon_n(\mathbf{R})]\,\chi(\mathbf{R})=E\chi(\mathbf{R}). \tag{2.8}$$

Moreover, each electronic eigenvalue, $\epsilon(\mathbf{R})$, will give rise to an electronic surface on which the nuclear dynamics is determined by a time-dependent Schrödinger equation for the time-dependent nuclear wavefunction $\chi(\mathbf{R},t)$:

$$[T_N+V_{NN}(\mathbf{R})+\epsilon_n(\mathbf{R})]\,\chi(\mathbf{R},t)=i\hbar\frac{\partial}{\partial t}\chi(\mathbf{R},t). \tag{2.9}$$

The physical interpretation of Eq. (2.9) is that the electrons respond instantaneously to the nuclear motion; therefore, it is sufficient to obtain a set of instantaneous electronic eigenvalues and eigenfunctions for each nuclear configuration, $\mathbf{R}$ (hence the parametric dependence of $\Phi(\mathbf{x},\mathbf{R})$ and $\epsilon_n(\mathbf{R})$ on $\mathbf{R}$). The eigenvalues, in turn, give, a family of (uncoupled) potential surfaces on which the nuclear wavefunction can evolve. Of course, these surfaces can (and often do) become coupled by so-called non-adiabatic effects not taken into account when using Eq. (2.5).
In many cases, non-adiabatic effects can be neglected, and we may consider motion *only* on the ground electronic surface described by

$$\begin{aligned}[T_e+V_{ee}(\mathbf{r})+V_{eN}(x,\mathbf{R})]\,\Phi_o(\mathbf{x},\mathbf{R})&=\epsilon_o(\mathbf{R})\Phi_o(x,\mathbf{R}),\\ [T_N+\epsilon_o(R)+V_{NN}(R)]\,\chi(R,t)&=i\hbar\frac{\partial}{\partial t}\chi(R,t).\end{aligned} \tag{2.10}$$

Moreover, if nuclear quantum effects can be neglected, then we may arrive at the classical nuclear evolution by assuming that $\chi(\mathbf{R}, t)$ is of the form

$$\chi(\mathbf{R}, t) = A(\mathbf{R}, t)e^{iS(\mathbf{R},t)/\hbar} \tag{2.11}$$

and neglecting all terms involving $\hbar$, which yields an approximate equation for $S(\mathbf{R}, t)$:

$$H_N(\nabla_1 S, \ldots, \nabla_N S, \mathbf{R}_1, \ldots, \mathbf{R}_N) + \frac{\partial S}{\partial t} = 0. \tag{2.12}$$

This is just the classical Hamilton-Jacobi equation with

$$H_N(\mathbf{P}_1, \ldots, \mathbf{P}_N, \mathbf{R}_1, \ldots, \mathbf{R}_N) = \sum_{I=1} \frac{\mathbf{P}_I^2}{2M} + V_{NN}(\mathbf{R}) + \epsilon_o(\mathbf{R}) \tag{2.13}$$

denoting the classical nuclear Hamiltonian. The Hamilton-Jacobi equation is equivalent to the classical motion of the nuclei on the ground-state surface with $E_o(\mathbf{R}) = \epsilon_o(\mathbf{R}) + V_{NN}(\mathbf{R})$ given by

$$\begin{aligned} \dot{\mathbf{R}}_I &= \frac{\mathbf{P}_I}{M_I}, \\ \dot{\mathbf{P}}_I &= -\nabla_I E_o(\mathbf{R}). \end{aligned} \tag{2.14}$$

Note that the force $-\nabla_I E_o(\mathbf{R})$ contains a term from the nuclear-nuclear repulsion and a term from the derivative of the electronic eigenvalue, $\epsilon_o(\mathbf{R})$. Because of the Hellman-Feynman theorem, the latter can be expressed as

$$\nabla_I \epsilon_o(\mathbf{R}) = \langle \Phi_o(\mathbf{R}) | \nabla_I H_e(\mathbf{R}) | \Phi_o(\mathbf{R}) \rangle. \tag{2.15}$$

Equations (2.14) and (2.15) form the theoretical basis of the *ab-initio* molecular dynamics (AIMD) approach. The practical implementation of the AIMD method requires an algorithm for the numerical solution of Eq. (2.14) with forces from (2.13) at each step of the calculation. Moreover, since an exact solution for the ground-state electronic wavefunction, $|\Phi_o(\mathbf{R})\rangle$, and eigenvalue, $\epsilon_o(\mathbf{R})$, is not available, in general, it is necessary to introduce an approximation scheme for obtaining these quantities.

2.2 Representation of electronic structure and various approximations

At this point, a simple form for $E_o(\mathbf{R})$ could be introduced, giving rise to a force field based approach. Such a form would necessarily be specific to a particular system and therefore, not be transferable to other situations. If, on the other hand, one derives forces directly from very accurate electronic structure calculations, the computational overhead associated with the method will be enormous. It is clear, therefore, that the practical utility of the AIMD approach relies on a compromise between accuracy and efficiency of the electronic structure representation based on available computing resources. One approach which has proved particularly successful in this regard is density functional theory (DFT) which is based on the Hohenberg-theorem [38].

2.2.1 The Hohenberg-Kohn theorem

If we consider specifically the ground-state to be calculated by Eq. (2.7), the total energy must be the extremal. That allows to formulate a strong condition as was done by Pierre Hohenberg and Walter Kohn [38]: In the ground-state, the total energy is a functional of the electronic density $n_o(\mathbf{r})$. In order to distinguish between the first and second Hohenberg-Kohn theorem, we begin by specifying once again the many-electron Hamiltonian in Eq. (2.7),

$$H[u] = \underbrace{-\frac{\hbar^2}{2m}\sum_{i=1}^{N_e}\nabla_i^2}_{\equiv T_e} + \underbrace{\sum_{i=1}^{N_e} u(x_i)}_{\equiv V_{eN}} + \underbrace{\frac{1}{2}\sum_{i\neq j} v(x_i,x_j)}_{\equiv V_{ee}}, \tag{2.16}$$

where

$$u(x_i) = \sum_J \frac{Z_J e}{|\mathbf{r}_i - \mathbf{R}_J|} \tag{2.17}$$

is some external potential due to the electron-nuclei interaction which is allowed to vary and

$$v(x_i,x_j) = \frac{e^2}{|\mathbf{r}_i - \mathbf{r}_j|} \tag{2.18}$$

stems from the electron-electron interaction, V_{ee}. Each external potential defines a corresponding ground-state wavefunction via solution of the Schrödinger equation. Such wavefunctions are of course different for u_1 and u_2, if $u_1(\mathbf{r}) \neq u_2(\mathbf{r})+$ constant. Let ψ_1 be the ground-state wavefunction corresponding to the external potential u_1, the corresponding total energy is:

$$\epsilon_1 = \langle\psi_1|H[u_1]|\psi_1\rangle = \langle\psi_1|T_{ee}+V_{ee}|\psi_1\rangle + \int u_1(\mathbf{r})n(\mathbf{r})d\mathbf{r}. \tag{2.19}$$

This must be lower than the expectation value obtained with *any* other wavefunction ψ_2 according to the variation principle, i.e,

$$\begin{aligned}\epsilon_1 &< \langle\psi_2|H[u_1]|\psi_2\rangle,\\ \epsilon_1 &< \langle\psi_2|H[u_2]-u_2+u_1|\psi_2\rangle,\end{aligned}$$

$$\epsilon_1 < \underbrace{\langle\psi_2|H[u_2]|\psi_2\rangle}_{\equiv\epsilon_2} + \int d\mathbf{r}\,[u_1(\mathbf{r})-u_2(\mathbf{r})]\underbrace{N_e\int\psi_2^*(\mathbf{r}_2\ldots\mathbf{r}_N)\psi_2(\mathbf{r}_2....\mathbf{r}_N)d\mathbf{r}_2\ldots d\mathbf{r}_N}_{\equiv n(\mathbf{r})}. \tag{2.20}$$

On the other side, the ground-state energy ϵ_2 calculated with its "true" wavefunction ψ_2 must be lower than the expectation value of $H[u_2]$ calculated with any other wavefunction, including ψ_1 :

$$\begin{aligned}\epsilon_2 &< \langle\psi_1|H[u_2]|\psi_1\rangle,\\ \epsilon_2 &< \langle\psi_1|H[u_1]-u_1+u_2|\psi_1\rangle,\end{aligned}$$

$$\epsilon_2 < \underbrace{\langle\psi_1|H\left[u_1\right]|\psi_1\rangle}_{\equiv\epsilon_1} + \int d\mathbf{r}\left[u_2(\mathbf{r}) - u_1(\mathbf{r})\right] \underbrace{N_e \int \psi_1^*(\mathbf{r}_2 \ldots \mathbf{r}_N)\psi_1(\mathbf{r}_2 \ldots \mathbf{r}_N)d\mathbf{r}_2 \ldots d\mathbf{r}_N}_{\equiv n(\mathbf{r})}. \tag{2.21}$$

Summing up the two inequalities, we arrive at $\epsilon_1 + \epsilon_2 < \epsilon_2 + \epsilon_1$, which is a contradiction. The origin of this contradiction is that we have assumed $n(\mathbf{r})$ to be the same for the two wavefunctions generated by the two different potentials, u_1 and u_2. Hence this assumption was wrong, and the external potential *uniquely* determines the density. Since $n\left[u_1\right] \neq n\left[u_2\right]$, for $u_1 \neq u_2+$ constant, for any given $n(\mathbf{r})$ there is at most one potential $u(\mathbf{r})$ for which $n(\mathbf{r})$ is the ground-state density. At this point, one sometimes singles out as the first Hohenberg-Kohn theorem:

- It states that the ground state energy ϵ of a system of electrons in an external potential, $u(\mathbf{r})$ given by

$$u(\mathbf{r}) \;=\; \sum_J \; -\frac{Z_J}{|\mathbf{r} - \mathbf{R}_J|}$$

  is a unique functional of the electron density $n(\mathbf{r})$, $\epsilon \equiv \epsilon\left[n\right]$. In other words, for an isolated many-electron system, its ground-state one-electron density $n_o(\mathbf{r})$ determines uniquely the external potential $u(\mathbf{r})$ (or simply $V_{eN}(\mathbf{r})$). The ground state density, $n_o(\mathbf{r})$, is given in terms of the ground-state wavefunction Φ_o by

$$n_o(\mathbf{r}) = \sum_{s, s_2, \ldots s_{N_e}} \int d\mathbf{r}_2 \ldots d\mathbf{r}_{N_e} |\Phi_o\left(\mathbf{r}, s, \mathbf{r}_2, s_2, \ldots, \mathbf{r}_{N_e}\right)|^2. \tag{2.22}$$

As second Hoheberg-Kohn theorem:

- The functional $\epsilon\left[n\right]$ has its minimum value when $n(r)$ is the ground state electron density, $n_{sc}(\mathbf{r})$,

$$\epsilon\left[n\right] \;\geq \epsilon\left[n_{sc}\right].$$

  The energy $\epsilon\left[n_{sc}\right]$ is the electronic part of the total energy $E(\{R_J\})$,

$$E(\{\mathbf{R}_J\}) \;=\; \epsilon\left[n_{sc}\right] + \frac{1}{2} \sum_{I,J} \frac{Z_I Z_J}{|\mathbf{R}_I - \mathbf{R}_J|},$$

  here $n_o \equiv n_{sc}$, i.e., self-consistent ground-state. In other words, the exact ground-state energy $\epsilon = \epsilon\left[\phi_o\right]$ of a many-electron system with the external potential $u(\mathbf{r})$ is a functional of the associated ground-state electron density $n_o(\mathbf{r})$, i.e., the electron density $n_o(\mathbf{r})$ minimizes the functionals. This second statement follows from the fact that since $u(\mathbf{r})$ uniquely fixes H and hence the many-particle ground state, the latter must be a unique functional of $n(\mathbf{r})$:

$$\epsilon\left[n\right] = F\left[n\right] + \int n(\mathbf{r})u(\mathbf{r})d\mathbf{r}. \tag{2.23}$$

$F[n]$ in Eq. (2.23) is a universal functional of n and the minimum value of the functional $\epsilon[n]$ is $\epsilon_o = \epsilon[n_o]$, the exact ground-state electronic energy. Levi [47] gave a particular simple proof of the second Hohenberg-Kohn theorem which is as follows: A function O is defined as

$$O[n(\mathbf{r})] = \min_{|\Phi\rangle \to n(\mathbf{r})} \langle \Phi | \hat{O} | \Phi \rangle, \tag{2.24}$$

where the expectation value is found by searching over all wavefunction Φ, given the density $n(\mathbf{r})$ and selecting the wavefunction which minimizes the expectation value of $\hat{O}$. $F[n(\mathbf{r})]$ is defined by

$$F[n(\mathbf{r})] = \min_{|\Phi\rangle \to n(\mathbf{r})} \langle \Phi | \hat{F} | \Phi \rangle, \tag{2.25}$$

so that from Eq. (2.23) $\hat{F}[n(\mathbf{r})]$ is given by

$$\hat{F}[n(\mathbf{r})] = -\frac{\hbar^2}{2m} \sum_i \nabla_i^2 + \sum_{i>j} \frac{e^2}{|\mathbf{r}_i - \mathbf{r}_j|}. \tag{2.26}$$

Considering an N_e ground-state wavefunction $\Phi_o(\mathbf{r}, s) \equiv \langle \mathbf{r}, s | \Phi_o \rangle$ which yields a density $n_o(\mathbf{r})$ as defined through Eq. (2.23), then from the definition of the functional ϵ in Eq. (2.23) using (2.24),

$$\epsilon[n(\mathbf{r})] = F[n] + \int n(r) u(\mathbf{r})\, d\mathbf{r} = \langle \Phi | \hat{F} + V_{eN} | \Phi \rangle. \tag{2.27}$$

The Hamiltonian is given by $\hat{F} + V_{eN}$ and so $\epsilon[n(\mathbf{r})]$ must obey the variational principle,

$$\epsilon[n(\mathbf{r})] \geq \epsilon_o. \tag{2.28}$$

This completes the first part of the proof, which places a lower bound on $\epsilon[n(\mathbf{r})]$. From the definition of $F[n(\mathbf{r})]$ in Eq. (2.25), we obtain

$$F[n_o(r)] \leq \langle \Phi_o | \hat{F} | \Phi_o \rangle, \tag{2.29}$$

since Φ_o is a trial wavefunction yielding $n_o(\mathbf{r})$. Combining $\int n(\mathbf{r}) u(\mathbf{r})\, d\mathbf{r}$ with the above equation gives

$$\epsilon[n_o(\mathbf{r})] \leq \epsilon_o, \tag{2.30}$$

which in combination with Eq. (2.28) yields the key result

$$\epsilon[n_o(\mathbf{r})] = \epsilon_o, \tag{2.31}$$

completing the proof.

2.2.2 The basic Kohn-Sham equations

Once the Born-Oppenheimer approximation has been made, the ground state energy, $\epsilon_o(\mathbf{R})$ (for any given arrangement of the nuclei) can be obtained by solving the Schrödinger equation for the interacting electrons moving in the fixed external potential due to the frozen nuclei. A consequence of the Hohenberg-Kohn theorem is that the exact ground-state according to the DFT, is the minimum of a certain functional, $\epsilon\,[n]$, over all electronic densities $n(\mathbf{r})$ that can be associated with an antisymmetric ground-state wavefunction, $|\Phi_o\rangle$, of a Hamiltonian H_e for some potential V_{eN} (the so-called $u-$representability condition, that is, the mathematical formulation of existence of one-to-one mapping between ground-state electronic densities and external potentials) subject to the restriction that

$$\int n(\mathbf{r})\; d\mathbf{r} = N_e. \tag{2.32}$$

The theorem can also be extended to so-called $N-$representable densities (obtained from any antisymmetric wavefunction) via Levy's prescription [39, 48]. The functional is given as

$$\epsilon\,[n] = T\,[n] + W\,[n] + V\,[n]\,, \tag{2.33}$$

where $T\,[N]$ and $W\,[N]$ represent the kinetic energy and Coulomb repulsion energies, respectively, and

$$V\,[n] = \int \mathbf{dr}\, V_{eN}(\mathbf{r}) n(\mathbf{r}). \tag{2.34}$$

Although the functional $T\,[N]+W\,[N]$ is universal (as earlier defined by $F\,[N]$ in Eq. (2.23)) for all systems of N_e electrons, its form is not known. Thus, in order that DFT be of practical utility, Kohn and Sham (KS) introduced the idea of a non-interacting reference system with potential $V_{\mathrm{KS}}(\mathbf{r}, \mathbf{R})$ such that the ground-state energy and density of the non-interacting system equal those of the true interacting system [37]. Within the KS formulation of DFT, a set of n_{occ} orthonormal single-particle orbitals, $\psi_i(\mathbf{r}),\ i = 1, \ldots, n_{occ}$, with occupation numbers f_i,

$$\sum_{i=1}^{n_{occ}} f_i = N_e \tag{2.35}$$

is introduced. These are known as the KS orbitals. In terms of the KS orbitals, the density is given by

$$n(\mathbf{r}) = \sum_{i=1}^{n_{occ}}\; f_i |\psi_i(\mathbf{r})|^2, \tag{2.36}$$

with

$$\int d\mathbf{r}\; |\psi_i(\mathbf{r})|^2 = 1. \tag{2.37}$$

From Eq. (2.23), the total energy functional $\epsilon = \epsilon[n]$ is divided into two parts for practical purpose,

$$\epsilon[n] = T_s[n] + F[n], \tag{2.38}$$

where $T_s[n]$ is the kinetic energy of an imaginary noninteracting (except via Pauli's exclusion principle) electron gas moving in that external potential which induces a ground-state density equal to $n(\mathbf{r})$. Since *not* all densities are possible ground-state densities of a system of noninteracting electrons, the functional T_s and therefore, F are not always defined (although, see Levy [49]). Densities which do correspond to the possible noninteracting ground states are called "wavefunction noninteracting u representable" as earlier discussed. These are the *only* densities for which Eq. (2.38) makes sense. $T_s[n]$ is not the same as the kinetic energy of the real interacting system, but the hope is that it is roughly similar in magnitude.
$F[n]$ must contain some simple electrostatic terms as stated in Eq. (2.33) and so we write

$$F[n] = \frac{e^2}{2}\iint d\mathbf{r}\, d\mathbf{r}'\ \frac{n(\mathbf{r})n(\mathbf{r}')}{|\mathbf{r}-\mathbf{r}'|} + \epsilon'_{xc}[n] + \int d\mathbf{r}\, n(\mathbf{r})\, V_{eN}(\mathbf{r},\mathbf{R}). \tag{2.39}$$

This equation also acts as a definition of the exchange and correlation functional $\epsilon'_{xc}[n]$. Since we have approximated the kinetic energy of the true system (T_{ee}), in which the interaction is actually present by T_s (or $T_{nonint}\{\psi_i\}$), in which the interaction is switched off by using the wavefunctions constructed from $\{\psi_i\}$ which are not truly one-particle representations of the density, this introduces errors which is attributed to the yet undefined part, which describes the electron-electron interaction. The total energy $\epsilon = E_{tot}$ from Eq. (2.23) using (2.39) is

$$E_{tot} = T_{ee}[n] + \frac{e^2}{2}\iint d\mathbf{r}\, d\mathbf{r}'\ \frac{n(\mathbf{r})n(\mathbf{r}')}{|\mathbf{r}-\mathbf{r}'|} + \epsilon'_{xc}[n] + \int d\mathbf{r}\, n(\mathbf{r})\, V_{eN}(\mathbf{r},\mathbf{R}). \tag{2.40}$$

which is now substituted by

$$E_{tot} = T_s[n_o] + \frac{e^2}{2}\iint d\mathbf{r}\ d\mathbf{r}'\ \frac{n(\mathbf{r})n(\mathbf{r}')}{|\mathbf{r}-\mathbf{r}'|} + \epsilon_{xc}[n] + \int d\mathbf{r}\, n(\mathbf{r})\, V_{eN}(\mathbf{r},\mathbf{R}), \tag{2.41}$$

where

$$\epsilon_{xc}[n] = \epsilon'_{xc}[n] + T_{ee}[n] - T_s[n_o]. \tag{2.42}$$

Here ϵ_{xc} contains also the correction term from the true kinetic energy T_{ee} which is now approximated by T_{nonint}. Equation (2.41) also takes the form

$$E_{tot} = \epsilon[\{\psi_i\}] = -\frac{\hbar^2}{2m}\sum_{i=1}^{n_{occ}} f_i\langle\psi|_i\nabla^2|\psi_i\rangle + \frac{e^2}{2}\iint d\mathbf{r}\, d\mathbf{r}'\ \frac{n(\mathbf{r})n(\mathbf{r}')}{|\mathbf{r}-\mathbf{r}'|} + \epsilon_{xc}[n]$$

$$+ \int d\mathbf{r}\, n(\mathbf{r})\, V_{eN}(\mathbf{r},\mathbf{R}),$$

$$\equiv T_{nonint}\left[\{\psi\}\right] + J\left[n\right] + \epsilon_{xc}\left[n\right] + V\left[n\right], \tag{2.43}$$

where $T_s\left[n\right] = T_{nonint}\left[\{\psi\}\right]$ in the functional represents the quantum kinetic energy of the non-interacting electron gas with density $n(\mathbf{r})$ and not the kinetic energy of the real system,

$$T_{nonint}\left[\{\psi\}\right] = -\frac{\hbar^2}{2m}\sum_{i=1}^{n_{occ}} f_i\langle\psi|_i\nabla^2|\psi_i\rangle, \tag{2.44}$$

and where the second term $J\left[n\right]$ is the direct Coulomb term from Hartree-Fock theory (which also includes self-interaction),

$$J\left[n\right] = \frac{e^2}{2}\iint d\mathbf{r}\, d\mathbf{r}'\,\frac{n(\mathbf{r})n(\mathbf{r}')}{|\mathbf{r}-\mathbf{r}'|}, \tag{2.45}$$

the third term is the exact exchange-correlation energy, whose form is unknown, and the fourth term is the interaction of the electron density with the external potential due to the nuclei. Equation (2.41) is re-casted into the form

$$E_{tot} = T_{nonint}\{\psi\} + \int V_{eff}(\mathbf{r})n(\mathbf{r})d\mathbf{r}. \tag{2.46}$$

In order to obtain V_{eff} in Eq. (2.46), we simply carry out the functional derivative of Eq. (2.41) bearing in mind that the functionals of the term containing the external potential and electron-electron interaction term are calculated to first order only (i.e., neglecting the second order or higher order terms), by using

$$n(\mathbf{r}) \rightarrow n(\mathbf{r}) + \delta n(\mathbf{r}). \tag{2.47}$$

In addition we use the second theorem of Hohenberg-Kohn, for the correct ground-state density,

$$\delta E_{tot}\left[n\right] \equiv \delta E_{tot}\left[n+\delta n\right] - E_{tot}\left[n\right] = 0. \tag{2.48}$$

Also we recall from (2.32) that

$$\int n(r)d\mathbf{r} = N_e \;\; \text{(which does not change)} \tag{2.49}$$

Equation (2.49) and (2.48) are then combined by using a Langragian multiplier (μ) to

$$\delta\left\{E_{tot}\left[n\right] - \mu\left[\int n(\mathbf{r})d\mathbf{r} - N_e\right]\right\} = 0. \tag{2.50}$$

This is true for *any* variation of n. Now using the functional derivative, we obtain:

$$\frac{\delta}{\delta n(\mathbf{r})}\left\{E_{tot}\left[n\right] - \mu\left[\int n(\mathbf{r})d\mathbf{r} - N_e\right]\right\} = 0. \tag{2.51}$$

By using this formalism and the definition ϵ'_{xc} in Eq. (2.41) we obtain,

$$\frac{\delta T_{nonint}}{\delta n} + V_{ee} + \frac{\delta \epsilon_{xc}}{\delta n} + V_{eN} = \mu. \tag{2.52}$$

or

$$\frac{\delta T_{nonint}}{\delta n} + V_{eff}(\mathbf{r}) = \mu. \tag{2.53}$$

Therefore, our V_{eff} is now

$$V_{eff}(\mathbf{r}, \mathbf{R}) = e^2 \int \frac{n(\mathbf{r}')}{|\mathbf{r} - \mathbf{r}'|} d\mathbf{r}' + \frac{\delta \epsilon_{xc}}{\delta n(\mathbf{r})} + V_{eN}(\mathbf{r}, \mathbf{R}). \tag{2.54}$$

Thus, the KS potential is given by V_{eff} in Eq. (2.54), i.e.,

$$V_{\mathrm{KS}}(\mathbf{r}, \mathbf{R}) = e^2 \int \frac{n(r')}{|\mathbf{r} - \mathbf{r}'|} d\mathbf{r}' + \frac{\delta \epsilon_{xc}}{\delta n(\mathbf{r})} + V_{eN}(\mathbf{r}, \mathbf{R}), \tag{2.55}$$

and the Hamiltonian of the non-interacting system is therefore known as *Kohn-Sham equations*:

$$H_{\mathrm{KS}} \psi_i(\mathbf{r}) = \epsilon_i \psi_i(\mathbf{r}), \tag{2.56}$$

where ϵ_i are the KS energies. Equation (2.56) constitutes a self-consistent problem because the KS orbitals ($\psi_i(\mathbf{r}) = \psi_i^{\mathrm{KS}}(\mathbf{r})$) are needed to compute the density,

$$n(\mathbf{r}) = \sum_i^{n_{occ}} f_i \, |\psi_i^{\mathrm{KS}}(\mathbf{r})|^2, \tag{2.57}$$

which is needed to specify the KS Hamiltonian. However, the latter must be specified in oder to determine the orbitals and orbital energies. The KS operator H_{KS} depends *only* on $\mathbf{r}$, and upon the index of the electron. Now, we can summarize the Kohn-Sham equations to be solved as follows:

$$\left(\frac{1}{2} \nabla^2 + V_{eff}(\mathbf{r}, \mathbf{R}) \right) \psi_i^{\mathrm{KS}}(\mathbf{r}) = \epsilon_i \psi_i^{\mathrm{KS}},$$

$$V_{eff}(\mathbf{r}, \mathbf{R}) = V_{es}(\mathbf{r}, \mathbf{R}) + V_{exc}([n(\mathbf{r})]\,; \mathbf{r}),$$

$$n(\mathbf{r}) = 2 \sum_i^{N_e/2} f_i \, |\psi_i^{\mathrm{KS}}(\mathbf{r})|^2,$$

$$V_{es}(\mathbf{r}, \mathbf{R}) = \int \frac{n(\mathbf{r}')}{|\mathbf{r} - \mathbf{r}'|} d\mathbf{r}' - \sum_J \frac{Z_J}{|\mathbf{r} - \mathbf{R}_J|},$$

together with the related Poisson equation,

$$\nabla^2 V_{es}(\mathbf{r}, \mathbf{R}) = -4\pi n(\mathbf{r}),$$

where $V_{xc} = \delta \epsilon_{xc} / \delta n(\mathbf{r})$ as defined in equation (2.52).

2.3 Approximation for the exchange-correlation energy

The exchange-correlation energy $\epsilon_{xc}[n(\mathbf{r})]$ can be interpreted as resulting from the interaction of an electron with the exchange-correlation hole surrounding it [50–52]:

$$\epsilon_{xc}[n(\mathbf{r})] = \frac{e^2}{2}\int d\mathbf{r}\; n(\mathbf{r}) \int d\mathbf{r}'\, \frac{n_{xc}(\mathbf{r}, \mathbf{r}' - \mathbf{r})}{|\mathbf{r} - \mathbf{r}'|}. \tag{2.58}$$

In general, the exchange-correlation hole $n_{xc}(\mathbf{r}, \mathbf{r}' - \mathbf{r})$ describes the effect of the Coulomb repulsion (an electron present at a point $\mathbf{r}$ changes the probability of finding another one at $\mathbf{r}'$). It is possible to derive an exact expression for $n_{xc}(\mathbf{r}, \mathbf{r}' - \mathbf{r})$ by considering a modified electron-electron interaction $\lambda/|\mathbf{r} - \mathbf{r}'|$ and varying λ from 0 (non-interacting system) to 1 (physical system). This has to be done in the presence of an additional external potential $V_\lambda(\mathbf{r})$ [42, 53], such that the ground state of the Hamiltonian

$$H_\lambda = -\frac{\hbar^2}{2m}\nabla^2 + V_{eN}(\mathbf{r}) + V_\lambda + \lambda V_{ee} \tag{2.59}$$

has the ground-state density $n(r)$ for *all* λ. The density $n_{xc}(\mathbf{r}, \mathbf{r}' - \mathbf{r})$ can be expressed in terms of the pair correlation function $g(\mathbf{r}, \mathbf{r}' - \mathbf{r}, \lambda)$ by

$$n_{xc}(\mathbf{r}, \mathbf{r}' - \mathbf{r}) \equiv n(\mathbf{r}') \int_0^1 d\mathbf{r}\, [g(\mathbf{r}, \mathbf{r}', \lambda) - 1]\,. \tag{2.60}$$

Three observations should be made from this expression:

- First, since $g(\mathbf{r}, \mathbf{r}') \to 1$ as $|\mathbf{r} - \mathbf{r}'| \to \infty$, the above separation into electrostatic and exchange correlation energies can be viewed as an approximate separation of the consequence of long- and short-range effects, respectively, of the Coulomb interaction. We may then expect that the total interaction energy will be less sensitive to changes in the density, since the long-range part can be calculated exactly.

- The second observation [50] arises from the isotropic nature of the Coulomb interaction V_{ee} and has important consequences. A variable substitution in Eq. (2.58) yields

$$\epsilon_{xc} = \frac{e^2}{2}\int d\mathbf{r}\, n(\mathbf{r}) \int_o^\infty d\mathbf{R}\, \mathbf{R}^2 \frac{1}{\mathbf{R}} \int d\Omega\; n_{xc}(\mathbf{r}, \mathbf{R}). \tag{2.61}$$

  Equation (2.61) shows that the exchange-correlation energy depends only on the average $n_{xc}(\mathbf{r}, \mathbf{R})$, so that the approximation for ϵ_{xc} can give an *exact* value even if the description of the nonspherical parts of n_{xc} is quite inaccurate.

- Third, from the definition of the pair correlation function, there is a sum rule which requires that the exchange-correlation hole contains one electron, i.e., for all $\mathbf{r}$,

$$\int d\mathbf{r}'\, n_{xc}(\mathbf{r}, \mathbf{r}' - \mathbf{r}) \;=\; -1. \tag{2.62}$$

This means that we can consider $-n_{xc}(\mathbf{r}, \mathbf{r}' - \mathbf{r})$ as a normalized weight factor and can define locally the radius of the exchange-correlation hole,

$$\left\langle \frac{1}{\mathbf{R}} \right\rangle_{\mathbf{r}} = -\int d\mathbf{r}\, \frac{n_{xc}(\mathbf{r}, \mathbf{R})}{|\mathbf{R}|}. \tag{2.63}$$

This leads to

$$\epsilon_{xc} = -\frac{1}{2} \int d\mathbf{r}\; n(\mathbf{r}) \left\langle \frac{1}{\mathbf{R}} \right\rangle_{\mathbf{r}}, \tag{2.64}$$

showing that, provided the sum rule (2.62) is satisfied, the exchange-correlation energy depends only weakly on the details of n_{xc} [50]. In fact, we can say that it is determined by the first moment of a function whose second moment we know exactly.

2.3.1 Local density approximation

The preceeding discussion makes clear that the DFT is in principle, an exact theory for the ground state of a system. However, because the exchange-correlation functional defined to be

$$\epsilon_{xc}[n] = T[n] - T_{nonint}[\{\psi\}] + W[n] - J[n] \tag{2.65}$$

is unknown, in practice, approximations must be made. One of the most successful approximations is the so-called *local-density approximation* (LDA) or *local-spin-density approximation* (LSDA), in which the functional is taken to be the spatial integral over a local function that depends *only* on the density:

$$\epsilon_{xc}[n] \approx \int d\mathbf{r}\, f_{LDA}(n(\mathbf{r})), \tag{2.66}$$

where $n(\mathbf{r})$ could also be extended to the spin polarized systems, i.e, $n(r)_\uparrow$ and $n(r)_\downarrow$. The LDA or LSDA is physically motivated by the notion that the interaction between the electrons and the nuclei creates only weak inhomogeneities in the electron density. Therefore, the form of f_{LDA} is obtained by evaluating the exact expressions for the exchange and correlation energies of a homogeneous electron gas of uniform density n at the inhomogeneous density $n(\mathbf{r})$.
Typically, the exchange-correlation term is split into exchange and correlation effects,

$$\epsilon_{xc}[n_\uparrow, n_\downarrow] = \epsilon_x[n_\uparrow, n_\downarrow] + \epsilon_c[n_\uparrow, n_\downarrow]. \tag{2.67}$$

The exchange part is easily evaluated via an analytic Hartree-Fock treatment of the uniform electron gas:

$$\epsilon_x[n_\uparrow, n_\downarrow] = -\frac{3}{2}\left(\frac{3}{4\pi}\right)^{\frac{1}{3}} \left[n_\uparrow^{\frac{4}{3}} + n_\downarrow^{\frac{4}{3}}\right], \tag{2.68}$$

and the correlation part is determined by a mixture of analytic treatments and Monte Carlo simulations. Usually these numerical results for ϵ_c are fitted to a simple parameterized form one of the most popular early parametrizations were given by Perdew and Zunger (PZ) [54] who fitted the non-polarized result $\varepsilon_c(\frac{n}{2}, \frac{n}{2})$ and the completely spin-polarized result $\varepsilon_c(n, 0)$. The result for a partially polarized gas is obtained by a weighting procedure [55]:

$$\varepsilon_c\left(n_\uparrow, n_\downarrow\right) = \varepsilon_c(\frac{n}{2}, \frac{n}{2}) + f(\xi)\left[\varepsilon_c(n,0) - \varepsilon_c(\frac{n}{2}, \frac{n}{2})\right], \tag{2.69}$$

where

$$\xi = \frac{n_\uparrow - n_\downarrow}{n} \tag{2.70}$$

and

$$f(\xi) = \frac{(1+\xi)^{\frac{4}{3}} + (1-\xi)^{\frac{4}{3}} - 2}{2^{\frac{4}{3}} - 2}. \tag{2.71}$$

An alternative parametrization has been given by Vosko-Wilk-Nusair (VWN) [56]. More recently, a new form has been been suggested by Perdew and Wang [57] with a number of improvements over the previous work. This may be the most accurate representation available at present, but for most computational purposes the PZ, VWN and VW parametrization give very similar results.
These formula have been widely used over the last two decades to model an enormous variety of systems ranging over atoms, molecules, clusters and solids and have made significant contribution to a number of areas of physics, chemistry, materials science and biology. The accuracy has been remarkable, and more than expected from such an approach, see the discussion in [58].

2.3.2 Generalized gradient approximation

In many instances of importance in chemistry, however, the electron density possesses sufficient inhomogeneities such that the LDA breaks down. This is in particular true in hydrogen-bonded systems, for example. In such cases, the LDA can be improved by adding an additional dependence on the lowest order gradients of the density:

$$\epsilon\left[n\right] \approx \int d\mathbf{r}\ f_{\mathrm{GGA}}(n(\mathbf{r}), |\nabla^2 n(\mathbf{r})|), \tag{2.72}$$

which is known as *generalized gradient approximation* (GGA). Among most widely used GGAs are those of Becke [59], Lee and Paar [60], Perdew and Wang [57], Perdew *et al.* [61] and Cohen and Handy [62–64]. Typically, these can be calibrated to reproduce some subset of the known properties by the exact exchange-correlation functional. GGAs such as these have been used successfully in nearly all the application areas of *ab-initio* calculations [29]. However, GGAs are also known to underestimate transition state barriers and

cannot adequately treat dispersions. Attempts to incorporate dispersion interactions in an empirical way have been recently proposed [65]. In order to improve reaction barriers, new approximation schemes such as Becke's 1992 functional [66], which incorporates exact exchange, and the so-called meta-GGA functionals [67–70], which include an additional dependence on the electron kinetic energy density,

$$\tau(\mathbf{r}) = \sum_{i}^{n_{occ}} f_i |\nabla \psi_{\mathbf{r}}|^2 \tag{2.73}$$

has successfully been used. However, the problem of designing accurate approximate exchange-correlation functionals remains one of the greatest challenges in DFT.
Finally, in order to overcome the limitations of DFT in the context of AIMD, it is, of course possible to employ a more accurate electronic structure method. Approaches using full configuration-interaction representations have been proposed [71]. Typically, these have a higher-computational overhead and, therefore, can only be used to study much smaller systems such as very small clusters. However, as computing platforms become more powerful and new algorithms are developed, it is conceivable that other electronic methods may be used more routinely in AIMD studies.

2.4 Basis set expansions and pseudopotentials

In order to use DFT for practical applications, the Kohn-Sham orbitals $\psi_i(r)$ need to be represented in some ways. Probably the most straight-forward approach is to solve the problem on a real-space grid without any further restrictions. However, since this approach leads to a lot of numerical difficulties, the majority of all DFT implementations is based on expanding the $\psi_i(r)$ in terms of suitable basis functions $\varphi_\mu(r)$:

$$\psi_i(\mathbf{r}) = \sum_{\mu=1}^{N} c_{\mu i} \varphi_\mu(\mathbf{r}), \tag{2.74}$$

where the $c_{\mu i}$ are termed expansion coefficients. In principle, any functional set $\{\varphi_\mu(\mathbf{r})\}$, which represents a complete basis in the considered configuration space, could be used. However, since such a complete set cannot be managed numerically, one has to resort to sufficiently accurate incomplete basis sets. Two classes of functions are commonly applied: plane waves (PW) and localized atomic-like orbitals (AO).

2.4.1 Plane-wave basis set

In molecular dynamics calculations like using VASP or other AIMD methods, the most commonly employed boundary conditions are periodic boundary conditions, in which the system is replicated infinitely in space. This is clearly a natural choice for solids and is particularly convenient for liquids. In an infinite periodic systems, the KS orbitals $\psi_{ik}(\mathbf{r})$ become Bloch functions of the form

$$\psi_{i\mathbf{k}}(\mathbf{r}) = e^{i\mathbf{k}\cdot\mathbf{r}} u_{i\mathbf{k}}(\mathbf{r}), \tag{2.75}$$

where $\mathbf{k}$ is a vector in the first Brillouin zone and $u_{i\mathbf{k}}(\mathbf{r})$ is a periodic function. A natural basis set for expanding a periodic function is the Fourier or plane-wave basis set, in which $u_{i\mathbf{k}}(\mathbf{r})$ is

$$u_{i\mathbf{k}}(\mathbf{r}) = \frac{1}{\sqrt{\Omega}} \sum_{\mathbf{g}} c_{i,\mathbf{g}}^{\mathbf{k}} e^{i\mathbf{g}\cdot\mathbf{r}}, \tag{2.76}$$

where Ω is the volume of the cell, $\mathbf{g} = 2\pi h^{-1}\hat{\mathbf{g}}$ is a reciprocal lattice vector, h is the cell matrix, whose columns are the cell vectors ($\Omega = det(h)$), $\hat{\mathbf{g}}$ is a vector of integers and $\{c_{i,\mathbf{g}}^{\mathbf{k}}\}$ are the expansion coefficients. An advantage of plane waves is that the sums needed to go back and forth between reciprocal space and real space can be performed efficiently using fast Fourier transformations (FFTs). In general, the properties of a periodic system are only correctly described if a sufficient number of $\mathbf{k}-$vectors are sampled from the Brillouin zone. However, for most applications to be considered in this work, which are concerned with nonmetallic systems but large unit cells, it is generally sufficient to consider a single $\mathbf{k}$ point, ($\mathbf{k} = (0,0,0)$) known as the Γ-point, so that the plane wave expansion reduces to

$$\psi_i(\mathbf{r}) = \frac{1}{\sqrt{\Omega}} \sum_{\mathbf{g}} c_{i,\mathbf{g}} e^{i\mathbf{g}\cdot\mathbf{r}}. \tag{2.77}$$

At the Γ-point, the orbitals can always be chosen to be real functions. Therefore, the plane-wave expansion coefficients satisfy the following property:

$$c_{i,\mathbf{g}}^{*} = c_{i,-\mathbf{g}} \tag{2.78}$$

which requires keeping only half of the full set of plane-wave coefficients. In actual applications, only plane waves up to a given cut-off, $\hbar^2|\mathbf{g}^2|/2m < E_{cut}$, are kept. Similarly, the density $n(\mathbf{r})$ given by Eq. (2.36) or (2.57) can now be expanded in a plane-wave basis:

$$n(\mathbf{r}) = \frac{1}{\Omega} \sum_{\mathbf{g}} n_{\mathbf{g}} e^{i\mathbf{g}\cdot\mathbf{r}}. \tag{2.79}$$

However, since $n(\mathbf{r})$ is obtained as a square of the KS orbitals, the cut-off needed for this expansion is $4E_{cut}$ for consistency with the orbital expansion.
Using Eq. (2.77) and (2.79) and the orthogonality of plane waves, it is straightforward to compute the various energy terms. From here on, we will employ atomic units ($\hbar = 1$, $e = 1$ and $m = 1$). Thus, the kinetic energy can be easily shown to be

$$\epsilon_{KE} = -\frac{1}{2} \sum_{i} \int d\mathbf{r}\, \psi_i^{*}(r) \nabla^2 \psi_i(\mathbf{r}) \;=\; \frac{1}{2} \sum_{i} \sum_{\mathbf{g}} \mathbf{g}^2 |c_{i,\mathbf{g}}|^2, \tag{2.80}$$

where $\mathbf{g} = |\mathbf{g}|$. Similarly, the Hartree energy becomes

$$\epsilon_H = -\frac{1}{2} \iint d\mathbf{r}\, d\mathbf{r}' \, \frac{n(\mathbf{r}) n(\mathbf{r}')}{|\mathbf{r} - \mathbf{r}'|} \;=\; \frac{1}{\Omega} \sum_{\mathbf{g}} \frac{'4\pi}{\mathbf{g}^2} |n_{\mathbf{g}}|^2, \tag{2.81}$$

where the summation excludes the $\mathbf{g} = (0,0,0)$ term as denoted by the prime on the summation.
The exchange and correlation energy, $\epsilon_{xc}[n]$ in LDA or GGA, is evaluated on the real-space FFT grid so that it can be expressed as

$$\epsilon_{xc}[n] = \frac{\Omega}{N_{grid}} \sum_{\mathbf{r}}' f_{\mathrm{GGA}}(n(\mathbf{r}), |\nabla n(\mathbf{r})|, \nabla^2 n(\mathbf{r})), \tag{2.82}$$

where N_{grid} is the number of real-space grid points. As shown by White and Bird [72], the use of the grid eliminates the complexity of functional differentiation by allowing the contribution to the KS potential from ϵ_{xc} to be computed from

$$\frac{d\epsilon_{xc}}{dn(\mathbf{r})} = \frac{\Omega}{N_{grid}} \frac{\partial f_{\mathrm{GGA}}}{\partial n(\mathbf{r})} + \frac{\Omega}{N_{grid}} \sum_{\mathbf{r}'}' \left[\frac{\partial f_{\mathrm{GGA}}}{\partial |\nabla n(\mathbf{r}')|} \frac{\partial |\nabla n(\mathbf{r}')|}{\partial n(\mathbf{r})} + \frac{\partial f_{\mathrm{GGA}}}{\partial \nabla^2 n(\mathbf{r}')} \frac{\partial \nabla^2 n(\mathbf{r}')}{\partial n(\mathbf{r})} \right]. \tag{2.83}$$

The gradient and (if needed) the Laplacian of the density can be computed efficiently using FFTs:

$$\nabla n(\mathbf{r}) = \sum_{\mathbf{g}}' i\mathbf{g} e^{i\mathbf{g}\mathbf{r}} \sum_{\mathbf{r}'} n(\mathbf{r}') e^{-i\mathbf{g}\cdot\mathbf{r}'},$$

$$\nabla^2 n(\mathbf{r}) = \sum_{\mathbf{g}}' \mathbf{g}^2 e^{i\mathbf{g}.\mathbf{r}} \sum_{\mathbf{r}'} n(\mathbf{r}') e^{-i\mathbf{g}\cdot\mathbf{r}'}. \tag{2.84}$$

Equation (2.84) also shows how the derivatives needed in Eq. (2.84) can be easily computed using combinations of forward and inverse FFTs.

2.4.2 The pseudopotential approximation

It has been shown by the use of Bloch's theorem [34], that a plane wave energy cut-off in the Fourier expansion of the wavefunction and careful **k**-point sampling allow to solve the Kohn-Sham equations for infinite crystalline systems. Unfortunately a plane wave basis set is usually very poorly suited to expand the electronic wavefunctions because a very large number of PWs is required to accurately describe the rapidly spatially oscillating wavefunctions of electrons in the core region and therefore, makes the external energy somewhat complicated.
It is well known that most physical properties of solids depend on the valence electrons to a much greater degree than on the tightly bound core electrons. It is for this reason that the pseudopotential approximation is introduced. This fact is used to remove the core electrons and the strong nuclear potential and replace them by a weaker pseudopotential [73–75] or to employ the augmented plane-wave techniques [76] which act on a set of pseudo wavefunctions rather than on the true valence wavefunctions. In fact, the pseudopotential can be optimized so that, in practice, it is even weaker than the frozen core potential [77]. The schematic diagram in Fig. 2.1 shows these quantities. The valence wavefunctions oscillate rapidly in the region occupied by the core electrons because

of the strong ionic potential. These oscillations maintain the orthogonality between the core and valence electrons. The pseudopotential is constructed in such a way that there are no radial nodes in the pseudo wavefunction in the core region and that the pseudo wavefunctions and pseudopotential are identical to the all-electron wavefunction and potential outside a radius cut-off. This condition has to be carefully checked as it is possible for the pseudopotential to introduce new non-physical states (so-called ghost states as discussed later) into the calculation. The pseudopotential is also constructed such that

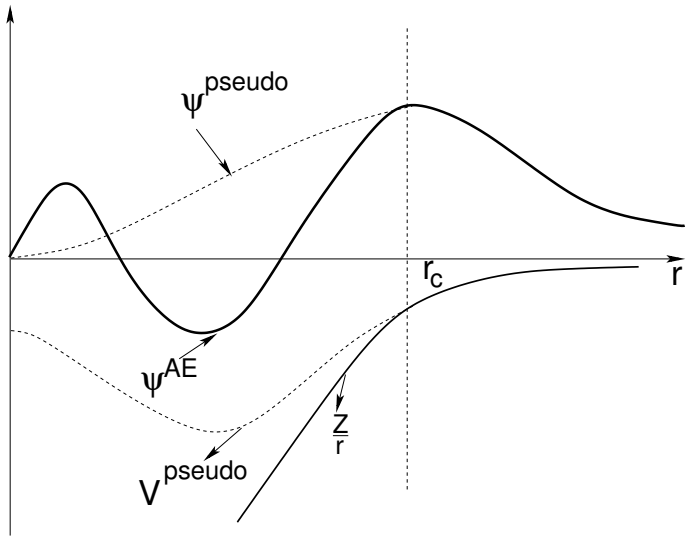

Figure 2.1: An illustration of the full all-electronic wavefunction (ψ^{AE}) and electronic potential (solid lines) plotted against distance, r, from the atomic nucleus. The corresponding pseudo wavefunction ($\psi^{pseudo} = \psi^{PS}$) and potential ($V^{pseudo}$) is plotted (dashed lines). Outside a given radius, r_c, the all electron and pseudo electron values are identical .

the scattering properties of the pseudo wavefunctions are identical to the scattering properties of the ion and core electrons. In general, this will be different for each angular momentum component of the valence wavefunction, therefore the pseudopotential will be angular momentum dependent. Pseudopotentials with an angular momentum dependence are called non-local pseudopotentials. The usual methods of pseudopotential generation firstly determine the all electron eigenvalues of an atom using the Schrödinger equation

$$\left\{-\frac{\bar{h}^2}{2m}\nabla^2 + V\right\}\psi_l^{AE} = \epsilon_l \psi_l^{AE}, \tag{2.85}$$

where ψ_l^{AE} is the wavefunction for the all-electron (AE) atomic system with angular momentum component l. The resulting valence eigenvalues are substituted into the Schrödinger equation but with a parametrized pseudo wavefunction of the form [78]

$$\psi_l^{PS} = \sum_{i=1} \alpha_i jl. \tag{2.86}$$

Here, jl denote spherical Bessel functions. The coefficients, α_i, are the parameters fitted to the conditions listed below. In general the pseudo wavefunction is expanded in three

or four spherical Bessel functions. The pseudopotential is then constructed by directly inverting the Kohn-Sham equation with the pseudo wavefunction, ψ_l^{PS}.
A pseudopotential is not unique, therefore several methods of generation exist. However they must obey several criteria which are:

- The core charge produced by the pseudo wavefunctions must be the same as that produced by the atomic wavefunctions. This ensures that the pseudo atom produces the same scattering properties as the ionic core.
- Pseudo-electron eigenvalues must be the same as the valence eigenvalues obtained from the atomic wavefunctions.
- Pseudo wavefunctions must be continuous at the core radius as well as its first and second derivative and also be non-oscillatory.
- On inversion of the all-electron Schrödinger equation for the atom, excited states may also be included in the calculation (if appropriate for a given condensed matter problem), for example, generating a d component for a non-local pseudopotential when the ground state of an atom does not contain these angular momentum components.

There are several ways in which these conditions can be satisfied leading to the non-uniqueness of a pseudopotential. This can be traced back to the expansion of the wavefunction in terms of a plane wave basis set. The set of plane waves, $e^{(\mathbf{k}+\mathbf{G})\mathbf{r}}$, forms a complete basis set (assuming a high enough cutoff) and the additional core states to which they are orthogonal results in a linearly dependent spanning set, that is, an over complete basis set. This linear dependence leads to non-unique pseudopotentials.

2.4.3 Norm-conserving pseudopotentials

To obtain the exchange-correlation energy accurately, it is necessary that outside the core region, the real and pseudo wavefunctions be identical so that both wavefunctions generate identical charge densities. Norm-conserving, DFT-based pseudopotentials were introduced by Hamann, Schlüter and Chiang in 1979 [79]. For a given reference atomic configuration, they must meet the following conditions (see the conditions listed above):

$$\epsilon_l^{PS} = \epsilon_l^{AE}, \tag{2.87}$$

$$\psi_l^{PS} \quad \text{is nodeless,} \tag{2.88}$$

$$\psi_l^{PS} = \psi_l^{AE} \quad \text{for } r > r_c, \tag{2.89}$$

$$\int_{r<r_c} |\psi_l^{PS}(\mathbf{r})|^2 \mathbf{r}^2 \, d\mathbf{r} = \int_{r<r_c} |\psi_l^{AE}(\mathbf{r})|^2 \, \mathbf{r}^2 \, d\mathbf{r}. \tag{2.90}$$

Also, generation of a pseudopotential which guarantees

$$\int_o^{r_c} \psi_l^{*PS}(\mathbf{r})\psi_l^{PS}(\mathbf{r})\ d\mathbf{r}\ = \int_o^{r_c} \psi_l^{*AE}(\mathbf{r})\psi_l^{AE}(\mathbf{r})\ d\mathbf{r}, \tag{2.91}$$

is required, here $\psi_l^{*AE}(r)$ is the all-electron wavefunction and $\psi_l^{*PS}(r)$ the pseudo wavefunction outside the core region [80]. In practice this is achieved by using a non-local pseudopotential which considers a different potential for each angular momentum component of the pseudo potential:

$$V_{pseudo}(\mathbf{r}) = \sum_l\ V_l(\mathbf{r})|l\rangle\langle l| \tag{2.92}$$

This also best describes the scattering properties from the ion core.
Pseudopotentials of this type are known as non-local norm-conserving pseudopotentials and are the most transferable since they are capable of describing the scattering properties of an ion in a variety of atomic environments. Also their construction ensures that they reproduce the logarithmic derivatives, i.e., the scattering properties, in a wide range of energies. The identity

$$-2\pi \left[(\mathbf{r}\psi(\mathbf{r}))^2 \frac{d}{d\epsilon}\left(\frac{d}{d\mathbf{r}} In\psi(\mathbf{r})\right)\right]_{r_c} \ = \ 4\pi \int_0^{r_c} |\psi(\mathbf{r})|^2\, \mathbf{r}^2\ d\mathbf{r} \tag{2.93}$$

is valid for any regular solution of the Schcrödinger equation at energy ϵ. The use of pseudopotentials has proved to be an extremely important step when using *ab-initio* methods to model large systems. An excellent review of this technique has been compiled by Pickett [81].

2.4.4 Non-local and Kleinman-Bylander pseudopotentials

We consider a potential operator of the form

$$\hat{V}_{\text{pseudo}} = \sum_{l=0}^{\infty} \sum_{m=-l}^{l} v_l(\mathbf{r})|lm\rangle\langle lm|, \tag{2.94}$$

where $\mathbf{r}$ is the distance from the ion, and $|lm\rangle\langle lm|$ is a projection operator onto each angular momentum component. In order to truncate the infinite sum over l in Eq. (2.94), we assume that for some $l \geq \bar{l}$, $v_l(r) = v_{\bar{l}}(r)$ and add and subtract the function $v_{\bar{l}}$ in Eq. (2.94):

$$\hat{V}_{pseudo} = \sum_{l=0}^{\infty} \sum_{m=-l}^{l} (v_l(\mathbf{r}) - v_{\bar{l}})|lm\rangle\langle lm| + v_{\bar{l}}(\mathbf{r}) \sum_{l=0}^{\infty} \sum_{m=-l}^{l} |lm\rangle\langle lm|$$

$$= \sum_{l=0}^{\infty} \sum_{m=-l}^{l} (v_l(r) - v_{\bar{l}})|lm\rangle\langle lm| + v_{\bar{l}}(\mathbf{r})$$

$$\approx \sum_{l=0}^{\bar{l}-1} \sum_{m=-l}^{l} \Delta v_l(\mathbf{r}) |lm\rangle\langle lm| + v_{\bar{l}}(\mathbf{r}), \tag{2.95}$$

where the second line follows from the fact that the sum of the projection operators is unity, $\Delta v_l(\mathbf{r}) = v_l(\mathbf{r}) - v_{\bar{l}}(\mathbf{r})$ and the sum in the third line is truncated before $\Delta v_l(\mathbf{r}) = 0$. The complete pseudopotential operator will then be

$$\hat{V}_{pseudo}(\mathbf{r}; \mathbf{R}_1, \ldots, \mathbf{R}_N) = \sum_{I=1}^{N} \left[v_{loc}\left(|\mathbf{r} - \mathbf{R}_I|\right) + \sum_{l=0}^{\bar{l}-1} \Delta v_l(|\mathbf{r} - \mathbf{R}_I|) |lm\rangle\langle lm| \right], \tag{2.96}$$

where $v_{loc}(\mathbf{r}) \equiv v_{\bar{l}}(\mathbf{r})$ is known as the local part of the pseudopotential (having no projection operator attached to it). Now, the external energy, being derived from the ground-state expectation value of a one-body operator, will be given by

$$\epsilon_{ext} = \sum_i f_i \langle \psi_i | \hat{V}_{pseudo} | \psi_i \rangle. \tag{2.97}$$

The first (local) term gives simply a local energy of the form

$$\epsilon_{loc} = \sum_{I=1}^{N} \int d\mathbf{r}\, n(\mathbf{r}) v_{loc}(|\mathbf{r} - \mathbf{R}_I|) \tag{2.98}$$

which can be evaluated in reciprocal space as

$$\epsilon_{loc} = \frac{1}{\Omega} \sum_{I=1}^{N} \sum_{\mathbf{g}} n^*_{\mathbf{g}} \bar{v}_{loc}(\mathbf{g}) e^{-i\mathbf{g}\cdot\mathbf{R}_I}, \tag{2.99}$$

where $\bar{v}_{loc}(\mathbf{g})$ is the Fourier transform of the local potential. Note that for $\mathbf{g} = (0,0,0)$, only the non-singular part of $\bar{v}_{loc}(\mathbf{g})$ contributes. In the evaluation of the local energy, it is often convenient to add and subtract a long-range term of the form $Z_I \mathrm{er}f(\alpha_I \mathbf{r})/\mathbf{r}$, where $\mathrm{er}f(x)$ is the error function, for each ion in order to obtain the non-singularity part explicitly and a residual short-range function

$$\bar{v}_{loc}(|\mathbf{r} - \mathbf{R}_I|) = \frac{v_{loc}(|\mathbf{r} - \mathbf{R}_I|) - Z_I \mathrm{er}f(\alpha_I |\mathbf{r} - \mathbf{R}_I|)}{|\mathbf{r} - \mathbf{R}_I|} \tag{2.100}$$

for each ionic core. For the non-local contribution, Eq. (2.77) is substituted into (2.96), and an expansion of the plane waves in terms of spherical harmonics is made. After some algebra, one obtains

$$\epsilon_{NL} = \sum_i f_i \sum_I \sum_{\mathbf{g},\mathbf{g}'} e^{-i\mathbf{g}\cdot\mathbf{R}_I} c^*_{i,\mathbf{g}} v_{NL}(\mathbf{g}, \mathbf{g}') c_{i,\mathbf{g}'} e^{i\mathbf{g}'\cdot\mathbf{R}_I}, \tag{2.101}$$

where

$$v_{NL}(\mathbf{g}, \mathbf{g}') = (4\pi)^2 \sum_{I=0}^{\bar{l}-1} \sum_{m=-1}^{l} \int d\mathbf{r}\, \mathbf{r}^2\, jl(\mathbf{g}\mathbf{r}) jl(\mathbf{g}'\mathbf{r}) \Delta v_l(\mathbf{r}) Y_{lm}(\theta_{\mathbf{g}}, \phi_{\mathbf{g}})\, Y^*_{lm}(\theta_{\mathbf{g}'}, \phi_{\mathbf{g}'}) \tag{2.102}$$

and $\theta_{\mathbf{g}}$ ($\theta_{\mathbf{g}'}$) and $\phi_{\mathbf{g}}$ ($\phi_{\mathbf{g}'}$) are the spherical polar angles associated with the vector $\mathbf{g}(\mathbf{g}')$, Y_{lm} are spherical harmonics and $jl(x)$ is a spherical Bessel function. Equation (2.102), which is known as the *semi-local* form, shows that the evaluation of the nonlocal energy can be computationally quite expensive. It also shows, however, that the matrix elements are *almost* separable into $\mathbf{g}$- and $\mathbf{g}'$-dependent terms. A fully separable approximation can be obtained by writing

$$v_{NL}(\mathbf{g},\mathbf{g}') = (4\pi)^2 \sum_{I=0}^{\bar{l}-1} \sum_{m=-1}^{l} \int d\mathbf{r}\, \mathbf{r}^2 \int d\mathbf{r}'\mathbf{r}'^2\; jl(\mathbf{gr}) jl(\mathbf{g}'\mathbf{r}') \Delta v_l(\mathbf{r}) \frac{\delta(\mathbf{r}-\mathbf{r}')}{\mathbf{r}\mathbf{r}'} \times Y_{lm}(\theta_{\mathbf{g}},\phi_{\mathbf{g}})\; Y^*_{lm}(\theta_{\mathbf{g}'},\phi_{\mathbf{g}'}) \tag{2.103}$$

where a radial $\delta-$function has been introduced. Next, the δ-function is expanded in terms of a set of radial eigenfunctions (usually taken to be the eigenfunctions of the Hamiltonian from which the pseudopotential is obtained) for each angular momentum channel,

$$\frac{\delta(\mathbf{r}-\mathbf{r}')}{\mathbf{r}\mathbf{r}'} = \sum_{n=0}^{\infty} \phi^*_{nl}(\mathbf{r}) \phi_{nl}(\mathbf{r}'). \tag{2.104}$$

If this expansion is now substituted into Eq. (2.102), the result is

$$v_{NL}(\mathbf{g},\mathbf{g}') = (4\pi)^2 \sum_{n=0}^{\infty} \sum_{I=0}^{\bar{l}-1} \sum_{m=-1}^{l} \left[\int d\mathbf{r}\, \mathbf{r}^2\; jl(\mathbf{gr})\, \Delta v_l(\mathbf{r})\, \phi^*_{nl}(\mathbf{r})\, Y_{lm}(\theta_{\mathbf{g}},\phi_{\mathbf{g}}) \right] \times \left[\int d\mathbf{r}'\; \mathbf{r}'^2\; jl(\mathbf{g}'\mathbf{r}')\, Y^*_{lm}(\theta_{\mathbf{g}'},\phi_{\mathbf{g}'})\; \phi_{nl}(\mathbf{r}') \right], \tag{2.105}$$

which is now fully separable at the expense of another infinite sum which needs to be truncated. The sum over n can be truncated after a finite number of terms, although some care is required in performing the truncation; the so called *Kleinman-Bylander approximation* [82] is the result of truncating it at just a single term. The result of this truncation can be shown to yield the approximate form

$$v_{NL}(\mathbf{g},\mathbf{g}') \approx (4\pi)^2 \sum_{I=0}^{\bar{l}-1} \sum_{m=-1}^{l} N^{-1}_{lm} \left[\int d\mathbf{r}\; \mathbf{r}^2\; jl(\mathbf{gr})\; \Delta v_l(\mathbf{r})\; \phi^*_l(\mathbf{r})\; Y_{lm}(\theta_{\mathbf{g}},\phi_{\mathbf{g}}) \right] \times \left[\int d\mathbf{r}'\, \mathbf{r}'^2\, jl(\mathbf{g}'\mathbf{r}')\, Y^*_{lm}(\theta_{\mathbf{g}'},\phi_{\mathbf{g}'})\; \phi_l(\mathbf{r}') \right], \tag{2.106}$$

where

$$N_{lm} \;=\; \int d\mathbf{r}\; \mathbf{r}^2\; \phi^*(\mathbf{r})\; \Delta v_l(\mathbf{r})\; \phi_l(\mathbf{r}) \tag{2.107}$$

and $\phi_l(\mathbf{r}) \equiv \phi_o(\mathbf{r})$. Finally, substituting Eq. (2.106) into (2.101) gives the nonlocal energy as

$$\epsilon_{NL} \;=\; \sum_{i=1}^{N_e} \sum_{I=1}^{N} \sum_{l=0}^{\bar{l}-1} \sum_{m=-l}^{l} Z^*_{iIlm}\; Z_{iIlm}, \tag{2.108}$$

where

$$Z_{iIlm} \;=\; \sum_{\mathbf{g}} \; c^{i}_{\mathbf{g}} e^{i\mathbf{g}\cdot\mathbf{R}_I} \widetilde{F}_{lm}(\mathbf{g}) \tag{2.109}$$

and

$$\widetilde{F}_{lm}(\mathbf{g}) \;=\; 4\pi \; N_{lm}^{-\frac{1}{2}} \; \int d\mathbf{r}\, \mathbf{r}^2 \, jl(\mathbf{gr})\, \Delta v_l(\mathbf{r}) \; \phi_l(\mathbf{r})\, Y_{lm}(\theta_{\mathbf{g}}, \phi_{\mathbf{g}}). \tag{2.110}$$

For certain elements, it has been shown that the simple Kleiman-Bylander form can lead to spurious or unphysical bound states known as *ghost levels*. The analysis and techniques for treating spurious ghost states are described in the review of Gonze *et al.* [83,84]. Alternatively, ghosts can be eliminated by taking more terms than just the first one in Eq. (2.106) [29] or working directly with the semi-local form.

2.4.5 Boundary conditions within the plane-wave description

Plane waves naturally describe fully periodic systems, such as solids, or systems that can be effectively treated with periodic boundary conditions, such as liquids. If we wish to study a system, such as a cluster, surface or wire, in which one or more boundaries is (are) *not* periodic, it turns out that such situations can be described rigorously within the plane-wave formalism. One approach is based on a direct solution of the Poisson equation in a box containing the cluster [85]. The simpler and more direct approach was developed by Martyna and Tuckerman, which involves the use of a screening function in the long-range energy terms, i.e., the Hartree and local pseudopotential terms. The idea is to use the so-called first image form of the average energy in order to form an approximation to the cluster, wire or surface system, whose error can be controlled by the dimensions of the simulation cell. The best reviews of this can be found in [86–88]. For calculation of non-periodic systems, e.g. defects in crystals, surfaces, alloys, amorphous materials, liquids and molecules and clusters, one uses supercells which introduce artificial periodicity. The geometry of the supercell is dictated by the type of system under investigation:

- Defects in crystals: The supercell is commensurate with the perfect crystal cell. The distance between periodic replica of the defects must be "large enough" to minimize spurious-defect interactions.
- Surfaces: For slab geometry, the number of layers of the materials must be "large enough" to have "bulk behaviour" in the furthest layer from the surface. The number of empty layers must be "big enough" to have minimal interactions between layers in different regions.
- Alloys, amorphous materials, liquids: The supercell must be "large enough" to a given reasonable description of physical properties.
- Molecules, clusters: The supercell must allow a minimum distance of at least a few Å (≈ 6) between the closest atoms in different periodic replica.

2.4.6 Slater-type and Gaussian atomic-like orbitals

In the following, two of the most widely used atomic-like orbitals (AO) basis set will be introduced. They are of particular importance in the DFTB method used in this work, since most of the results presented, based on the use of this method, depend on them. In general, AO basis sets have the form:

$$\{\varphi_\mu\} = \{\varphi_1(\mathbf{r}-\mathbf{R}_1), \varphi_2(\mathbf{r}-\mathbf{R}_1), \ldots, \varphi_j^k(\mathbf{r}-\mathbf{R}_k), ...,\}, \tag{2.111}$$

where $\varphi_j^k(\mathbf{r}-\mathbf{R}_k)$ is the j-th basis function on the k-th atom. Since every atom is assigned a set of atoms, the φ_μ explicitly depend on the locations of the atomic nuclei. Slater-type orbitals (STOs) have the following form:

$$\varphi_{nlm\alpha}(r) = r^{n+l}e^{-\alpha\mathbf{r}}Y_{lm}(\frac{\mathbf{r}}{r}), \quad n = 0,1,\ldots, n_{\max}\ . \tag{2.112}$$

In Eq. (2.112), $r = |\mathbf{r}|$, $\mathbf{r}$ is the coordinate vector, l and m denote the angular momentum quantum numbers, and Y_{lm} are spherical harmonics. STOs are based on the well known analytical solution of the Schrödinger equation for a single electron in the field of a fixed point charge [89]. Although they represent very efficient basis functions, many DFT implementations employ Gaussian orbitals instead:

$$g_{nlm\alpha}(r) = r^{n+l}e^{-\alpha r}Y_{lm}(\frac{\mathbf{r}}{r}), \quad n\ =\ 0,\ ,\ 1,\ ,\ldots,\ n_{max}. \tag{2.113}$$

There is a great advantage to be gained by the use of localized basis sets over delocalized basis like plane waves. In particular, the computations scale better for well localized orbitals. One of the most widely used localized basis sets is the Gaussian basis which exhibits more favourable numerical properties than STOs. However, they suffer from another drawback. In Gaussian basis, the KS orbitals ψ_i are expanded according to

$$\psi_i = \sum_{\alpha,\beta,\gamma} C^i_{\alpha,\beta,\gamma}\ G_{\alpha,\beta,\gamma}(\mathbf{r};\mathbf{R}), \tag{2.114}$$

where the basis functions, $G_{\alpha,\beta,\gamma}(\mathbf{r};\mathbf{R})$, are centered on atoms and, therefore, are dependent on the positions of the atoms. The basis functions generally take the form

$$G_{\alpha,\beta,\gamma}(\mathbf{r};\mathbf{R}_\mu) = N_{\alpha,\beta,\gamma}\ x^\alpha y^\beta z^\gamma exp\left[-\frac{|\mathbf{r}-\mathbf{R}_\mu|^2}{2\sigma^2_{\alpha,\beta,\gamma}}\right] \tag{2.115}$$

with integers α, β and γ for the Gaussian functions centered on atom μ. Equation (2.115) has an expansion of this form if we consider the exponential function at $x = 0$:

$$e^{-bx^2} = 1\ -\ bx^2 + \frac{1}{2}b^2x^4 + O(x^6). \tag{2.116}$$

Apparently, the terms which show a linear dependence on x, i.e, $(|\mathbf{r}-\mathbf{R}|)$ are missing in Eq. (2.115) or (2.116). In other words, Gaussians do not have a cusp at the origin.

Consequently, a rather large number of functions is needed to accurately describe the true atomic orbitals. In order to avoid large basis sets and the high numerical efforts associated with them, the *primitive* Gaussians $g_{nlm\alpha}$ can be used to construct *contracted* Gaussians:

$$\varphi_{nlm}(r) = \sum_i \sum_\alpha d_{nli\alpha}\, g_{ilm\alpha}(r). \tag{2.117}$$

Here, the contraction coefficients $d_{nli\alpha}$ are fixed. Contracted Gaussians resembles Slater-type orbitals more closely than the primitive ones. For this reason, they are able to attain the efficiency of STOs without losing any numerical advantages. However, the generation of both accurate and computational efficient basis sets of contracted Gaussians requires an optimization of the exponents α and the coefficients $d_{nli\alpha}$ for each atom. Several standard basis sets are available along with commercial program packages [90]. However, most of them are rather small and have to rely on error cancellations. While this might not be a critical problem for any applications, it is clearly undesirable if highly accurate benchmark results are required.

2.4.7 Self-consistency condition

So far, we have discussed the Kohn-Sham equations and the basis sets expansion needed to make the computational implementation feasible. In order to evaluate the total energy functional $\epsilon\,[n]$ at a given density, $n(\mathbf{r})$, the procedure is as follows.

- (a) Find the one-electron potential $V(\mathbf{r})$ (unique within a constant) which gives the imaginary system of noninteracting electrons a ground-state density equal to $n(\mathbf{r})$. The Schrödinger equation for the non-interacting system separates to give one-electron equations of the form

$$\left[-\frac{1}{2}\nabla^2 + V(\mathbf{r})\right]\psi_i(\mathbf{r}) = \epsilon_i\psi_i(\mathbf{r}), \tag{2.118}$$

  and the required density, $n(\mathbf{r})$, is the sum of the densities associated with the lowest N ($=N_e$ in the systems) one-electron eigenfunctions:

$$n(\mathbf{r}) = \sum_{i=1}^{N} f_i\ \psi_i^*(\mathbf{r})\psi_i^*(\mathbf{r}). \tag{2.119}$$

- (b) $T_{nonint}\,[n]$ is given by

$$T_{nonint}\,[n] = \sum_i^N \int \psi_i^*(\mathbf{r})(-\frac{1}{2}\nabla^2)\psi_i\, d\mathbf{r} \tag{2.120}$$

$$= \sum_i^N \epsilon_i - \int V(\mathbf{r})n(\mathbf{r})\, d\mathbf{r}. \tag{2.121}$$

- (c) We recall that $\epsilon[n] = T_{noint}[n] + F[n]$ (from the Hohenberg theorem). Within LDA, it is straightforward to evaluate $F[n]$ from $n(\mathbf{r})$. Hence, $\epsilon[n]$ is known as required.
  The step (a) is not simple and so the first part of this procedure is usually reversed: One starts with a one electron potential $V(\mathbf{r})$ and uses it together with Eqs. (2.118) and (2.119) to calculate the density at which the electronic energy functional is then evaluated.

We now know how to evaluate the functional at a given density, but to determine the ground-state energy and density we must find its minimum value. For densities $n(\mathbf{r})$ which make $E[n]$ stationary, we have

$$\delta E[n(r)] = E[n(r) + \delta n(r)] - E[n(r)] \;=\; 0([\delta n(r)]^2)$$

for all small fluctuations, $\delta n(\mathbf{r})$, satisfying

$$\int \delta n(\mathbf{r})\, dr = 0.$$

Consideration of the independent-electron problem used to generate $T_{nonint}[n(\mathbf{r})]$ shows that

$$\delta T_{\text{noint}}[n(\mathbf{r})] \;=\; -\int V(\mathbf{r})\delta n(\mathbf{r}) d\mathbf{r} + 0([\delta n(\mathbf{r})]^2), \tag{2.122}$$

and hence,

$$\delta E[n(\mathbf{r})] \;= \delta T_{\text{noint}}[n(\mathbf{r})] + \delta F[n(\mathbf{r})] \tag{2.123}$$

$$= \int \left\{ \left[\frac{\delta F}{\delta n}\right]_{n(\mathbf{r})} - V(\mathbf{r}) \right\} \delta n(\mathbf{r}) d\mathbf{r} + 0([\delta n(\mathbf{r})]^2). \tag{2.124}$$

From this it follows that $E[n]$ is stationary whenever

$$\left[\frac{\delta F}{\delta n}\right]_{n(r)} = V(\mathbf{r}) + \text{constant}. \tag{2.125}$$

The value of the constant is arbitrary for a closed system and can be set to zero.

3 Tight-binding methods

Starting with Slater and Koster's work [33], TB theory since then has addressed an important topic of computational material science, namely, the development of rapid, robust, generally transferable and accurate methods to calculate atomic and electronic structures, energies and forces of large molecular and condensed systems [32]. The standard TB method works by expanding eigenstates of a Hamiltonian in an usually orthogonalized basis of atomic-like orbitals and representing the exact many-body Hamiltonian operator with a parametrized Hamiltonian matrix, where the matrix elements are fitted to the band structure of a suitable reference system. The set is not, in general, explicitly constructed, but it is atomic-like in that it has the same symmetry properties as the atomic orbitals. A small number of basis functions are usually used, those roughly corresponding to the atomic orbitals in the energy range of interest. For example, when modelling graphite or diamond, the $1s$ orbitals are neglected, and only $2s$ and $2p$ orbitals are considered.
Although the original Slater-Koster scheme was only used to investigate the electronic structures of periodic solids, the TB ideas later on have been generalized to atomistic total-energy methods. A common actual TB calculation and its results, hence, clearly depend on the parametrization scheme and transferability to various scale systems and problems is rather limited. Successful applications include (review in [31]) highly accuracy band structure evaluations [91], band calculations in semiconductor hetero-structures [92], device simulations for optical properties [93], simulation of amorphous solids [94] and prediction of low energy silicon clusters [95, 96]. However, if the accuracy of the scheme is particularly tuned for dealing with a certain structure, deficiencies may arise when describing the bonding situations which were not covered by the parametrization. Non-orthogonality is a step forward to improve transferability [96]
More sophisticated and yet efficient TB schemes within multiconfigurational space has been recently developed in order to avoid the difficult parametrization. These include TB-LMTO (linear-muffin-tin-orbitals) [97], the Hartree-Fock-based TB [98], a successful DFT parametrization of TB [99], *ab-initio* multicenters TB [100] and DF-based (two center) TB approach [101]. Here the Hamiltonian matrix elements are explicitly calculated with a non-orthogonal basis of atomic orbitals. These schemes yield accurate results of a broad range of bonding situations, for which the superposition of overlapping atomic-like densities serves as a good approximation for the many-atom structure.

3.1 Derivation of the tight-binding model

The TB model can be rigorously derived from density functional theory [102] as this will be discussed later. However, the easy way to understand it is to start from the Fock equation with the framework of the Hartree-Fock-Roothaan approximation. First of all, we assume that there exist a minimal set of short-range basis functions. These functions can be orthogonal or non-orthogonal to each other. We actually do not need the explicit form of these functions because we will not evaluate matrix elements but approximate

them as analytical functions of atomic coordinates. The total energy E_{tot} of the electron system is represented as a sum of the electronic energy and pair terms, but instead of the Coulomb law used in the previous Sections, an analytical short-ranged function f of atom positions is introduced:

$$E_{tot}^{HF} = E_{el}^{HF} + \frac{1}{2}\sum_{I,J} \frac{Z_I Z_J}{|\mathbf{R}_I - \mathbf{R}_J|} \rightarrow E_{el}^{TB} + \frac{1}{2}\sum_{I,J} f(Z_I, Z_J, \mathbf{R}_{IJ}). \tag{3.1}$$

Here, self-consistency is neglected completely, or approximated in the expression for the electronic energy by the on-site terms defined below ($p = q = r = s$, which actually means that we account for the repulsion of two electrons only when they are localized near one and the same atom). Thus, instead of

$$E_{el}^{\mathrm{HF}} = \sum P_{pq}h_{pq} + \frac{1}{2}\sum_{pq} P_{pq}P_{rs}\left[\langle pr|g|qs\rangle - \frac{1}{2}\langle pr|g|sq\rangle\right], \tag{3.2}$$

where the electron density is

$$P_{pq} = 2\sum_{k}^{occup} C_{pk}C_{qk}^{*}, \tag{3.3}$$

we simply have (no consistency)

$$E_{el}^{TB} = \sum_{pq} P_{pq} = 2\sum_{k}^{occup} C_{pk}C_{qk}^{*}h_{pq}. \tag{3.4}$$

Given that for the orthogonal TB (overlap matrix is supposed to be the unity matrix)

$$\epsilon_k = \sum_{pq} C_{pk}C_{qk}^{*}h_{pq}, \tag{3.5}$$

as follows from the eigenvalue equation

$$\mathbf{F}\mathbf{C}_k = \epsilon_k \mathbf{C}_k, \tag{3.6}$$

we can write the electronic energy as the sum of electronic eigenvalues over all occupied states,

$$E_{el}^{TB} = 2\sum_{k}^{occup} \epsilon_k, \tag{3.7}$$

(the factor of 2 is due to summation over electron spin).
This same expression is correct for the non-orthogonal scheme, given that the density operator has a different form in this case. We can also account for the electron Coulomb repulsion. If the on-site Coulomb interaction is taken into account, then the energy is

$$E_{el}^{TB} = 2\sum_{k}^{occup} \epsilon_k + \sum_{p} u_p(q_p - q_p^0)^2. \tag{3.8}$$

The term is called the Hubbard-like term after J. Hubbard who introduced a class of models in order to describe strongly-correlated systems [103], the constant u_p corresponds to the effective electron repulsion energy, and q_p has the physical meaning of the Mulliken charge at atom p, which can be expressed in terms of the electron density. q_p^0 is the "reference" charge. It can be seen that this term favours the configurations with a smooth charge distribution over the system. The key moment is that matrix elements h_{pq}, S_{pq},

$$h_{pq} = \langle \chi_p | h | \chi_q \rangle = \int dr\ \chi_p^*(r) \left[-\frac{1}{2}\nabla^2 - \sum_J \frac{Z_J}{|R_J - r|} \right], \chi_q(r) \tag{3.9}$$

$$S_{pq} = \langle \chi_p | \chi_q \rangle = \int dr\ \chi_p^*(r)\chi_q(r), \tag{3.10}$$

are not explicitly calculated as integrals with some orbital functions but are approximated by analytical functions which depend on atom types, atom separation and orbital mutual orientation (Slater-Koster scheme). In the orthogonal TB approach **S** is just the identity matrix expressed by the Kronecker symbol.

3.1.1 The Slater-Koster scheme

We consider two atoms separated by a distance r, as shown in Fig. 3.1. For the sake of definiteness, let them be carbon atoms with the $2s$, $2p$ basis states on the first atoms $|s_1\rangle$, $|x_1\rangle$, $|y_1\rangle$, $|z_1\rangle$ and on the second atom $|s_2\rangle$, $|x_2\rangle$, $|y_2\rangle$, $|z_2\rangle$. The overlap between these states in, e.g. diamond, is substantial. However, as described above, we can treat these orbitals as being orthogonal if we modify the Hamiltonian matrix elements.

Let the on-site matrix elements be (on-site means that we consider orbitals localized on one and the same atom)

$$h_{qq} = E_s = \langle q | H | q \rangle \quad \text{q is the s orbital,} \tag{3.11}$$

$$h_{qq} = E_p = \langle q | H | q \rangle \quad \text{q is any of the orbitals.} \tag{3.12}$$

E_s and E_p are chosen to fit the results of experiments or first-principle simulations. Let us further assume that the off-diagonal matrix elements for s orbitals centred on different atoms can be calculated as follows:

$$h_{p_s q_s} = s(r)E_{s,s} = s(r)V_{ss}, \tag{3.13}$$

where $s(r)$ is an analytic function which, because s orbitals are isotropic, depends on the atom separation only, see Fig. 3.1. V_{ss} is a parameter chosen to fit the reference system. These integrals are called hopping integrals because in the second-quantization formalism, the corresponding elements of the Hamiltonian matrix describe "hopping" of electrons between orbitals localized on different atoms. For s and p_x orbitals centred on different atoms we write

$$h_{q_s q_{px}} = s(r)E_{s,x} = s(r)V_{sp\sigma l}, \tag{3.14}$$

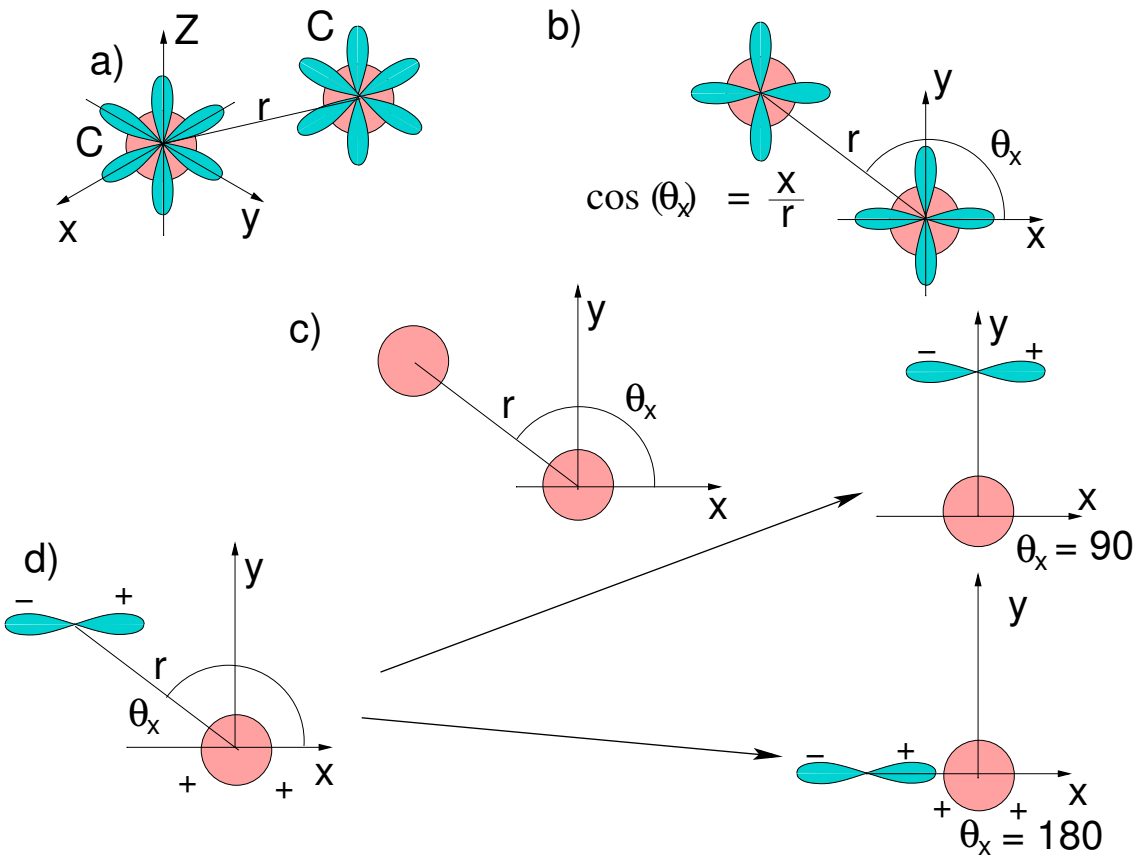

Figure 3.1: Calculation of the hopping integrals between two carbons atoms. (a) Three dimensional representation. (b) Projection onto $x - y$ plane. (c) Overlap between $2s$ orbitals centred on different atoms. (d) Overlap between s and p_x orbitals.

where $l = \cos(\theta) = x/r$ is the direction cosine of the vector between the atoms. l reflects the anisotropy of p orbitals and the fact that the sign of the orbital is different in different "leaves" of the orbitals. Thus, if $\theta_x = 90^o$, the overlap integral between the s and p_x orbitals is zero (we recall that $2p$ functions change their sign at the origin!). $V_{ss\sigma}$ is the parameter which depends on atom type.

For two p_x orbitals centered on different atoms we have

$$h_{p_x p_x} = s(r)E_{x,x} = s(r)\left[l^2 V_{pp\sigma} - (1-l^2)V_{pp\pi}\right], \tag{3.15}$$

Similarly, all the overlap integrals for s and p orbitals can be expressed in terms of four non-zero parameters (see. Fig. 3.2) and the direction cosine $l = x/r$, $m = y/r$ and $n = z/r$. For example,

$$h_{p_x p_y} = s(r)E_{x,y} = s(r)\left[lmV_{pp\sigma} - lmV_{pp\pi}\right], \tag{3.16}$$

$$h_{p_z p_z} = s(r)E_{z,z} = s(r)\left[n^2 V_{pp\sigma} - (1-n^2)V_{pp\pi}\right], \tag{3.17}$$

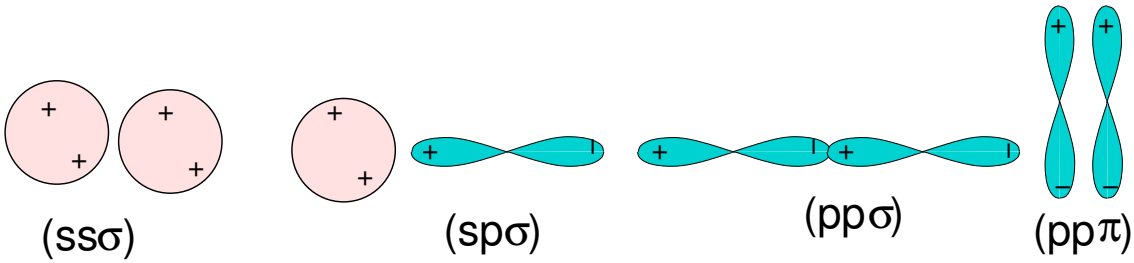

Figure 3.2: The four fundamental hopping integrals between s and p orbitals.

We can also derive analogous formula for d orbitals. This was done by Slater and Koster in 1954. All the non-equivalent hopping integrals for s, p and d atomic states are listed in Table 3.1

3.2 The density-functional basis of the tight-binding method (DFTB)

Here we shall discuss the full density functional basis of tight-binding theory and the various approximations of the model in order to see how the self-consistency is implemented in the code used in this work and also, how it is different from the traditional TB model. According to Section 2.2.2, the total energy of a system of N_e electrons in the field of M nuclei at positions R may be written within DFT as a functional of the charge density $n(r)$:

$$E = \sum_{i}^{occup} \left\langle \psi_i \right| -\frac{1}{2}\nabla^2 + V_{ext} + \frac{1}{2}\int d\mathbf{r}' \frac{n(\mathbf{r}')}{|\mathbf{r}-\mathbf{r}'|} \left|\psi_i\right\rangle + E_{xc}\left[n(\mathbf{r})\right] + \frac{1}{2}\sum_{\alpha,\beta}\frac{Z_\alpha Z_\beta}{|\mathbf{R}_\alpha - \mathbf{R}_\beta|}, \tag{3.18}$$

where the first sum is over occupied Kohn-Sham eigenstates ψ_i, the second term is the xc contribution and the last term covers the ion-ion core repulsion, E_{ii}. Following Foulkes and Haydock [102], we can re-write the total energy in order to transform the leading matrix elements. We substitute the charge density into Eq. (3.18) by a superposition of a reference or input density $n_0' = n_0(\mathbf{r}')$ and a small fluctuation $\delta n' = \delta n(\mathbf{r}')$,

$$E = \sum_{i}^{occup} \left\langle \psi_i \right| -\frac{1}{2}\nabla^2 + V_{ext} + \int d\mathbf{r}' \frac{n_0'}{|\mathbf{r}-\mathbf{r}'|} + V_{xc}\left[n_0\right] \left|\psi_i\right\rangle - \frac{1}{2}\iint d\mathbf{r}\, d\mathbf{r}' \frac{n_0'(n_0+\delta n)}{|\mathbf{r}-\mathbf{r}'|} - \int V_{xc}\left[n_0\right](n_0+\delta n) + \frac{1}{2}\iint d\mathbf{r}\, d\mathbf{r}'\, \frac{n_0'(n_0+\delta n)}{|\mathbf{r}-\mathbf{r}'|} + E_{xc}\left[n_0+\delta n\right] + E_{ii}. \tag{3.19}$$

The second term of this equation corrects the double counting of the new Hartree, the third term for the new xc contribution in the leading matrix element, and the fourth term comes from dividing the full Hartree energy in Eq. (3.18) into a part related to n_0 and to

Table 3.1: Hopping integrals between s, p and d atomic states as a function of the direction cosines l, m, and n of the vector from the left state to the right state [33].

$E_{s,s} = V_{ss\sigma}$
$E_{s,x} = lV_{sp\sigma}$
$E_{x,x} = l^2V_{pp\sigma} + (1-l^2)V_{pp\pi}$
$E_{x,y} = lmV_{pp\sigma} - lmV_{pp\pi}$
$E_{x,z} = lnV_{pp\sigma} - lnV_{pp\pi}$
$E_{s,xy} = \sqrt{3}lmV_{sd\sigma}$
$E_{s,x^2-y^2} = \frac{1}{2}\sqrt{3}(l^2-m^2)V_{sd\sigma}$
$E_{s,3z^2-r^2} = [n^2 - \frac{1}{2}(l^2+m^2)]V_{sd\sigma}$
$E_{x,xy} = \sqrt{3}l^2mV_{pd\sigma} + m(1-2l^2)V_{pd\pi}$
$E_{x,yz} = \sqrt{3}lmnV_{pd\sigma} \ -2lmnV_{pd\pi}$
$E_{x,zx} = \sqrt{3}l^2nV_{pd\sigma} + n(1-2l^2)V_{pd\pi}$
$E_{x,x^2-y^2} = \frac{1}{2}\sqrt{3}l(l^2-m^2)V_{pd\sigma} + l(1-l^2+m^2)V_{pd\pi}$
$E_{y,x^2-y^2} = \frac{1}{2}\sqrt{3}m(l^2-m^2)V_{pd\sigma} - m(1+l^2-m^2)V_{pd\pi}$
$E_{z,x^2-y^2} = \frac{1}{2}\sqrt{3}n(l^2-m^2)V_{pd\sigma} - n(l^2-m^2)V_{pd\pi}$
$E_{x,3z^2-r^2} = l[n^2 - \frac{1}{2}(l^2+m^2)]V_{pd\sigma} - \sqrt{3}ln^2V_{pd\pi}$
$E_{y,3z^2-r^2} = m[n^2 - \frac{1}{2}(l^2+m^2)]V_{pd\sigma} - \sqrt{3}mn^2V_{pd\pi}$
$E_{z,3z^2-r^2} = n[n^2 - \frac{1}{2}(l^2+m^2)]V_{pd\sigma} + \sqrt{3}n(l^2+m^2)V_{pd\pi}$
$E_{xy,xy} = 3l^2m^2V_{dd\sigma} + (l^2+m^2-4l^2m^2)V_{dd\pi} + (n^2+l^2m^2)V_{dd\delta}$
$E_{xy,yz} = 3lm^2nV_{dd\sigma} + ln(1-4m^2)V_{dd\pi} + ln(m^2-1)V_{dd\delta}$
$E_{xy,zx} = 3l^2mnV_{dd\sigma} + mn(1-4l^2)V_{dd\pi} + mn(l^2-1)V_{dd\delta}$
$E_{xy,x^2-y^2} = \frac{3}{2}lm(l^2-m^2)V_{dd\sigma} + 2lm(m^2-l^2)V_{dd\pi} + \frac{1}{2}lm(l^2-m^2)V_{dd\delta}$
$E_{yz,x^2-y^2} = \frac{3}{2}mn(l^2-m^2)V_{dd\sigma} - mn[1+2(l^2-m^2)]V_{dd\pi} + mn[1+\frac{1}{2}(l^2-m^2)]V_{dd\delta}$
$E_{zx,x^2-y^2} = \frac{3}{2}nl(l^2-m^2)V_{dd\sigma} + nl[1-2(l^2-m^2)]V_{dd\pi} \ -nl[1-\frac{1}{2}(l^2-m^2)]V_{dd\delta}$
$E_{xy,3z^2-r^2} = \sqrt{3}lm[n^2 - \frac{1}{2}(l^2+m^2)]V_{dd\sigma} - 2\sqrt{3}lmn^2V_{dd\pi} + \frac{1}{2}\sqrt{3}lm(1+n^2)V_{dd\delta}$
$E_{yz,3z^2-r^2} = \sqrt{3}mn[n^2 - \frac{1}{2}(l^2+m^2)]V_{dd\sigma} + \sqrt{3}mn(l^2+m^2-n^2)V_{dd\pi} - \frac{1}{2}\sqrt{3}mn(l^2+m^2)V_{dd\delta}$
$E_{zx,3z^2-r^2} = \sqrt{3}ln[n^2 - \frac{1}{2}(l^2+m^2)]V_{dd\sigma} + \sqrt{3}ln(l^2+m^2-n^2)V_{dd\pi} - \frac{1}{2}\sqrt{3}ln(l^2+m^2)V_{dd\delta}$
$E_{x^2+y^2,x^2-y^2} = \frac{3}{4}(l^2-m^2)^2V_{dd\sigma} + [l^2+m^2-(l^2-m^2)^2]V_{dd\pi} + [n^2+\frac{1}{4}(l^2-m^2)^2V_{dd\delta}$
$E_{x^2-y^2,3z^2-r^2} = \frac{1}{2}\sqrt{3}(l^2-m^2)[n^2 - \frac{1}{2}(l^2+m^2)]V_{dd\sigma} + \sqrt{3}n^2(m^2-l^2)V_{dd\pi} + \frac{1}{4}\sqrt{3}(1+n^2)(l^2-m^2)V_{dd\delta}$
$E_{3z^2-r^2,3z^2-r^2} = [n^2 - \frac{1}{2}(l^2+m^2)]^2V_{dd\sigma} + 3n^2(l^2+m^2)V_{dd\pi} + \frac{3}{4}(l^2+m^2)^2V_{dd\delta}$

δn.
Finally, we expand E_{xc} at the reference density and obtain the total energy correct to second oder in the density fluctuations by a simple transformation. Note that the terms linear in δn cancel each other at any arbitrary input density n_0:

$$E = \sum_{i}^{occup} \langle\psi_i|H_0|\psi_i\rangle - \frac{1}{2}\iint d\mathbf{r}d\mathbf{r}'\,\frac{n_0' n_0}{|\mathbf{r}-\mathbf{r}'|} + E_{xc}\left[n_0\right] - \int d\mathbf{r} V_{xc}\left[n_0\right] n_0 + E_{ii}$$

$$+\frac{1}{2}\iint d\mathbf{r}\,d\mathbf{r}'\,\left(\frac{1}{|\mathbf{r}-\mathbf{r}'|} + \left.\frac{\delta^2 E_{xc}}{\delta n \delta n'}\right|_{n_0}\right)\delta n \delta n' \tag{3.20}$$

3.2.1 Zeroth-order non-self-consistent charge approach, standard DFTB

The traditional non-self-consistence-charge TB approach is to neglect the last term in the final expression in Eq. (3.20), with H_0 as the Hamiltonian operator resulting from an input density n_0. As usual, a frozen-core approximation (discussed in Section 2.1.2) is applied to reduce the computational efforts by only considering the valence orbitals. The Kohn-Sham equations are solved non-self-consistently and the second-order correction is neglected. The contributions in Eq. (3.20) which depend on the input density n_0 only and the core-core repulsion are taken to be the sum of one- and two-body potentials [102]. The latter, denoted by E_{rep}, are strictly pairwise, repulsive and short ranged. The total energy then reads

$$E_0^{TB} = \sum_{i}^{occup} \langle\psi_i|H_0|\psi_i\rangle + E_{rep}, \tag{3.21}$$

which is similar to the general TB energy equation introduced in Section 3.1 using the general Hartree-Fock-Roothaan approximation.
In order to solve the KS equations, the single-particle wavefunctions ψ_i within an LCAO ansatz are expanded into a suitable set of localized atomic orbitals φ_ν (see Section 2.4.6),

$$\psi_i(r) \;=\; \sum_{\nu}\; c_{\nu i}\varphi_\nu(\mathbf{r}-\mathbf{R}_\alpha). \tag{3.22}$$

If we employ confined atomic orbitals in a Slater-type representation [101], these are determined by solving a modified Schrödinger equation for a free neutral pseudoatom with self-consistence field (SCF)-LDA calculations [104]. The effective one-electron potential of the many-atom structure [101] is approximated to a sum of spherical KS potentials of neutral pseudoatoms due to their *confined* electron density.
By applying the variational principle to the zeroth-order energy functional (3.21), we obtain the non-SCF KS equations, which, finally, within the pseudoatomic basis, transform to a set of algebraic equations:

$$\sum_{\nu}^{N_e}\; c_{\nu i}\;(H^0_{\mu\nu} - \epsilon_i S_{\mu\nu}) \;=\; 0, \quad \forall\;\mu,\, i\;, \tag{3.23}$$

$$H^0_{\mu\nu} = \langle\varphi_\mu|H_0|\varphi_\nu\rangle,\ S_{\mu\nu} = \langle\varphi_\mu|\phi_\nu\rangle \quad \forall\ \mu \in \alpha\ , \tag{3.24}$$

Consistent with the construction of the effective one-electron potential we neglect several contributions to the Hamiltonian matrix elements $H_{\mu\nu}$ [105] yielding

$$H^0_{\mu\nu} = \begin{cases} \epsilon_\mu^{\text{neutral free atom}} & \text{if} \quad \mu = \nu; \\ \langle\varphi^\alpha_\mu|T + V^\alpha_0 + V^\beta_0|\varphi^\beta_\nu\rangle & \text{if} \quad \alpha \neq \beta; \\ 0 & \text{otherwise}\ . \end{cases} \tag{3.25}$$

Since indices α and β indicate the atoms on which the wavefunctions and potentials are centred, only two-centre Hamiltonian matrix elements are treated and explicitly evaluated in combination with the two-centre overlap matrix elements. As follows from Eq. (3.25), the eigenvalues of the free atom serve as diagonal elements of the Hamiltonian, thus guaranteeing the correct limit for isolated atoms.
By solving the general eigenvalue problem, Eq. (3.23), the first term in Eq. (3.21) becomes a simple summation over all occupied KS orbitals with energy ϵ_i (occupation number n_i), while E_{rep} can easily be determined as a function of distance by taking the difference of the SCF-LDA cohesive and the corresponding TB band-structure energy for a suitable reference system,

$$E_{rep}(\mathbf{R}) = \left\{ E^{\text{SCF}}_{\text{LDA}}(\mathbf{R}) - \sum_i^{occup} n_i\epsilon_i(\mathbf{R}) \right\}\Bigg|_{\text{reference structure}}\ . \tag{3.26}$$

Interatomic forces for molecular dynamics simulation applications can easily be derived from an explicit calculation of the gradients of the total energy at the considered atom sites,

$$M_\alpha\ddot{\mathbf{R}}_\alpha = -\frac{\partial E^{TB}_0}{\partial \mathbf{R}_\alpha}$$

$$= -\sum_i\ n_i \sum_\mu \sum_\nu c_{\mu i}c_{\nu i}\left[\frac{\partial H^0_{\mu\nu}}{\partial \mathbf{R}_\alpha} - \epsilon_i\frac{\partial S_{\mu\nu}}{\mathbf{R}_\alpha} - \sum_{\beta\neq\alpha}\frac{\partial E_{rep}(|\mathbf{R}_\alpha - \mathbf{R}_\beta|)}{\mathbf{R}_\alpha}\right]. \tag{3.27}$$

This is the non-SCC-DFTB approach, which has been successfully applied to various problems in different systems and materials, covering carbon [101], silicon [106], and germanium structures [107], boron and carbon nitride [108, 109], silicon carbide [110] and oxides and GaAs surfaces [111]. Provided an educated guess of the initial or input charge density of the system, the energies and forces are correct to second order in the charge density fluctuations. Furthermore, the short-range two-particle repulsion (determined once using a proper reference system) operates transferably to very different bonding situations and various scale systems.

3.2.2 Second-order self consistent charge extension, SCC-DFTB

The previous scheme discussed above is suitable when the electron density of the many-atom structure may be represented as a sum of atomic-like densities in good approximation. The uncertainties within the standard DFTB variant, however, increase if the chemical bonding is controlled by a delicate charge balance between different atomic constituents, especially in heteronuclear molecules such as biomolecules, and in polar semiconductors. Biomolecules are challenging systems for computational methods for several reasons to be discussed later. The extension of the approach is necessary in order to improve total energies, forces and transferability in the presence of long-range Coulomb interactions. Starting from Eq. (3.20), and now explicitly consider the second-order term in the density fluctuations in order to include associated effects in a simple and efficient TB concept, $\delta n(r)$ is decomposed into atom-centered contributions, which decay fast with increasing distance from the corresponding center. The second-order term then reads

$$E_{2nd} = \frac{1}{2}\sum_{\alpha,\beta}^{M} \iint d\mathbf{r}\, d\mathbf{r}' \Gamma\left[\mathbf{r}, \mathbf{r}', n_0\right] \delta n_\alpha(r)\delta_\beta(\mathbf{r}'), \tag{3.28}$$

where we have used the functional Γ to denote the Hartree and xc coefficients. Second, δn_α may be expanded in a series of radial and angular functions:

$$\delta_\alpha(\mathbf{r}) = \sum_{l,m} K_{ml} F^\alpha_{ml}(|\mathbf{r} - \mathbf{R}_\alpha|) Y_{lm}\left(\frac{\mathbf{r} - \mathbf{R}_\alpha}{|\mathbf{r} - \mathbf{R}_\alpha|}\right)$$

$$\approx \Delta q_\alpha F^\alpha_{00}(|\mathbf{r} - \mathbf{R}_\alpha|) Y_{00}, \tag{3.29}$$

where F^α_{ml} denotes the normalized radial dependence of the density fluctuation on atom α for the corresponding angular momentum. While the angular momentum of the charge density, e.g. in covalently bonded systems, is usually described very well within the non-SCC approach, charge transfers between different atoms are not properly handled in many cases. Truncating the multipole expansion (3.21) after the monopole term accounts for the most important contributions of this kind while avoiding a substantial increase in the numerical complexity of the scheme. Also, it should be noted that higher-order interactions decay much more rapidly with increasing interatomic distance. Finally, the expression (3.29) preserves the total charge in the system, i.e.,

$$\sum_\alpha \Delta q_\alpha \;=\; \int \delta n(r). \tag{3.30}$$

Substitution of Eq. (3.29) into (3.28):

$$E_{2nd} = \frac{1}{2}\sum_{\alpha,\beta}^{M} \Delta q_\alpha \Delta q_\beta \gamma_{\alpha\beta}, \tag{3.31}$$

where

$$\gamma_{\alpha\beta} = \iint d\mathbf{r}\, d\mathbf{r}'\, \Gamma\left[\mathbf{r}, \mathbf{r}', n_0\right] \frac{F_{00}^{\alpha}\left(|\mathbf{r} - \mathbf{R}_{\alpha}|\right) F_{00}^{\beta}\left(|\mathbf{r} - \mathbf{R}_{\beta}|\right)}{4\pi} \tag{3.32}$$

is introduced as shorthand notation. In the limit of large interatomic distances, the xc contribution vanishes within LDA and E_{2nd} may be viewed as a pure Coulomb interaction between two point charges Δq_{α} and Δq_{β}. In the opposite case, where the charges are located at one and the same atom, a rigorous evaluation of $\gamma_{\alpha\alpha}$ would require the knowledge of the actual charge distribution. This could be calculated by expanding the charge density into an appropriate basis set of localized orbitals. In order to avoid the numerical effort associated with the basis set expansion of δn and to consider at least approximately the self-interaction contributions, a simple approximation of $\gamma_{\alpha\alpha}$, which is widely used in semiempirical quantum chemistry methods relying on Pariser observation that $\gamma_{\alpha\alpha}$ can be approximated by the difference of atomic ionization potential and the electron affinity [112]. This is related to the chemical hardness η_{α}, or the Hubbard parameter U_{α}, (discussed in Section 3.1),

$$\gamma_{\alpha\alpha} \approx I_{\alpha} - A_{\alpha} \approx 2\eta_{\alpha} \approx U_{\alpha}. \tag{3.33}$$

The expression for $\gamma_{\alpha\beta}$ then only depends on the distance between atoms α and β and on the parameters U_{α} and U_{β}. The latter constants can be calculated for any atom type within LDA-DFT as the second derivative of the total energy of a single atom with respect to the occupation number of the highest occupied atomic orbital. These values are therefore neither adjustable nor empirical parameters. Indeed, the necessary corrections for a TB total energy in the presence of charge fluctuations turns out to be a typical Hubbard-type correlation in combination with long-range interatomic Coulomb interactions. There are common functional forms of $\gamma_{\alpha\beta}$, examples are presented in the work of Ohno [113], Klopman [114] and Mataga-Nishimoto [115]. It has been observed that these may cause severe numerical problems when applied to periodic systems since Coulomb-like behaviour is only accomplished for at large atomic distance. By using expressions like in [113, 114] for periodic systems yield ill-conditioned energies with respect to Hubbard parameters, i.e., small changes in the Hubbard parameters may result in considerable variations of total energy and should therefore not be used.
In order to obtain a well-defined expression useful for all scale systems and consistent with previous approximations, an analytical approach is made to obtain the functional $\gamma_{\alpha\beta}$. In accordance with the Slater-type orbitals used as a basis set to solve the Kohn-Sham equations [101], an exponential decay of the normalized spherical charge densities

$$n_{\alpha}(r) = \frac{\tau^3}{8\pi} e^{-\tau_{\alpha}|\mathbf{r}-\mathbf{R}_{\alpha}|} \tag{3.34}$$

is assumed. Neglecting for the moment the second-order contributions of E_{xc} in Eq. (3.28) we obtain:

$$\gamma_{\alpha\beta} = \iint d\mathbf{r}\, d\mathbf{r}' \frac{1}{|\mathbf{r} - \mathbf{r}'|} \frac{\tau_{\alpha}^3}{8\pi} e^{-\tau_{\alpha}|\mathbf{r}-\mathbf{R}_{\alpha}|} \frac{\tau_{\beta}^3}{8\pi} e^{-\tau_{\beta}|\mathbf{r}-\mathbf{R}_{\beta}|}. \tag{3.35}$$

Integrating over $\mathbf{r}'$ gives

$$\gamma_{\alpha\beta} = \int d\mathbf{r} \left[\frac{1}{|\mathbf{r} - \mathbf{R}_\alpha|} - \left(\frac{\tau_\alpha}{2} + \frac{1}{|\mathbf{r} - \mathbf{R}_\alpha|} \right) e^{-\tau_\alpha |\mathbf{r} - \mathbf{R}_\alpha|} \right] \frac{\tau_\beta^3}{8\pi} e^{-\tau_\beta |\mathbf{r} - \mathbf{R}_\beta|}. \tag{3.36}$$

By setting $R = |\mathbf{R}_\alpha - \mathbf{R}_\beta$ and , after some coordinate transformations [32], one obtains

$$\gamma_{\alpha\beta} = \frac{1}{R} - S(\tau_\alpha, \tau_\beta, R). \tag{3.37}$$

S is an exponentially decay short-range function [32] with

$$S(\tau_\alpha, \tau_\alpha, R)|_{R \to 0} = \frac{5}{16}\tau_\alpha + \frac{1}{R}. \tag{3.38}$$

Here it is assumed that at $R = 0$ the second order contribution can be expressed approximately via the so-called chemical hardness for a spin-polarized atom or Hubbard parameter U_α, to obtain

$$\frac{1}{2}\Delta q_\alpha^2 \gamma_{\alpha\alpha} = \frac{1}{2}\Delta q_\alpha^2 U_\alpha, \tag{3.39}$$

and therefore from Eq. (3.38) for the exponents:

$$\tau_\alpha = \frac{16}{5} U_\alpha. \tag{3.40}$$

The results are interpreted by noting that elements with a high chemical hardness tend to have localized wavefunctions. The chemical hardness for a non-spin-polarized atom is the derivative of the highest molecular orbital with respect to its occupation number. This chemical hardness is calculated with a fully self-consistent *ab-initio* method and therefore include the influence of the second-order contribution of E_{xc} in $\gamma_{\alpha\beta}$ for small distances where it is important. In the limit of large interatomic distances, $\gamma_{\alpha\beta} \to 1/R$ and thus represents the Coulomb interaction between two point charges Δq_α and Δq_β. This accounts for the fact that at large interatomic distances, the exchange-correlation contributions vanish within the local density approximation. In periodic systems, this long range part is evaluated using the standard Ewald technique, whereas the short-range part S decays exponentially and can therefore be summed over a small number of unit cells. Hence, Eq. (3.37) is a well-defined expression for extended and periodic systems.
Finally, the DFT total energy in (3.20) is conveniently transformed to a transparent TB form,

$$E_2^{TB} = \sum_i^{occup} \langle \psi_i | H_0 | \psi_i \rangle + \frac{1}{2} \sum_{\alpha\beta}^{M} \gamma_{\alpha\beta} \Delta q_\alpha \Delta q_\beta + E_{\text{rep}}, \tag{3.41}$$

where $\gamma_{\alpha\beta} = \gamma(U_\alpha, U_\beta, (|\mathbf{R}_\alpha - \mathbf{R}_\beta|)$. As discussed earlier, the contribution due to H_0 depends only on n_0 and is therefore exactly the same as in previous non-SCC studies [101].

However, since the atomic charges depend on the one-particle wavefunction ψ_i, a self-consistent procedure is required to find the minimum of expression (3.41).
To solve the KS equations, the single-particle wavefunctions ψ_i are expanded into a suitable set of localized atomic orbitals φ_ν, (as discussed in Section 2.4.6), denoting the expansion coefficients by $c_{\nu i}$. According to the previous scheme [101], confined Slater-type atomic orbitals are employed. These are determined by solving the Schrödinger equation for a free atom within SCF-LDA calculations. By applying the variational principle to the energy functional (3.41), we obtain the KS equations, which, within the pseudoatomic basis, transform to a set of algebraic equations. In order to estimate the charge fluctuations $\Delta q_\alpha = q_\alpha - q_\alpha^0$, a Mulliken charge analysis is employed. With

$$q_\alpha = \frac{1}{2} \sum_i^{occup} n_i \sum_{\mu\in\alpha} \sum_\nu^M (c_{\mu i}^* c_{\nu i} S\mu\nu + c_{\nu i}^* c_{\mu i} S_{\nu\mu}), \tag{3.42}$$

we obtain

$$\sum_\nu^{N_e} c_{\nu i}(H_{\mu\nu} - \epsilon_i S_{\mu\nu}) = 0, \quad \forall\ \mu,\ i\ , \tag{3.43}$$

$$H_{\mu\nu} = \langle\varphi_\mu|H_0|\varphi_\nu\rangle + \frac{1}{2} S_\mu\nu \sum_\xi^M (\gamma_{\alpha\xi} + \gamma_{\beta\xi})\Delta q_\xi = H_{\mu\nu}^0 + H_{\mu\nu}^1,$$

$$S_{\mu\nu} = \langle\varphi_\mu|\varphi_\nu\rangle, \quad \forall\ \mu\in\alpha,\ \forall\nu\in\ \beta\ . \tag{3.44}$$

Since the overlap matrix elements $S_{\mu\nu}$ generally extend over a few nearest-neighbour distances, they introduce multiparticle interactions. The second-order correction due to charge fluctuations is now represented by the non-diagonal Mulliken charge dependent contribution $H_{\mu\nu}^1$ to the matrix elements $H_{\mu\nu}$.
A simple analytic expression for the interatomic forces for use in MD simulations is easily derived by taking the derivative of the final TB energy Eq. (3.41) (for SCC-DFTB method) with respect to the nuclear coordinates yielding,

$$F_\alpha = -\sum_i^{occup} n_i \sum_{\mu\nu} c_{\mu i} c_{\nu i} \left[\frac{\partial H_{\mu\nu}^0}{\partial \mathbf{R}_\alpha} - \left(\epsilon_i - \frac{H_{\mu\nu}^1}{S_{\mu\nu}}\right) \frac{\partial S_{\mu\nu}}{\partial \mathbf{R}_\alpha}\right]$$

$$-\Delta q_\alpha \sum_\xi^M \frac{\partial \gamma_{\alpha\xi}}{\partial \mathbf{R}_\alpha} \Delta q_\xi - \frac{\partial E_{\text{rep}}}{\partial \mathbf{R}_\alpha}. \tag{3.45}$$

4 Molecular dynamics simulation

In order to deal with a molecular system using the equations discussed in the previous Sections, there are three typical stages

- Minimization,
- Equilibration,
- Dynamics.

4.1 Minimization

Quite frequently, the main goal of atomistic simulations is to find an energy minimum, a local or global one, with respect to the nuclear coordinates, i.e., optimize the system geometry. Usually, one can expect more than one minimum for systems like polymers, biopolymers, flexible molecules of cyclodextrins or liquids under periodic boundary conditions. A geometry optimization procedure consists of sampling points on the potential energy surface, searching for a minimum. The technique used to search for the minimum is called the optimization algorithm which usually is based on one of the following schemes:

- Conjugate gradients,
- Steepest descents,
- Monte Carlo simulations,
- Genetic algorithms,
- Molecular dynamics.

In principle there will be a global minimum, but this will not likely to be found without a conformational search. In order to accelerate the search, many of the algorithms use the past history of points sampled to determine the next point to examine. For some quantum-mechanical force models, there are difficulties (as compared to their classical counterparts) attributed to discontinuous changes (at times) in the total energy from iteration to iteration. Throughout this work, we used two of these methods of geometry optimization i.e., the conjugate gradient relaxation and molecular dynamics methods, implemented both in the Vienna Ab-initio Simulation Package (VASP) [36], and the (SCC-DFTB) code [32]. We shall discuss briefly only the special features of this as detail of the algorithms can be found in [80].

4.2 Conjugate gradient algorithm

The conjugate gradient technique provides an efficient method for locating the minimum of a general function such as the Kohn-Sham energy function already discussed. It is similar to the steepest descent method as the line of search for the minimum is required. The steepest descent method uses the first derivatives of the function in order to determine the direction towards the minimum. Thus, in the absence of any information about the function $F(x)$, the optimum direction to move from x_1 to minimize the function is just the steepest-descent given by

$$g_1 = -\left.\frac{\partial F}{\partial x}\right|_{x=x_1}, \tag{4.1}$$

or simply written as negative of the gradient operator

$$g_1 = -Gx_1. \tag{4.2}$$

This is not particular efficient because it must combine with a line search to determine the step size. The line search uses the direction vector obtained from the first derivative of the potential function to find the optimum step size along this vector direction. Thus, the function $F(x)$ is reduced by moving from the point x_1 in the steepest-descent direction g_1 to the point x_2,

$$x_2 = x_1 + b_1 g_1, \tag{4.3}$$

where the function is a minimum (the subscripts below x label the iterations). Once this local minimum along the direction of the derivative is found, the step can be taken. The next derivative will be orthogonal to the first. This step described above can be repeated to generate a series of vectors x_m such that the value of the function $F(x)$ decreases at each iteration. Hence $F(x_l) < F(x_k)$ for $l > k$. A line search of this scheme requires several function evaluations, however, in order to determine the optimum step size. The technique is robust and is used to minimize initially when the structure is far from the minimum configuration.
More efficient minimization can be obtained using conjugate gradients. The conjugate gradient technique uses information from previous first derivatives to determine the optimum direction for a line search. Therefore, in conjugate gradients, the new direction vector, h_{i+1} leading from point x_{i+1} is computed by adding a term to the gradient, g_{i+1} used to be the steepest descent. This term is a constant times the old direction h_i written as:

$$h_{i+1} = g_{i+1} + \gamma h_i, \tag{4.4}$$

where γ is a scalar defined by

$$\gamma = \frac{g_{i+1}\dot{g}_{i+1}}{g_i \dot{g}_i}, \tag{4.5}$$

where g_i and g_{i+1} are the gradients (first derivatives) calculated at points x_i and x_{i+1}. Therefore, no matter what the initial point is, g times the old direction always provides a correction to the gradient, which then produces a direction conjugate to all previous directions. A line search is still required as in steepest descent. Figure 4.1 schematically illustrates the methods of convergence for a centre of an anisotropic harmonic potential. The pictures illustrate how the functions $F(x)$ decreases rapidly to the minimum. The

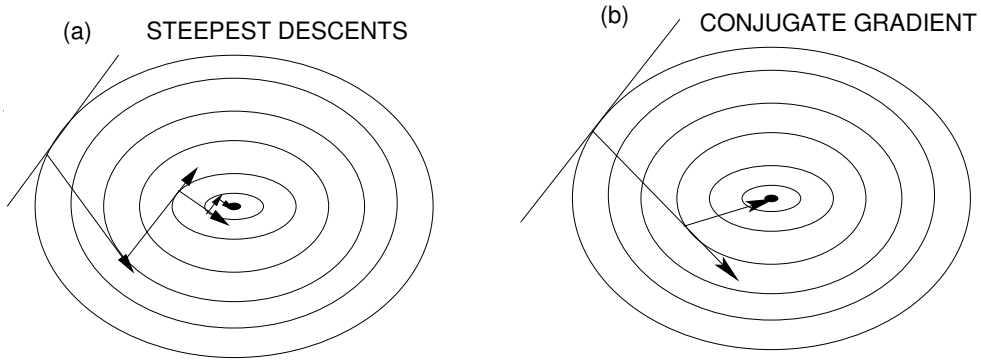

Figure 4.1: Schematic illustration of two methods of convergence for the center of an anisotropic harmonic potential. (a) The steepest-descent method requires many steps to converge. (b) Conjugate-gradient method allows convergence in two steps.

major difference between the two techniques is that, in the method of steepest descent, each direction is chosen only from information about the function at the present sampling point. In contrast to this, in conjugate-gradient technique, the search direction is generated using information about the function obtained from all the sampling points along the conjugate-gradient path. The conjugate-gradient technique therefore provides an efficient method for locating a minimum of a general function such as the Kohn-Sham energy function. The computational speed and memory requirement depend on the methods of implementation. Both the steepest-descent and conjugate-gradient methods are implemented in the VASP code in updating the positions of the ions during the minimization procedure and it is very expensive for the calculation of large molecular systems. In the DFTB method, the conjugate gradient method is implemented such that the computational speed and memory requirement are optimum to handle the minimization of large molecular systems such as cyclodextrin complexes for which the major calculations were done with these two codes.

4.3 Molecular dynamics algorithm

Molecular dynamics, with classical or quantum mechanical force models, describes the motion of particles in space under the influence of forces acting between the particles and external forces. The major difference between this method and the conjugate gradient algorithm previously discussed is that upgrading of the positions of the particles is at finite temperature for molecular dynamics while conjugate gradient method is at zero temperature. The starting point for the solution of classical equations of motion for

a system of N particles interacting via a potential Φ are the Lagrangian equations of motion:

$$\frac{d}{dt}\frac{\partial \mathcal{L}}{\partial \dot{q_k}} - \frac{\partial \mathcal{L}}{\partial q_k} = 0, \qquad (\mathrm{k} = 1, \ldots, 3\mathrm{N}), \tag{4.6}$$

where the Lagrangian $\mathcal{L}(q, \dot{q})$ is a function of the generalized coordinates q_k and their time derivatives $\dot{q_k}$. Such a Lagrangian is defined in terms of kinetic and potential energies:

$$\mathcal{L} = \mathcal{K} - \Phi, \tag{4.7}$$

and total energy E

$$E = \mathcal{K} + \Phi. \tag{4.8}$$

As discussed in the beginning of Section 2.1.1, if we consider a system of atoms, with Cartesian coordinates $\mathbf{R}_I$ and mass M_I, the kinetic energy reads:

$$\mathcal{K} = \frac{1}{2}\sum_{I}^{N} M_I \dot{\mathbf{R}}_I^2, \tag{4.9}$$

and the potential energy:

$$\Phi = V(\mathbf{R_I}, \ldots, \mathbf{R_N}). \tag{4.10}$$

Using these definitions, Eq. (4.6) becomes:

$$M_I \ddot{\mathbf{R}}_I = \mathbf{F_I} \tag{4.11}$$

and

$$\mathbf{F_I} = -\nabla_{\mathbf{R_I}} \mathbf{V}, \tag{4.12}$$

is the force on the atom I. The equation of motion (4.11) can be integrated numerically. The simpler method of integration is the Verlet algorithm [116], which is a direct solution of Eq. (4.11). It is this method which is implemented in both the DFTB and VASP codes. Following this algorithm, we have

$$q(t + \delta t) = 2q(t) - q(t - dt) + \frac{\delta t^2 \mathbf{F_I}(t)}{M_I}. \tag{4.13}$$

In this approach, the velocities do not appear at all. The velocities are not needed to compute the trajectories, but they are useful for estimating the kinetic energy. They may be obtained using finite differences:

$$\dot{q}(t + \delta t) = \frac{q(t + \delta t) - q(t - \delta t)}{2\delta t}. \tag{4.14}$$

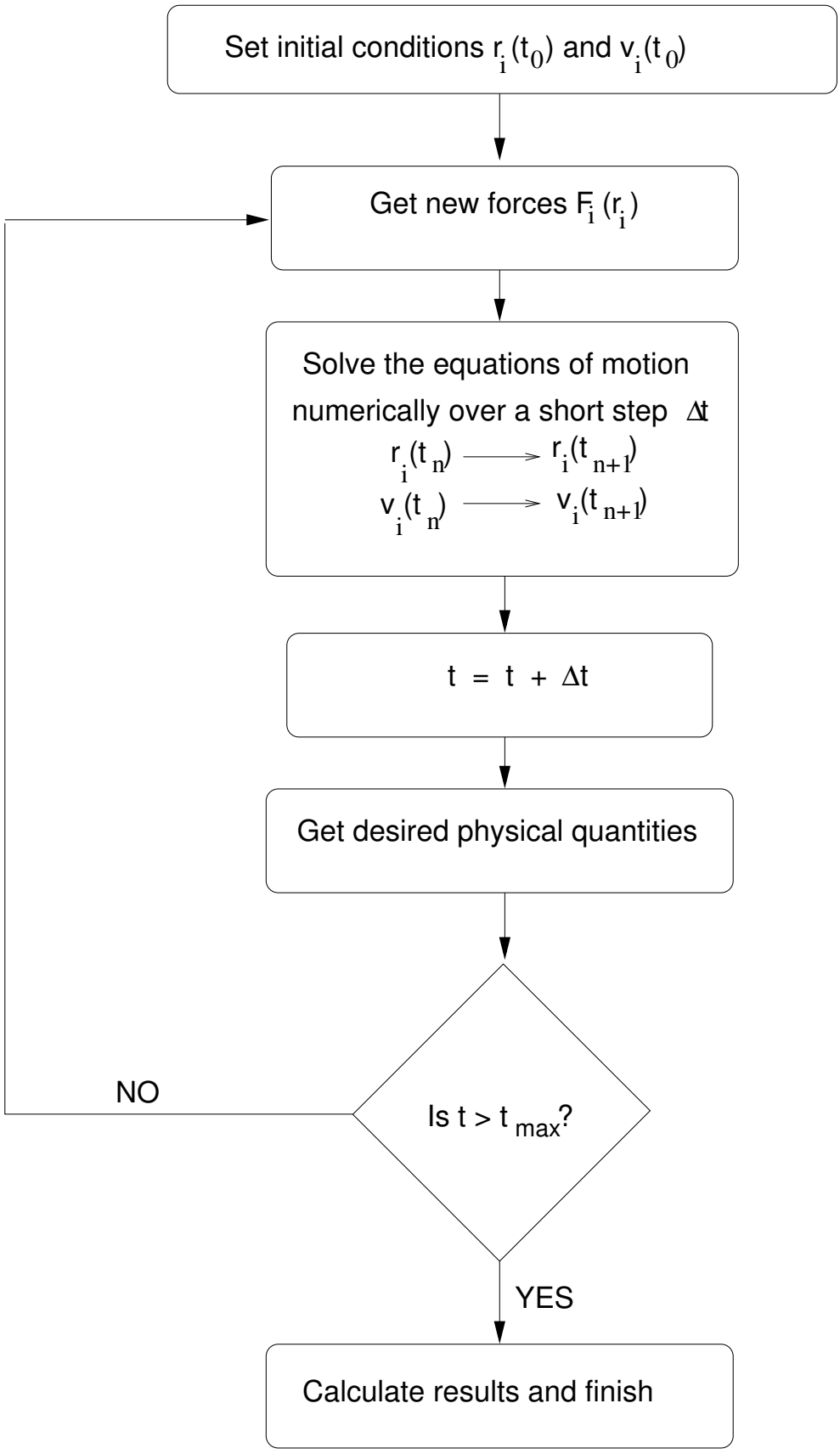

Figure 4.2: Flow chart describing the molecular dynamics algorithm.

Whereas Eq. (4.13) is of order δt^4 the velocities from Eq. (4.14) are subject to errors of order δt^2. In order to solve this problem several algorithms were introduced.
In DFTB, the geometry update is due to velocity, $\dot{q}(t)$ and force, $\mathbf{F}(t)$. That means, we have the coordinates for $q(t + dt)$, but not the velocities. But we definitely need these velocities to determine the temperature or kinetic energy of the system. A compromise is made by using

$$\dot{q}(t + \delta t) = \frac{q(t + \delta t) - q(t)}{\delta t} \tag{4.15}$$

in order to determine the temperature and to rescale the velocities. Also, there is one more thing to take care of: There are a lot of cases when $\dot{q}(t)$ is exactly known: Either in the very first step of the MD simulation or after we did a rescaling of the velocities according to the current temperature. In either case, the velocity of the atoms is determined using the formula

$$\dot{q}(t) = \frac{q(t) - q(t - \delta t)}{\delta t}, \tag{4.16}$$

which is in contrast to the general Verlet Eq. (4.14) but the error is corrected in the code by resetting $q(t - \delta t)$ according to

$$q(t - \delta t) = q(t - \delta t) + \frac{\delta t^2 \mathbf{F_I}(t)}{2M_I}, \tag{4.17}$$

which is solved iteratively until the convergence is reached (see the detail in the DFTB code).
Both DFTB and VASP methods applied in this work, make use of the Born-Oppenheimer approximation as described in detail in Section 2.1.2. It means in this case that the particles are nuclei. The equations of motion for a system of atoms follow laws of classical mechanics according to Newton (but the forces are calculated quantum mechanically). The Eqs. (4.11) and (4.12) form the theoretical basis of *ab-initio* molecular dynamics simulation.
A Flow chart describing a typical molecular dynamics algorithm is presented in Fig. 4.2. Molecular dynamics can be used for finding local minima by removing gradually kinetic energy from the system. Or, the other way round, heating up the system followed by its slow cooling makes it possible to go from a local minimum to a different one or to the global one (simulated annealing) as illustrated in Fig. 4.3. Depending on temperature at which the simulation is run, MD allows barrier crossing and exploration of multiple configurations. In order to initiate MD, we need to assign initial velocities. This is done by using a random number generator and employing the constraint of the Maxwell-Boltzmann distribution. The temperature T is defined by the average kinetic energy of the system according to the kinetic theory of gases whereby the internal energy of the system, U, is given by

$$U = \frac{3}{2} N k_B T, \tag{4.18}$$

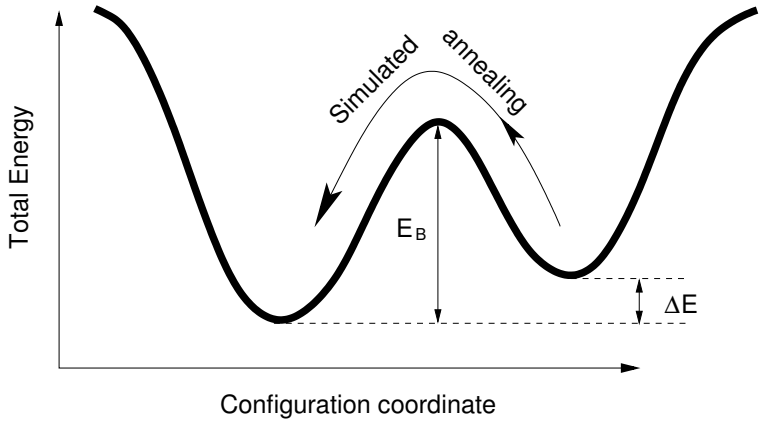

Figure 4.3: Representation of two energy minima separated by a barrier. Artificially high temperatures make it possible for the system to overcome the potential barrier in a realistic simulation time.

while the kinetic energy, $\mathcal{K}$, is defined by Eq. (4.9). By averaging over the velocities of all the atoms in the system (or over all the degree of freedoms), the temperature can be estimated. It is assumed that once an initial set of velocities has been generated, the Maxwell-Boltzmann distribution will be maintained throughout the simulation.
Figure 4.4 shows an example of simulation annealing done with VASP in which 32 molecules of water were arbitrary placed in a simulation box. In order to obtain a good geometry for this configuration at the real density of water, the kinetic energy (or temperature to be discussed), is gradually removed from this system until a low energy configuration is reached. Following the minimization we can consider the temperature as being essentially zero (not exactly because of fluctuation due to zero point motion of the atoms which, however, are absent if we treat the atoms as classical particles). In order to initialize the dynamics, the system must be brought up to the temperature of interest. This is done by assigning velocities at some low temperature and then following the dynamics according to the equations of motion. The geometry obtained at the end of 1.0 ps run in Fig. 4.4 is used for further calculations discussed in the next Section. This is done by fixing the temperature of interest by assigning the velocities on the low energy configuration of the system obtained. After a number of iterations, the temperature is scaled upwards. The most common means of temperature scaling is velocity scaling. Since the velocity for each atom is distributed about the average of $v = (3k_BT/m)^{\frac{1}{2}}$, one can multiply all of the velocities by a common factor to obtain a new temperature. This is done systematically during the equilibration (initialization) stage.

4.4 How the temperature is calculated

The temperature is a thermodynamic quantity, which is only meaningful at equilibrium. It can be related to the average kinetic energy of a classical system through the equipartition principle. This principle states that every degree of freedom (either in momenta or

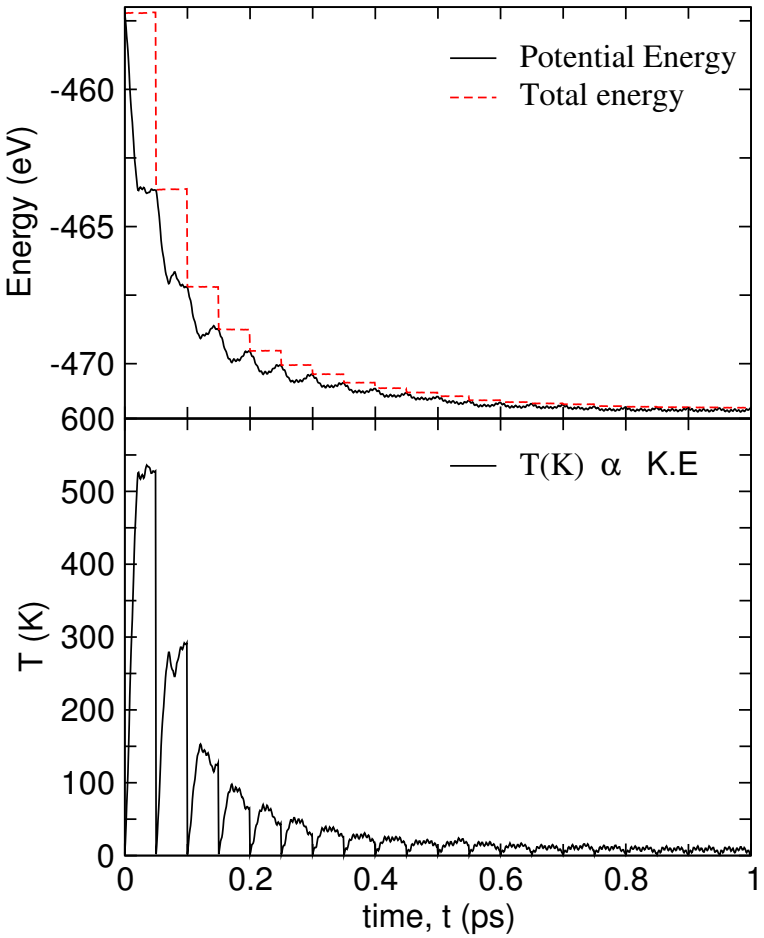

Figure 4.4: Calculation done with VASP on 32 molecules of water in a simulation box illustrating the gradual removal of excess heat until some local minimum is reached.

coordinates), which appears as a squared term in the Hamiltonian, has an average energy of $k_BT/2$ associated with it. This is the case for momenta $\mathbf{p_i}$ which appear as $\mathbf{p_i}^2/2m$ in the Hamiltonian. Hence we have:

$$\left\langle \sum_i^N \frac{\mathbf{p_i}^2}{2m} \right\rangle = \langle \mathcal{K} \rangle = \frac{N_f k_B T}{2}. \tag{4.19}$$

The left side of Eq. (4.19) is called the average kinetic energy, $\mathcal{K}$ of the system, N_f is the number of degrees of freedom, and T in this case the thermodynamic temperature. In an unrestricted system with atoms, N_f is $3N$ because each atom has three velocity components, i.e., $\dot{q} = v_\alpha$, with $\alpha = x,\ y$ and z. Because of this, it is convenient to define an instantaneous kinetic temperature function whose average is the thermodynamic temperature T as

$$T_{instan} = \frac{2\mathcal{K}}{N_f k_B T}. \tag{4.20}$$

The average of the instantaneous temperature is the thermodynamic temperature. The instantaneous temperature is calculated from the total kinetic energy and the total number of degrees of freedom. Therefore, for a *non-periodic* system where we have,

$$\frac{(3N-6)k_BT}{2} = \sum_{i=1}^{N} \frac{m_i v_i^2}{2}, \tag{4.21}$$

where six degrees of freedom are subtracted because the translation and rotation of the centre of mass are ignored. In the DFTB, the temperatures are calculated according to Eq. (4.21) whenever we consider systems with open boundary conditions while for periodic systems both in the DFTB and VASP codes we use

$$\frac{(3N-3)k_BT}{2} = \sum_{i=1}^{N} \frac{m_i v_i^2}{2}. \tag{4.22}$$

In the latter case, only the three degrees of freedom corresponding to translational motion can be ignored, since the rotation of a central cell imposes a torque on its neighbouring cells.

4.5 How the temperature is controlled

Although the initial velocities are generated so as to maintain a Maxwell-Boltzmann distribution at desired temperature, the distribution does not remain constant as the simulation continues. This is especially true when the system does not stay in an equilibrated configuration. This often occurs, since the system is minimized to eliminate the hot spots. During dynamics, kinetic energy is changed to potential energy as the minimized structure changes to the equilibrium structure, and the temperature also changes. In order to maintain the correct temperature, the computed velocities have to be adjusted appropriately. Beside getting the temperature to the right target, the temperature-control mechanism also must produce the correct statistical ensembles. This means that the probability of occurrence of a certain configuration obeys the laws of statistical mechanics. For constant-temperature, constant-volume dynamics to generate the canonical ensemble means that $P(E)$, the probability that a configuration with energy E will occur, is proportional to $\exp(E/k_BT)$. Several methods for temperature control exist but the ones which are mostly used in this work are:

- Velocity scaling
- Nosé dynamics

while both methods are implemented in VASP, only the direct velocity scaling method is implemented in the DFTB.

4.5.1 Direct velocity scaling

Direct velocity scaling is a drastic way to change the velocities of the atoms so that the target temperature can be exactly matched whenever the system temperature is higher or lower than the target one by some user-defined amount. Usually we use 0.1 (or 10 percent) when employing the DFTB method in our calculations. The value has been tested to give the desired temperatures. The velocities of all atoms are scaled uniformly as follows:

$$\left(\frac{v_{\text{new}}}{v_{\text{old}}}\right)^2 = \frac{T_{\text{target}}}{T_{\text{system}}}. \tag{4.23}$$

This adds (or subtracts) energy from the system efficiently, but it is important to recognize that the fundamental limitation to achieve equilibrium is how rapidly energy can be transfered to, from, and among the various internal degrees of freedom of the molecule. The speed of this process depends on the potential energy expression, the parameters, and the nature of the coupling between the vibrational, rotational, and translational modes. It depends directly on the size of the systems, larger systems take longer time to equilibrate.

4.5.2 Berendsen's method of temperature-bath coupling

After equilibration, a more gentle exchange of thermal energy between the system and a heat bath can be introduced through the Berendsen method [117], in which each velocity is multiplied by a factor λ given by:

$$\lambda = \left[1 + \frac{\Delta t}{\tau}(T - T_0)\right]^{\frac{1}{2}} \tag{4.24}$$

where Δt is the time step size, τ is a characteristic relaxation time, T_0 is the target temperature, and T the instantaneous temperature. To a good approximation, this treatment gives a constant-temperature ensemble that can be controlled, both by adjusting the target T_0 and by changing the relaxation time.

4.5.3 Nosé dynamics

Nosé dynamics is a relatively new method for performing constant-temperature dynamics, which produces true canonical ensembles. The actual formalism implemented in VASP is based on a simplified reformulation by Hoover in 1985 [118]. Thus, the method is called the Nosé-Hoover thermostat (or Nosé-Hoover dynamics). The main idea behind Nosé-Hoover dynamics is that an additional (fictitious) degree of freedom is added to the real physical system which is given a mass Q. The equations of motion for the extended (i.e., real plus fictitious) system are then solved. If the potential chosen for that degree of freedom is correct, the constant-energy dynamics (or the micro canonical dynamics,

NVE) of the extended system produces the canonical ensemble (NVT) of the real physical system. The Hamiltonian H^* of the extended system is:

$$H^* = \sum_i \frac{p_i^2}{2m_i} + \phi(q) + \frac{Q}{2}\zeta^2 + gk_{\mathrm{B}}T\mathrm{In}s. \tag{4.25}$$

The corresponding equations of motion for the real-atom coordinates $\mathbf{q}$ and momenta $\mathbf{p}$, as well as for the fictitious coordinates s and associated momentum ζ (where ϕ is the interaction potential) are given by

$$\frac{dq_i}{dt} = \frac{p_i}{m_i}, \tag{4.26}$$

$$\frac{dp_i}{dt} = -\frac{\phi}{dq_i} - \zeta p_i, \tag{4.27}$$

$$\frac{d\zeta}{dt} = \frac{\sum \frac{\mathbf{p}_i^2}{m_i} - gk_BT}{Q}, \tag{4.28}$$

where Q = the user-defined $\mathbf{q}_{\mathrm{ratio}}$ × a constant $\times g \times T$;
g = number of degrees of freedom;
T = temperature.
The choice of the fictitious mass Q of that additional degree of freedom is arbitrary but is critical to the success of a run. If Q is too small, the frequency of the harmonic motion of the extended degree of frequency is too high. This forces a smaller time step to be used in integration. However, if Q is too large, the thermalization process is not efficient, as Q approaches infinity, there is no energy exchange between the heat bath and the real system. In addition the Nosé method requires that an accurate integrator, for energy to be conserved, is used. Q should be different for different systems. Nosé suggests that Q should be proportional to gk_BT.

4.6 Measured observables from *ab-initio* molecular dynamics

All the methodology discussed so far will be useless if one could not compute experimentally measured observables. In this regard, *ab-initio* molecular dynamics simulations have some distinct advantages over force field based molecular dynamics in that former permit direct access to the electronic structure and, hence, any observable can be derived directly from it.
In MD calculations, obersvables are computed by performing averages of appropriate functions, $A(p, q)$, of the momenta and coordinates of the particles in the system. The procedure relies on the ergodic hypothesis which states that given an infinite amount of

time, a system will visit all of its accessible phase space so that ensemble averages of $A(\mathbf{p},\mathbf{q})$ can be directly related to the time averages of the MD trajectory:

$$\langle A(\mathbf{p},\mathbf{q})\rangle = \lim_{T\to\infty}\frac{1}{T}\int_0^T dt\ A(\mathbf{p}(t),\mathbf{q}(t)). \tag{4.29}$$

Equation (4.29) will therefore yield an equilibrium average of the system. The ensemble average (4.29) could refer to any pertinent ensemble. For example, a microcanonical (NVE) ensemble average would be given by

$$\langle A(\mathbf{p},\mathbf{q})\rangle = \frac{1}{N!h^{3N}\Omega(N,V,E)}\int d^N\mathbf{p}\ d^N\mathbf{q}\ A(\mathbf{p},\mathbf{q})\delta(H_N(\mathbf{p},\mathbf{q})-E), \tag{4.30}$$

where $H_N(\mathbf{p},\mathbf{q})$ is the classical nuclear Hamiltonian Eq. (2.13), and $\Omega(N,V,E)$ is the partition function of the microcanonical ensemble. An average in the canonical (NVT) ensemble is given by

$$\langle A(\mathbf{p},\mathbf{q})\rangle = \frac{1}{N!h^{3N}Q(N,V,T)}\int d^N\mathbf{p}\,d^N\mathbf{q}\ A(\mathbf{p},\mathbf{q})\exp(-\beta H_N(\mathbf{p},\mathbf{q})). \tag{4.31}$$

Here $Q(N,V,T)$ is the partition function of the canonical ensemble. For practical purpose, if δt is the chosen time step of the molecular dynamics for M runs, such that the time step of each run is

$$t_m \ = \ m\delta t, \ \text{ with } \qquad m = 1,2,\ldots,M,$$

the time average of the quantity of the observable $A(\mathbf{p},\mathbf{q})$ is computed from

$$\langle A(\mathbf{p},\mathbf{q})\rangle_{time\ ave.} = \frac{1}{M}\sum_{m=1}^{M} A(\mathbf{q_1}(t_m),\ldots,\mathbf{q_N}(t_m),\mathbf{p_1}(t_m),\ldots,\mathbf{p_N}(t_m)), \tag{4.32}$$

which is expected to be equal to

$$\langle A(\mathbf{p},\mathbf{q})\rangle_{ensemble\ ave.} = \lim_{T\to\infty}\frac{1}{T}\int_0^T dt\, A(\mathbf{q_1}(t),\ldots,\mathbf{q_N}(t),\mathbf{p_1}(t),\ldots,\mathbf{p_N}(t)), \tag{4.33}$$

so that the ergodicity hypothesis

$$\langle A(\mathbf{p},\mathbf{q})\rangle_{\text{time ave.}} = \langle A(\mathbf{p},\mathbf{q}))\rangle_{\text{ensemble ave.}} \tag{4.34}$$

holds.

4.6.1 Static properties

The static structure of matter can be characterized by the radial distribution function $g(r)$ which describes the spatial organization of molecules about a cental molecules, i.e., it measures how atoms organize themselves around one another. Specifically, it is proportional to the probability of finding two atoms separated by distance $r \pm \Delta r$. It

plays a central role in statistical mechanical theories of dense substances, and, for atomic substances, it can be extracted from X-ray and neutron diffraction experiments. Since molecular dynamics provide positions of individual atoms as functions of time, $g(r)$ can be readily computed from molecular dynamics trajectories.
As concrete example to Eq. (4.31), the radial distribution function is given as an average:

$$g(r) = \frac{1}{4\pi r^2 \rho N Q(N,V,T)} \int d^N\mathbf{p}\, d^N\mathbf{R} \sum_{I\neq J} \delta(|\mathbf{R}_I - \mathbf{R}_J| - r)\exp(-\beta H_N(\mathbf{p},\mathbf{R})),$$

$$g(r) = \frac{1}{4\pi r^2 \rho} \left\langle \frac{1}{N} \sum_{I\neq J} \delta(|\mathbf{R}_I - \mathbf{R}_J| - r) \right\rangle. \tag{4.35}$$

For simulation, purpose, $g(r)$ can be easily computed by using another expression,

$$g(r) = \frac{\langle N(r,\Delta r)\rangle}{\frac{1}{2}N\rho V(r,\Delta r)}, \tag{4.36}$$

where $N(r,\Delta r)$ is the number of atoms found in a spherical shell of radius r and thickness Δr, with the shell centred on another atom. Writing the time average explicitly over a total of M time-steps gives

$$g(r) = \frac{\sum_{k=1}^{M} N_k(r,\Delta r)}{M(\frac{1}{2}N)\rho V(r,\Delta r)}, \tag{4.37}$$

where N_k is the result of the counting operation defined by

$$g(r) = \sum_{i}^{N} \sum_{j<i}^{N} \delta\left[r - r_{ij}\right] \Delta r = N(r,\Delta r) \tag{4.38}$$

at time t_k in the run. Physically, Eq. (4.38) can be interpreted as the ratio of a local density $\rho(r)$ to the system density ρ [119]. The choice of a value for the shell thickness Δr is a compromise. It must be small enough to resolve important features of $g(r)$, but it must also be large enough to provide a sufficiently large sampling population for statistically reliable results. Most of our simulations were carried out in a cubic box of length L, so that the values of $g(r)$ were determined up to $\frac{1}{2}L$.
The radial distribution function (RDF), depends on density and temperature, and therefore serves as a helpful indicator of the nature of the phase assumed by the simulated system. We have used this function to identify the phase behaviour of water clusters especially below and above the solid-liquid transition regions (see the next Section). The RDF can also be used to find the coordination numbers. The coordination number, N_{ij}, represents the number of type i-atoms around a type j-atom plus the number of type

j-atoms around a type i-atom at a distance r. The average coordination number can then be expressed as

$$\langle N_{ij}(r)\rangle = \rho_{ij}\int_0^r dr\, 4\pi r^2\, g(r). \tag{4.39}$$

In practice, the elastic neutron scattering structure factor can be computed by Fourier transforming the RDF or by directly performing an ensemble (or trajectory) average over

$$S(k) = \frac{1}{N}\left|\sum_{I=1}^{N}\exp(i\mathbf{k}.\mathbf{R}_I)\right|^2. \tag{4.40}$$

4.6.2 Dynamical properties

Dynamical properties such as spectra and transport coefficients can be obtained within classical linear response theory from time correlation functions. The time correlation between two observable, $A(\mathbf{p},\mathbf{q})$ and $B(\mathbf{p},\mathbf{q})$ is given by

$$\langle A(0)B(t)\rangle = \frac{1}{Q(N,V,T)}\int d^N\mathbf{q}d^N\mathbf{p}\, A(\mathbf{p},\mathbf{q})B(\mathbf{p}_t(\mathbf{p},\mathbf{q}),\mathbf{q}_t(\mathbf{p},\mathbf{q})) \times\exp(-\beta H_N(\mathbf{p},\mathbf{q})), \tag{4.41}$$

where $(\mathbf{p}_t(\mathbf{p},\mathbf{q}),\mathbf{q}_t(\mathbf{p},\mathbf{q}))$ designates the phase space trajectory obtained from the initial condition $(\mathbf{p},\mathbf{q})$. For $A = B$, Eq. (4.41) is the autocorrelation function. For instance, the diffusion coefficient (D) can be computed from the velocity autocorrelation function:

$$D = \frac{1}{3}\int_0^\infty dt\ \frac{1}{N}\ \sum_I^N \langle\mathbf{v}_I(0)\mathbf{v}_I(t)\rangle. \tag{4.42}$$

In addition, the velocity autocorrelation function can be used to obtain the frequency spectrum for the system known as *power spectrum* by computing its Fourier transform

$$I(\omega) = \int_{-\infty}^{\infty} dt\, e^{i\omega t}\ \frac{1}{N}\ \sum_{I=1}^{N}\langle\mathbf{v}_I(0)\mathbf{v}_I(t)\rangle \tag{4.43}$$

whereby the velocity autocorrelation function, $C_{vv}(t)$, is computed from

$$C_{vv}(t) = \langle\mathbf{v}(t)\mathbf{v}(0)\rangle = \frac{1}{NM}\sum_i^N\sum_{t_0}^M \langle\mathbf{v}_i(t+t_0)\mathbf{v}(t_0) \tag{4.44}$$

with $\mathbf{v}_i(t)$ the center-of-mass velocity of particle i at time t. N is the total number of molecules of interest. Also, M is the total number of available time origins; its value changes with the delay time t,

$$M = N_t - \frac{t}{\Delta t}, \tag{4.45}$$

and Δt is the time increment at which velocities have been stored. N_t is the length of the simulation period. In our molecular dynamics simulation we have further evaluated the mean-square centre of mass displacement (MSD) the expression defined,

$$\mathrm{MSD} = \Delta r^2(t) = \langle |r(t) - r(0)|^2 \rangle = \frac{1}{NM} \sum_{i}^{N} \sum_{t_0}^{M} |\mathbf{r}_i(t + t_0) - \mathbf{r}(t_0)|^2. \tag{4.46}$$

In Eq. (4.46), $\mathbf{r}_i(t)$ is the center-of-mass position of the particle i at time t. From this equation, through the Einstein relation [120], the diffusion (or self-diffusion) coefficients can alternatively be calculated from

$$D = \frac{1}{6t} \left\langle |\mathbf{r}_i(t + t_0) - \mathbf{r}(t_0)|^2 \right\rangle, \tag{4.47}$$

or

$$D = \frac{1}{6N} \lim_{t \to \infty} \frac{d}{dt} \left\langle \sum_{i}^{N} [\mathbf{r}_i(t) - \mathbf{r}(0)]^2 \right\rangle. \tag{4.48}$$

The last equation shows that D is proportional to the slope of MSD at long time. This measured quantity can be used to distinguish the fluid from solid-like behaviour. For a solid, $\Delta r^2(t)$ remains nearly constant, while for a fluid it increases almost linearly with time. The self-diffusion coefficients of a fluid is usually several orders of magnitude larger than that of a solid.
Another useful quality to test the liquid or solid-like behaviour, for instance, of water clusters is the root-mean-square bond-length fluctuation, δ_{OO}, of oxygen:

$$\delta_{\mathrm{OO}} = \frac{2}{N(N-1)} \sum_{i<j} \frac{\sqrt{\langle r_{ij}^2 \rangle - \langle r_{ij} \rangle^2}}{\langle r_{ij} \rangle}, \tag{4.49}$$

where $\langle\rangle$ means time average, and r_{ij} is the distance between the atoms i and j. The phase change in the system gives rise to a jump in the plot of δ_{OO} against the temperature as will be seen in the next Section.

4.6.3 Geometrical properties

Other properties of interest that were measured during the simulation of ensembles of molecules are the geometrical fluctuations of bond lengths, the angles and the dihedral angles. The equations used in the computation of these quantities are as follows [121]: For bond the length r between two atoms 1 and 2 and the bond vector, $\mathbf{R}$, we define according to Fig. 4.5(a),

$$\mathbf{R} = (x_2 - x_1)\mathbf{i} + (y_2 - y_1)\mathbf{j} + (z_2 - z_1)\mathbf{k}, \tag{4.50}$$

$$r = \sqrt{(x_2 - x_1)^2 + (y_2 - y_1)^2 + (z_2 - z_1)^2}. \tag{4.51}$$

The bond angle, θ, from the two vectors and the lengths is calculated according to Fig. 4.5(b) from

$$\cos\theta = \frac{\mathbf{R}_1 \cdot \mathbf{R}_2}{r_1\ r_2}. \tag{4.52}$$

In order to measure the torsion or dihedral angle, $\phi_{1,2,3,4}$ in Fig. 4.5(c), between the four atoms 1,2, 3 and 4, we used

$$\cos\phi_{1,2,3,4} = \frac{[\mathbf{R}_1 \times \mathbf{R}_2] \cdot [\mathbf{R}_3 \times \mathbf{R}_2]}{|\mathbf{R}_1 \times \mathbf{R}_2|\,|\mathbf{R}_3 \times \mathbf{R}_2|}. \tag{4.53}$$

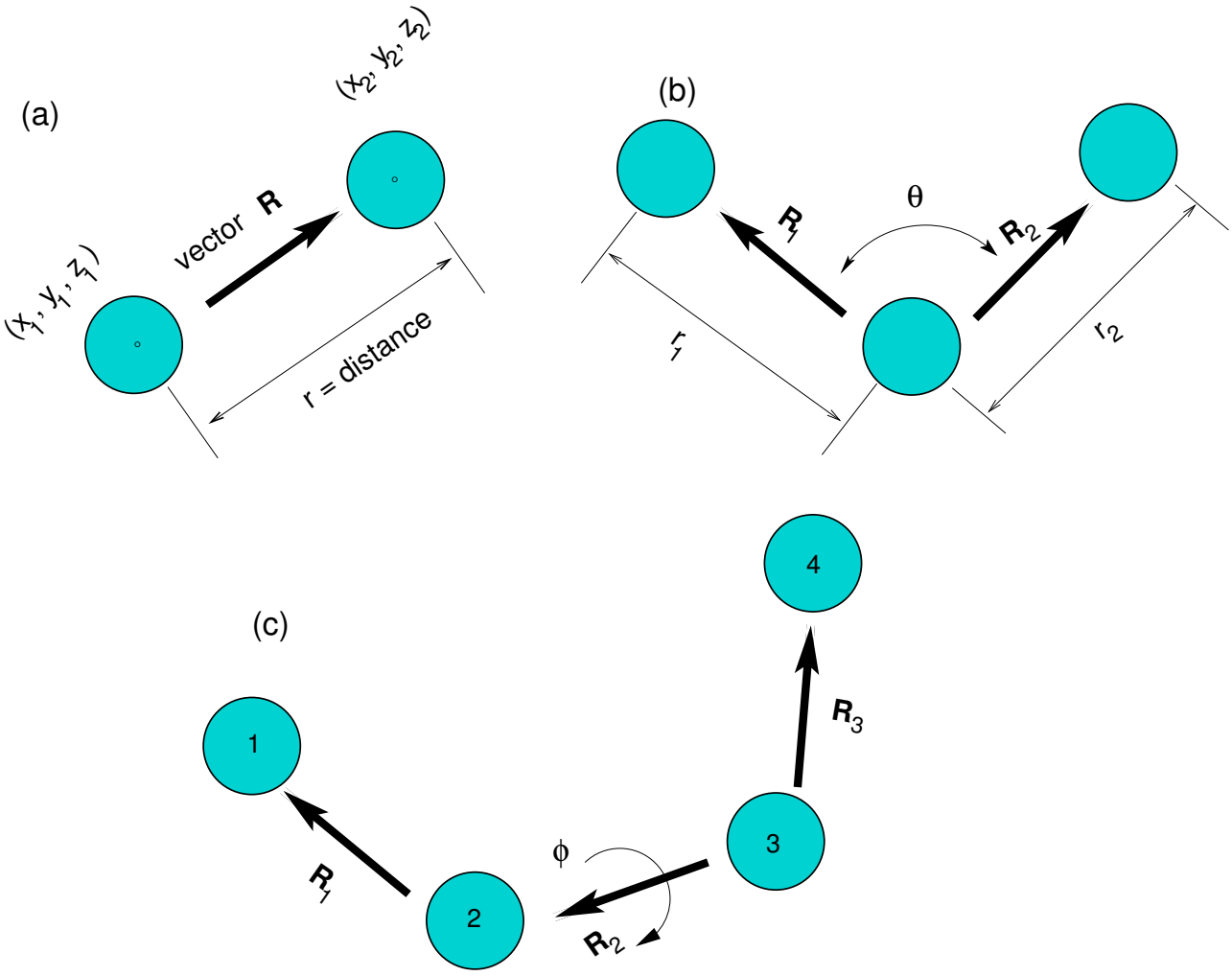

Figure 4.5: Geometrical definition of (a) bond length, (b) angle and (c) dihedral angle.

5 Water clusters and their transition temperatures

From this Chapter onward we present our results based on the applications of state-of-the-art *ab-initio* methods and molecular dynamics simulation discussed so far.
Our present goal in this Chapter is to assess the ability of density functional based *ab-initio* MD of both the DFTB method and VASP to describe some of the properties of water at its cluster units level since these form the bases of most of the important features of the structure of ice found in nature and the so-called glassy behaviour of water. We calculate the binding energy and melting transition of water clusters of n-mer with $n = 2, 3, \ldots, 36$ and compare our *ab-initio* results to some classical modelled potentials. Two different configurations of water clusters were considered; the SCC-DFTB structures which consists of some local minimum configurations and the global minimum configurations of TIP4P classical pairwise additive potential in order to investigate the effect of initial configurations on both binding energies and the melting temperatures. The melting transitions of these water clusters were determined by using the abrupt change in the slope of energy versus temperature of the calorific curve along with Lindemann's criteria of melting. Though, it is sometimes difficult to determine accurately the breaking point or melting region of the heated structures as a result of the pronounced fluctuations of the bonding network of the system giving rise to fluctuations in the observed properties, but nevertheless we used the range or average region where the breakdown occurs to define the melting temperature of the clusters.

5.1 Water clusters

A realistic simulation of the behaviour of aqueous solutions is of crucial importance in biology, chemistry, and physics. The modelling of pure water and other hydrogen bonding liquids based on effective [122, 123] or *ab-initio* [124] potentials has reached a high degree of sophistication. Many *ab-initio* simulations such as Car and Parrinello molecular dynamics schemes have been devoted to the modelling and the calculation of hydrogen bonding liquids such as water [125]. In this scheme just as in VASP, the interatomic forces are not preassigned before the MD run but have been calculated using the Born-Oppenheimer approximation from accurate electronic structure calculations during the simulation
Water displays unusual physical and chemical properties in its condensed phases. It is among the most studied "chemicals", owing, in part, to its ubiquity and its necessity for all life. In addition to these "natural" reasons, water is an interesting inorganic compound because it has unique physical properties and is a model hydrogen-bonded liquid. Micro clusters of water molecules are important and an interesting area of nature considering its major role in the metabolic functions and the significant role in the structural changes

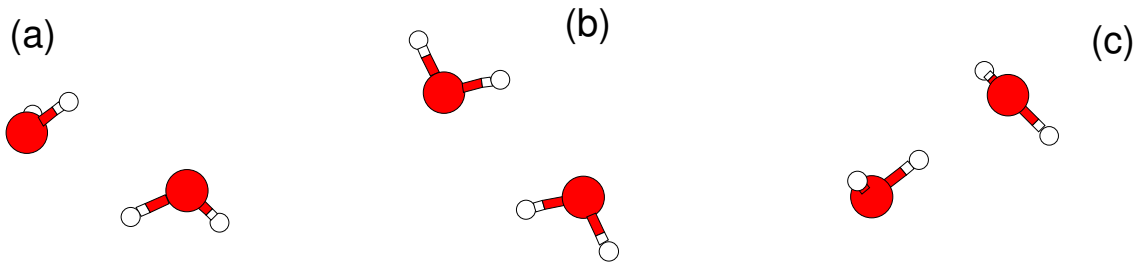

Figure 5.1: Stable water dimer geometries for DFTB and VASP studies.

in our body [3]. An understanding of small clusters in general and how their properties evolve with size will provide an insight into the bulk behaviour [8].

5.1.1 Investigation of the water dimer, $(H_2O)_n$, $n = 2$

For both DFTB and VASP methods, stable dimer geometries and corresponding interaction potential values (i.e, local minimum energies) are obtained. The lowest minimum energy geometries obtained with VASP and DFTB are shown Fig. 5.1. The geometry 5.1(c) is found to be the global minimum by many ab-initio calculations [126] and experimental studies [127]. Calculations based on VASP and the DFTB method also confirmed 5.1(c) as the global minimum structure. The configurations shown are the same for both VASP and the DFTB except for the energy scales and the distances between the oxygen atoms, for example, we obtained $R_{OO} \approx 2.83$ Å (DFTB) and 2.849 Å (VASP with GGA) to be compared to the value of 2.98 Å obtained from molecular beam electronic resonance spectroscopic study [127]. By considering this most stable minimum configuration of the

Table 5.1: Interaction potential energy values (in eV) and R_{OO} (in Å) for the stable water dimer calculated by using DFTB method and VASP.

	DFTB		VASP	
	Energy (eV)	Distance, R_{OO} (Å)	Energy (eV)	Distance, R_{OO} (Å)
(a)	-21.5458	2.8941	-28.693703	2.7921
(b)	-21.5512	2.9404	-28.702163	2.8073
(c)	-21.6085	2.8637	-28.766198	2.8490

water dimer (c), we translated one of the molecules of the dimer in O-O direction (without changing the orientation) and calculated the variation of the total binding energy, E_b(total), with respect to the O-O separation according to

$$E_b(\text{total}) = E(H_2O)_2 - 2E(H_2O). \tag{5.1}$$

Here, $E(H_2O)_2$ is the total interaction energy calculated for the stable dimer, and $2(H_2O)$ is the potential energy of the monomer. $E(H_2O)$ is found to be -10.723 eV for the DFTB calculation and -14.262637 eV when using VASP. The DFTB and VASP results are plotted in Fig. 5.2 for the range R_{OO} = 2-12 Å. In the calculation with VASP, the water dimer was placed in a large cubic supercell of $20 \times 20 \times 20$ Å^3 in order to prevent interaction of the real molecule with its images. The large supercell can be considered to be equivalent to the open boundary conditions used in the DFTB calculation. The variation of the total binding energy, with respect to the O-O distance was then calculated according to the Eq. (5.1) using the Γ-point only. The general features are found to be the same for the two graphs. They both exhibit sharply repulsive interactions at short-range, $R_{OO} < (R_{OO_{min}})$, and attractive tails for $R_{OO} > (R_{OO_{min}})$. The two graphs are found to differ in quantitative details: The minimum is at $(R_{OO_{min}}) = 2.853$ Å} (DFTB), and corresponding E_b = -0.144 eV, while $(R_{OO})_{min} = 2.850$ Å (VASP) and E_b = -0.240 eV. The total binding

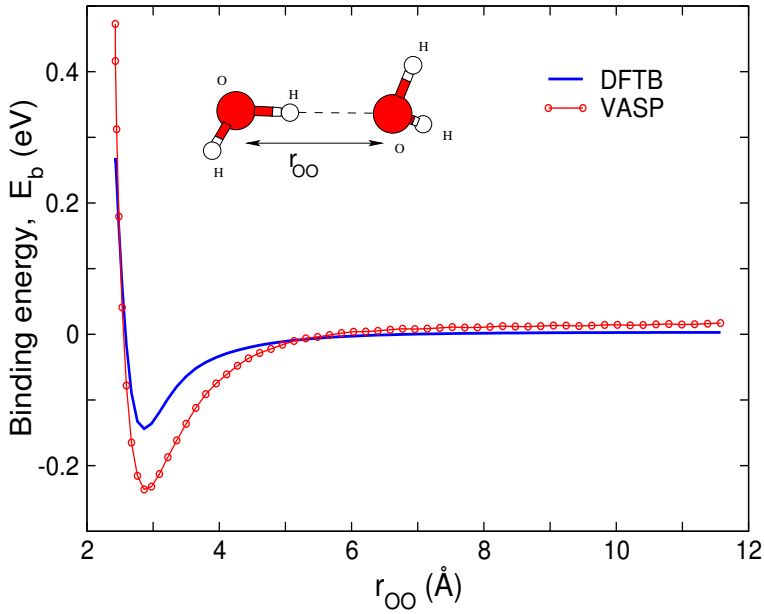

Figure 5.2: Binding energy between two water molecules, as a function of O-O separation.

energy reaches the value 0 at a distance of about 2.59 Å for DFTB and about 2.525 Å} for VASP. A similar study was performed using the central force model 1 and 2 (CF1 and CF2) [128], showing that zeros of total binding energies occur at 2.69 Å and 2.66 Å, respectively. Lemberg and Stillinger [129] have performed a similar study for the same class of potential CF.

5.1.2 Binding energy of water clusters for $n > 2$

The local minimum energies and corresponding geometries for some selected water clusters, $(H_2O)_n$, were briefly studied for the purpose of the next Section, where the melting temperatures of these clusters are investigated. We used the DFTB code to calculate the

binding energies of some minimum energy configurations (which are not necessarily the global minimum structure) of the water clusters with n = 2, 3, 4, 5, 6, 8, 10, 12, 15, 18, 24, 20, 27, 30, and 36 as shown in Fig. 5.3. Some of these geometries, (n = 2, 3, 4, 5, 8, 10 and 15 correspond to the global minimum configurations obtained by Wales [130]). Both DFTB and VASP methods were then used to calculate the binding energies of these global minimum structures of Wales shown in Fig. 5.3 in order to compare the effect of the initial configuration on the melting as discussed in the next Section. Equation (5.1) for the dimer is generalized for the n-water clusters to calculate the binding energy per water molecules, E_b, as

$$E_b = \frac{1}{n}\left[E(\mathrm{H_2O})_n - nE(\mathrm{H_2O})\right], \tag{5.2}$$

where n is the number of water molecules in the cluster, $E(\mathrm{H_2O})_\mathrm{n}$ is the total interaction energy for the stable n-water cluster, and $E(\mathrm{H_2O})$ is the energy of the water monomer which was calculated to be -14.262637 eV (VASP) and -10.732327 eV (DFTB), see Table 5.2 for the DFTB results and Table 5.3 for the results obtained with the DFTB method, VASP, and other classical potential models such as TIP4 (classical pairwise additive potential (CPAP)) [128, 131], TIP4P of Wales [130], MMC [132] and CCD [133]. We also plotted the variation of these binding energies per water molecule, E_b, as a function of the cluster size, n as shown in Fig. 5.5. The inset of Fig. 5.5 shows the calculated binding energies for the clusters $n \leq 8$ in order to compare them with some of the available data in the literature. All curves in this inset are almost parallel for clusters larger than the trimer, and there is no evidence of increased stability of a particular size relative to neighbouring ones in either case. However, this Figure must be regarded with some caution, since the minimum structures for the different potentials are not the same. It can be observed that the binding energy per water molecule increases negatively in exponential sense as the size of the cluster grows and saturates as it can be seen in the outset of the same Figure for the clusters $n > 8$. It is not clear whether there are some magic numbers of water molecules, as was observed for some other clusters like argon and sodium [134]. Though, from all the binding energy per water molecule curves shown in Fig. 5.5, there is a sudden negative increase of E_b at the value of $n = 8$. One may be tempted to consider that $n = 8$ is the first magic number for water clusters as was reported in the calculation done by Sakir *et. al* using the central force model potential (CF1 and CF2) [128]. This anomalous behaviour might be due to the complexity of water connected with the formation of the hydrogen bonding networks.

5.1.3 Melting temperature of water clusters

The structures and properties of molecular clusters have been an active area of research during the last decades because of their importance in chemical, physical and biological processes. There are a number of phenomena in which small clusters of atoms or molecules are believed to play a central role. In the phase transition (melting), the formation of small clusters in a particular phase is a precursor to the transition. Hence, a description

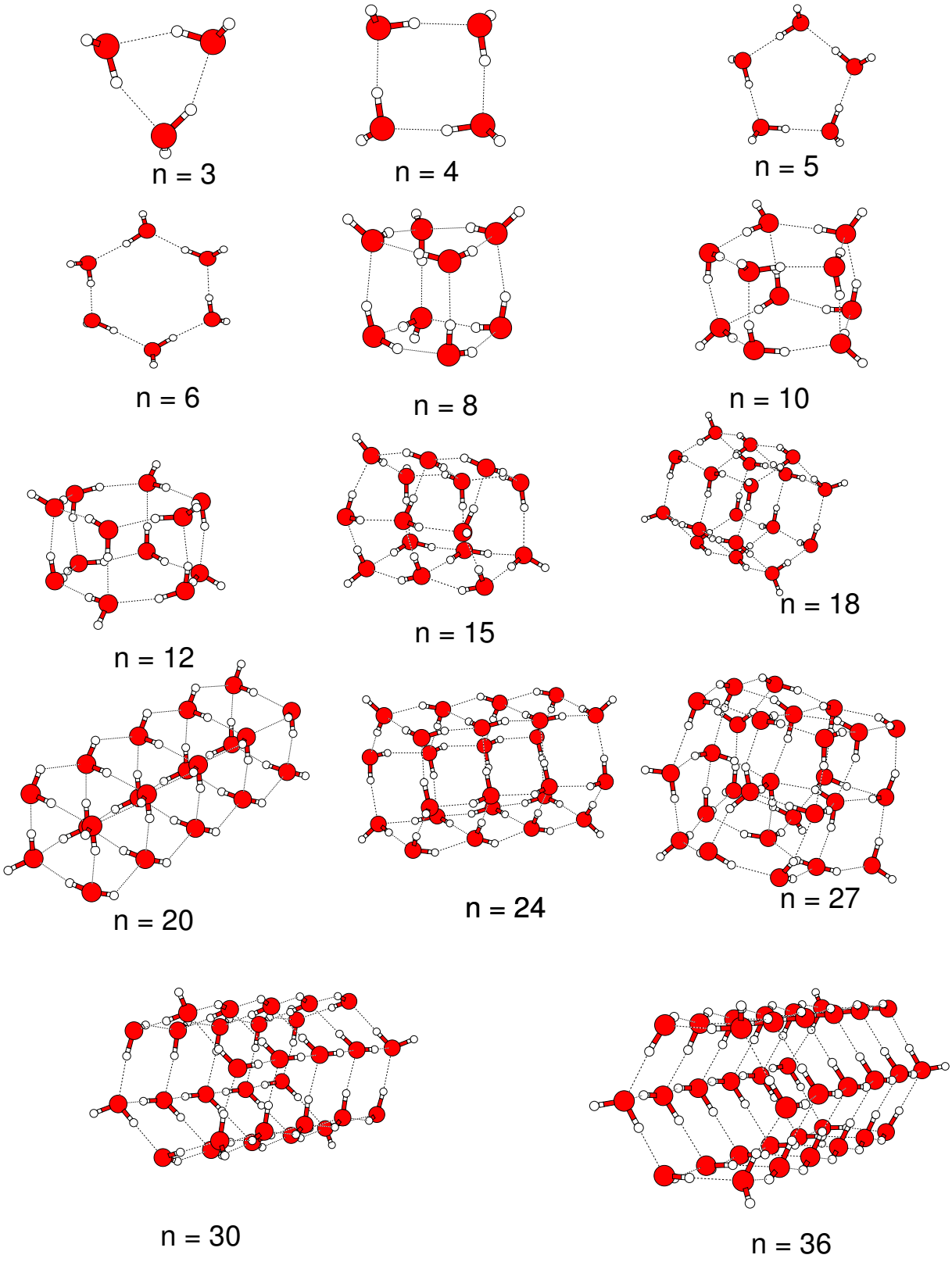

Figure 5.3: Initial configuration for some selected clusters $(H_2O)_n$ of water molecules. The geometries have been relaxed by using the conjugate gradient method of DFTB.

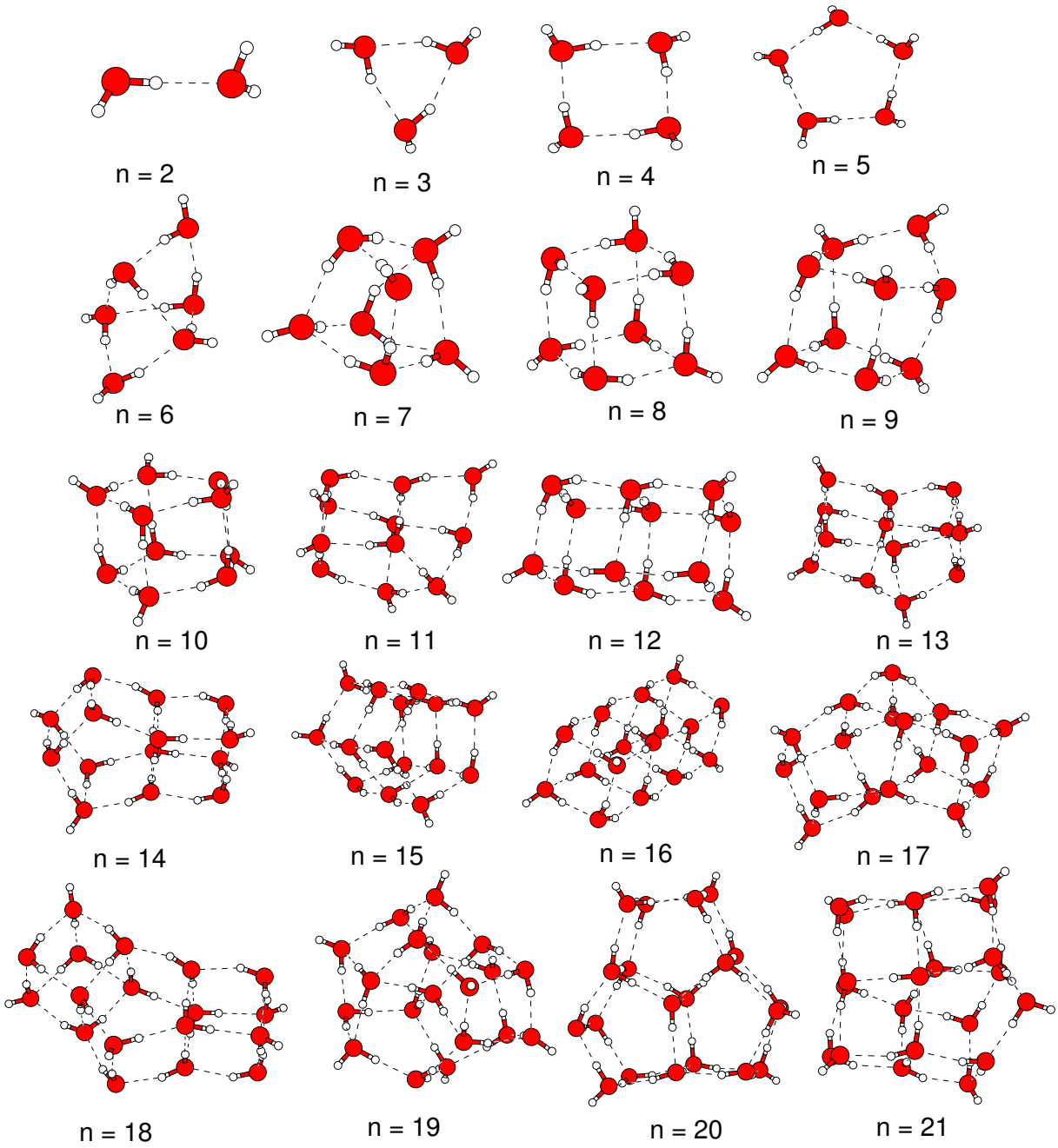

Figure 5.4: Initial global minimum configurations for some clusters $(H_2O)_n$ taken from (the works of Wales and Hodges) [130].

Table 5.2: Calculated binding energy per water molecule, E_b, with DFTB, in eV, of the stable structure in Fig. 5.3. E_b was calculated according to Eq. (5.2).

n	$E(H_2O)_n$ (eV)	E_b (eV)
2	-21.608541	-0.071945301
3	-32.614163	-0.13906079
4	-43.696117	-0.19170221
5	-54.660025	-0.19967817
6	-65.618161	-0.20403323
7	-76.558371	-0.20458309
8	-87.667367	-0.22609385
10	-109.892182	-0.25689104
12	-131.938292	-0.26253054
15	-165.124347	-0.27596312
18	-198.209976	-0.27933846
20	-220.376313	-0.28646145
24	-264.502785	-0.28862229
30	-315.183000	-0.29414211
36	-397.085054	-0.29781331

of the structure and thermodynamic properties of these clusters is an essential element in analyzing the phase change [135]. Numerous studies have been devoted to understand the dynamics of small clusters of water since the beginning of simulation studies in 1970s, using molecular dynamics (MD) and Monte Carlo (MC) simulation techniques bound by the simple Lennard-Jones (LJ) potential [35]. Some studies are concentrated on the nature of the pseudo-first-order melting transition, culminating in a detailed explanation of the observed trends in terms of the underlying potential energy surface (PES) including both minimal and transition states [136]. Our present study is one of a series of MD simulations which are being undertaken to investigate the properties of small water clusters. Our aim is to simulate the melting temperature of water clusters $(H_2O)_n$ of selected sizes using the initial minimum geometry of the clusters obtained from the conjugate gradient (CG) relaxation of the DFTB calculations, such as n = 3, 4, 5, 6, 8, 10, 12, 15, 18, 24, 20, 27, 30, and 36 selected from Fig. 5.3. We also carried out the same study on the global minimum geometries obtained by the TIP4P method of Wales, shown in Fig 5.4 [130], in order to see the effect of the initial configuration on the melting of water clusters.
The molecular dynamics simulation of melting of water clusters was carried out with the DFTB method. In these simulations the equations of motions have been integrated

Table 5.3: Calculated binding energy per water molecule, E_b, with DFTB method and VASP, in eV, on the global minimum configurations in Fig. 5.3 predicted by TIP4P [130]. Also shown, are the corresponding energies of each cluster taken from the same reference.

	DFTB		VASP		TIP4P	
$(H_2O)_n$	$E(H_2O)_n$ (eV)	E_b (eV)	$E(H_2O)_n$ (eV)	E_b (eV)	$E(H_2O)_n$ (eV)	E_b (eV)
2	-21.608541	-0.071943	-28.769093	-0.121904	-0.270379	-0.135189
3	-32.614164	-0.139061	-43.568115	-0.260062	-0.725435	-0.241812
4	-43.696207	-0.191725	-58.461398	-0.352707	-1.208375	-0.302094
5	-54.660075	-0.199688	-73.187964	-0.374950	-1.576499	-0.315300
6	-65.666763	-0.212133	-87.853572	-0.379619	-2.049851	-0.341642
7	-76.718826	-0.227505	-102.66419	-0.403670	-2.524450	-0.360636
8	-87.862819	-0.250525	-117.72898	-0.453480	-3.166474	-0.395809
9	-98.849468	-0.250947	-132.52182	-0.462004	-3.569819	-0.396647
10	-109.892188	-0.256892	-147.35192	-0.472549	-4.052664	-0.405266
11	-120.879006	-0.256674	-161.94311	-0.459458	-4.472069	-0.406552
12	-132.038734	-0.270901	-176.85262	-0.475075	-5.108634	-0.425719
13	-143.013064	-0.268678	-191.66969	-0.481179	-5.523850	-0.424912
14	-154.115371	-0.275914	-206.57709	-0.492863	-6.042277	-0.431591
15	-165.125603	-0.276047	-221.31833	-0.491912	-6.512619	-0.434175
16	-176.227047	-0.281863	-236.06018	-0.491118	-7.060064	-0.441254
17	-187.198906	-0.279373	-250.87702	-0.494829	-7.501739	-0.441279
18	-198.321203	-0.285518	-265.82545	-0.505438	-8.013984	-0.445221
19	-209.300536	-0.283491	-280.69861	-0.510968	-8.509448	-0.447866
20	-220.424627	-0.288904	-295.56028	-0.515371	-9.047891	-0.452395
21	-231.407068	-0.287057	-310.09930	-0.503990	-9.501003	-0.452429

with the help of the velocity form of the Verlet algorithm using a time step of 0.5 fs. The iso-kinetic ensemble method in which the velocities are rescaled according to some probability was used to achieve the desired temperature steps. All the simulations carried out on these clusters were done in large supercells to prevent the interaction of the real system with its images. The effect of the supercell on the binding energy calculated for the pentamer ($n =$ 5 cluster), is shown in Fig. 5.6. The box length is taken to be greater than the maximum diameter of the cluster and does not influence the calculated value of the binding energy. Since the maximum average diameter of pentamer is about 5.0 Å, we have chosen a supercell of about two times the size of the cluster which approximates open boundary conditions. Starting from the minimum configurations of each water cluster, the gradual heating was done in steps using the structure at each equilibrated temperature from the previous run. The dynamics of each run was done for 10000 MD steps. We have determined the average temperature of each run through the equipartition law by calculating the long-time averages of the kinetic energy (E_{kin}),

$$T = \frac{2}{3N-6}\frac{E_{\mathrm{kin}}}{k_B}, \tag{5.3}$$

where N is the number of degrees of freedom corresponding to the number of atoms of each cluster (from which the centre of mass motion has been removed); k_B is the Boltzmann

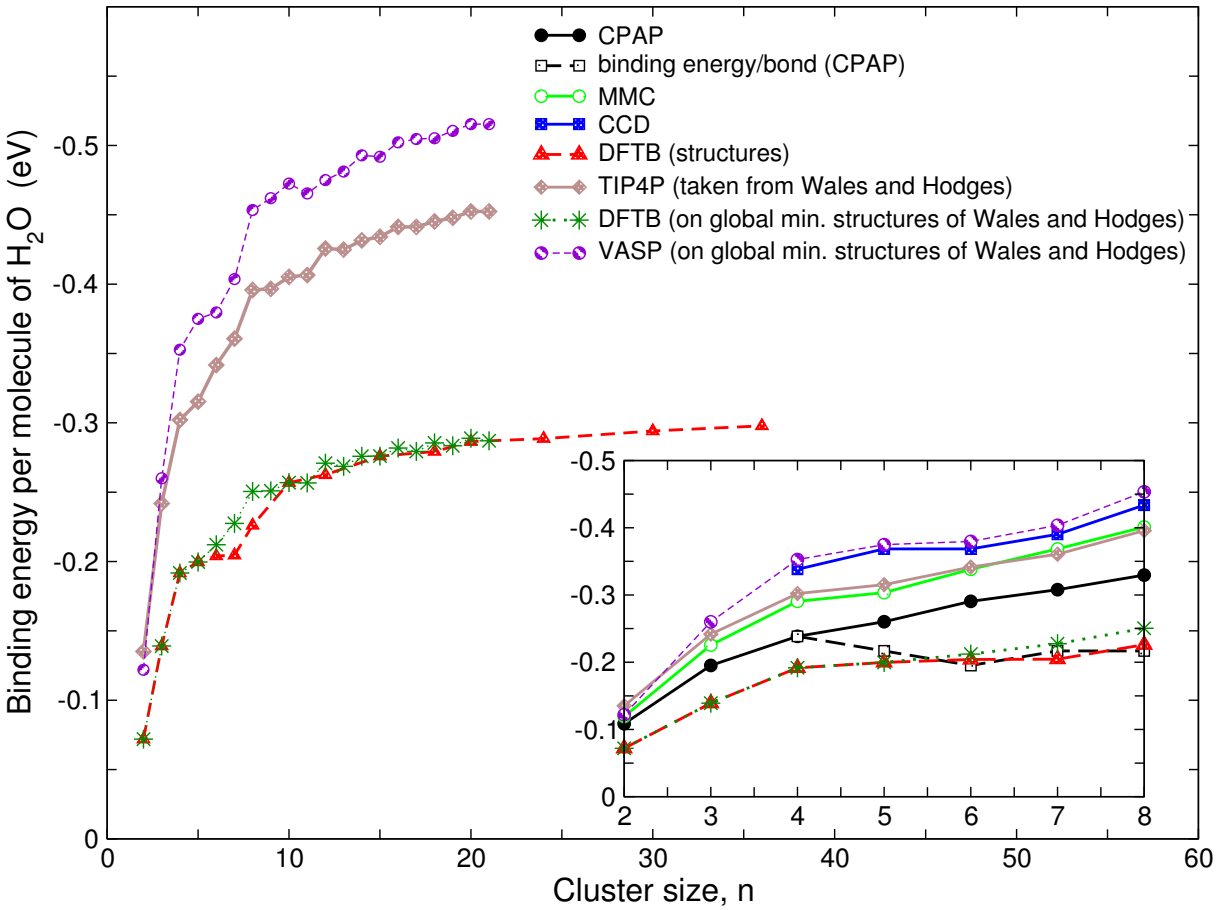

Figure 5.5: Variation of binding energy per water molecule as a function of cluster size.

constant. The energy is then plotted versus temperature (calorific curve) from which the melting temperature T_m is obtained by finding the point of inflexion of this curve. Usually these modelled clusters exist in the solid-like phase at low temperatures and the liquid-like phase at high temperatures. These two phases shown in Fig. 5.7 are connected by a van der Waals like loop defining a first-order-like transition [8]. Sometimes, it is difficult to see the jump in the energy or the abrupt change in the slope of E versus T of the calorific curve, instead, Lindemann's criteria of melting is used along with the former condition of change of slope. Lindemann's criterion is expressed in terms of the root-mean-square bond-length fluctuation δ_{OO} of oxygen in each of the clusters according to the equation:

$$\delta_{\mathrm{OO}} = \frac{2}{N(N-1)} \sum_{i<j} \frac{\sqrt{\langle r_{ij}^2 \rangle - \langle r_{ij} \rangle^2}}{\langle r_{ij} \rangle}. \tag{5.4}$$

Here $\langle\rangle$ means the time average, and r_{ij} is the distance between the atoms i and j. In our case, i and j are the oxygen atoms since it is the centre of each molecule of water. The summation is over all molecules, N. The Lindemann's criterion states that a solid melts when δ is greater than 0.1. According to this criterion, melting in solids is caused by a

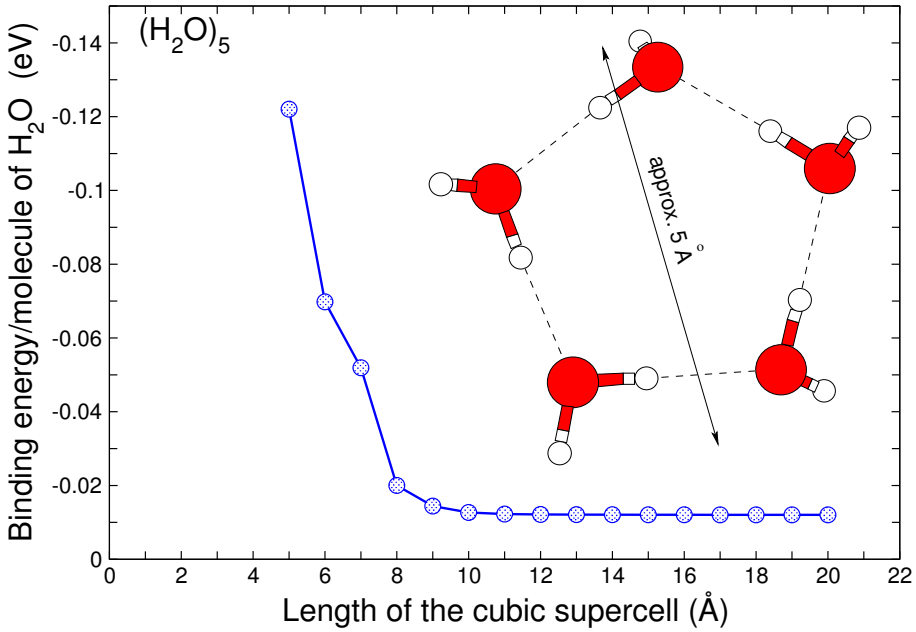

Figure 5.6: Effect of the size of the supercell on the binding energy.

vibrational instability of the crystal lattice when the root-mean-square displacement of the atoms reaches a critical fraction (δ_L) of the distance between them [137]. The greater movement of the particles in the liquid cluster, which leads to their disorder, can be seen very clearly after melting has taken place, especially for the smaller clusters. In addition to the oxygen-oxygen Lindemann index, an analogous quantity may be defined to monitor the switching of hydrogen bonds; this is the so called "bifurcation rearrangement" [138], where, for a given molecule, the free and H-bonded hydrogen atoms switch roles. Just as Eq. (5.4), this quantity is defined by

$$\delta_{\mathrm{OH}} = \frac{2}{N(N-1)} \sum_{i<j}^{\text{neigbouring OHpairs}} \frac{\sqrt{\langle r_{ij}^2 \rangle - \langle r_{ij} \rangle^2}}{\langle r_{ij} \rangle}. \tag{5.5}$$

The summation in Eq. (5.5) is only between a given oxygen atom and the two hydrogen atoms on the adjacent molecule which acts as the hydrogen donor to that oxygen atom. This quantity becomes meaningless if the water molecules switch places. So this is not considered when evaluating (5.5). Another quantity which may also be used as an order parameter in identifying phase transition is ring puckering measured by the root-mean-square oxygen (RMS) dihedral angle. This can be used for water clusters such as pentamer or hexamer which form a perfect ring structure. This is defined using Fig. 5.8(a) by

$$\phi_{\mathrm{RMS}} = \left[\frac{1}{N} \sum_{i=1}^{N} (\phi_i^{\mathrm{OOOO}})^2 \right]^{\frac{1}{2}}. \tag{5.6}$$

Here the summation is over the N different sequences of four consecutive oxygen atoms. The average and standard deviation of this quantity can be calculated in order to quantify

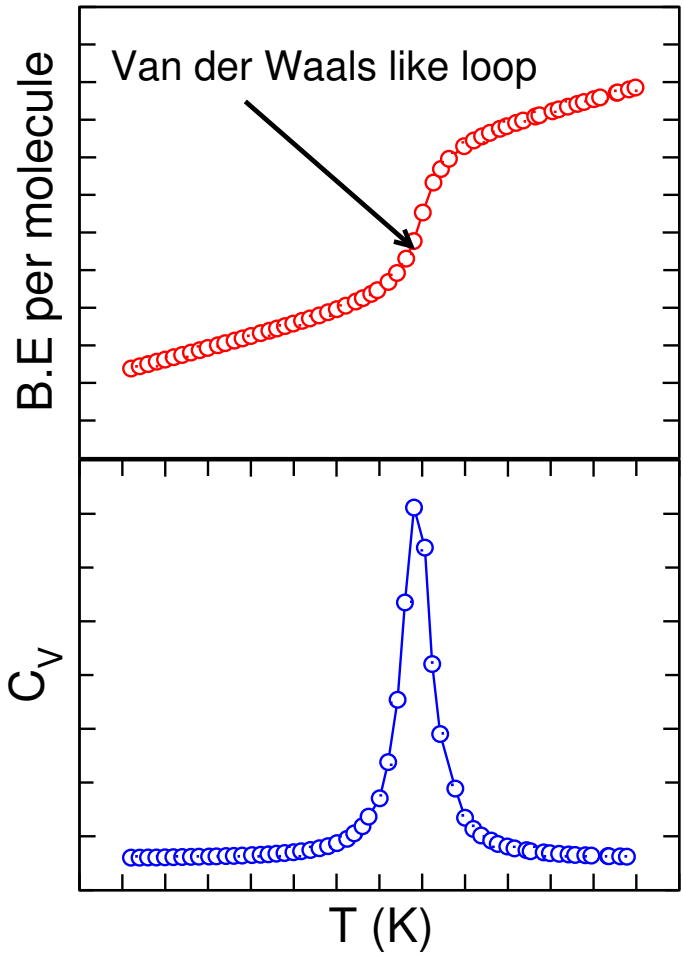

Figure 5.7: Binding energy and specific heat (C_v) versus temperature illustrating the van der Waals like loop defining a first-order-like transition.

the magnitude of the ring puckering and unpuckering. Since the dihedral angle is defined in terms of four specific oxygen atoms, this quantity also becomes meaningless if two water molecules switch places during the course of the simulation and also most of the structures dealt with here are not only rings but more complicated structures. In addition, the motion of free hydrogen atoms can be monitored by considering

$$\sigma_{\mathrm{H}} = \frac{1}{N}\sum_{i=1}^{N}\left[\langle(\phi_i^{\mathrm{HOOH}})^2\rangle - \langle\phi_i^{\mathrm{HOOH}}\rangle^2\right]^{\frac{1}{2}}, \tag{5.7}$$

where the HOOH dihedral angles are defined for the sequence of HOOH atoms as for ϕ_{RMS} as indicated in Fig. 5.8(b). When σ_{H} becomes large, the non-hydrogen bonded hydrogen atoms are freely "flipping" past the pseudo plane of the cluster. As with ϕ_{RMS}, this quantity has a limited range of relevance; the only assumption one needs to make is that there is no switching of hydrogen bonds (or of molecules) during the simulation, and, since we are not dealing with a particular ring structure, this quantity is not calculated.

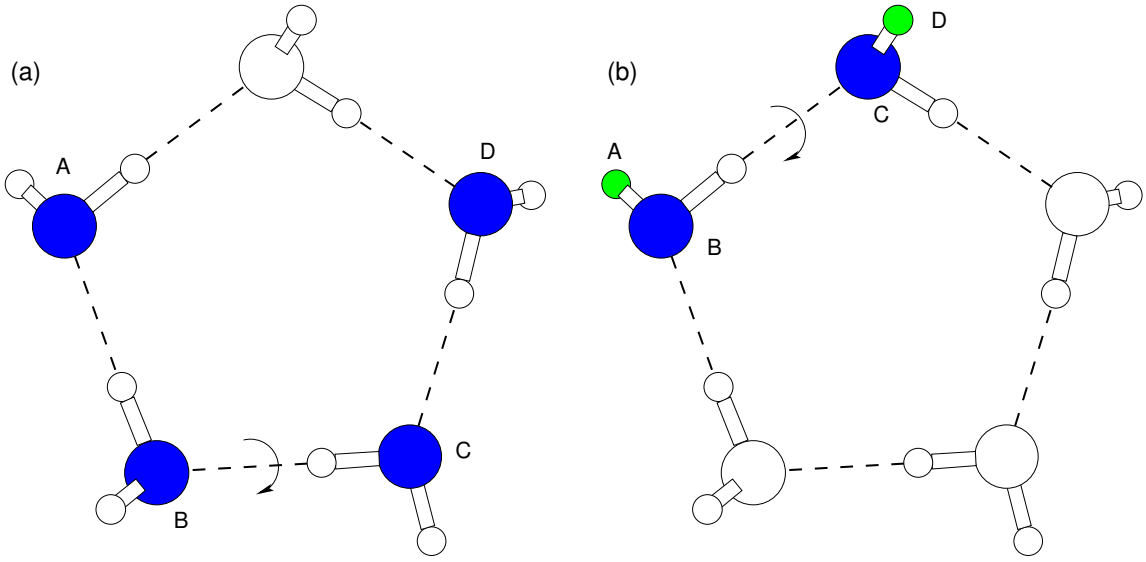

Figure 5.8: Dihedral angles used in the reference. Each dihedral angle is defined for the atom sequence A-B-C-D, so that a change in the dihedral angle represents torsion about the B-C axis. (a) Used in defining ϕ_i^{OOOO}, which is the sequence of angles between four successive O atoms [Eq. (5.6)]. (b) Corresponding angle ϕ_i^{HOOH}, used in defining σ_{H} [Eq. (5.7)].

In this work, we only considered the Lindemann index along with the jump or change of slope in the calorific curve as an indication as to whether a cluster is solid-like or liquid-like. Water clusters are very complicated structures because of the hydrogen bonding network. We took caution in the way we define the melting temperature T_m for a particular cluster. A cluster of water may have different isomerizations in which there are interconversions of a water cluster from one form of isomer to another when the hydrogen bond-breaking and reforming is substantial, leading to the formation of the new structure before the final melting occurs. This behaviour is marked by fluctuations in both, the calorific curve and the δ_{OO} versus T curve. Examples of molecular dynamics investigations of structure and stability of small clusters of water pentamers at various temperatures have been carried out by Plummer [139]. Melting-like transitions have been predicted for this cluster with wide temperature range. These structural transitions or the isomerization show up as pseudo-transitions, for example in pentamer, $n = 5$, in the curve shown in Fig. 5.9 (illustrated with first broken line) as the heating proceeds. Therefore, the transition temperature may sometimes depend on how the initial structure is prepared especially for the water clusters. We tried to cross-check the structures of some of these clusters before the transition temperature is reached and after. Below the transition, at low temperatures, the considered cluster exhibits a solid-like behaviour and above it a liquid-like behaviour. The information about the structural behaviour can be deduced from the analysis of the peaks of the oxygen-oxygen distribution functions computed according to Eq. (4.37) [8]. The liquid-like behaviour of the cluster at a temperature above the melting region can be compared to the behaviour of the real liquid. Figures 5.9, 5.10, and 5.11, show the results of MD simulations in which the energies are plotted as a func-

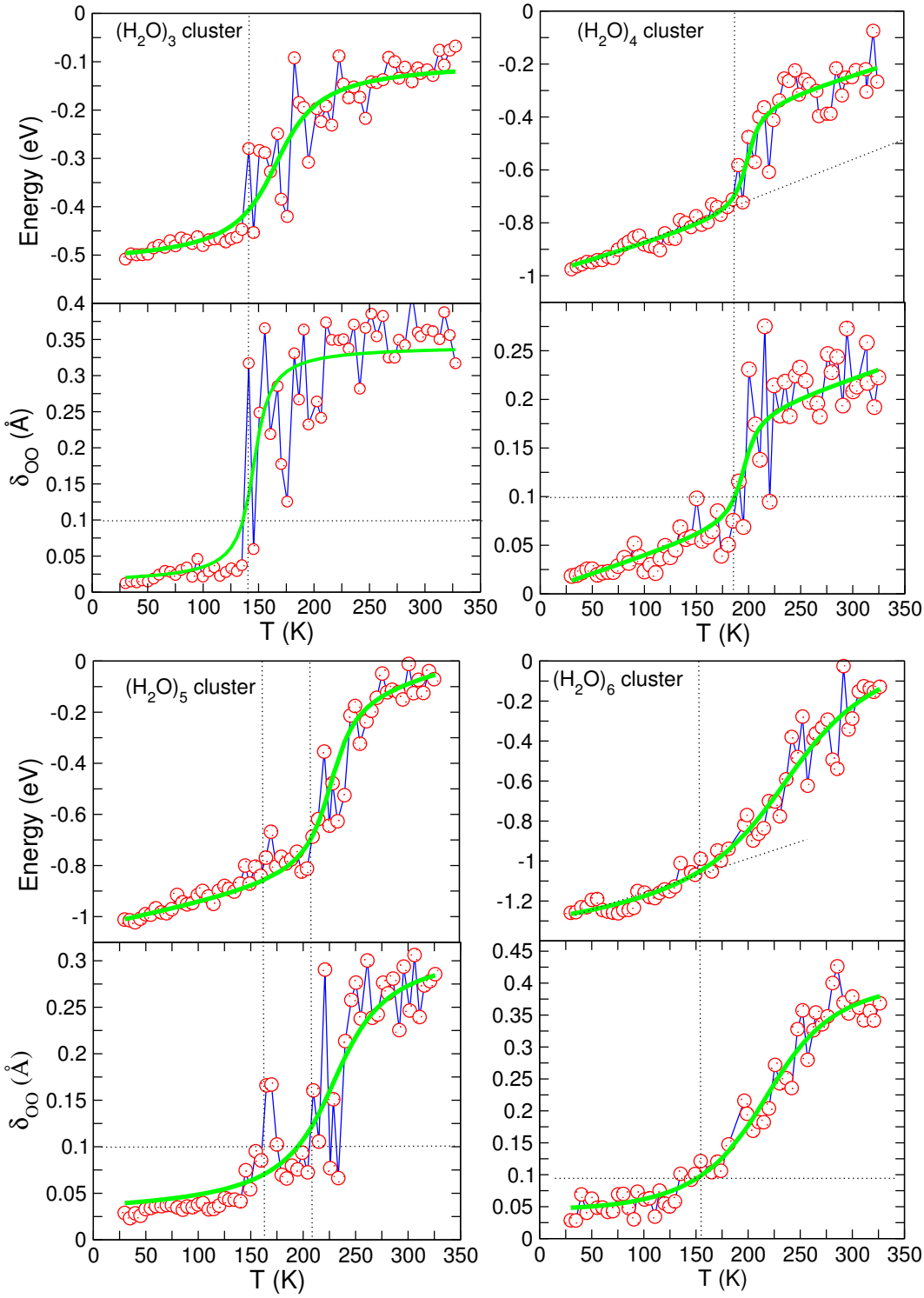

Figure 5.9: Plots of the energy against temperature together with the root mean square fluctuations in the O-O bond lengths for water cluster with n = 3, 4, 5 and 6. The vertical broken line illustrates the region where the average melting temperature is taken. For pentamer, two vertical broken lines are drawn. The first vertical broken illustrates pseudo-transition which is attributed to the isomerization process explained in the text. The horizontal broken line at δ_{OO} =0.1 illustrates the Lindemann's line.

tion of temperature. These plots of energy versus kinetic temperatures are shown together with the plots of δ_{OO} versus T. For all the clusters, the transition regions are marked by the change in the slope of the $E(T)$ curves. The melting temperature predicted by the inflexion point of the calorific curve correlates with the calculated value of $\delta_{OO} > 0.1$ of Lindemann's method, in which the relative fluctuation of the interparticle separation is about 10 percent. At low temperature (below T_m), the clusters show a small change in δ_{OO} (which implies an approximate constant structure) until T_m is reached. In the high temperature regime above T_m, we observe pronounced fluctuations of the structure, which is characterized by the larger value of δ_{OO}. We used some non-linear curve-fitting shown as solid thick lines as visual aid to show both the behaviour of the $E(T)$ curve and $\delta_{OO}(T)$. In determining the transition temperature, one should be carefully aware of the fluctuations of the structure which show a kind of "pseudo-transition" especially as change of the slope of the $E(T)$ curve or when Lindemann's line is approached. This pseudo-transition is what we attribute to the isomerization process, where a cluster is found to be stable at a particular temperature. In order to show that there is a change in the structure of these clusters from the solid-like to the liquid like behaviour, we plotted the radial distribution function of the oxygen-oxygen distance in H_2O-H_2O for $n = 5$, 12, 20 and 36 below and above the transition temperature for mere illustration of the change of state of the structure. These are shown in Fig. 5.12. The results show that the first sharp peak occurs for all clusters at an average distance of 2.87 Å, which is roughly the same as the minimum distance obtained from the total energy per water molecule in the dimer against the O-O distance. These first O-O peaks also show the extent of the hydrogen-bond formation in the clusters. At low temperatures below T_m, other peaks appear such as the second peak showing the effect of the second nearest-neighbour distance. Above T_m, the second peaks broaden and then flatten due to the gradual formation of the liquid-like structure; the disappearance of the second peak then at high temperatures is an indication of a complete liquid-like regime with larger intermolecular amplitude vibrations. It is not clear if the transitions obtained from the $E(T)$ curves are first order phase transitions in which there is a discontinuity in the derivative of E with respect to T, especially for smaller clusters $n = 3$, 4, and 5. All the T_m reported are just averages of the final transition regions observed. The summary of the cluster size effect with T_m for the different methods is listed in Table 5.4 and shown in Fig. 5.13. In the inset of Fig. 5.13 is also shown the behaviour of $T_m(N^{-1})$. The table/plot illustrates the difference in the melting temperature predicted by DFTB and classical pairwise additive potential calculations. Also shown is a result obtained from the simple point charge (SPC) model calculation of the vibrational temperature of pentamer [2]. If we compare the DFTB results with the pairwise additive potential calculation, one can notice some correlation in the values of T_m, predicted by both methods, especially for the bigger clusters. Both calorific curve and Lindemann's criterion from $\delta_{OO}(T)$ show some agreements in locating T_m especially for the smaller clusters below $n = 20$. It becomes difficult to see clearly the transition point in $\delta_{OO}(T)$ because of the fluctuations. This might be due to the fact that 10000 iterations are not sufficient to calculate any meaningful averages for the bigger clusters. But the calorific curve behaviour does not change as much within this limit of

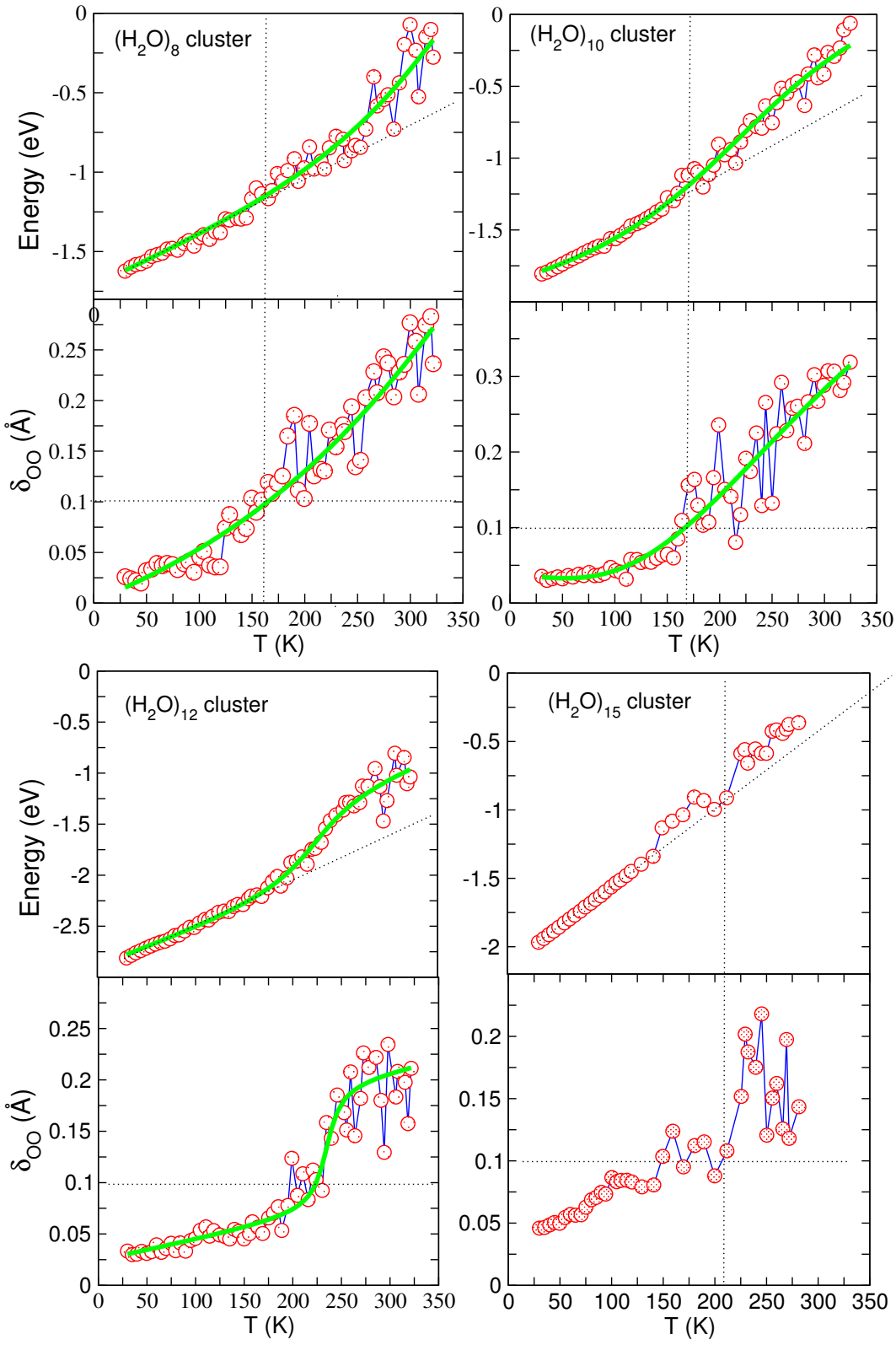

Figure 5.10: Plots of the energy against temperature together with the root mean square fluctuations in the O-O bond lengths for water cluster with $n = 8$, 10, 12 and 15. The explanation for the broken lines is the same as in Fig 5.9.

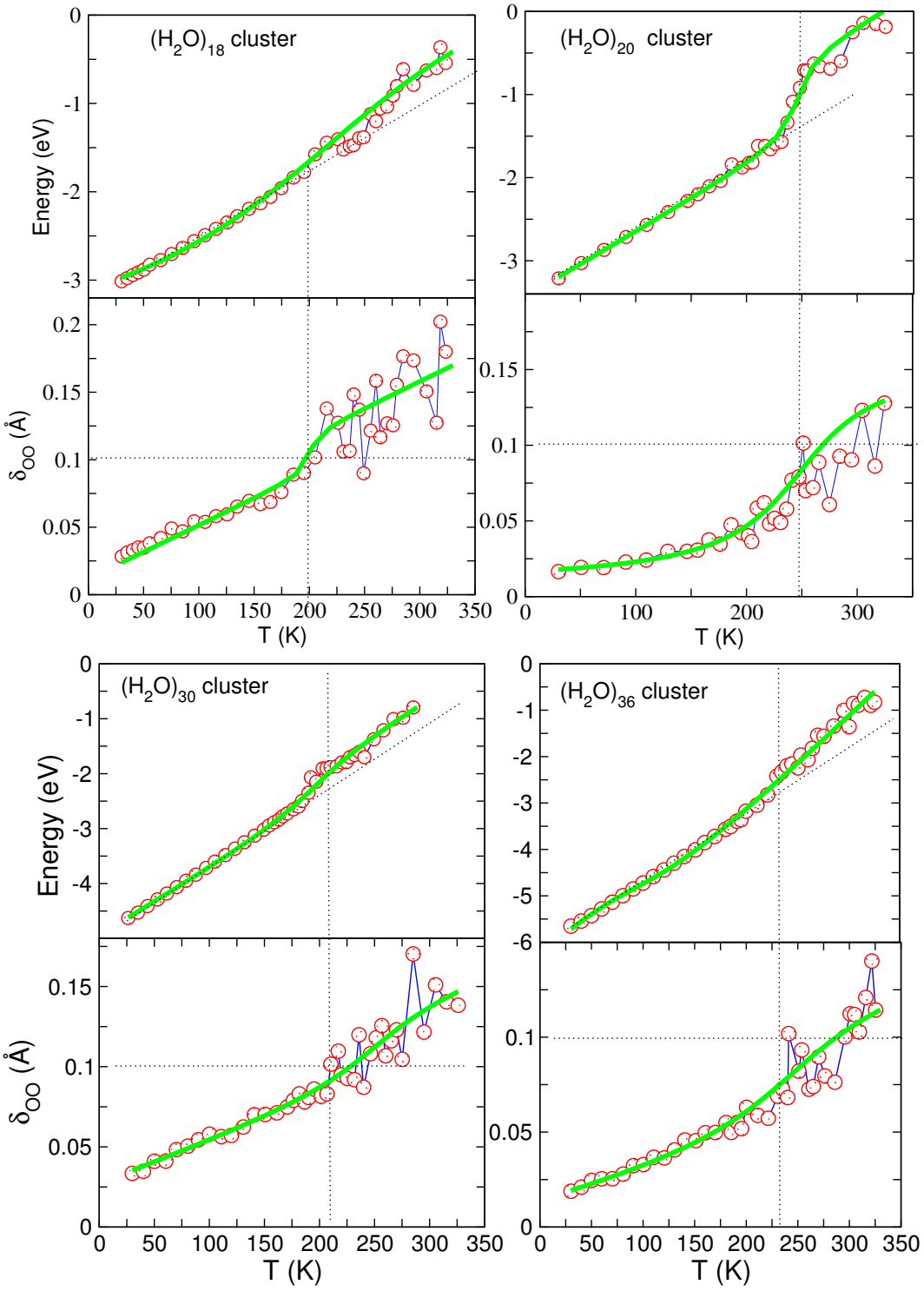

Figure 5.11: Plots of the energy against temperature together with the root mean square fluctuations in the O-O bond lengths for water cluster with n = 18, 20, 30 and 36. The explanation for the broken lines is the same as in Fig 5.9.

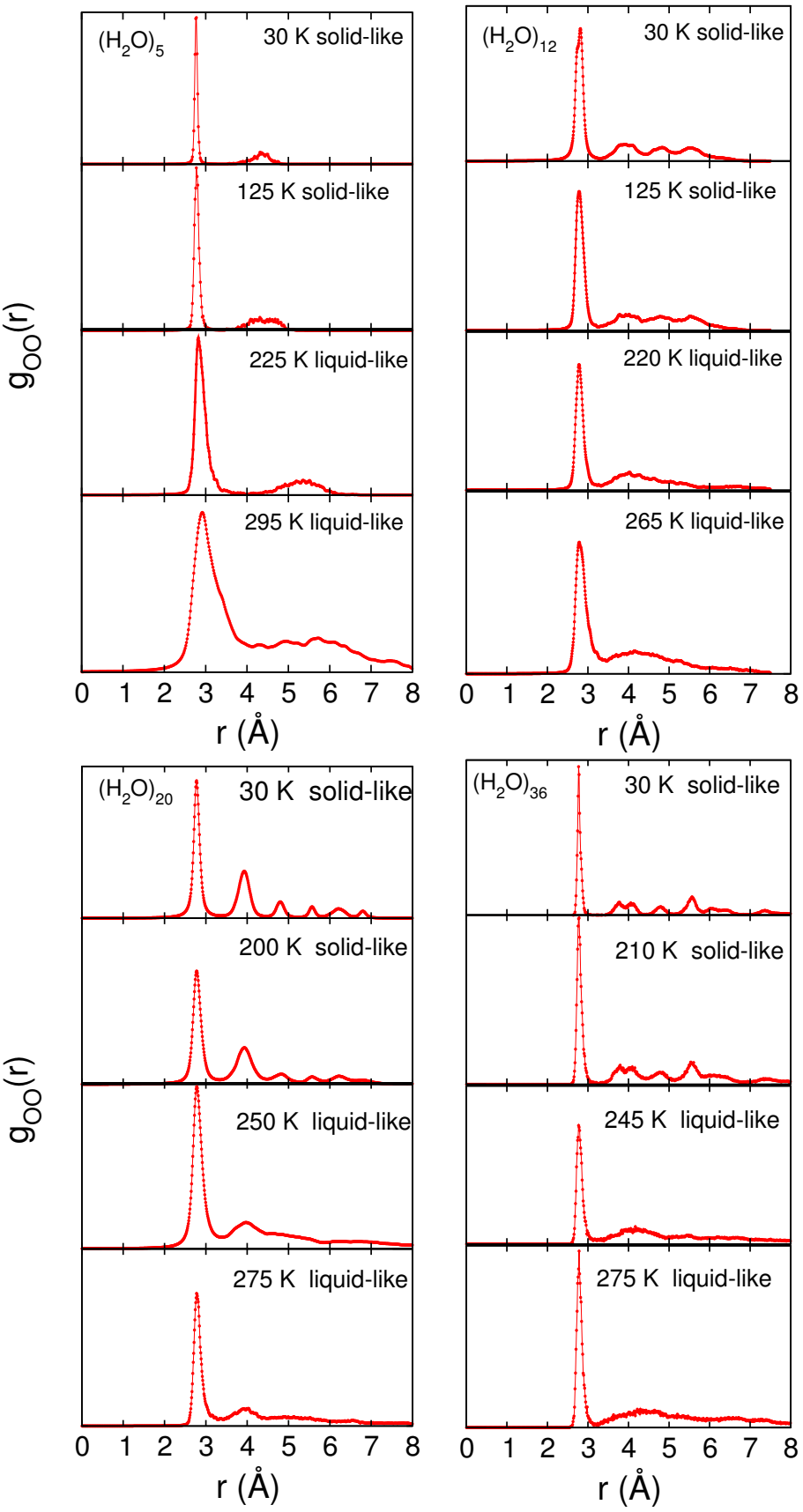

Figure 5.12: Plots of the radial distribution functions near melting below and above, for water cluster with $n = 5$, 12, 20 and 36, to show the extent of the change in the structure from the solid-like to liquid-like regime.

iterations. In order to see the effect of initial configurations on melting temperatures,

Table 5.4: The melting temperatures against the number of molecules. Both results of our DFTB calculations and simulations using the CPAP and TIP4 classical additive pairwise potential, (CPAP) are plotted. Also shown is the T_m value obtained with the SPC model.

	DFTB	TIP4 (CPAP)	SPC model
$(H_2O)_3$	137	198	
$(H_2O)_4$	190	186	
$(H_2O)_5$	217	95	315
$(H_2O)_6$	155	122	
$(H_2O)_8$	160	168	
$(H_2O)_{10}$	170		
$(H_2O)_{12}$	197	205	
$(H_2O)_{15}$	203		
$(H_2O)_{18}$	198		
$(H_2O)_{20}$	218	200	
$(H_2O)_{30}$	210		
$(H_2O)_{35}$		230	
$(H_2O)_{36}$	235		

we also tried our simulations using the same DFTB method on the global minimum geometries of TIP4P shown in Fig. 5.4 [130]. The same procedure described above was used on this method. The melting curves for these global minimum structures are shown in Fig. 5.14-5.20. Some of these new configurations of the global minimum structure show differences in the region where the melting takes place. The plot of melting temperatures as a function of the cluster size n in this case shows, in comparison with the previous calculations, a small increase in the melting temperature above the cluster of the same number of atoms but different geometry.

Just as melting and cooling of other systems, water clusters also shows some hysteresis as illustrated for the tetramer ($n = 4$) in Fig. 5.21. We tried to cool this highly disordered cluster from high temperature to the low temperature following the path of initial heating. While the heating shows the average melting temperature of 195 K, the average freezing temperature is about 180 K as shown in Fig. 5.21.

Figure 5.22 illustrates the summary of these two different configurations. The result is not surprising because the global minimum configuration is more stable and has stronger binding energy than a corresponding local minimum counterpart. Therefore, a higher temperature is required to dissociate these clusters from their original ordered arrange-

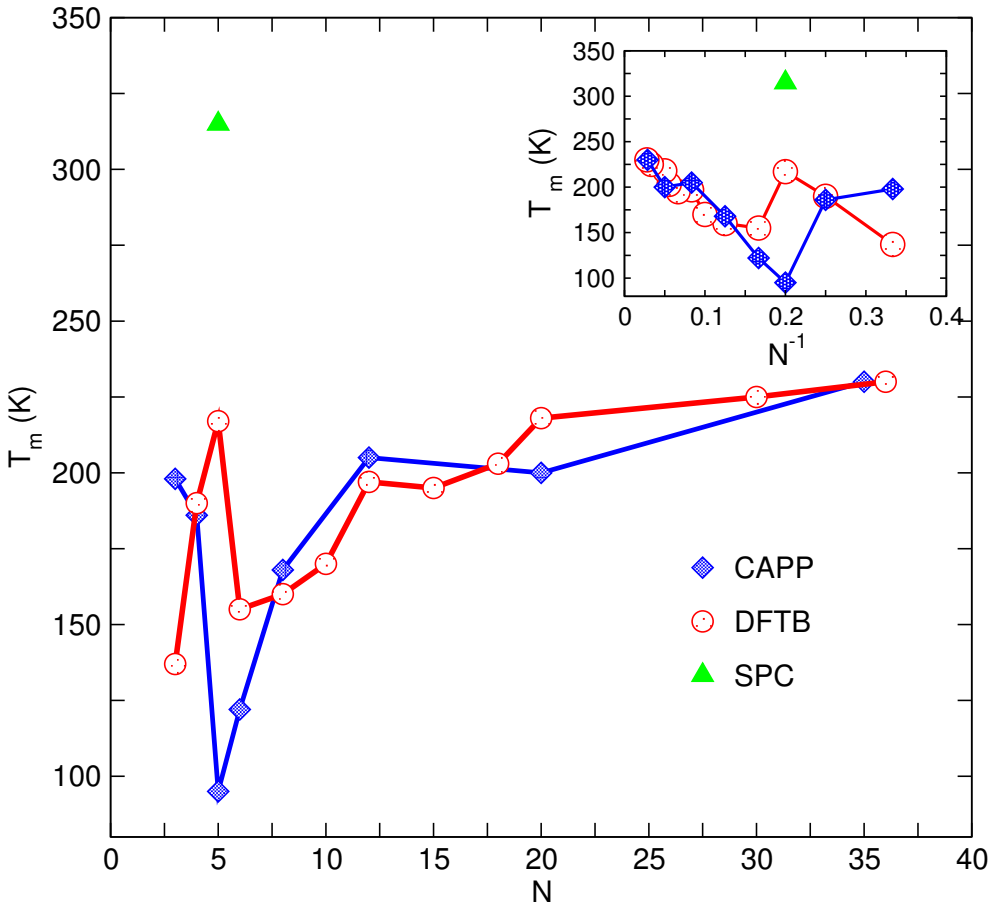

Figure 5.13: The melting temperatures against the number of molecules. Both results of our DFTB calculations and simulations using the CPAP and TIP4 classical additive pairwise potential, (CPAP) are plotted. Also shown is the T_m value obtained with the SPC model.

ment to a disordered configuration. This observation explains the fact mentioned earlier that melting could depend on the initial configurations of the cluster under study and also the potential used in the calculation.

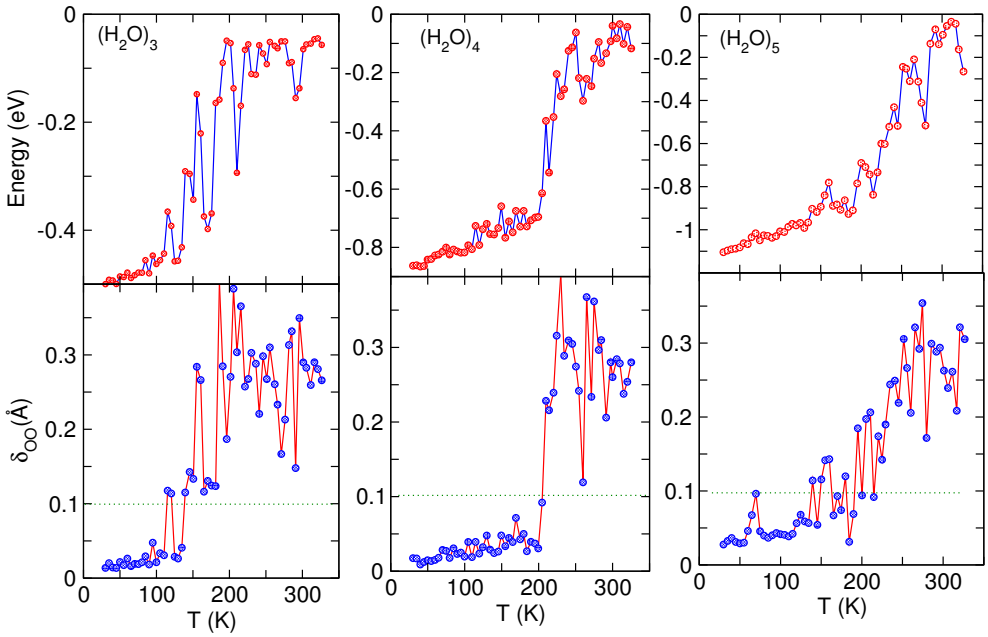

Figure 5.14: Energy and $\delta_{OO}(T)$ versus temperature, T(K), for global minimum geometry of TIP4P for $n = 3$, 4 and 5. Again, the horizontal broken line is the Lindemann's line and also in the following figures.

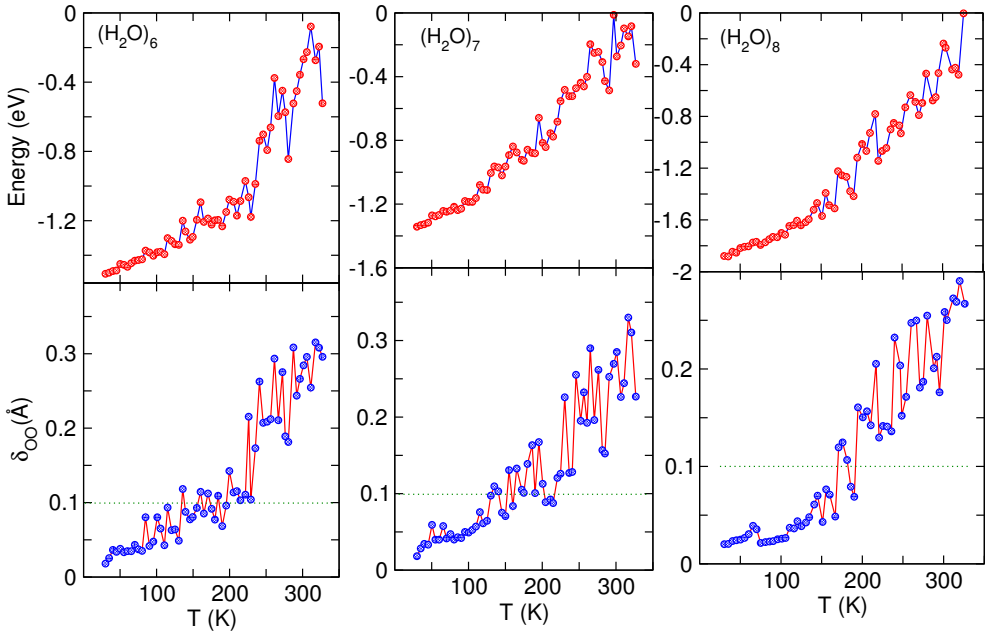

Figure 5.15: Energy and $\delta_{OO}(T)$ versus temperature, T(K), for global minimum geometry of TIP4P for $n = 6$, 7 and 8.

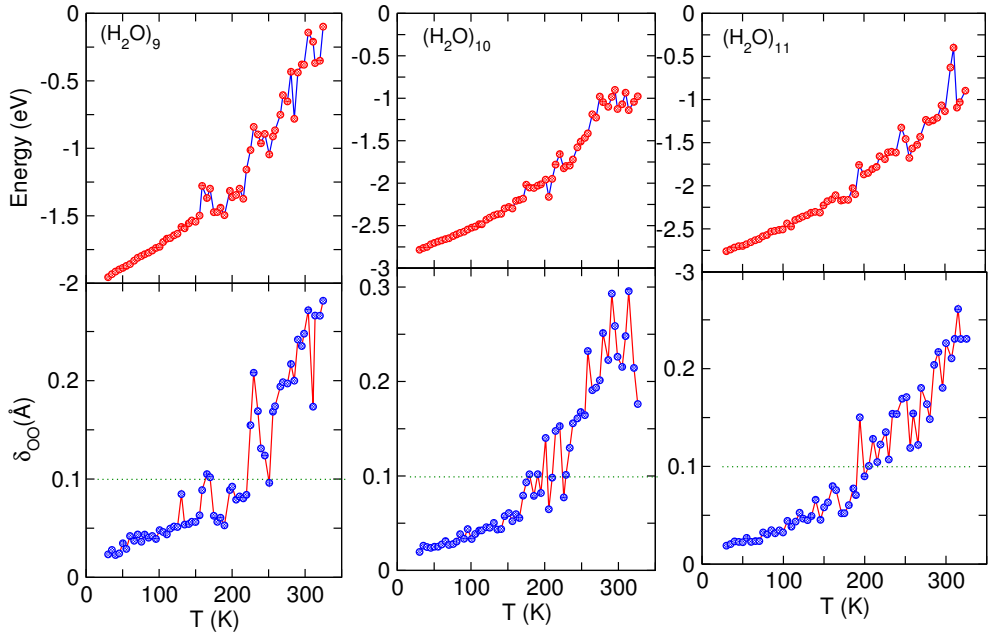

Figure 5.16: Energy and $\delta_{\mathrm{OO}}(T)$ versus temperature, T(K), for global minimum geometry of TIP4P for $n = 9$, 10 and 11.

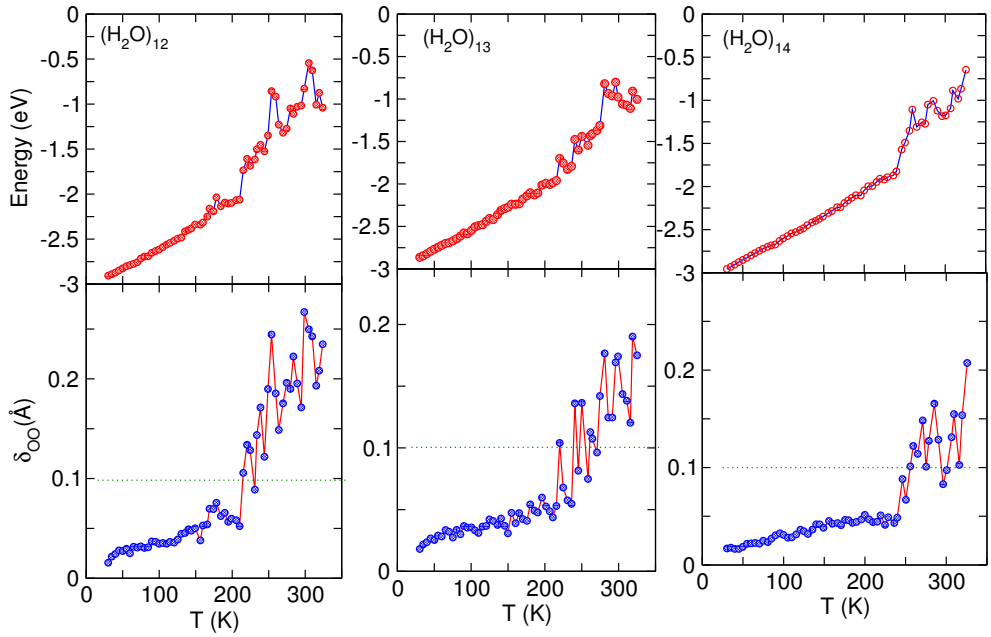

Figure 5.17: Energy and $\delta_{\mathrm{OO}}(T)$ versus temperature, T(K), for global minimum geometry of TIP4P for $n = 12$, 13 and 14.

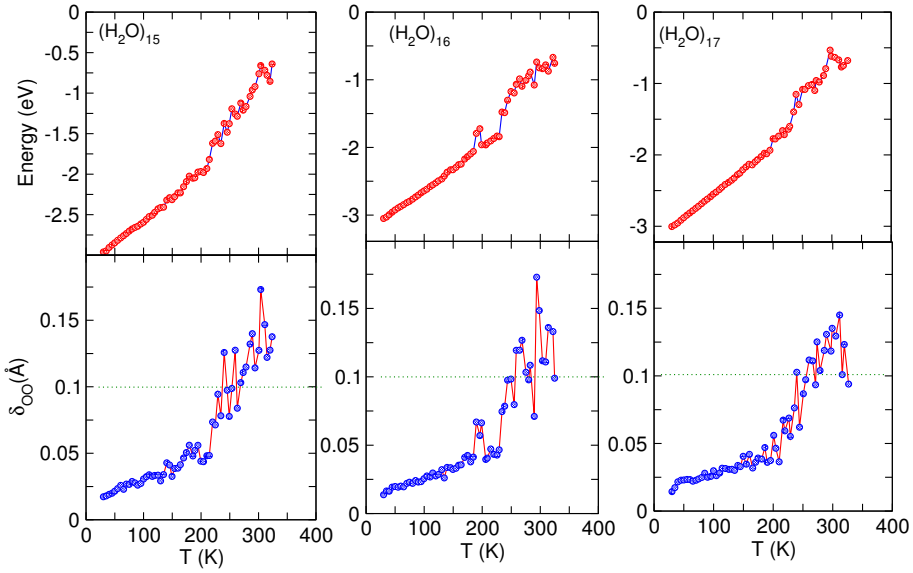

Figure 5.18: Energy and $\delta_{OO}(T)$ versus temperature, T(K), for global minimum geometry of TIP4P for $n = 15$, 16 and 17.

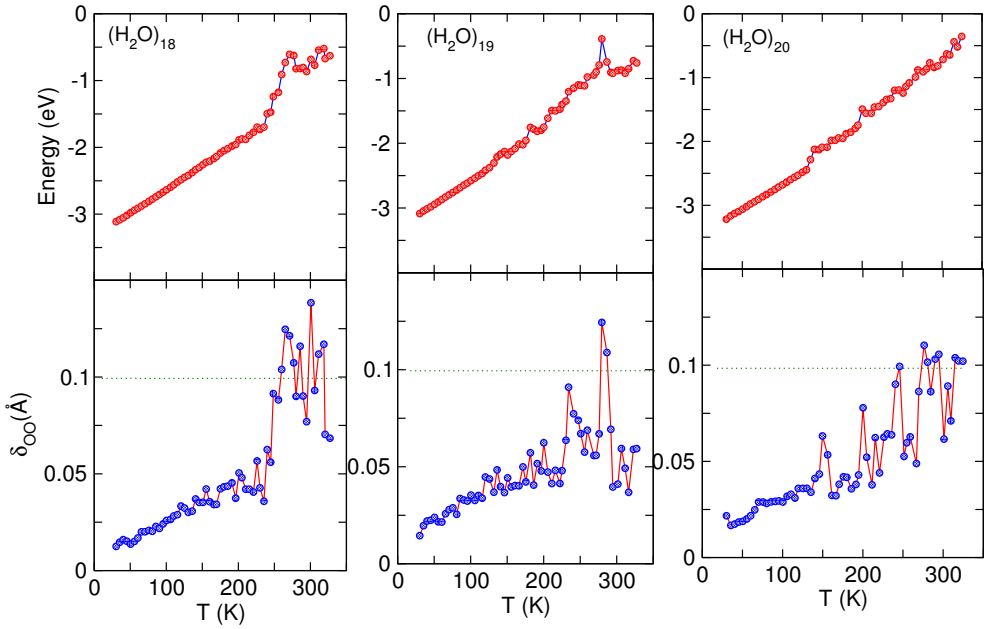

Figure 5.19: Energy and $\delta_{OO}(T)$ versus temperature, T(K), for global minimum geometry of TIP4P for $n = 18$, 19 and 20.

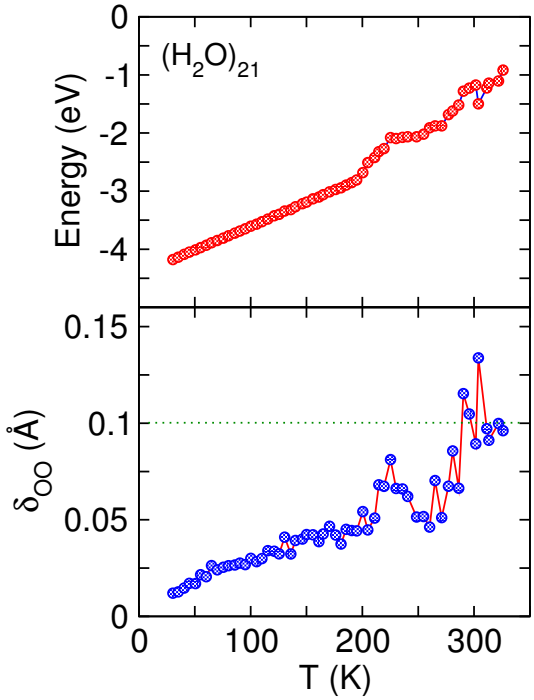

Figure 5.20: Energy and $\delta_{\mathrm{OO}}(T)$ versus temperature, T(K), for global minimum geometry of TIP4P for $n = 21$.

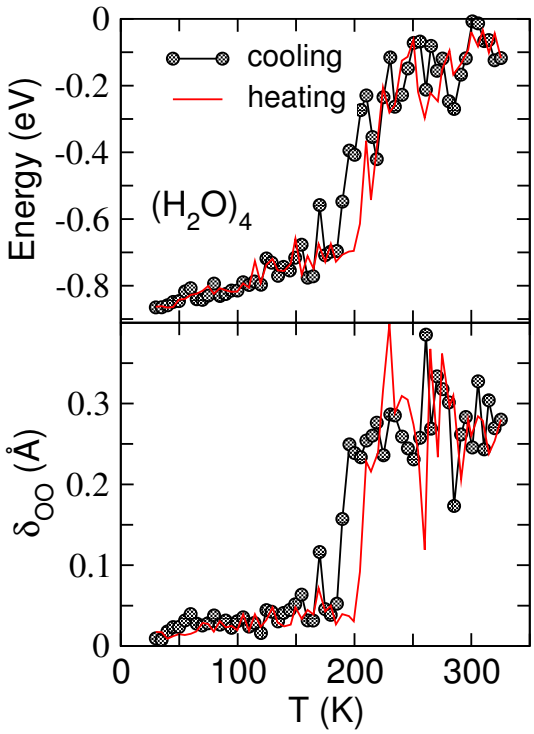

Figure 5.21: Heating and cooling of water tetramer. The transition temperatures of both heating and cooling differ as can be noticed in both the calorific curves and the $\delta_{\mathrm{OO}}(T)$ curves.

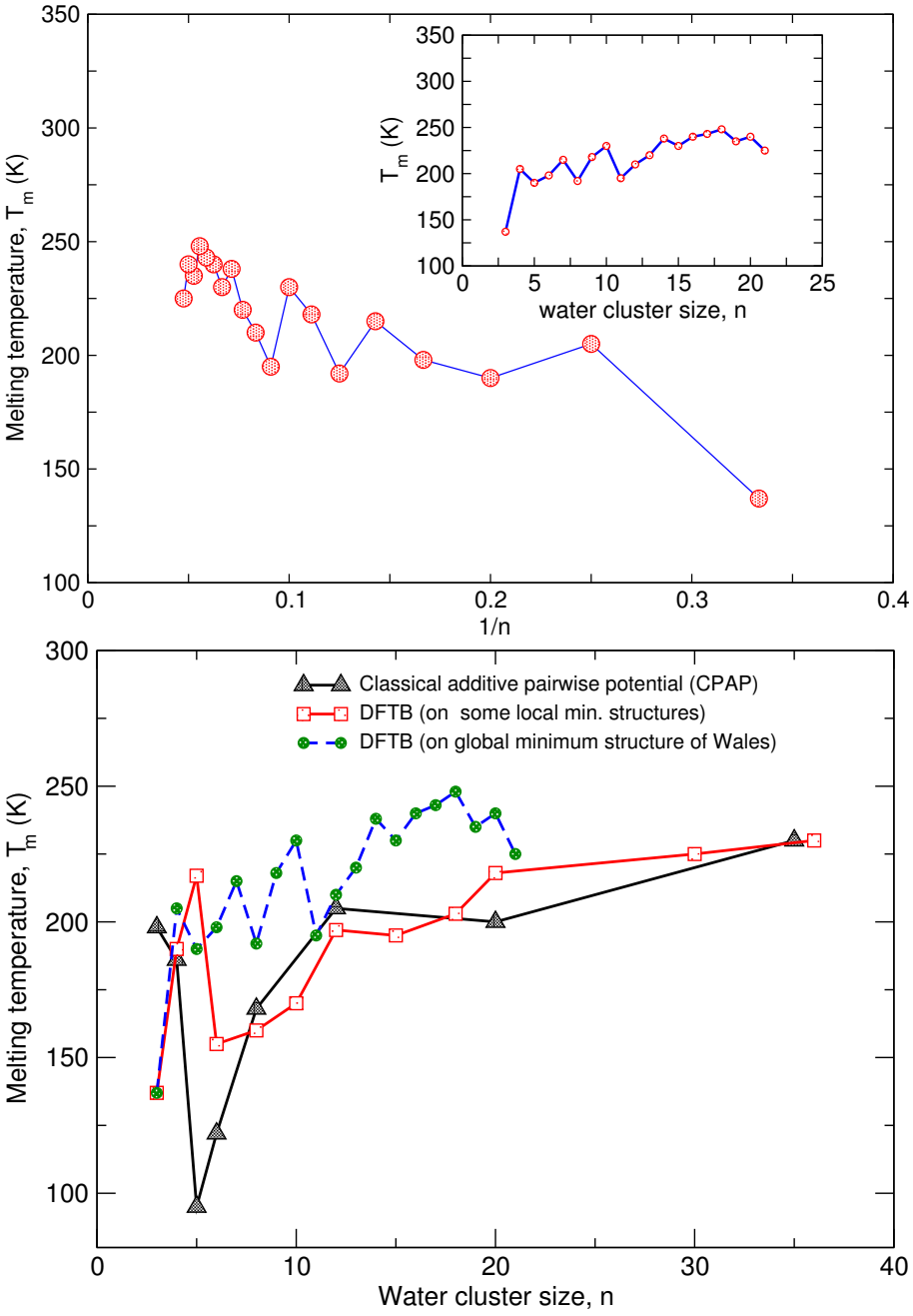

Figure 5.22: (a) The upper Figure shows the plots of melting temperatures vs. water cluster sizes, $1/n$ (and n in the inset) for DFTB on global minimum configurations. (b) The lower Figure shows the result of melting of DFTB calculations on the global minimum geometry compared with DFTB calculations for the local minimum configuration. The third graph on the same plot is the result of melting using the classical pairwise additive potential of TIP4 [131]. The result shows the effect of initial configuration and the potential used.

6 Liquid water and other hydrogen bonding solvents

Our aim in this Chapter is to present our main results based on the applications of density functional theory to describe the results of structural and dynamical properties of liquid water and crystalline ice from molecular dynamics simulation through the analysis of calculation of radial distribution functions as discussed in Chapter 4 4. Also investigated in this Chapter are the applications of lattice dynamics discussed in Appendix A.1 to a hexagonal tetrahedrally coordinated type of ice through the analysis of the phonon spectra. Because of the complication of the ordering network of the hydrogen bonding in ice, the use of the hexagonal Brillouin zone (BZ) in the phonon dispersions calculations is arbitrary since such BZ does not actually exist for ice. Our calculated phonon dispersions are investigated along k_x direction of the cell with cubic symmetry since the physics results do not differ for the modelled BZ of this structure. It is also stressed that in our calculation of phonon dispersions the polarization charges of water molecules arising from dipole-dipole interactions were not taken into account in the version of the VASP code we used, which is expected to give rise to the so-called longitudinal/transverse optical (LO/TO) splitting at the Γ-point of the BZ.
The molecular dynamics calculations of other hydrogen bonding liquid methanol briefly presented in this Chapter through the analysis of radial distribution functions from molecular dynamics simulation is to serve as a benchmark for calculation of other organic compounds such as cyclodextrin and its complexes comprising the same type of elements to be discussed in Chapter 7.

6.1 Some general features of water

As stated before liquid Water is of crucial important to life. It is so important that most biomolecules would not work at all or even maintain a three-dimensional structure without a surrounding solvent. How does this come? A single water molecule in its liquid state is tetrahedral, a property which might not be entirely evident from the usual way of drawing the oxygen and hydrogen atoms. This geometry is explained by the electronic configuration of the oxygen which is referred to as sp^3 hybridization, meaning that there are four equivalent valence orbitals, just as in methane CH_4 or ammonium ion (NH_4^+). The oxygen atom is located at the center of the tetrahedron, the hydrogen atoms in two of the apex sites and two pairs of non-bonding electrons form the other two. Since oxygen is more electronegative than hydrogen, the electrons in the bonds will be displaced slightly towards oxygen. The two bonds in the molecules are therefore polarized and have permanent dipole moments directed from oxygen (negative) to hydrogens (positive). Another two dipoles are formed with their positive ends at the oxygen, extending towards each of the non-bonding pairs of electrons. In the presence of other charged or polar molecules, all these dipoles will become considerably stronger due to the external field.
The vacuum dipole moment of an isolated H_2O molecule has been calculated with our

DFTB code, the calculated value is 1.63 Debye for a single isolated molecule and the calculated bulk value is 2.001 Debye while the experimental average value is 1.86 Debye [140]. Water is thus not only polar, but also highly polarizable, which explains its effective screening possibility and very high dielectric constant $\epsilon_r \approx 80$ relative to vacuum. The index r below ϵ symbolizes the value relative to vacuum since 0 is used for vacuum itself. This means it is quite hard to perform accurate simulations of water molecules. The interplay between water molecules is dominated by electrostatic interactions of these dipoles. Their most favourable configuration is achieved when the dipole in the O-H bond is aligned with the dipole moment of the non-bonding electrons on a different water molecule. Such dipole-dipole interaction brings the hydrogen and oxygen atoms of the two molecules so close to each other such that a weak bond is created. These hydrogen bonds form a very complex network among the water molecules. Even in liquid water there are about 1.7 hydrogen bonds on average per molecule, not far from the value of 2 found in perfect ice. The thermal motions of the atoms in liquid water at room temperature are large enough so that a typical pair of these bonded molecules will separate and form new bonds in clusters with other neighbours [141] in a time of roughly 4 ps. There are also smaller displacements of the molecules, corresponding to deformations or transient breaks in hydrogen bonds, which occur on a shorter time scale. As a result of this underlying molecular mobility, bulk water behaves as a moderately viscous fluid except at times below 0.1 ps, where the rigidity of the hydrogen bond network becomes apparent [142].

6.2 Calculated electronic density of liquid water

The Kohn-Sham equations (discussed in Section 2.2.2) can be solved for different liquid configurations leading to a thermal-averaged densities of states defined by the relation

$$D(\epsilon) = \left\langle \sum_i \delta(\epsilon - \epsilon_i) \right\rangle \tag{6.1}$$

The distribution of Kohn-Sham eigenvalues for the occupied and for some unoccupied levels is illustrated by the calculated full density of states of liquid water at 298 K states in Fig. 6.1. Three sharp peaks centered at respectively at -19.0, -12.0 and -1.5 eV respectively are observed with a broad manifold starting at -5.5 eV terminating with a sharp peak of highest occupied molecular orbital states at -1.5 eV. The unoccupied molecular orbital region has a broad peak in the region between 2 and 12 eV. The position of the Fermi level is indicated by the arrow.

6.3 Molecular dynamics study of liquid water

Because of its special importance, liquid water at room temperature has received considerable attention in the *ab-initio* molecular dynamics literature. Obtaining accurate RDFs compared to experimental measurements has proved to be challenging because of the difficulty of extracting these quantities directly from the neutron and X-ray diffraction

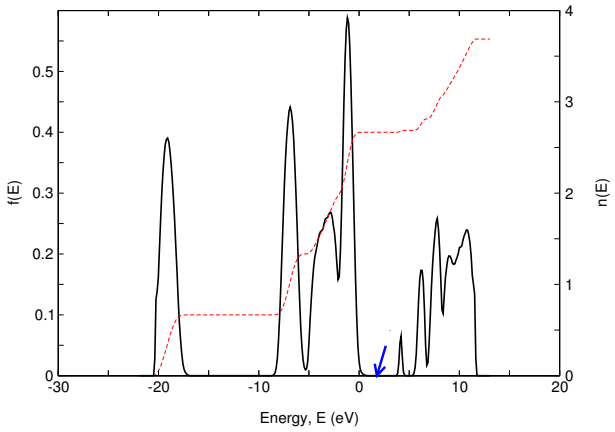

Figure 6.1: Electronic density of states of water together with the integral over the number of states calculated using VASP. The arrow marks the position of the "Fermi level" which separates the occupied states from the unoccupied states.

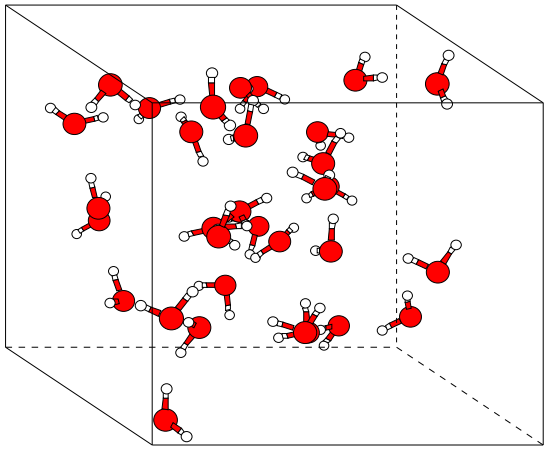

Figure 6.2: 32 molecules of water in the boundary cubic box of length 9.78 Å.

data. However, the most recent studies have shown that reasonable agreement is obtained with experimental data, using a system of 64 water molecules. In our present work, we have calculated the RDFs of 32 molecules water using VASP and SCC-DFTB method. A simulation length of 4 ps was considered using a time step of 0.5 fs. In order to simulate the real density of liquid water, we used the fact that n molecules of water at standard temperature and pressure occupies an approximate volume of

$$\left(\frac{M}{\rho} \times \frac{10^{24}}{6.02 \times 10^{23}}\right) \times n \quad \text{in Å}^3, \tag{6.2}$$

where M is the molecular mass of water, which is 18 g and ρ is the chosen density which is 0.997 gcm^{-3}. Therefore, for 32 molecules of water, we have chosen a cubic box of length 9.78 Å for the corresponding density of 0.997 gcm^{-3}. The calculated oxygen-oxygen radial distribution calculated with VASP agrees fairly well with the neutron diffraction data; the position of the first peak of $g_{OO}(r)$ is found to be at 2.8 Å. The positions of the peaks predicted by using the DFTB method agrees with experimental predictions but

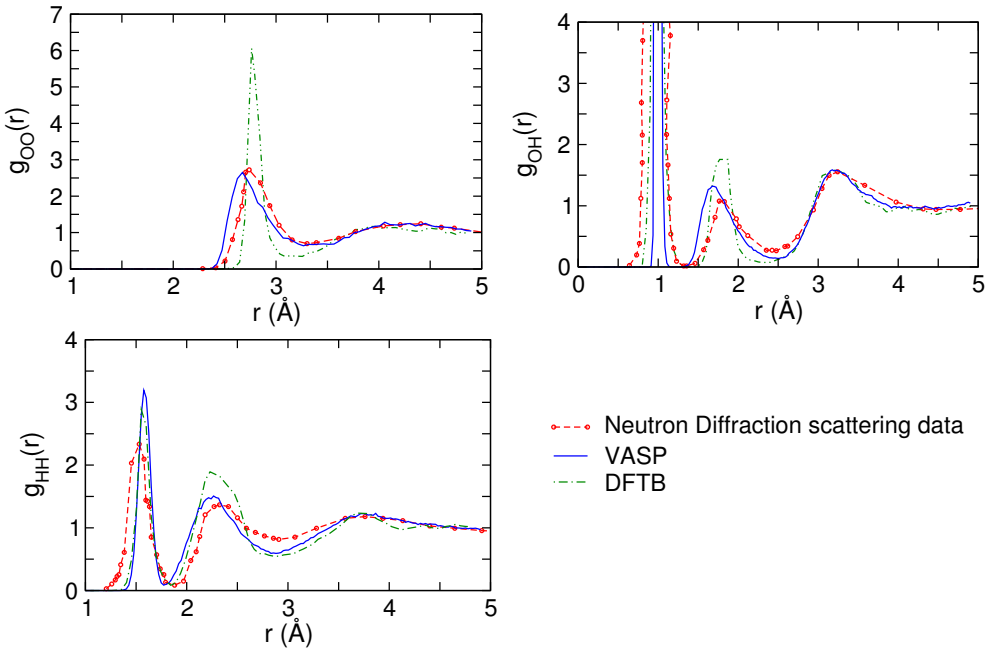

Figure 6.3: Plots of the radial distribution functions $g_{\mathrm{OO}}(r)$, $g_{\mathrm{OH}}(r)$ and $g_{\mathrm{HH}}(r)$ of real liquid water of 32 molecules for DFTB, VASP and neutron diffraction scattering data [143]. The $g_{\mathrm{OO}}(r)$ in this picture shows broader behaviour in the second peaks compared to the corresponding peaks of the water clusters in Fig. 5.12 above the melting temperature.

the heights of the peaks show over-structure due to the inbuilt approximation of the method.

6.3.1 Properties of liquid water at various temperatures

Both static and dynamic properties of liquid water were studied at different thermodynamics conditions. Among the static properties of interest studied are partial radial distribution functions and the variation of the strength of hydrogen bonding formation as the temperature increases. In order to study these structural behaviours of liquid water at various thermodynamics conditions, we started our simulation with an ensemble of 32 molecules of water in the box shown in Fig. 6.2. Since it is quite expensive by *ab-initio* calculations to obtain the crystalline structure of ice upon cooling from the low order phase of liquid water in order to obtain the long-range order-like ice structure, such as, as shown in Fig. 6.4, a special rule of ice formation [144] is used as will be discussed in the next Section. The main difference between liquid water and ice is that liquid water has a partially ordered structure in which the hydrogen bonds are constantly being formed and breaking, while on the other hand ice has a rigid lattice structure. Also, in ice each water molecule forms four hydrogen bonds with O—O distances of 2.76 Å to the nearest oxygen neighbour. The O-O-O angle is 109°, typical for tetrahedrally coordinated lattice structures. The hexagonal form of ice is found naturally, although there are more than thirteen different forms of crystalline ice which are known (see Appendix A.2). The main

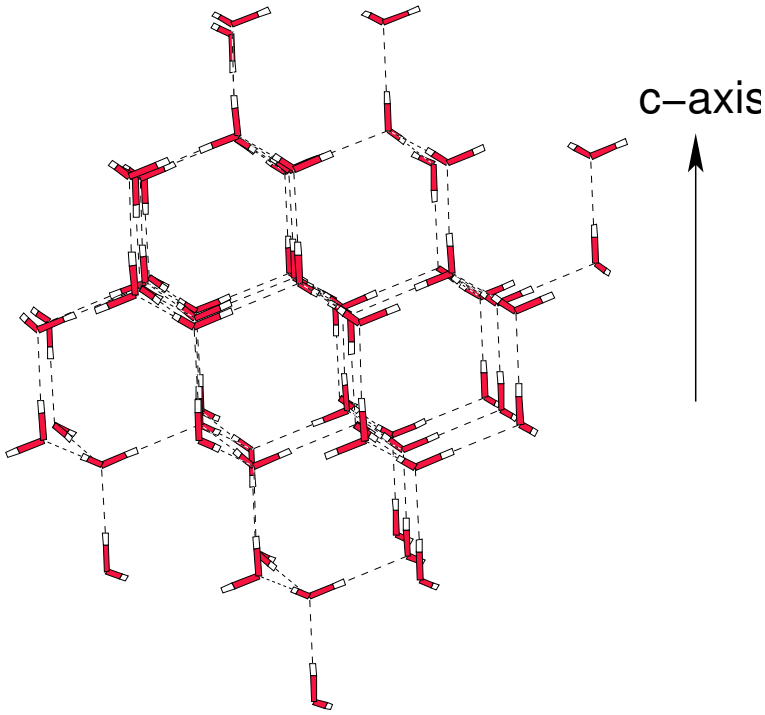

Figure 6.4: Relaxed crystalline structure of ice.

calculation done with VASP, which agreed fairly well with the experimental data of neutron diffraction of Soper [143], are shown in Fig. 6.3. In addition, test calculations were done with the DFTB method. In our molecular dynamics simulation we used the structure shown in Fig. 6.2 in a periodic box of dimension $9.7 \times 9.7 \times 9.7$ Å^3. The MD results have been obtained from MD-runs for a time of about 3000 fs. The RDFs of the structure of cold and ambient water and super-heated and supercritical water, which correspond to the high density and low density, respectively, were compared at various temperatures. The pronounced first and second peaks of RDFs at low temperature are an indication of the extent of the strong hydrogen bonding existing within the molecules. The positions of the peaks predicted by both VASP and DFTB calculations methods are comparable to the experimental results, but VASP results give the correct heights of the peaks which are well comparable to the experimental data. As the temperature is raised above the normal boiling point, the water network becomes progressively more disordered, so that by 573 K, it has largely disappeared, and the hydrogen bonding network itself is considerably weakened, as can be seen in Fig. 6.5, 6.6, 6.7 and 6.8, which show the behaviour of liquid water at various temperatures compared with experimental data. The weakness of the structure can be seen from the disappearance of the peak at 4.35 Å (VASP result) in $g_{\mathrm{OO}}(\mathrm{r})$, in addition there is weakening of the first intermolecular peaks in the $g_{\mathrm{HH}}(\mathrm{r})$ and $g_{\mathrm{OH}}(\mathrm{r})$. At 673 K the OH peak has weakened to the point of becoming a shoulder rather than a distinct peak especially for VASP. This analysis is in agreement with the experimental analysis of supercritical data of Soper et. al. [145], where it was claimed that

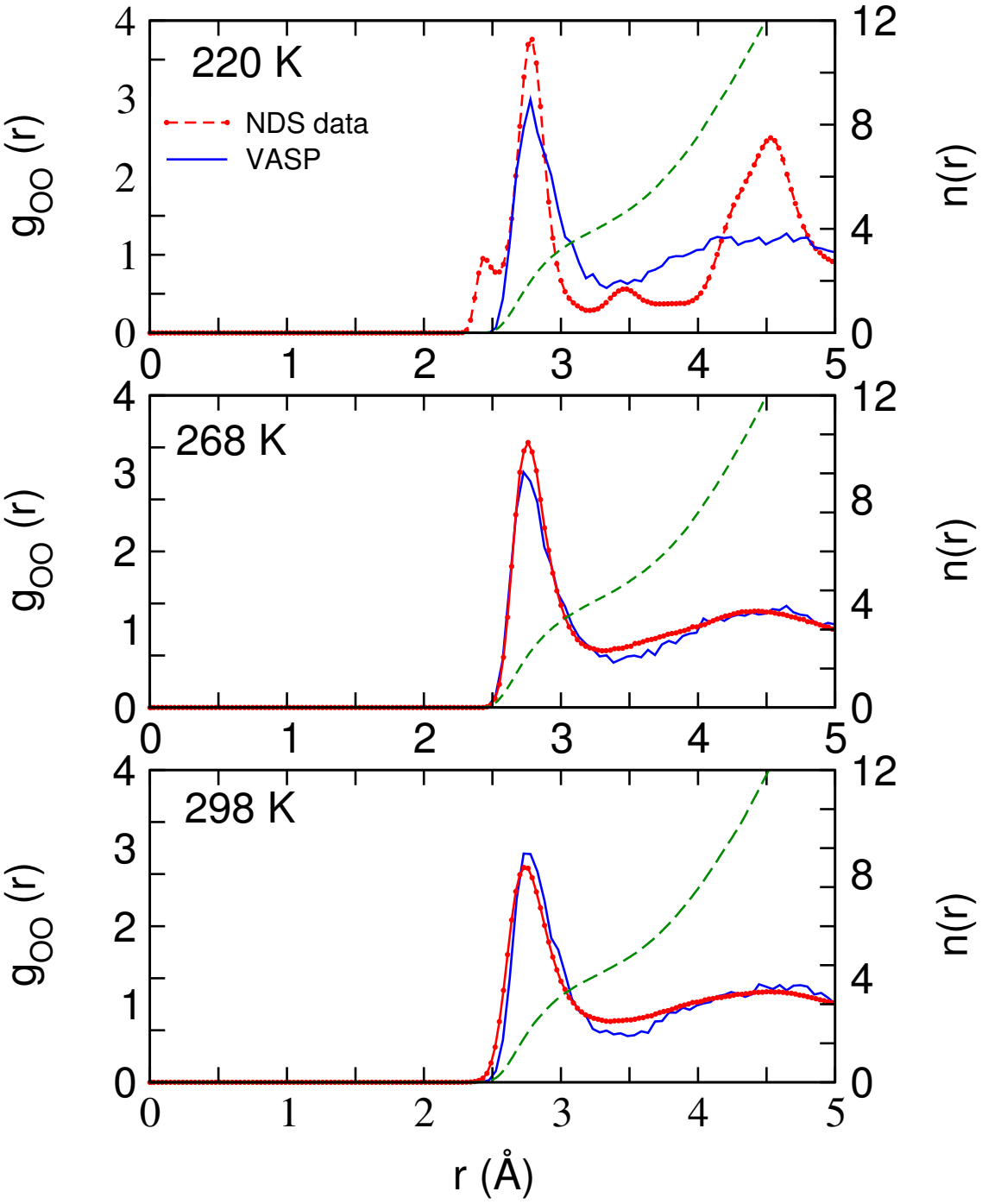

Figure 6.5: Oxygen-oxygen radial distribution functions, $g_{OO}(r)$, together with $n(r)$ of 32 water molecules at various temperatures.

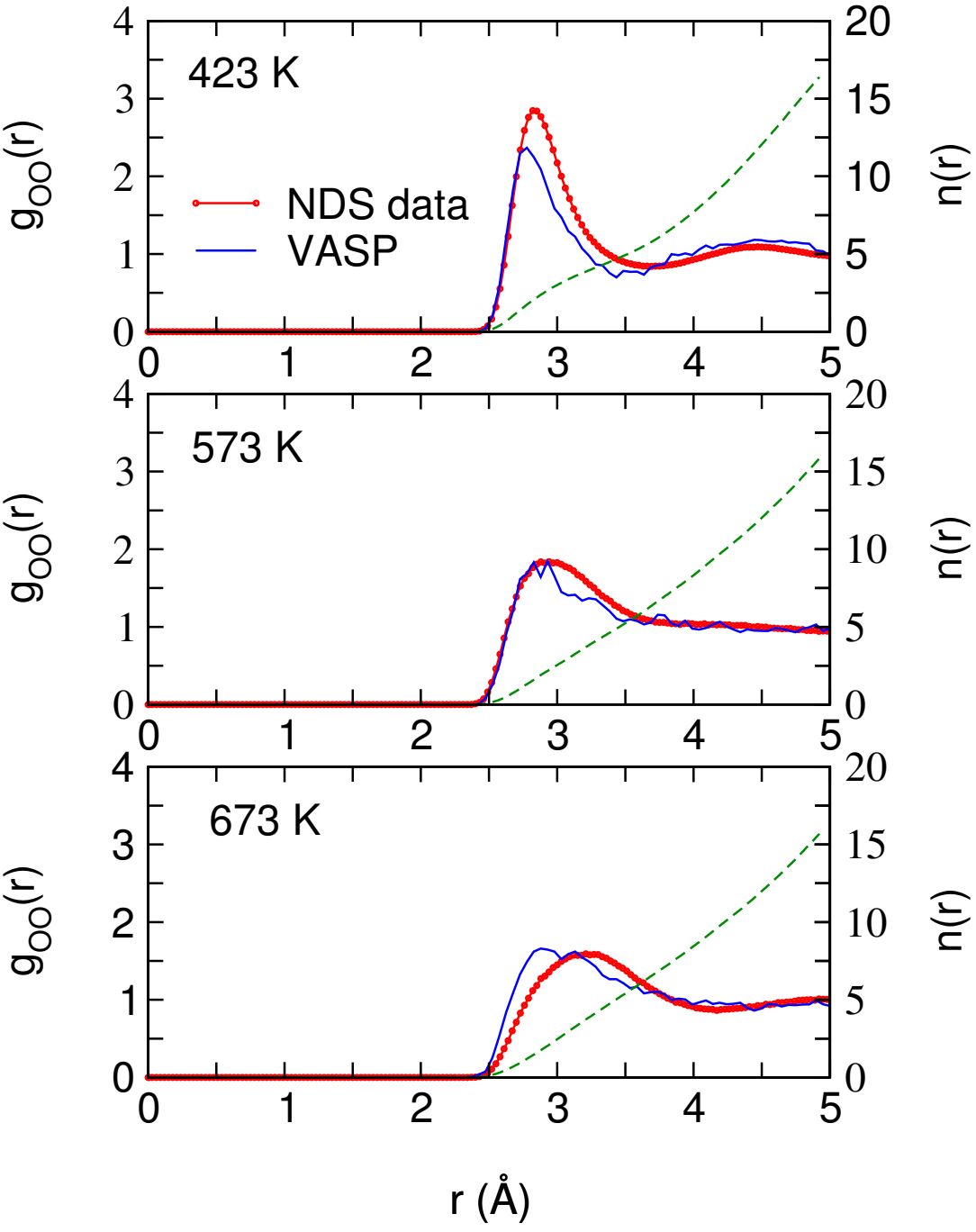

Figure 6.6: Oxygen-oxygen radial distribution functions, $g_{OO}(r)$, together with $n(r)$ of 32 water molecules at various temperatures.

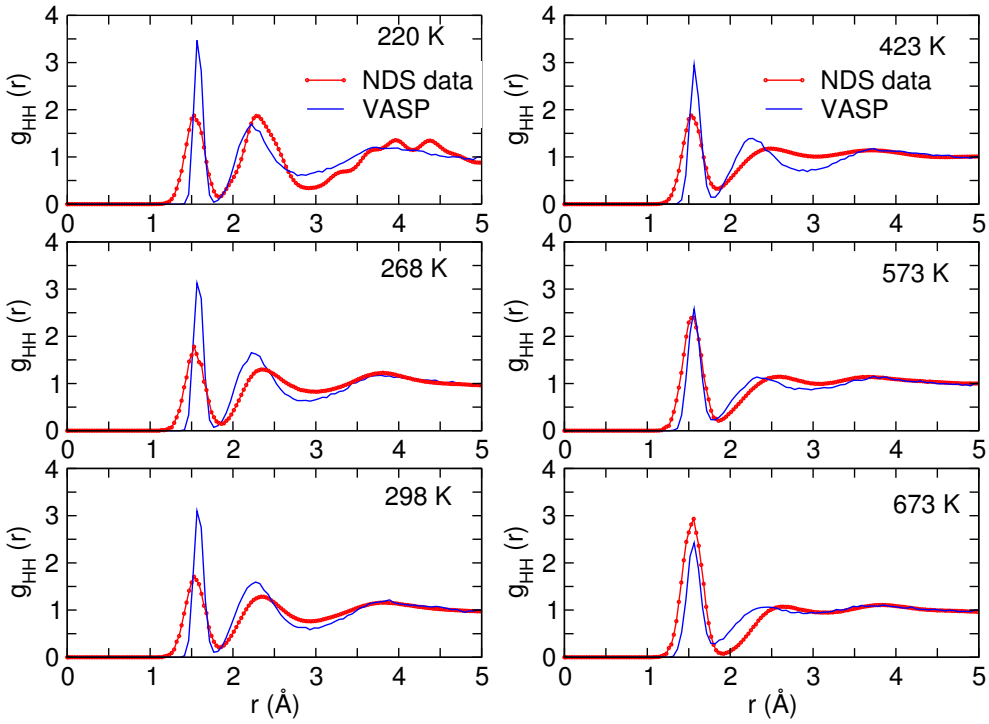

Figure 6.7: Hydrogen-hydrogen radial distribution functions, $g_{\mathrm{HH}}(\mathrm{r})$ of 32 water molecules at various temperatures.

there is complete breakdown of the hydrogen bond under this condition. Other *ab-initio* simulations using the Car-Parinello approach also confirm this agreement with experiment [146]. Also shown in each of Figs. 6.5 and 6.6 along with $g_{\mathrm{OO}}(\mathrm{r})$ in dashed line are the corresponding integration numbers $n(r)$ calculated according to Eq. (4.39) and discussed in Section 4.6.1. It can be noticed that at low temperature (from 220 K) to room temperature (298 K) $n(r)$ decreases gradually with the hump in the middle and become completely flattened out at high temperature in the supercritical region (from 423 K to 673 K). The inflexion point of $n(r)$ occurs at around 4 in $g_{\mathrm{OO}}(r)$ at the position of the minimum of $g_{\mathrm{OO}}(r)$ of about 3.25 Å at 298 K. This experimental value of position taken from Ref. [147] occurs in $g_{\mathrm{OO}}^{min}(r)$ at 3.5 Å with $n(r)$ equal 5.2 at 298 K. The degree of coordination which decreases at higher temperature (from 423 K to 673 K), as can be seen in the disappearance of humps of $n(r)$, also reveals the important role of the hydrogen bonding in the coordination of liquid water.

Several analysis have suggested that the height of the OH peak is not a reliable measure of the degree of hydrogen bonding in water [148–150], and several geometric or energetic or combined geometric and energetic definitions are used. Unfortunately, such definitions cannot be applied directly to measured site-site correlation functions, but a sensible geometric definition can be applied to establish the degree of hydrogen bonding in the real liquid. In our work we have used the assumption that a hydrogen bond occurs if the separation of the oxygen atoms on neighbouring water molecules is less than 3.5 Å and

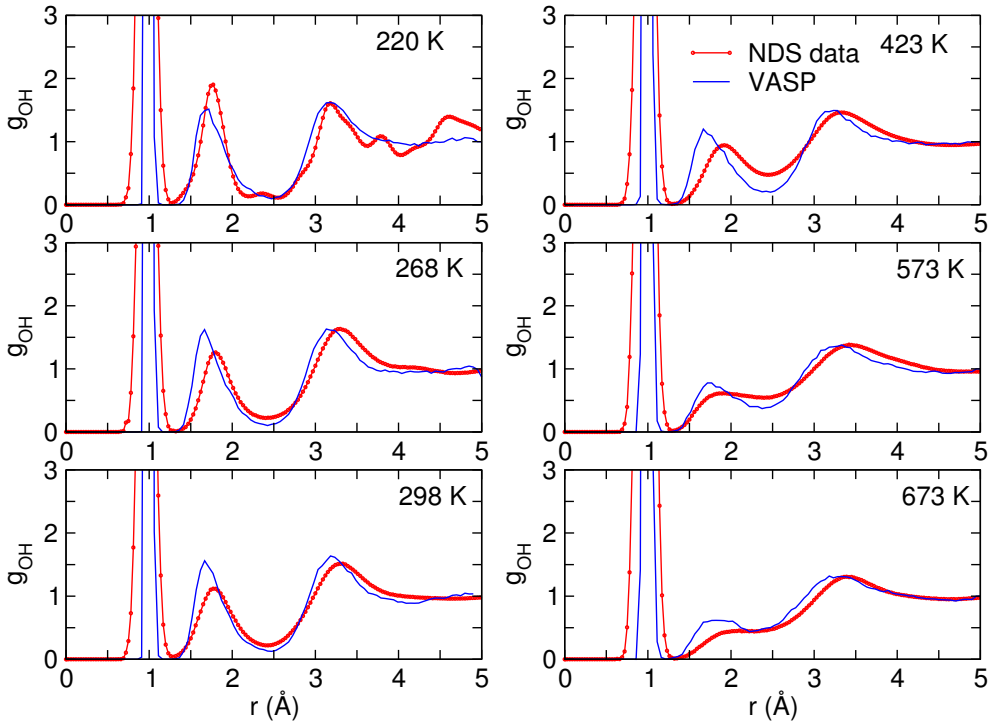

Figure 6.8: Oxygen-hydrogen radial distribution functions, $g_{\mathrm{OH}}(\mathrm{r})$, of 32 molecules of water at various temperatures.

the O...H-O angle θ is greater than 150° [151]. In this case, the angle $\theta = 0$ corresponds to the O-H bond of the molecule pointing directly away from the neighbouring oxygen, while $\theta = 180°$ corresponds to the O-H bond of one molecule pointing directly towards a neighbouring oxygen. Thus a high degree of hydrogen bonding will show up as pronounced peak at $\theta = 180°$ in the bond distribution. Figure 6.9 shows the distribution of O..H-O angles as a function of cos θ calculated with VASP and DFTB for some thermodynamic states at different temperatures. Clearly, from both methods of calculation, there is a pronounced decrease in the degree of hydrogen bonding as the temperature increases (i.e., as the density of water falls). This does not however vanish entirely at 673 K, i.e., above the so called super-critical temperature, as might be supposed on the basis of the height and shape of the first peak in the OH correlation function of neutron diffraction data shown in Fig. 6.8, and the width of the distribution of hydrogen bond angles increases only slowly with increasing temperature. By carefully looking at Fig. 6.9, we notice that the hump is centered around $\cos\theta = 0.22$ for DFTB and 0.26 for VASP at 250 K temperatures and is smeared out at the higher temperatures. This is an evidence of the loss of long range coordination as the temperature increases.

In addition to the static structure properties of water at various temperatures, we also investigated the dynamical properties such as self-diffusion calculated according to the Eq. (4.46) at different temperatures for liquid water containing 32 molecules in a simulation box. The result of the self-diffusion supports this analysis of the picosecond

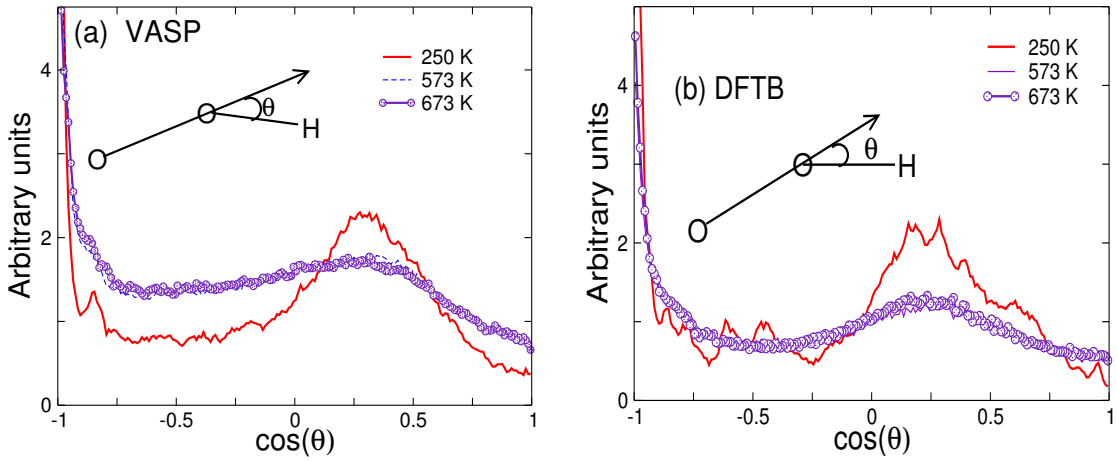

Figure 6.9: Plots of the distribution of the cosine of angle θ between the intermolecular O-O direction and the intramolecular O-H direction at different temperature using VASP and DFTB.

time-scale dynamics. Figure 6.10 shows the plots of mean-square-displacement of liquid water at various temperatures. The diffusion coefficients can be estimated from the slope of mean-square-displacement against time in order to compare the self diffusion at different temperatures. Fig. 6.11 shows the variation of the diffusion coefficient (D) of water calculated from the slopes of Δr^2 vs. time (t) in Fig. 6.10 with temperature. The diffusivity obeys the natural law from the observation in Fig. 6.11 in which the diffusion increases with temperature but is not completely linear at very low temperature because of anomalous behaviour of water. The value of the diffusion coefficient obtained at 298 K, $D \approx 0.23$ Å^{2}ps^{-1}, compares well with the transport rate, $D \approx 0.24$ Å^{2}ps^{-1}, obtained from the experiment [152]. Though it is known that if the liquid water is sufficiently cold, its diffusivity increases upon compression. Pressure disrupts the tetrahedral hydrogen-bond network, and the molecular mobility consequently increases [153]. In contrast, the compression of most other liquids leads to a progressive loss of fluidity as molecules are squeezed closer together. The anomalous pressure dependence of water's transport coefficients occurs below 283 K for the diffusivity and below 306 K for the viscosity, and persists up to pressures of around 2 kbar. Our inability to observe this effect is that there is no pressure constraint in our calculation. The quantitative physical explanation for this anomalous pressure dependence is Le Chatelier principle: When a thermodynamical system is at equilibrium and external conditions are altered, the equilibrium will adjust so as to oppose the imposed change. Recent molecular dynamics simulations of diffusion show that as the temperature is lowered into supercooled region, motion becomes increasingly complex. During a randomly selected picosecond time interval in low temperature simulations, most of the water molecules are not translating; instead, they are confined or "caged" by the hydrogen-bonded network. A small fraction of the molecules, however, are breaking out of their cages. [153].

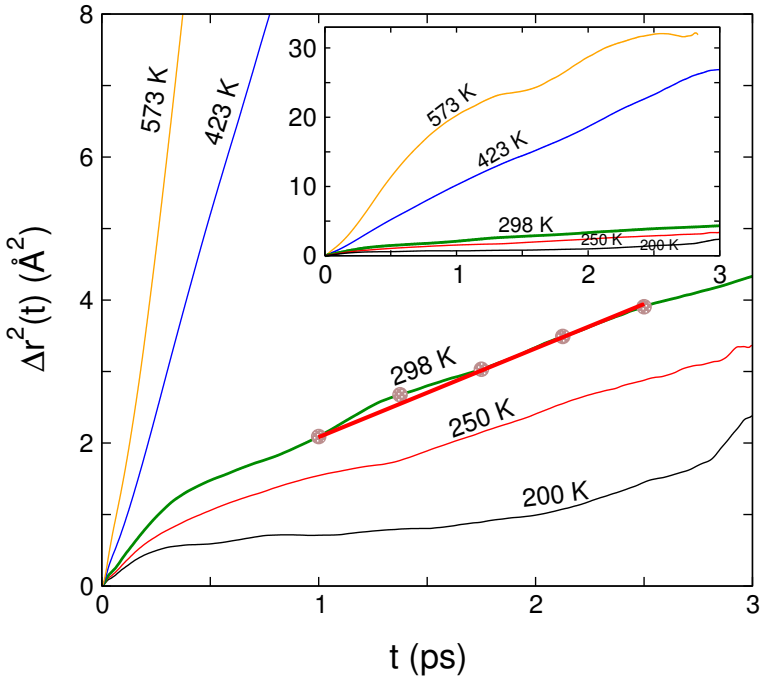

Figure 6.10: Mean square displacement of liquid water containing 32 water molecules at various temperatures.

6.3.2 Spectral analysis of liquid water

The vibrational spectra of aqueous systems are an important source of information on the hydrogen bonding. For example, the shift and broadening of the OH stretch is a reliable measure of the hydrogen bonds. The vibrational properties of liquid water was studied through the calculation of the velocity-velocity autocorrelation function calculated according to Eq. (4.44) from which the spectrum in Eq. (4.43) is obtained by Fourier transformation. The calculated spectrum obtained for our liquid H_2O is shown in Fig. 6.12. Three peaks are observed at $\omega = 800$, 1600 and 2800 cm^1. They correspond to the H-O stretching mode, the bending mode and the librational and vibrational modes, respectively. The stronger hydrogen bond leads to a higher librational mode. The result can be related with the neutron scattering data experiment [154], though there is a small discrepancy in the height of the third peak which is too small.

6.4 Molecular dynamics study of crystalline ice structure

Here we present the structural behaviour of ice from the results of molecular dynamics simulations calculated at two different temperatures for comparison with the available experimental data. It is quite computational expensive to obtain the ice configuration from a super-cooled liquid water using the *ab-initio* code. Also one needs the external constraint such as pressure in order to achieve this purpose. However, in the version of VASP code we use there is no such constraint which allows to alter the pressure of the

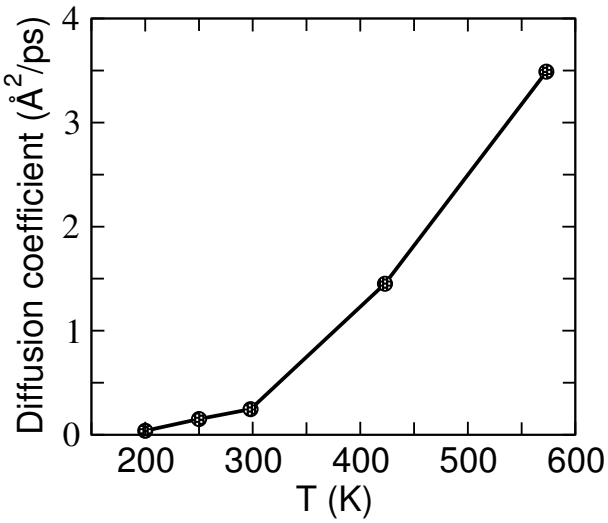

Figure 6.11: Variation of diffusion coefficients (D) of water calculated from the slopes of Δr^2 vs. time in Fig. 6.10 with temperature.

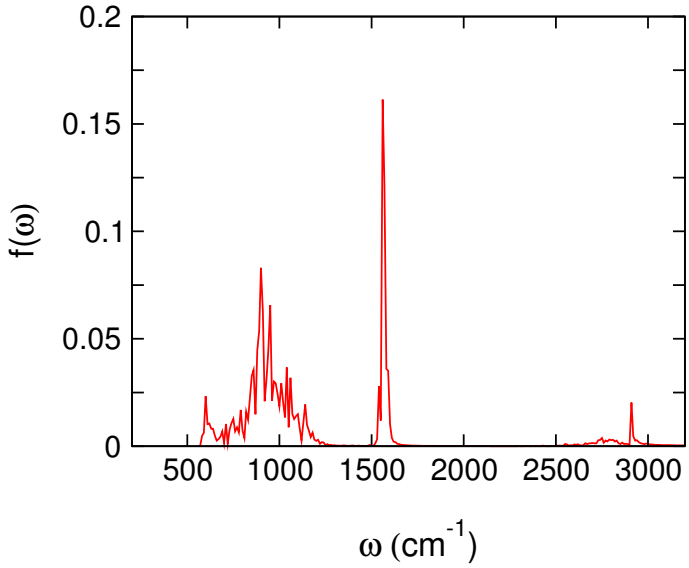

Figure 6.12: Vibrational density of states of liquid water at 300 K calculated from the velocity autocorrelation function with VASP.

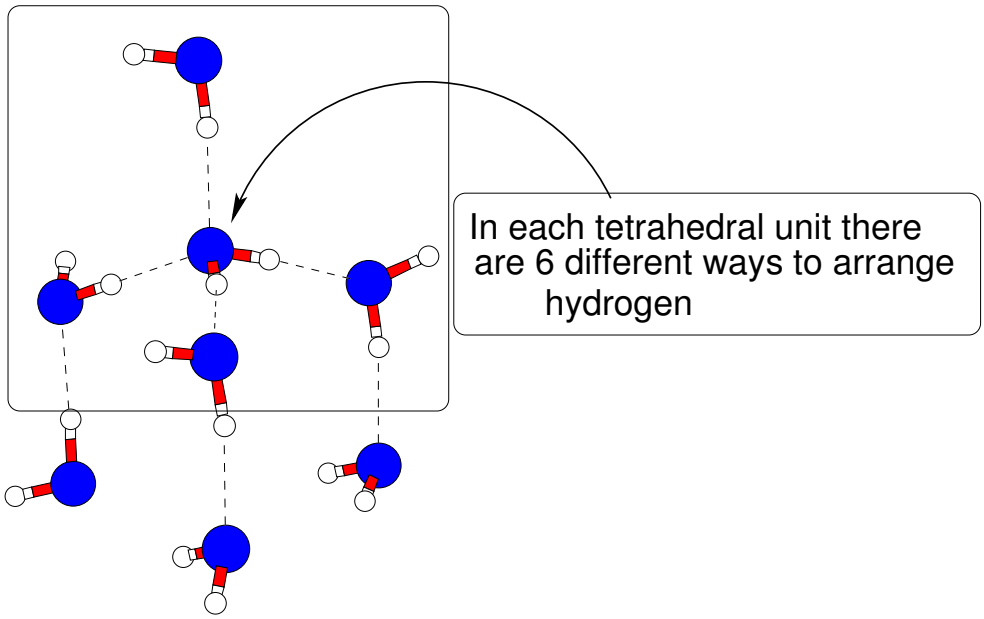

Figure 6.13: The tetrahedral unit from which the hexagonal ice is created.

system as we do for the temperature case. Figures 6.5, 6.6, 6.8 and 6.7 show the radial distribution functions of both the super-cooled like liquid obtained from VASP molecular dynamics calculation and the neutron diffraction scattering data (NDS) of ice at 220 K. The radial distribution function of oxygen atoms, oxygen-hydrogen atoms and hydrogen-hydrogen atoms for liquid VASP water at 220 K matches fairly well with the experimental data reported by Soper [143]. In order to investigate the structural properties of ice, we started with the construction of ice using the Bernal and Fowler rule [144]. The rule is based on a statistical model of the position of hydrogen atoms produced by Pauling [155] based on the six possible configurations of hydrogen atoms within Ice Ih. It is defined as ideal crystal based on the assumptions that:

- Each oxygen atom is bonded to two hydrogen atoms at a distance of 0.95Å to form a water molecule;
- Each molecule is oriented so that its two hydrogen atoms face two, of the four, neighbouring oxygen atoms that surround in tetrahedral coordination;
- The orientation of adjacent molecules is such that only one hydrogen atom lies between each pair of oxygen atoms;
- Ice Ih can exist in any of a large number of configurations, each corresponding to a certain distribution of hydrogen atoms with respect to oxygen atoms.

The Figure shown in Fig. 6.13 satisfies one out of the six possible orientations of protons of the central water molecule according to this rule. Each of the oxygen atoms can be linked to another oxygen by the combination of a covalent bond plus a hydrogen bond

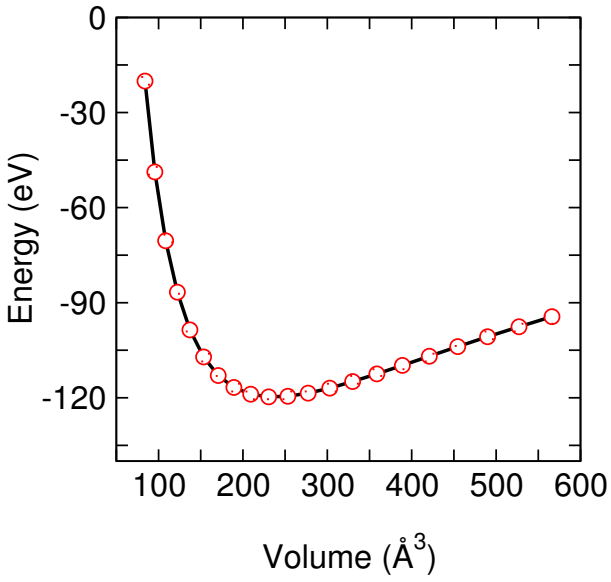

Figure 6.14: Plot of energy against the volume of the unit cell of ice structure. The estimated minimum volume $\approx$ 236 Å^3. The values of the lattice constants are $a = 6.1568$ Å, $b = 6.1565$ Å, $c = 6.0816$ Å with c/a ratio ≈ 0.988.

to form tetrahedral arrangement of oxygen atoms. A unit cell of this ice was prepared in a cubic box with 8 molecules of water. All the atomic degrees of freedom were relaxed using VASP with the projected-augmented wave (PAW) formalism at high precision. The optimum Monkhorst Pack $4 \times 4 \times 4$ k-point was used in addition to the generalized gradient approximation (GGA) of Perdew-Wang 86 in order to describe the xc and to give good description of the hydrogen bonding of water. We used a high energy cut-off of 500 eV because hydrogen atoms require a larger number of planes waves in order to describe localization of its charge in real space. The lattice constants of the unit cell were calculated by plotting the energy against the volume as shown in Fig. 6.14. The estimated minimum volume $\approx$ 236 Å^3. The estimated values of the lattice constants are $a = 6.1568$ Å, $b = 6.1565$ Å, $c = 6.0816$Å. The values of $a \approx b \neq c$ which implies that the relaxed structure is tetragonal with c/a ratio ≈ 0.988. The experimental lattice constant reported in Ref. [9] is 6.35012652 Å for a cubic geometry.

The final geometry obtained was used for studying the lattice dynamics of this structure and the molecular dynamics simulation at two thermodynamic temperatures. For molecular dynamics simulation, the final relaxed geometry was replicated in all directions using the calculated value of the lattice parameters to produce 64 molecules of water which forms the hexagonal structure shown in Fig. 6.4. Here the molecular dynamics simulation was done for the Γ-point only in a cubic box of dimension $12.411356 \times 12.411356 \times 12.259675$ Å^3 corresponding to the density 1.01 gcm^{-3} to be compared to the real density of ice Ih and ice Ic which is 0.92 gcm^{-3}. Molecular dynamics was carried out for 3 ps using a time step of 0.5 fs. The angle H-O-H of ice structure was compared with liquid water at the different temperatures as can be seen in Fig. 6.15. For ice structure, the H-O-H angle

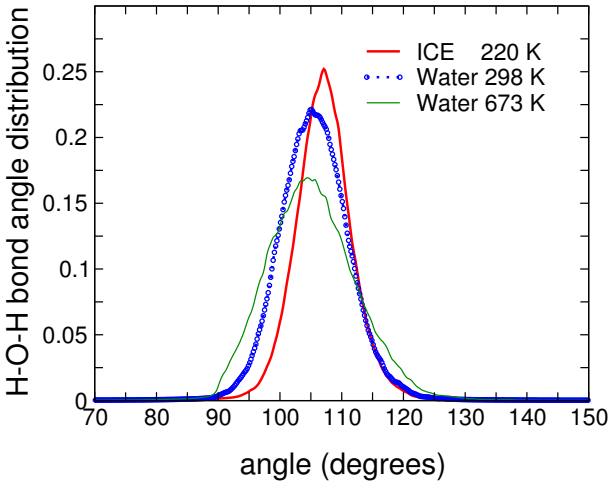

Figure 6.15: Distribution of H-O-H angle in ice and water (in arbitrary unit). The comparison is done for the ice at 220 K and liquid water simulated at room temperature (298 K) and at high temperature in the supercritical regime. The H-O-H angles of ice structure are larger compared to those of liquid water.

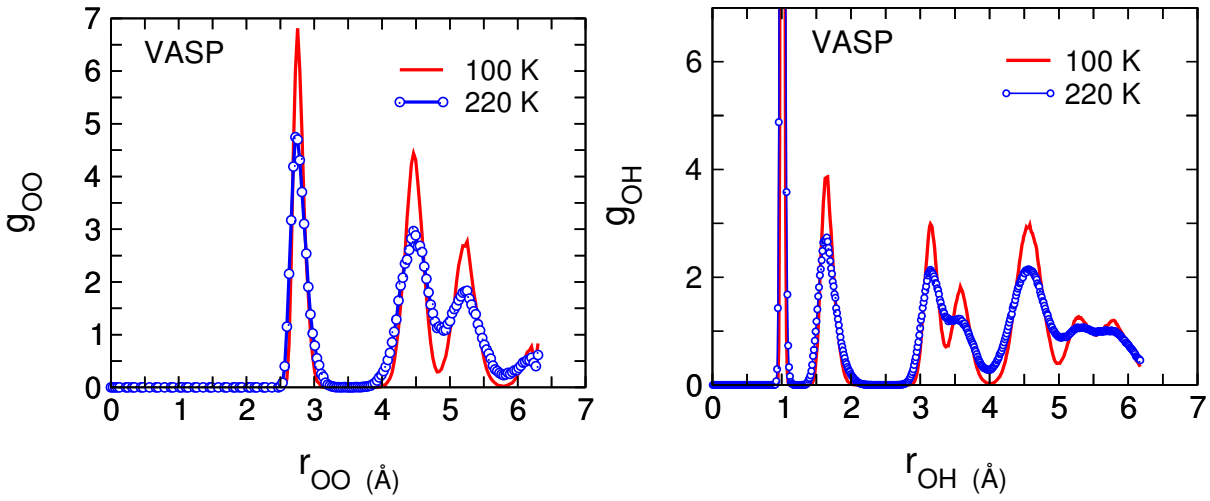

Figure 6.16: Radial distribution functions g_{OO} and g_{OH} at 100 K and 220 K obtained with VASP. There is a gradual loss of long-range order at 220 K as can be noticed in its 2nd and 3rd peaks of g_{OO} when compared to the results for 100 K.

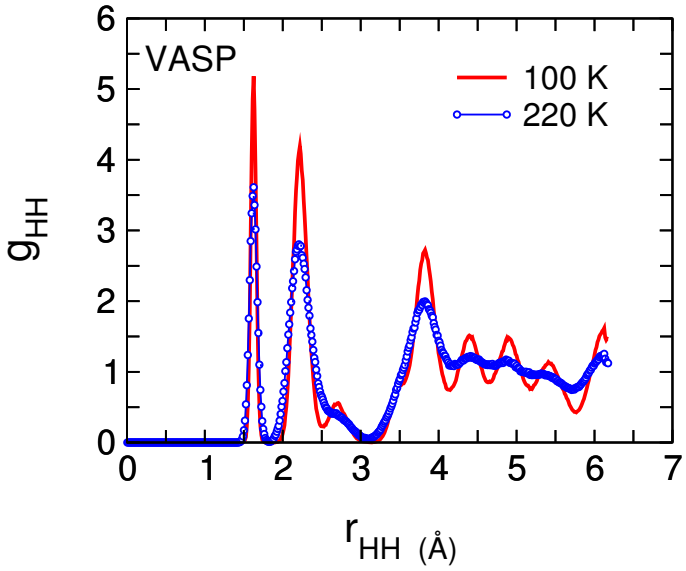

Figure 6.17: Radial distribution functions g_{HH} at 100 K and 200 K obtained with VASP. There is a gradual "loss of peaks" observed for temperature 100 K at 2.5, 4.4, 4.8 and 5.4 Å due to the loss of long-range order as the temperature increases.

was found to be 107.8° compared to liquid water case at different temperature or isolated water molecule also calculated with VASP which is found to be 104.5° and 105.4° degree, respectively, as can be seen in Fig. 6.15. The angle shown by solid ice is an indication that the oxygen centre preserves its tetrahedral structural units. Also, the range of the angular distribution for the high temperature water (or supercritical water) is wider and broader than the corresponding liquid water at ambient temperature and the solid ice cases.

The radial distribution functions for the solid ice accumulated over a 3 ps run are plotted at two different temperatures, 100 K and 220 K. The g_{OO} and g_{OH} in Fig. 6.16, and g_{HH} in Fig. 6.17 at 100 K, all exhibit the long-range like order when compared to the short range orders of liquid water obtained in Fig 6.5- 6.8 in the previous Section. There is a well pronounced first peak of g_{OO} at 2.75 Å at 100 K and also the position of the first minimum is deeper when compared to the liquid water radial distribution functions. This result is comparable to the result obtained using the classical TIP4P modelled potential [10].

The result of the radial distribution function of oxygen atoms, g_{OO}, oxygen-hydrogen atoms g_{OH} (Fig. 6.18), and hydrogen atoms (Fig. 6.19) at 220 K were fairly comparable with available neutron diffraction scattering data of Soper [143]. The position of first peak (VASP calculation) shows very little difference from 100 K while the height of the peak is lower for 220 K due to the effect of entropy increase of the hydrogen atoms which results from re-orientation of protons that tends to force apart more oxygen atoms to a larger distance. The positions of the second minimum for 100 K and 220 K solid ice are, respectively, 4.8 Å and 4.9 Å. The experimental result is slightly shifted to the right to the value 5.1 Å for 220 K. The deviation from experimental value might be due to the

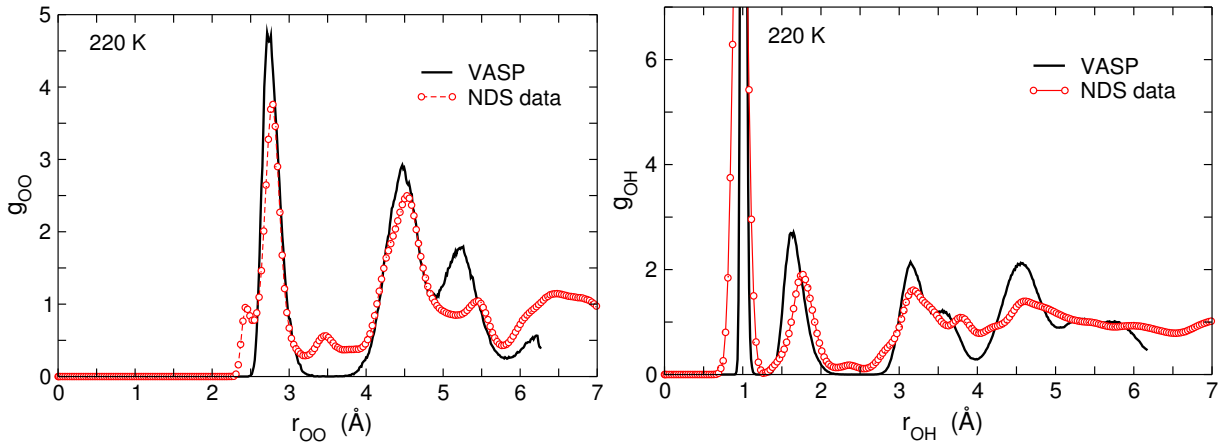

Figure 6.18: Radial distribution functions g_{OO} and g_{OH} at 220 K obtained with VASP, compared to neutron diffraction scattering data (NDS) [143].

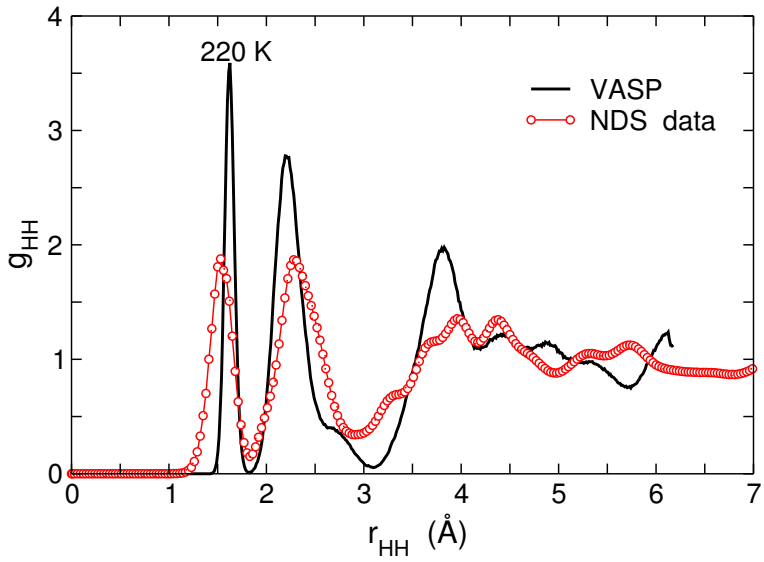

Figure 6.19: Radial distribution functions g_{HH} obtained with VASP at 220 K compared to neutron diffraction scattering data (NDS) [143].

phase of crystalline ice under consideration.

6.5 Lattice dynamical properties of ice

Numerous attempts have been made for the past decades to understand the nature of the lattice vibrations of ice, in particular, ice Ih [156]. Experimental information has been obtained from infrared absorption [157], Raman scattering [158] and both coherent and incoherent inelastic neutron scattering [159,160]. On the theoretical side, three basic approaches have been adopted to study the lattice modes. The earliest studies involved the application of lattice dynamics to hypothetical proton ordered structures [157, 160]. Later workers used lattice dynamics to study more realistic orientationally disordered structures [161, 162]. The most recent work has utilized the molecular dynamics simulation techniques [163]. Many of these theoretical studies involved the use of classical modelled potentials through empirical method in order to describe the interaction of the system [156,164]. As result of all these works, the overall features of the lattice mode vibrational spectrum in the translational region (0-300 cm^{-1}) and in the librational region (450-950 cm^{-1}) are reasonably well understood. Potential-based empirical modelling has had some success towards the end, but to date, there are no empirical potentials capable of ice dynamics and related properties across its whole spectra range and describing certain key spectra features. The *ab-initio* method has recently gained ground not only because of its reliability in the study of static and dynamical properties of ice [11, 12] but also because it allows to model some important features such as periodic ice structures [13], and also allows to probe the nature of hydrogen bond in different geometries [14]. Our present study makes use of VASP in order to understand the microscopic nature and lattice vibrations of ice.

6.5.1 Phonon calculation of ice

In this study phonon dispersion curves are calculated by using the PHONON package developed by K. Palinski [165] which has been designed to take input data of Hellmann-Feymann forces calculated with the help of an *ab-initio* electronic structure simulation program. We carried out the lattice dynamics study of ice by using the geometry of eight-molecule primitive cell discussed in the previous Section. The calculations of force constants was carried out by considering a $3 \times 1 \times 1$ supercell containing 24 molecules of water which is obtained by matching 3 tetragonal unit cells. At the first step of the calculation, the PHONON package is used to define the appropriate crystal supercell for use of the direct method discussed below (also see Appendix A.1). As done for the primitive unit cell, all the internal coordinates were relaxed until the atomic forces were less than 10^{-4} eV/Å. The relaxed geometry for a $1 \times 1 \times 1$ supercell from the initial configurations containing 8 molecules is shown in Fig. 6.20. The starting geometry of the molecules in the simulation box shown is such that no hydrogen bonds were present but the positions of oxygen atoms follows the tetrahedral orientation. After the relaxation, all the protons perfectly point to the right direction of oxygen atoms and make the required

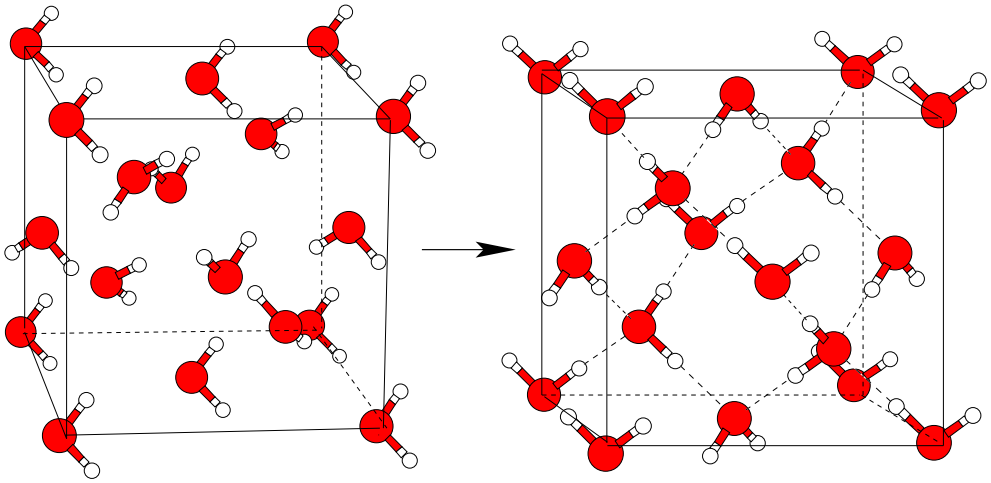

Figure 6.20: Initial and the relaxed geometry of the unit cell of ice. The ice structure was initially packed in a cubic unit cell with initial lattice constant taken from the literature [13] to be 6.35 Å. There are no hydrogen bonds in the initial prepared structure shown on the left but were perfectly formed after the relaxation. The relaxed geometry has the values of $a \approx b \neq c$ which implies that the relaxed structure is tetragonal with c/a ratio ≈ 0.988.

hydrogen bonds necessary as indicated by the dotted lines in Fig. 6.20 to preserve the tetrahedral orientation of the ice structure.

Figure 6.21(a) shows Brillouin zone belonging to the relaxed structure of our (model) ice shown in Fig. 6.20 (for the actual ice structure occurring in nature see Appendix A.2). Figure 6.21(b) shows the Brillouin zone used in the analysis of the measured phonon spectra for the model structure of D_2O ice. Let us say once again that the relaxed structure shown in Fig. 6.20 has the long-range orientational order while the actual structure of ice Ih (see Appendix A.2) has no long-range orientational order. Therefore, in the analysis of the measured phonon dispersion curves of D_2O, one uses another model for ice shown in Fig. 6.4. We have to keep this in mind when comparing our calculated dispersion with the measured frequencies. For the evaluation of the phonon dispersion curves, we have used the direct *ab-initio* force constant method proposed by Parlinski [167], whereby the forces are calculated with VASP via the Hellmann-Feymann theorem in the total energy calculations. Usually, the calculations are done on a supercell with periodic boundary conditions. In such a supercell, a displacement $\mathbf{u}(0,k)$ of a single atom induces forces $\mathbf{F}(lk)$ acting on all other atoms,

$$F_\alpha(lk) = \sum_{l'k'\beta} \Phi_{\alpha\beta}(lk;l'k').u_\beta(l'k'). \tag{6.3}$$

This expression allows to determine the force constant matrix directly from the calculated forces (see Parlinski *et. al.*) [165, 167]. The phonon dispersion branches calculated by the direct method are exact for discrete wave vectors defined by the equation

$$\exp\left(2\pi\imath\mathbf{k}_L \cdot \mathbf{L}\right) = 1, \tag{6.4}$$

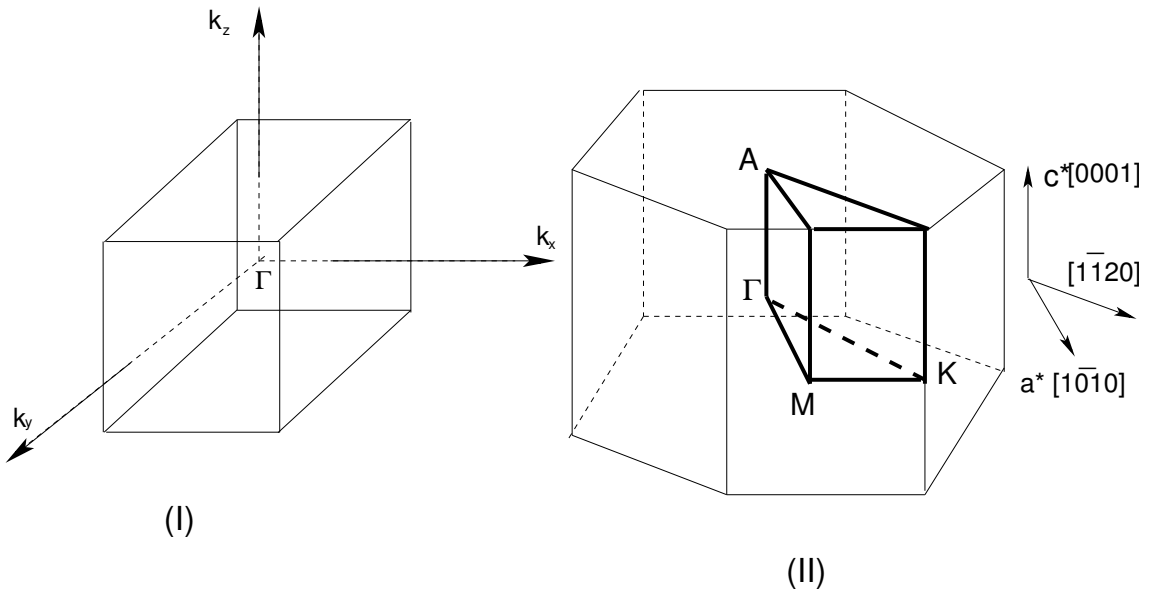

Figure 6.21: (I) Brillouin zone for the cubic symmetry used in our VASP calculation of the ice system. Our phonon dispersions are calculated in [100] k_x-direction, (II) The first Brillouin zone for the structure of ice Ih with origin at the point Γ. ΓA $=\frac{1}{2}c^*$ and ΓM $=\frac{1}{2}a^*$, where a^* and c^* are the vectors of the reciprocal lattice [166]. The dispersion curves are commonly drawn along the lines of symmetry ΓA, ΓM, and ΓK.

Table 6.1: Velocities of sound calculated from the initial slope of the phonon dispersion curves of ice in [100] direction compared to the experimental result.

$\times 10^3$ m/s	Experiment[a]	Theory
v_{LA}	4.04	4.86
v_{TA}	1.80	3.02

[a] Gammon*et. al.* 1996 [168]

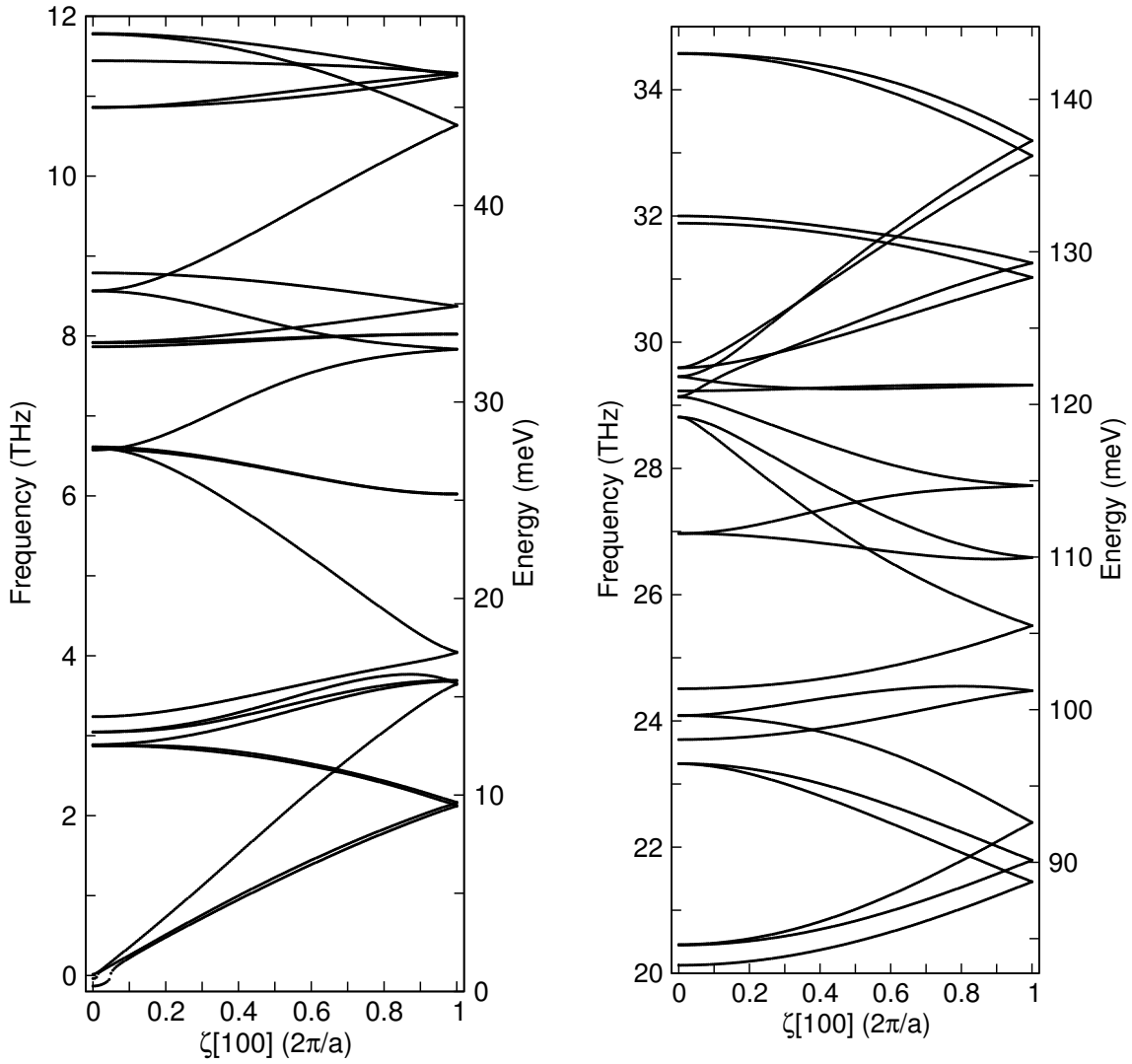

Figure 6.22: VASP calculated phonon dispersion curves of ice in [100] direction of the cubic symmetry. The first Figure on the left shows the dispersion relations in the molecular translational region. The right Figure shows the dispersion relations in the molecular librational region.

where $\mathbf{L} = (L_a, L_b, L_c)$ are lattice parameters of the supercell. A related technique has recently been used to obtain accurate full phonon dispersions in highly symmetric structures of Ni_2GaMn [169]. For a detailed discussion of this method and theoretical discussion of lattice dynamics, see the Appendix A.1.
In order to obtain the complete information of the values of all force constants, every atom of the primitive unit cells was displaced by 0.02 Å in both positive and negative non-coplanar, x, y and z directions to obtain pure harmonicity of the system. We use a $3 \times 1 \times 1$ supercell which implies that 3 points in the direction [100] are treated exactly according to the direct method. The points are $[\zeta 00]$, with $\zeta = 1, 1/3, 2/3$. We calculate forces induced on all atoms of the supercell when a single atom is displaced from its equilibrium position, to obtain the force constant matrix, and hence the dynamical matrix. This is then followed by diagonalization of the dynamical matrix which leads to a set of eigenvalues for the phonon frequencies and the corresponding normal-mode eigenvectors. Vibrational density of states (VDOS) are obtained by integrating over k-dependent phonon frequencies from the force-constant matrix in supercells derived from the primitive molecule unit cells.

6.5.2 Phonons and related properties of the crystal ice

The phonon dispersion curves calculated for our ice crystal in [100] direction are shown in Fig. 6.22 and 6.23 for low lying energy and high energy vibrations, respectively. According to the geometry of the supercell, the low-frequency (or low-energy 0-50 meV) acoustic modes can be compared to Renker's inelastic neutron scattering measurement [170] along the [0001] direction (ΓA) of hexagonal symmetry shown in Fig. 6.21, taken from reference [171] though our calculation was done only along the Cartesian direction [100] of the tetragonal cell. Our transverse and longitudinal acoustic (LA/TA) dispersions are well behaved when compared to some other modelled calculations or experimental results [170] in the high symmetry directions ΓA of hexagonal ice as shown in Fig. 6.24(c). We can also compare our result to the Cote *et. al.* result in Fig. 6.24(b) [11], where they have recently used the *ab-initio* method to obtain the phonon dispersions in the translational frequency range for the ice structure in the Brillouin zone of the orthorhombic eight-molecule unit cell. Altogether our LA and TA dispersions are better than Cote's LA/TA in comparison to the experimental curves in Fig. 6.24(c). Our dispersion curves in [100] direction can as well be compared to the dispersion curves obtained using a dynamical model with two force constants to describe the low frequencies of vibrations of hexagonal ice as proposed by Faure [172].
Although everywhere along the Γ-point, our dispersions are completely degenerate in the optic region whereas Cote's dispersions in Fig. 6.24(b) show some splittings, the so-called longitudinal/transversal optic (LO/TO) splittings whose origins is explained below, while at the zone boundary, some of the dispersions are non-degenerate unlike our results. This might be due to the fact that when the LO/TO splittings were taken into account in their calculations, they were over-estimated. Our inability to reproduce these splittings at the Γ-point is due to the direct method approach in which absolute periodicity of the

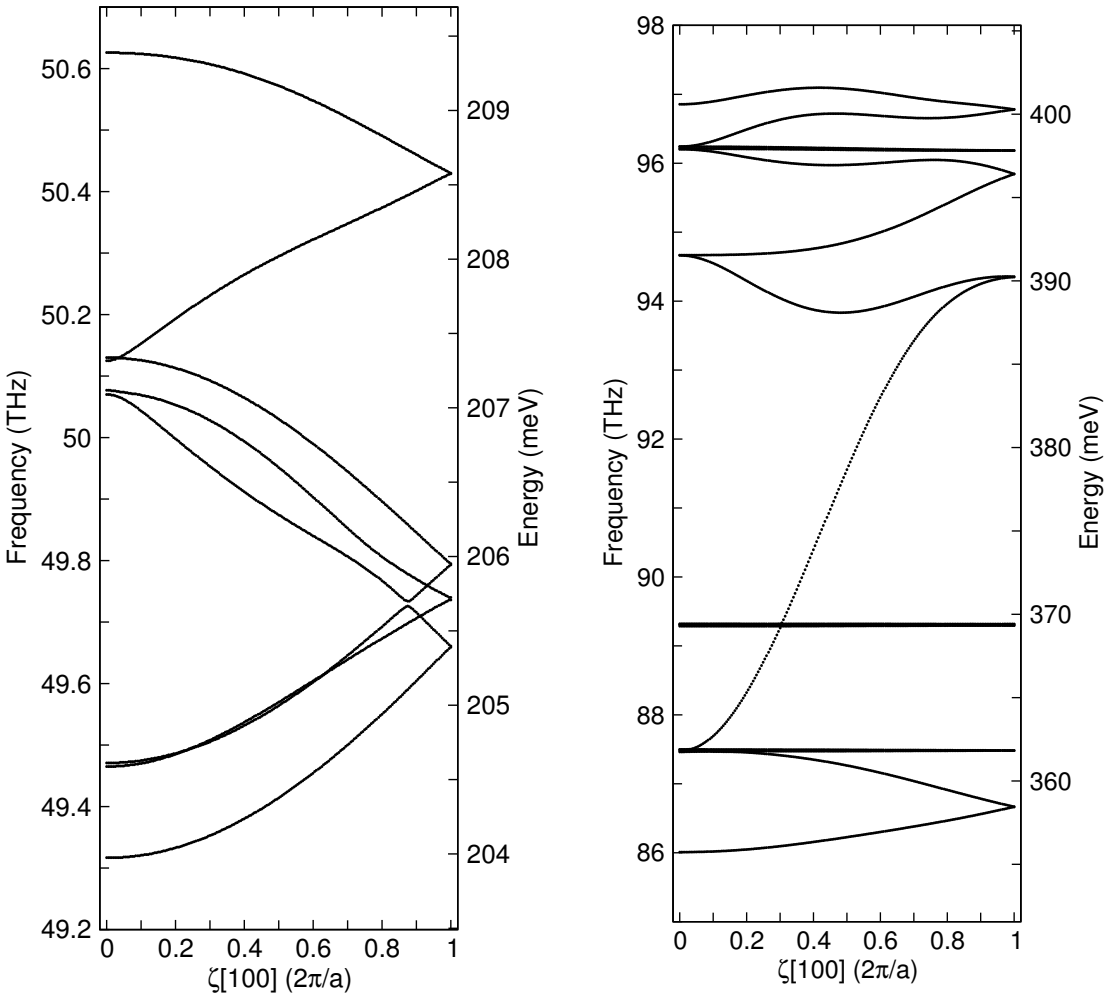

Figure 6.23: VASP calculated phonon dispersion curves of ice in [100] direction of the cubic symmetry. The first Figure on the left shows the dispersion relations in the bending region. The right Figure shows the dispersion relations in the higher frequency stretch range.

crystal according to Born-von Kármán conditions was considered. The splitting of LO and TO branches for long wavelengths occurs in almost all crystals which are heteropolar (partially ionic such as GaAs) or ionic (such as NaCl) at the Γ-point, and only for infrared active modes [173]. The long-range part of the Coulomb interaction causes the splitting of the $k = 0$ optic modes raising the frequency of LO modes above those of TO modes. The long-range part of the Coulomb interaction corresponds to the macroscopic electric field arising from ionic displacements. Ice is a tetrahedrally covalently bonded polar system whose dipole-dipole interactions give rise to the electric field when they are disturbed. The origin of the splitting is therefore the electrostatic field created by long wavelength modes of vibrations in such crystals. Usually a microscopic electric field influences only the LO modes while TO modes remain unaltered. The field therefore breaks the Born-von Kármán conditions, as a consequence with a direct method only finite wave vector $\mathbf{k} \neq 0$ calculations are possible. Elongated sub-supercells are needed to recover the $\mathbf{k} \rightarrow 0$ limit

of the LO phonon branch [165].

Also in our result there are two transverse acoustic branches which are highly degenerate

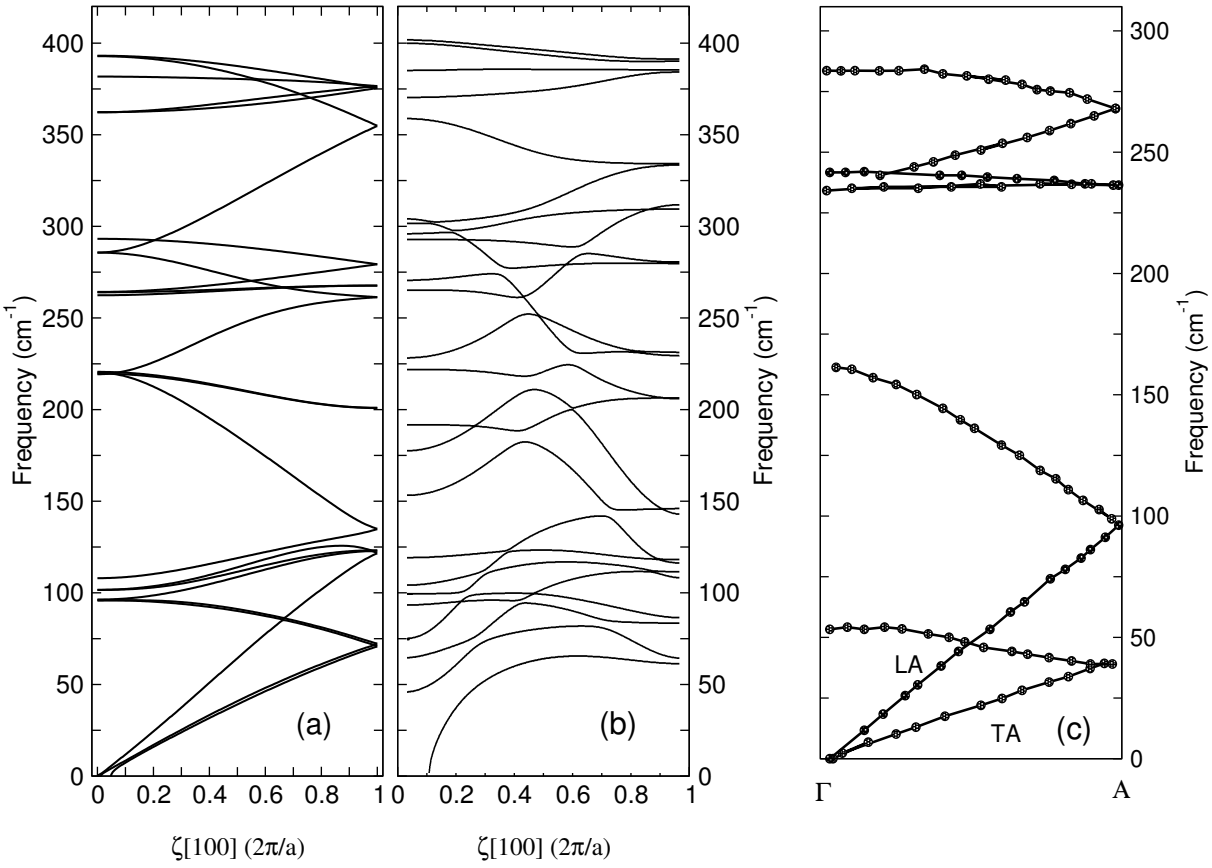

Figure 6.24: (a) VASP calculated phonon dispersion curves of ice in [100] direction of the tetragonal unit cell compared to (b) dispersion relations in the translational frequency range for the ice structure plotted along the Cartesian directions from zone center to zone edge in the Brillouin zone of the orthorhombic eight-molecule unit cell (Cote *et. al.* [11]) and (c) the experimental dispersion of D_2O ice according to Renker's model [170]. The difference in scale of (c) from (a) and (b) is due to the isotopic effect because of difference in the mass of hydrogen and Deuterium atoms.

and a longitudinal acoustic branch. The first optical branch of the dispersion curves is degenerate with the transverse acoustic branches at energy ∼9.0 meV. The transverse and longitudinal velocities of sound are calculated from the initial slopes of the corresponding transverse and longitudinal acoustic branches of the dispersion curves at the long wavelength limit. The experimental values of velocities reported in Table 6.5.1 are those of longitudinal and transverse sound waves propagating along the *c*-direction of single crystals of ice at 257 K. It is well known that velocities of sound depend much on the direction of propagation and also on the temperature. Inelastic X-ray scattering data from water at 5 °C shows a variation of the sound velocity from 2000 to 3200 m/s in the momentum range of 1-4 nm^{-1}. The so-called transition from *normal* to *fast* sound in liquid water at ≈ 4 meV, the energy of sound excitations which is equal to the observed

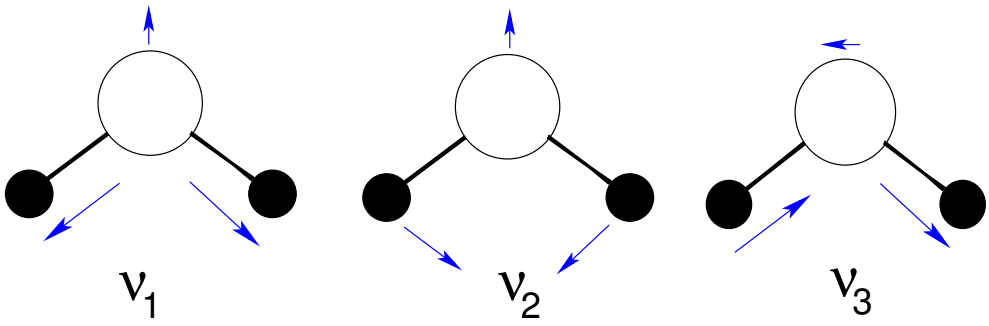

Figure 6.25: The three normal modes of an isolated water molecule. Motion with frequency ν_1 can be regarded as symmetric stretch, ν_2 as bending and ν_3 as anti-symmetric [166].

second weakly dispersed mode, was reported to be due to the reminiscent of a phonon branch of ice Ih of known optical character [174]. We can conclude that our calculated values of longitudinal velocity, v_L is in a reasonable range of velocity of sound in ice along the [100]-direction chosen for our calculation. We must also stress the fact that our phonon dispersions were calculated at 0 K. The elastic constants C associated with the calculated velocities v of sound in the direction of propagation can in principle be obtained according to the equation

$$v = \left(\frac{c}{\rho}\right)^{\frac{1}{2}}, \tag{6.5}$$

where ρ is the density of the ice crystal. These are related to the other elastic properties of polycrystalline ice such as bulk, Young's and shear modulus as well as the Poisson's ratio (see Ref. [166]).

6.5.3 How to calculate LO/TO splitting

As mentioned above, elongated supercells (or sub-supercells) are needed to recover the $\mathbf{k} \to 0$ limit of the LO phonon branch in order to break down the Born-von Kármán conditions as it is strictly implemented in the direct-method approach [165]. In the case when the large size of the elongated unit cell is not accessible, one may use the phenomenological *point effective charges* and calculate the LO mode frequencies in semi-empirical way: The *displacive* particle, specified by three degrees of freedom (x, y, z), could have electric charge given in the form of *Born effective charge tensor* $\mathbf{Z}^*(\mu)$. In polar crystals the macroscopic electric field leads to a non-analytical term of the dynamical matrix at wave vector $\mathbf{k} = 0$. In the phonon calculation this non-analytical contribution is taken into account in approximate form by calculating

$$\begin{aligned}\mathbf{D}^M_{\alpha,\beta}(\mathbf{k};\mu\nu) &= \mathbf{D}_{\alpha,\beta}(\mathbf{k};\mu\nu) \\ &+ \frac{4\pi e^2}{V\epsilon_\infty\sqrt{M_\mu M_\nu}}\frac{[\mathbf{k}\cdot\mathbf{Z}^*(\mu)]_\alpha[\mathbf{k}\cdot\mathbf{Z}^*(\nu)]_\beta}{|\mathbf{k}|^2}\end{aligned}$$

$$\times \exp[-2\pi i \mathbf{g} \cdot (\mathbf{r}(\mu) - \mathbf{r}(\nu))]$$
$$\times d(\mathbf{q}) \exp\left\{-\pi^2 \left[\left(\frac{k_x}{\rho_x}\right)^2 + \left(\frac{k_y}{\rho_y}\right)^2 + \left(\frac{k_z}{\rho_z}\right)^2\right]\right\}, \tag{6.6}$$

where the damping factor is

$$d(\mathbf{q}) = \begin{cases} \frac{1}{2}\left\{1 + \cos\left[\pi \left(\frac{\sqrt{q_1^2 + q_2^2 + q_3^2}}{\sqrt{b_1^2 + b_2^2 + b_3^2}}\right)^n\right]\right\} & \text{if } n \geq 1.0; \\ \frac{1}{2}\left\{1 - \cos\left[\pi \left(1 - \frac{\sqrt{q_1^2 + q_2^2 + q_3^2}}{\sqrt{b_1^2 + b_2^2 + b_3^2}}\right)^{\frac{1}{n}}\right]\right\} & \text{if } 0.0 < n < 1.0, \end{cases} \tag{6.7}$$

where $\mathbf{k} = (k_x, k_y, k_z)$ is the wave vector. In the non-analytical term, $\mathbf{k}$ is counted from the closest Brillouin zone (BZ) centre given by the reciprocal lattice vector $\mathbf{g}$, $\mathbf{q} = (q_1, q_2, q_3)$ is the wave vector. If V is the volume of the primitive unit cell, M_μ, $\mathbf{r}_\mu$ are the atomic masses and positions within the primitive unit cell, ϵ_∞ is the electronic dielectric constant, $\mathbf{D}_{\alpha,\beta}(\mathbf{k}; \mu\nu)$ is the dynamical matrix given by Eq. (A.16) in Appendix (A.1), constructed from the force constants or obtained by the direct method from the Hellmann-Feymann forces. Here $\mathbf{b} = (b_1, b_2, b_3)$ is the lattice vector from the BZ center to the Brillouin zone surface in the direction specified by $\mathbf{q}$. The index n, called *power of interpolation function*, allows to model the *longitudinal* phonon dispersion curve between the Brillouin zone center and Brillouin zone surfaces. When $n > 1.0$ the longitudinal dispersion curve will be, for most wave vectors, closer to the value at the Brillouin zone center, except in the close vicinity to the Brillouin zone surfaces, where $d(\mathbf{q}) = 0$. The case $0.0 < n < 1.0$ describes the opposite situation, where the dispersion curve reaches the longitudinal phonon mode only quite close to the BZ center. The $\rho_i = \rho_{k_i}$, where k_i is the wave vector distance from BZ center to the BZ surface along x, y and z directions of the Cartesian coordinate system. The ρ, denoting the *macroscopic electric field range factor*, is a free parameter which could further suppress the influence of the second term of Eq. (6.6), once $\mathbf{k}$ moves away from $\mathbf{k} = \mathbf{g}$. The dispersion curve calculated with the non-analytical term are periodic with $\mathbf{k}$ in reciprocal space. In practice, one should only introduce the effective charges and dielectric constant. If the effective charge is considered as a point charge, then one has to replace tensor $\mathbf{Z}^*(\mu)$ by a matrix with all diagonal elements equal to $Z^*_{ij}(\mu) = e(\mu)\delta_{ij}$, and set the electronic dielectric constant to $\epsilon_\infty = 1$. The semi-empirical approach influences only the LO modes, and leaves unaltered the TO modes. One should also notice that the LO modes contribute very little to the density of states, since they differ from TO modes only in a small volume of the reciprocal lattice in the vicinity of the Γ-point.

6.5.4 Vibrational density of state

In order to understand the mode of collective vibration of molecules of water in ice from spectroscopic point of view, we need to consider the three normal modes of an isolated

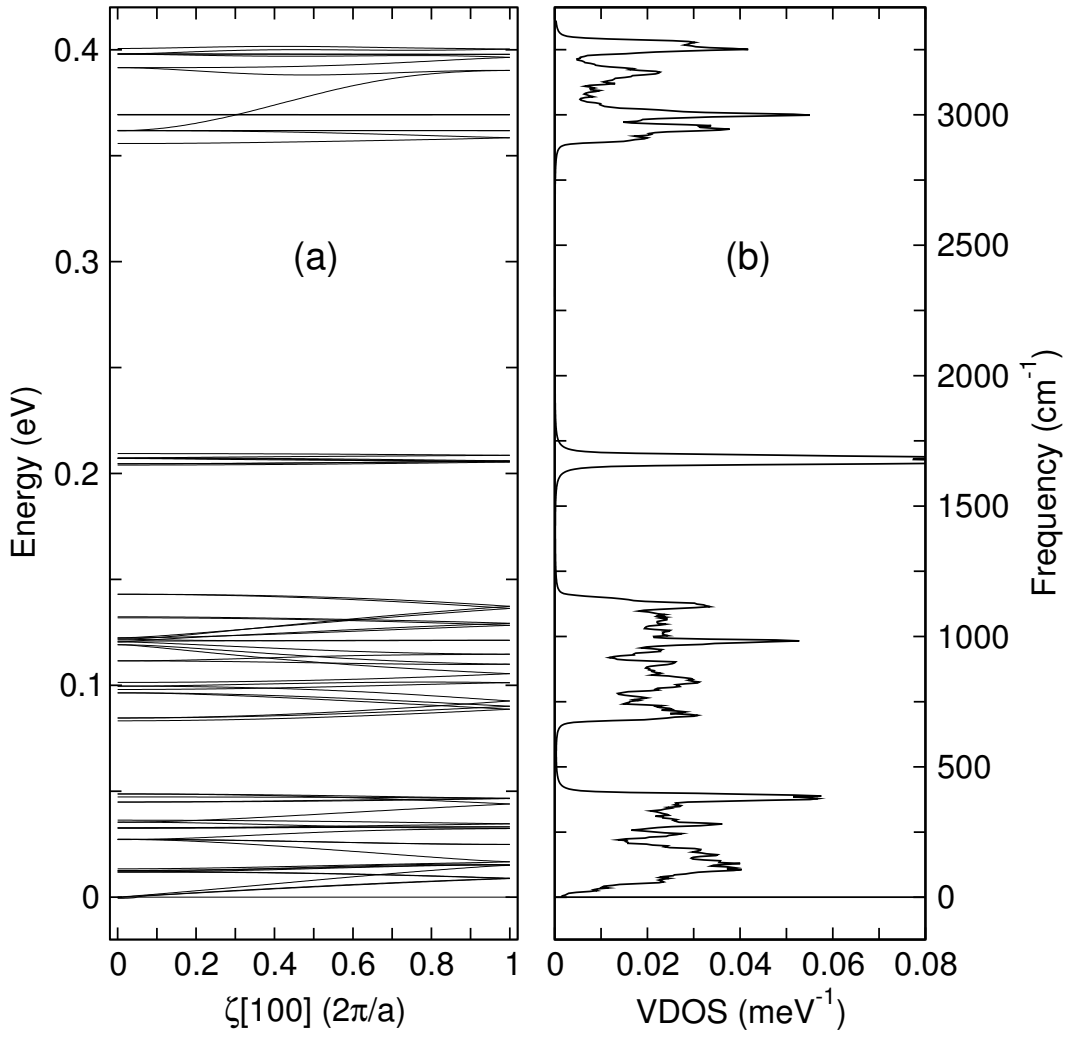

Figure 6.26: Total vibrational density of states (VDOS) of ice based on the lattice dynamics together with full phonon dispersion curves. The VDOS show all the important regions such as the intermolecular translational, librational, bending and the stretching frequency range.

water molecule shown in Fig. 6.25 as phases of water vapour; liquid water and ice consist of distinct H_2O molecules recognized by Bernal and Fowler in 1933, which explained one of the factors leading to the Pauli model of the crystal structure of ice. The fact that the forces between the molecules are weak in comparison with the internal bonding results in a simple division of the lattice modes into three groups involving the internal vibrations, rotations, and translations of the molecules. The frequency of the first two groups depend primarily on the mass of the hydrogen or deuterium nuclei, and the frequencies of the translations depend on the mass of the whole molecule [166]. A free H_2O molecule has just three normal modes of vibration illustrated in Fig. 6.25. The comparatively small motions of the oxygen atoms are required to keep the centre of mass stationary, and these motions result in the frequency ν_3 being slightly higher than ν_1; these depend on the force constant for stretching the covalent O-H bond, while the bending mode ν_2 depends on the force constant for changing the bond angle. In the vapour the free molecules have a rich rotation-vibration infrared spectrum [175], from which the frequencies of the molecular modes are deduced to be:

$$\begin{aligned}\nu_1 &= 3656.65\ \text{cm}^{-1} \equiv 453.4\ \text{meV},\\ \nu_2 &= 1594.59\ \text{cm}^{-1} \equiv 197.7\ \text{meV},\\ \nu_3 &= 3755.79\ \text{cm}^{-1} \equiv 465.7\ \text{meV}.\end{aligned}$$

For ice the band around 400 meV is thus ratified with the O-H bond stretching modes ν_1 and ν_3. The frequencies are thus lowered from those of the free molecules by the hydrogen bonding to the neighbouring molecules, but as a single molecule cannot vibrate independently, this coupling also leads to complex mode structures involving many molecules.
We can now discuss the vibrational density of states, VDOS for H_2O ice based on the lattice dynamics obtained from the results of our calculation and compare them to some of the well known spectra of ice such as infrared and Rahman spectra and inelastic neutron scattering data. The total VDOS calculated from the phonon dispersions for our ice structure is shown in Fig. 6.26. Also shown in Fig. 6.28 is the corresponding partial VDOS for both hydrogen and the oxygen atoms in the ice system. We note that these phonon DOS are not complete since the summation is not done over the whole Brillouin zone, but only in the [100] direction of the cubic symmetry. The distribution of the partial DOS is given by

$$g_{\alpha,k}(\omega) = \frac{1}{nd\Delta\omega} \sum_{\mathbf{k},j} |e_\alpha(k;\mathbf{k},j)|^2\, \delta_{\Delta\omega}(\omega - \omega(\mathbf{k},j)), \tag{6.8}$$

where $e_\alpha(k;\mathbf{k},j)$ is the α-th Cartesian component of the polarization vector for the k-th atom; n is the number of sampling points and d is the dimension of the dynamical matrix [165]. The total VDOS is calculated by summing all the partial contributions. Figure 6.26 shows the total VDOS together with the full phonon dispersion curves along the [100] direction. Also shown in Fig 6.27 is the enlargement of the intermolecular frequency range on which we superimpose the inelastic neutron-scattering spectra data extracted

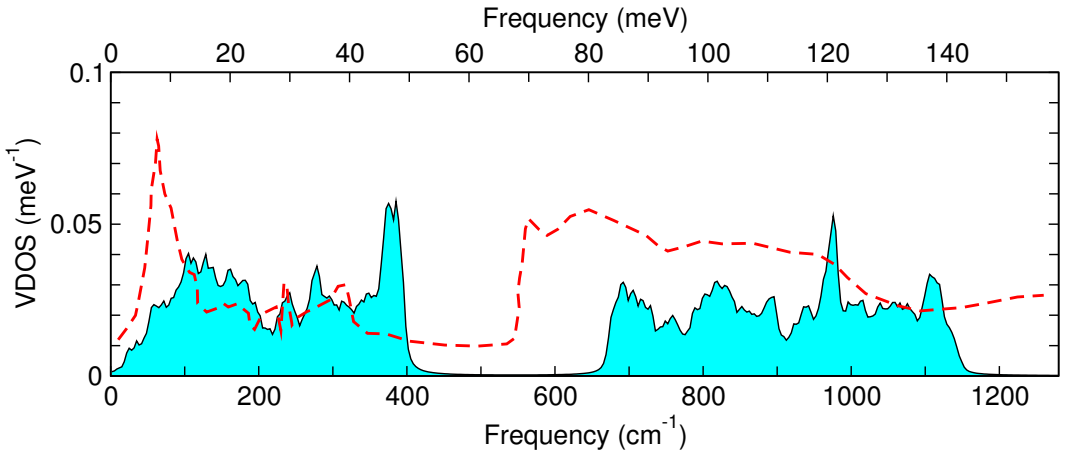

Figure 6.27: Enlargement of calculated total vibrational density of states in Fig. 6.26 showing the intermolecular range of frequencies. The broken line is the inelastic neutron scattering data available through ref. [11].

from Ref. [11]. The comparison is made with the ice Ih data though our ice structure is not perfectly hexagonal but still there is very little difference between the neutron data for ice Ih and ice geometry used in our calculation in the translational region as explained below. There are well defined separated peaks in the whole range of the vibrations. The illustrative discussion in Fig. 6.25 can be well understood if we consider the partial DOS in Fig 6.28. The covalently O-H stretching mode of both phase and anti-phase, analogous to the frequency ν_1 and ν_3 for isolated free water molecules, can be seen clearly in Fig 6.28(b) in the energy range (350-410 meV) or frequency range (3010-3400 cm^{-1}). We can notice that the collective motion of oxygen is almost static when compared to the collective contributions from the hydrogen atoms. According to the Rahman spectra, a strong peak is observed at 382.3 meV (3083 cm^{-1} at 95 K) [157,176] for D_2O. If we take into account the mass difference between deuterium and hydrogen atoms (i.e., isotope effect), the peaks which are observed at 2950, 3000 (very short), 3250, and 3270 cm^{-1} are in good range when compared to the experimentally observed values for ν_1 and ν_3. In the intra-molecular bending region, analogous to the frequency ν_2 for an isolated water molecule (1580-1680 cm^{-1}), there is an interesting feature. Our results show that, of all the contributions resulting from collective motion of hydrogen atoms as contribution from collective motion of oxygen atoms is recessive, only *one* of the components of the collective motions of hydrogen atoms contributes to the intra-molecular bending modes and it is one that is dominant. Figure 6.28(b) gives an example of such contribution being dominated mainly by the y-component of the intra-molecular vibration of the O-H. This means that intra-molecular bending of the angular motion takes place mostly in one direction.

Tanaka (1998) [177] has identified hydrogen-bond bending modes with negative expansion coefficients associated with this region (also see Appendix A.3). If we go further down to the low frequency region such as 600-1200 cm^{-1} called the molecular librational region and then (0-400 cm^{-1}) called the molecular translational region, where we estimated the

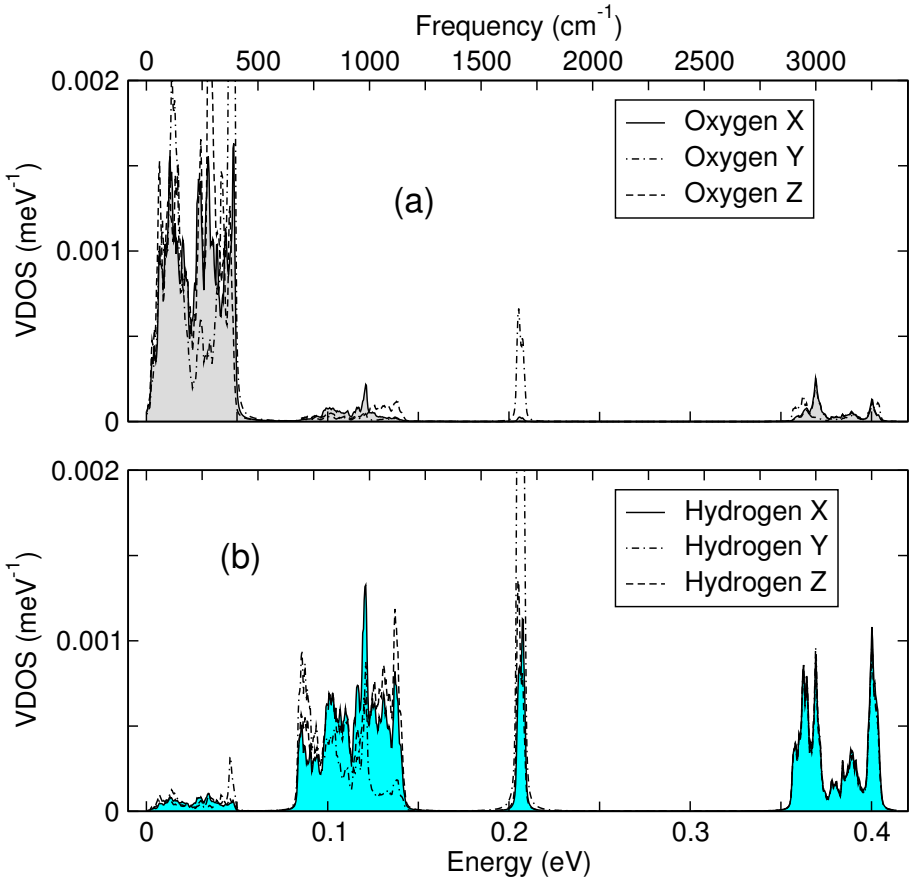

Figure 6.28: Partial density of states of ice based on the lattice dynamics. (a) shows the x, y and z components of VDOS for the oxygen atoms in the H_2O ice. (b) shows the x, y and z VDOS for corresponding hydrogen atoms for the whole range of frequencies. It is interesting to notice that in the intra molecular bending region (1580-1680 cm^{-1}), only one of the components of the VDOS of hydrogen (say y) dominates while x and z contribute less. The contribution from the oxygen atoms can be regarded as being completely recessive in this region.

sound velocities from the corresponding phonon dispersion curve, the VDOS peaks of these modes of vibration agree very well with the experimental observation from inelastic neutron scattering data. The general agreement of the features in the translational optic region is good with all the three distinct peaks present at 400, 270 and 105 cm^{-1} [171].

6.5.5 The boson peak in ice

Vitreous silica, or in general, glasses are amorphous solids, in the sense that they display elastic behaviour. In the crystalline solids, elasticity is associated with phonons, which are quantized vibrational excitations. Phonon-like excitations also exist in glasses at very high (10^{12} Hz)frequencies; surprisingly, these persist in the supercooled liquids. A universal feature of such amorphous systems is the boson peak (BP): The vibrational density of states or low-energy excitations are in *excess* compared to the Debye squared-frequency

law. The origin of this anomalous behaviour is still subject of scientific debates. There have been many experimental investigations to understand the dependence of this behaviour such as the densification of the system under consideration [178]. Also recently, there has been a theoretical study which tries to give a model of harmonic vibrations in topologically disordered systems based on the so-called Euclidean random matrix theory (see the Ref. [179]). The high frequency (0.1-10 THz) or energy (0.4136-41.36 meV)

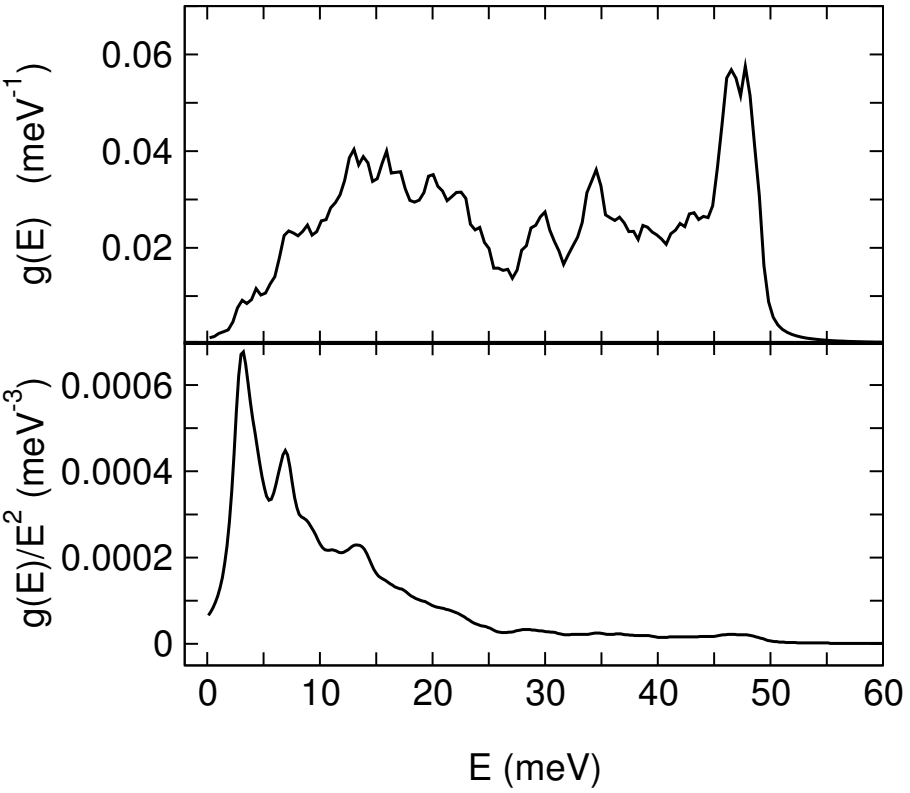

Figure 6.29: Plot of the VDOS $g(E)$ and the corresponding $g(E)/E^2$ vs. E for the region of translational mode. The boson peak is found in the low-energy region at 3.5 meV.

excitations has been experimentally shown to have linear dispersion relations in the mesoscopic momentum region ($\sim$ 1-10 nm^{-1}). A standard way of extracting the BP from the vibrational spectrum is to plot $g(E)/E^2$ (as done in Fig. 6.29(b)), since in the Debye approximation $g(E) \approx E^2$ at low energy. In Fig. 6.29 we show the plot of $g(E)$ and the corresponding $g(E)/E^2$ in the translational low energy range for the ice geometry in our calculation. According to the Debye law, it is expected that $g(E)/E^2$ should be constant for the whole range of energy. This constant relation is only obtained at energies larger than 40 meV in agreement with the experimental observation range for the BP as mentioned above. There is an anomalous sharp tall peak at 3.5 meV which can be ascribed to the region of low-energy *excess* vibrational excitation of the so-called BP. The reason for this peak is still not fully known since we have a crystalline structure for our ice geometry. The peak reveals the anomalous behaviour of hydrogen bonding in the crystal ice which

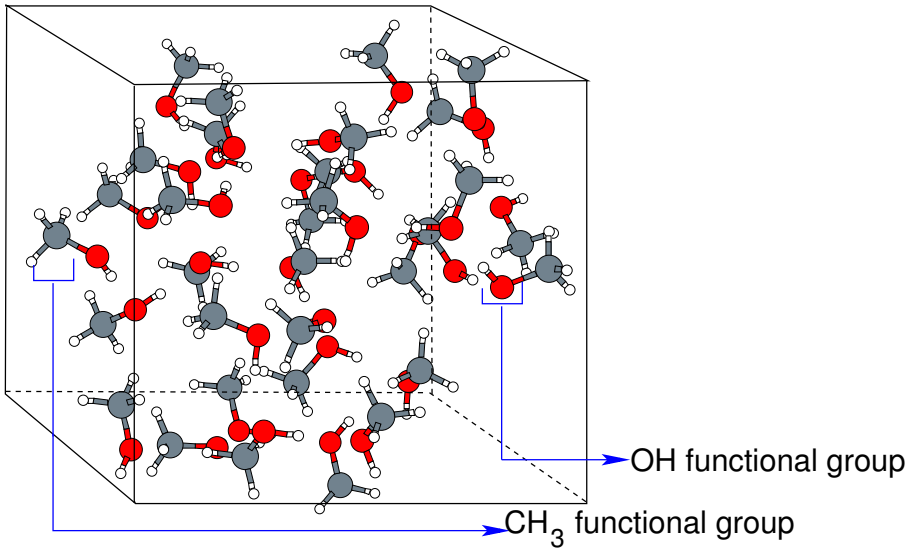

Figure 6.30: The simulation box showing 32 molecules of a liquid methanol. A methanol molecule consists of CH_3 (methyl) functional group covalently bonded with OH (hydroxyl) functional group.

shows similarity in the behaviour as in the results of an inelastic neutron scattering study of a crystalline polymorph of SiO_2 (α-quartz), and a number of silicate glasses (pure silica, SiO_2) with tetrahedral coordination [180]. Also amorphous solids, most supercool liquids and the complex systems show this anomalous character [181]. The origin of this anomalous behaviour of this abnormal peak in non-crystalline solids and supercool liquids is still subject of scientific debate.

6.6 Methanol structural properties

The molecular dynamics simulations results of both DFTB method and VASP on the structure of the liquid water at various thermodynamics conditions give a good idea of the effectiveness and accuracy of VASP method over the DFTB when compared the results with the experimental data. Methanol (CH3OH) is another important hydrogen-bonded liquid. Like water, methanol is used as a solvent in many common organic reactions including, in the modification of cyclodextrin derivatives. It is also an industrially important liquid because of its role in emerging fuel-cell technologies. The structure of liquid methanol has also been determined recently by neutron diffraction [182,183], again, making partial structure factors and radial distribution functions readily available for comparison with AIMD calculations. The AIMD simulation protocol employed 32 methanol molecules in a periodic box of length 12.93 Å in each direction as shown in Fig 6.30. Fig. 6.31 shows the computed partial radial distribution functions by using both the VASP and DFTB method compared to neutron scattering data (NSD). For this simulation, a time step of 1.0 fs was used. The whole length of simulation run was carried out for 1.5 ps. Though our obtained simulation data were not large enough to get rid-off the fluctuations in the RDF curves, nevertheless, the simulation results show the ability of both VASP

and DFTB methods in reproducing the experimental results of the hydro-carbon organic solvents, which forms a benchmark for calculations of other organic compounds such as cyclodextrins and their complexes as discussed in the next Chapter.

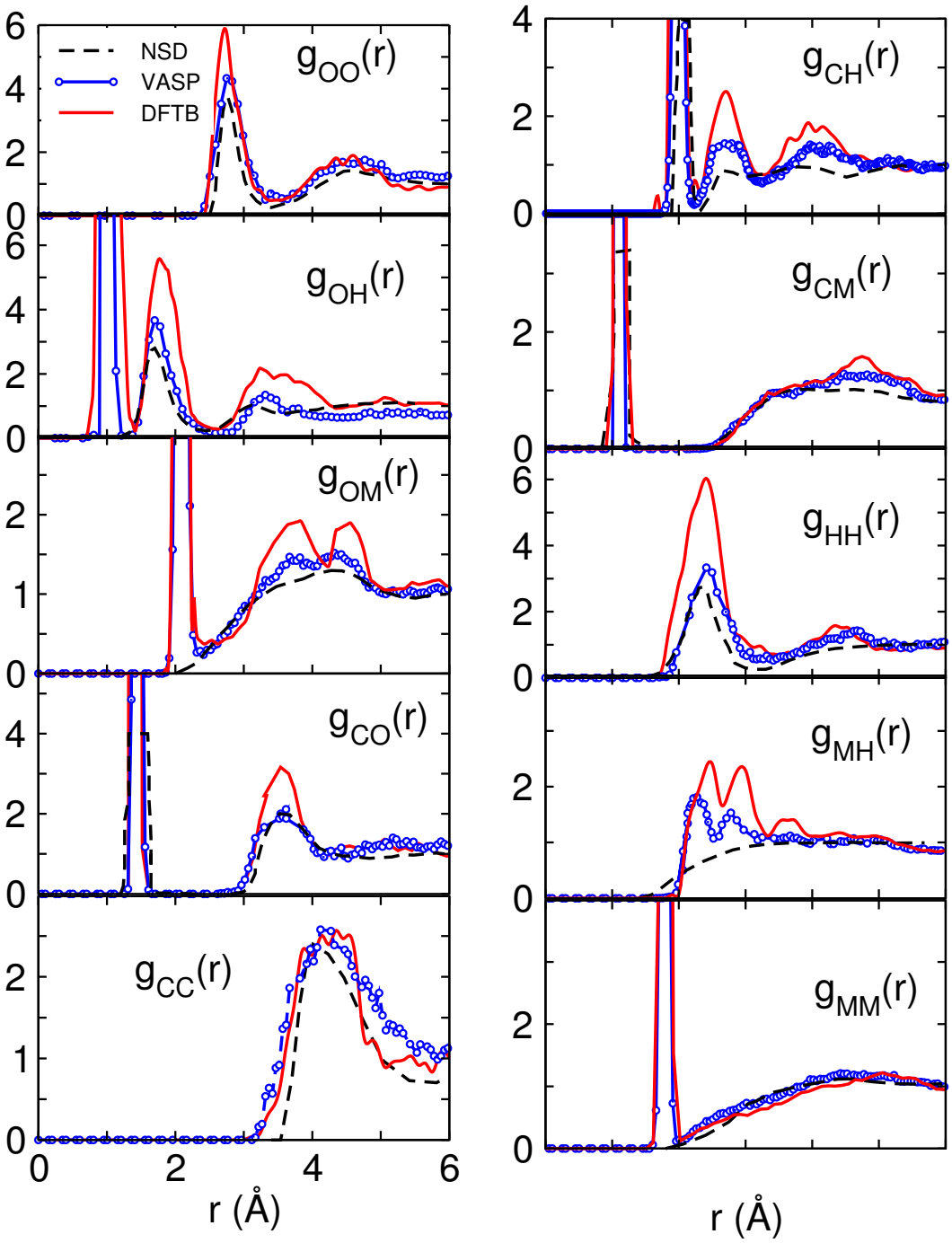

Figure 6.31: VASP and DFTB computed and experimental [182] (dashed line) radial distribution functions for liquid methanol at 300 K. The alcohol hydroxyl hydrogen is represented by 'H', while methyl hydrogens are denoted by 'M'.

7 A first-principles study of inclusion complexes of cyclodextrins

Here in this Chapter we present our results based on the application of density functional theory and *ab-initio* molecular dynamics to the inclusion complexes of cyclodextrins with the various guest molecules in water as the solvent which provides the driving force for the complexation. Some of the investigated guest compounds include phenol, aspirin, chromophore dye and the binaphtols. The very large number of atoms involved in these complex systems makes the computation to be too expensive especially for VASP and therefore restricts most of our investigations to be based on the use of the SCC-DFTB method which is a compromise between simulation of large system size, and the demand for accuracy simultaneously. In few possible cases VASP is used despite of its computational cost to check some of the results of DFTB, though some of them are still in good agreement with the experiments.

7.1 Introduction to cyclodextrins

Cyclodextrins (CDs) are water-soluble cyclic oligosaccharides composed of six (α-), seven (β-), or eight (γ-) units of D-(+)-glucopyranose units arranged in a truncated cone-shaped structure as shown in Fig. 7.1 and 7.2. The higher order of these compounds exist in nature but these mentioned three are the most prominent ones, they exist abundantly and have many important fascinating applications. These molecules were discovered about 100 years ago and are produced by degradation of amylose by glucosyltransferases, in which one or several turns of the amylose helix are hydrolyzed off and their ends are joined together to form cyclic oligosaccharides called cyclodextrins. Cyclodextrins are one class of the most fascinating naturally occurring molecular receptors to variety of

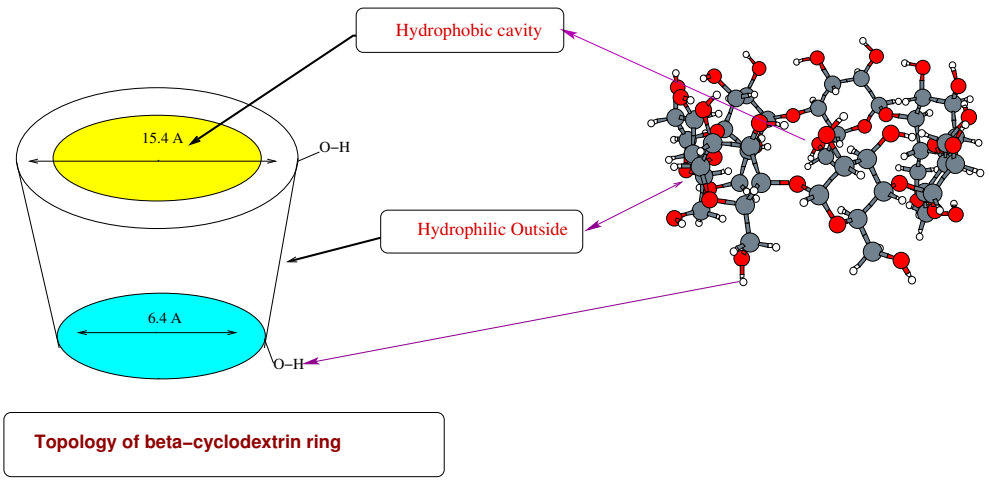

Figure 7.1: Topology of β-cyclodextrin.

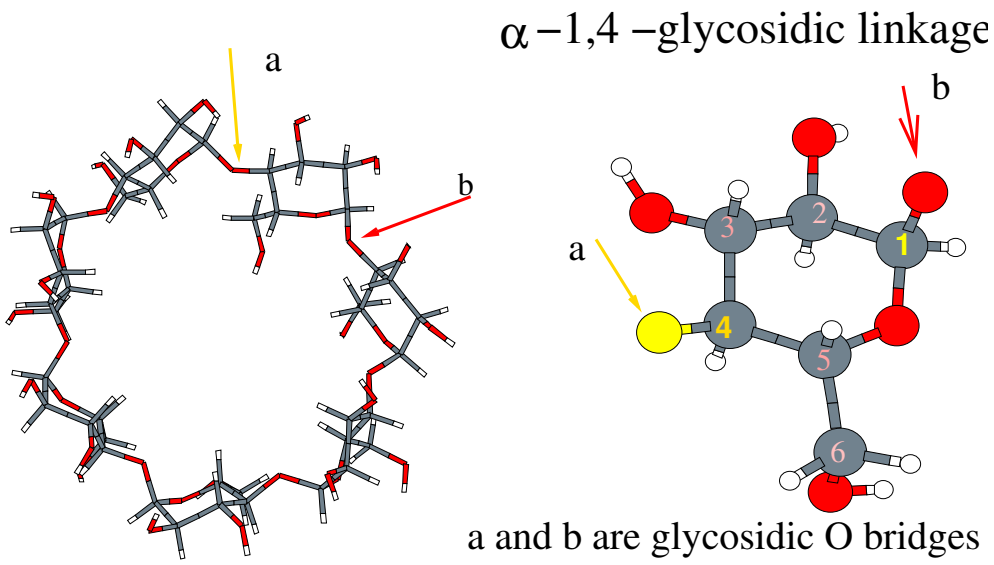

Figure 7.2: Glucose unit from cyclodextrin.

Table 7.1: Some physicochemical properties of cyclodextrins [191]

Property	α-CD	β-CD	γ-CD
no. of glucose units	6	7	8
empirical formula (anhydrous)	$C_{36}H_{60}O_{30}$	$C_{42}H_{70}O_{35}$	$C_{48}H_{80}O_{40}$
mol. wt (anhydrous)	972.85	1134.99	1297.14
cavity length, Å	8	8	8
cavity diameter, Å (approx)	∼5.2	∼6.6	∼8.4
heat capacity (ahyd. solid), J $mol^{-1}K^{-1}$	1153	1342	1568

inorganic and organic molecules, i.e., their internal hydrophobic cavity can host a large variety of organic and inorganic compounds to form a non covalent host-guest inclusion complex as shown Fig. 7.3. Their exterior, bristling with hydroxyl groups, is fairly polar, whereas the interior of the cavity is nonpolar relative to the exterior and relative to usual external environments, water in particular. The chemical reactivity [184, 185] and the spectroscopic properties [186] of the guest molecules are modified as a result of the inclusion. The internal hydrophobic cavity and the external hydrophilic rim of the chemically modified CDs render them ideal for modelling enzyme-substrate binding, drug delivery [187], catalysis [188], host-guest interaction [189], chiral separation and molecular recognition in self-assembled monolayer [190].

Table 7.1 lists some of the physiochemical properties of interest of the native CDs taken from reference [191]. The cavity dimensions given in the table are approximate, being composites resulting from a molecular modelling treatment of nearly 100 published X-ray structures of cyclodextrin hydrates and other complexes. We recall from Table 7.2

Table 7.2: Calculated dipole moments of cyclodextrins (in Debye, D)

Method	α-CD	β-CD	γ-CD
DFTB calculation (on anhydrous)	3.95	2.28	3.17
DFTB calculation (hydrated)	4.82	3.68	7.45
AMI calculation [a]	7.06	2.03	2.96

[a]Bako *et. al. 1994* [192]

that the cavity diameter narrows on proceeding from the secondary hydroxyl rim to the primary hydroxyl rim and within the cavity the van der Waals radii of the oxygens and hydrogens show further variability. Measured dipole moments of CDs have not been reported, but several calculated values are available. The results are highly variable. The calculations of Kitagawa, Sakurai and co-workers [193,194] are based on published X-ray crystal structures of CD complexes, and the resulting dipole moments are influenced by the guest. Very large moments in the range of 10-20 D, were obtained and they found that the CD cavity is highly polarized. Our calculation based on the DFTB method on the anhydrous cyclodextrins shows the dipole moment values of 3.95, 2.28 and 3.17 D for α-CD, β-CD and γ-CD, respectively. Bakó and Jicsinsky [192] used AMI calculations, the results are shown in Table 7.1. Botsi *et. al* [195] calculated two different values of dipole moments, 2.9 D and 14.9 D, for different orientation of the hydroxyl groups.
In general, the orientation of the functional groups in solution are influenced by the interaction with solvents. This may give rise to the intermediate value as reflected in the calculation done with the DFTB method on the hydrated β and γ-CD. Cyclodextrins are flexible molecules which are often studied experimentally in aqueous environments such as water because of their solubility [20]. They are found to crystallize in water hydrates of variable composition; α-CD is usually encountered as hexahydrate, α-CD.6H_2O, which can exist in crystal form I and II [196, 197], the third (III) has been crystallized from $BaCl_2$; β-CD exists as the undecahydrate, β-CD.11H_2O, and as the dodecahydrate, β-CD.12H_2O, but these integral ratios are idealizations, the actual composition depends on relative humidity; γ-CD is sometimes described as an octahydrate, but it can crystallize from 7 to 18 molecules of water; δ-CD with 9 glucose units, (not considered in this work) has been crystallized as δ-CD13.75H_20.
α-cyclodextrin (Form I) has two water molecules in the CD cavity and four molecules outside the cavity, the positions of the two included molecules are fixed by the hydrogen bonding to each other O(6) hydroxyl groups. Form II of α is reported to have one water inside the cavity while form three has 2.57 molecules distributed statistically over four sites [20, 191] with an occupancy of 0.64 per site. β-CD.12H_2O has 6.5 molecules of water among eight sites and γ-CD.13.3H_2O, has 5.3 waters distributed among the 13 sites according to the X-ray data results.

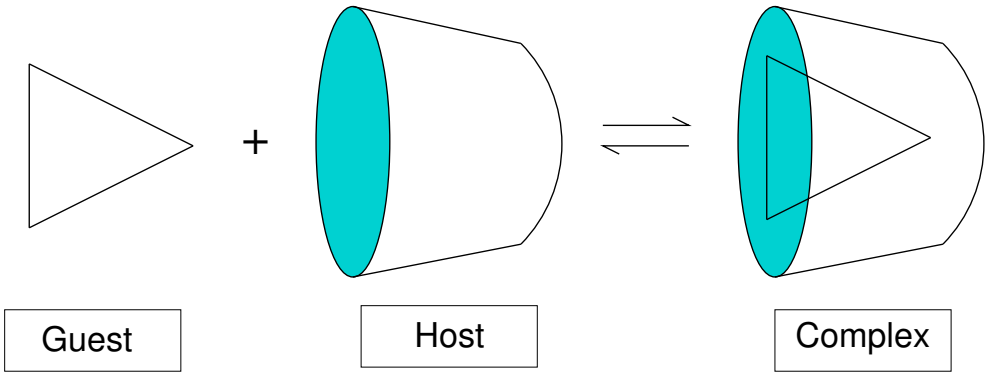

Figure 7.3: Inclusion of a guest within a cyclodextrin host to form a complex.

7.2 Some useful applications of cyclodextrins

The applications of cyclodextrins and derivatives are found to be growing fast in the pharmaceutical domain. In pharmaceutical industry, CDs have mainly been used as complexing agents to increase the aqueous solubility of poorly water-soluble drugs, and to increase their bio-availability and stability. In addition, they can be used to reduce or prevent gastro-intestinal or ocular irritation, reduce or eliminate unpleasant smells or tastes, prevent drug-drug or drug-additive interactions, or even to convert oils and liquid drugs into micro crystalline or amorphous powders. The ability of CDs to form complexes with a variety of organic compounds, helps to alter the apparent solubility of the molecules by increasing it and also, to increase their stability in the presence of light, heat and oxidizing conditions and to decrease the volatility of compounds through complexation. Cyclodextrins can also be used as processing aids to isolate compounds from natural sources and to remove undesired compounds such as cholesterol from food products. It has also been found useful in chemistry to enhance the sensitivity and selectivity of analytical methods. Also, CDs encapsulate rapidly deteriorating flavour substances, volatile fragrances, toxic pesticides, dangerous explosives, and, in some cases, gases. All of these applications involve inclusion in the CDs cavity. Therefore, a thorough understanding of the complexation process is important. Our main aim is to use the *ab-initio* simulation methods to study the structural behaviour of some of these host-guest complexes whose applications are well known in order to correlate the results with some of the experimental findings of induced circular dichroism. Most of the studies of these complexes were carried out with the DFTB method while in few cases VASP is used despite of its computational cost.

7.3 Inclusion complexes of cyclodextrins

Inclusion complexes of cyclodextrins with various organic guest compounds are usually studied both experimentally and theoretically. It is well known that the behaviour of these guests compounds changes when complexed with various cyclodextrins or its derivatives.

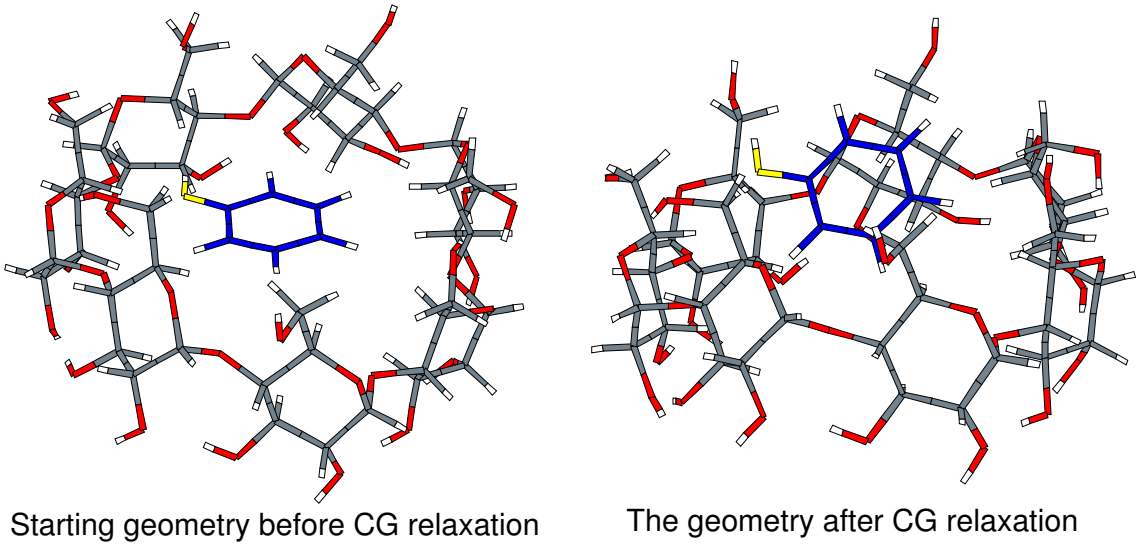

Figure 7.4: The geometry of phenol β-cyclodextrin complex showing the starting geometry of the complex before the DFTB CG relaxation is performed and after the CG relaxation. Water molecules are omitted for clarity. The starting geometry is flat inside the cyclodextrin but becomes inclined and partially included after the relaxation. The carbon and the oxygen atoms of phenol molecule are shown in blue and yellow colour respective for clear illustration.

In this work, we carried out the *ab-initio* study of various guest molecules complexed with cyclodextrins. Some of these guests compounds include hydroxyl benzene (phenol), pinacyanol chloride (organic dye), aspirin (acetylsalicylic acid) and a binaphthyl derivative (2,2'-dihydroxy-1,1'-binaphthyl).

7.3.1 Inclusion complex with phenol

Here we investigated the structural properties of a mono-substituted benzene (phenol, C_6H_5OH) complex with β-cyclodextrin in a supercell with periodic boundary conditions by means of molecular dynamics simulations. The trajectory for this complex was calculated by imposing a 1:1 host-guest stoichiometry with 50 molecules of water. The adduct of this compound with β-cyclodextrin is well known [198–200]. Phenol is included with its molecular axis strongly inclined according to the DFTB conjugated gradient (CG) result shown in Fig.7.4 and MD performed at 300 K shown in Fig.7.5. The $g(r)$ shown in Fig. 7.6 indicate the formation of hydrogen bonds between the hydroxyl groups of the top torus in the BCD and O atom of the guest molecule. These findings are compatible with the observations of Kamiya *et. al.* [200] according to whom the phenolic hydroxyl group is reluctant to enter the hydrophobic BCD cavity and remains in the vicinity of the top torus with some preferred orientation. The phenol axis is strongly inclined at an average angle $\theta = 55^\circ$ as shown in Fig. 7.5 according to the result of DFTB MD simulation performed at 300 K for 800 fs with a time step of 0.5 fs to further investigate the result of CG relaxation. The starting geometry for the MD simulation was taken from the relaxed

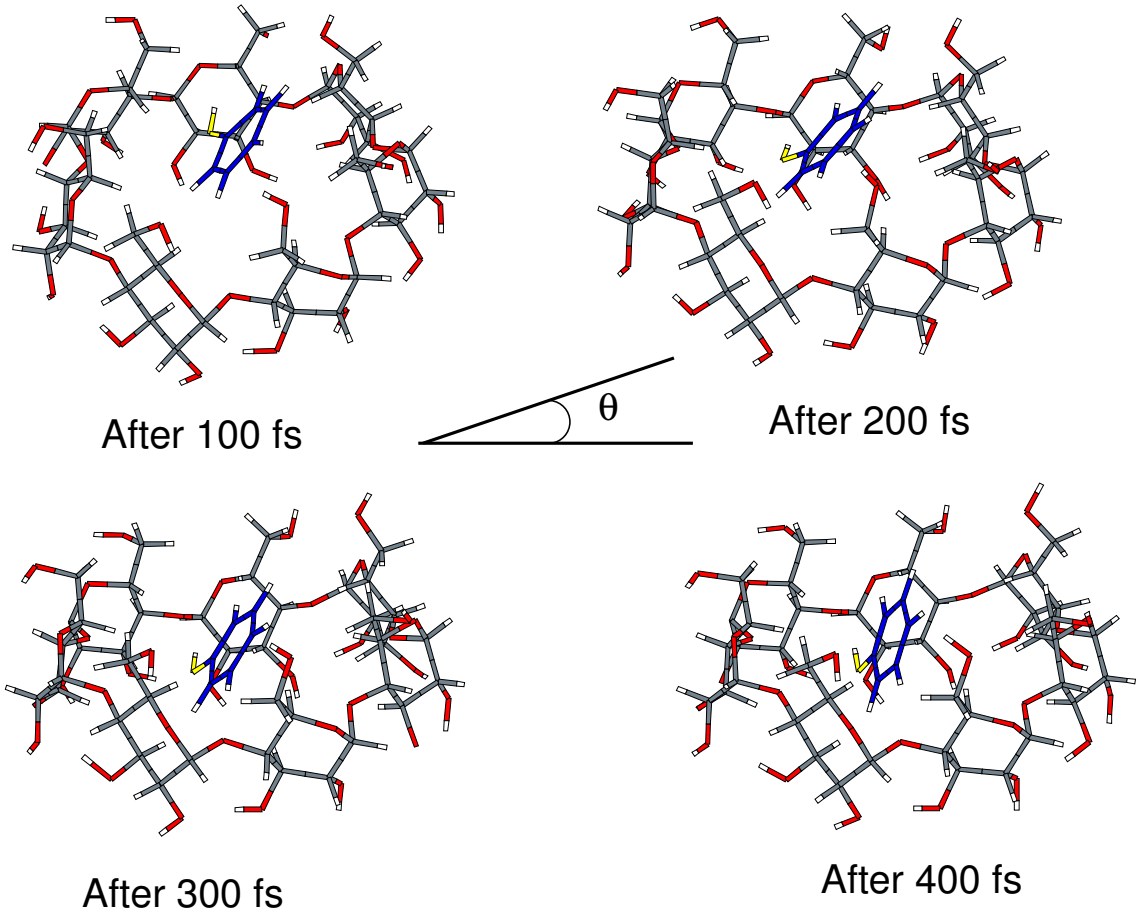

Figure 7.5: The geometry of the phenol β-cyclodextrin complex showing the results of molecular dynamics simulation performed on the relaxed structure obtained by CG relaxation shown in Fig 7.4. The angle θ illustrates the inclination of molecular axis of phenol with the equatorial surface of β-cyclodextrin. Water molecules are omitted for clarity. The carbon and the oxygen atoms of phenol molecule are shown in blue and yellow colour respective for clear illustration.

geometry of CG in Fig. 7.4. The result of circular dichroism data [200] reports the values of 27.5° for the inclination angle of the symmetry axis of phenol from the cavity axis.

7.3.2 Inclusion complex with aspirin

Aspirin (acetylsalicylic acid) is a phenolic acetate ester which was introduced by Bayer to the world's market about 100 years ago [201]. It is a well-known molecule with a number of pharmaceutical applications. It's synthesis was first described by Gerhardt in 1853. The drug has its origins in the salicylates and glycosides of Willow Bark which has a long history of use in the treatment of rheumatic conditions [202]. The molecular formulae of aspirin compound is $C_9H_8O_4$. The known structure, containing a non-planar conformer as shown in Fig. 7.7, has been compared to a number of other low energy structures, many based on a planar conformer [203]. Ignoring rotation of the methyl groups, aspirin

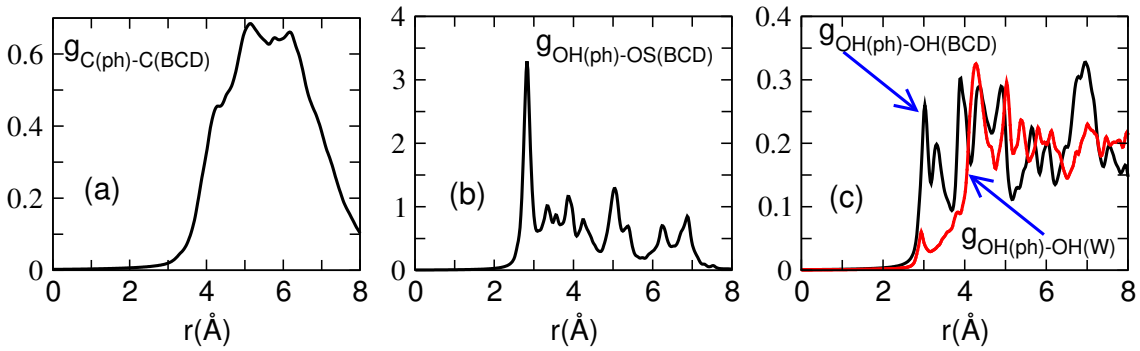

Figure 7.6: Radial distribution functions of a complex formed by β-cyclodextrin-phenol. (a) shows the phenol carbon-BCD carbon RDF. There is a broad peak at around 5 Å which shows that the phenol molecule is located at the central portion of the axis of entry. (b) shows the phenol hydroxyl oxygen(OH)-BCD glycosidic oxygen RDF. The first peak at around 2.8 Å can be compared to the first peak of $g_{OO}(r)$ of the bulk liquid water discussed in the previous Chapter which signifies the formation of the hydrogen bond as OH of phenol partially points towards one of the glycosidic oxygen. The rest of the peaks shows the relative distances of the OH of phenol to the other glycosidic oxygen atoms of BCD. (c) contains the RDFs of phenolic hydroxyl(OH)- water (OH). There is a small peak appearing at around 3.0 Å for the OH(ph)-OH(W). Exactly at the same position above this peak, there is a OH(ph)-OH(BCD) peak which shows the hydrogen bond formation between the solvent water and the phenolic hydroxyl group and also the hydroxyl group of BCD and that of phenol. The rest of the peaks shows the relative distances of other OH groups in water and in the BCD.

has three dihedral angles that could vary. These are denoted by τ_1, τ_2 and τ_3 as shown in Fig. 7.7. It is well known from the experiment that *only* unionized aspirin forms stable (1:1) inclusion complexes with the various β-cyclodextrins. Nuclear magnetic resonance (NMR) studies on both unionized and ionized form of aspirin have shown that that in the complex the benzene ring is located well inside the cavity with the acetyl ester group protruding from the cavity for the unionized complex, while the ionized complex failed to form any complex with the β-cyclodextrin according to the same NMR results [25].

Our *ab-initio* investigation with the DFTB method on aspirin with β-cyclodextrin shows the formation of a stable complex shown in Fig. 7.8 in agreement with the predicted orientational geometry in the cavity of BCD. In our study, we carried out the molecular dynamics simulation of this complex in 50 molecules of water with a time step of 0.5 fs. A periodic cubic cell of dimension $17.4 \times 17.4 \times 17.4$ Å^3 was used. Two temperatures, 300 and 338 K were considered during the runs. We monitored the dynamic evolution of three important dihedral angles τ_1, τ_2 and τ_3 as mentioned above. Also, measured during the molecular dynamics simulation is the weak intramolecular hydrogen bond which gives extra stability to the aspirin complex. The result at 300 K shows that the OH length in Fig. 7.9 (a) equilibrates at a distance of 2.23 Å, which means there is formation of a hydrogen bond which stabilizes the complex in the hydrophobic cavity of β-cyclodextrin. The formation of this bond is possible as a result of bond rotation τ_1 which also decreases drastically from the initial value of about 125° to about 50° according to Fig. 7.9(b). τ_2 decreases to about 10° from its initial angle of 25° as shown in Fig. 7.9(c) while τ_3 equilibrates to about 163° from staring angle of about 160°. These decreases of dihedral

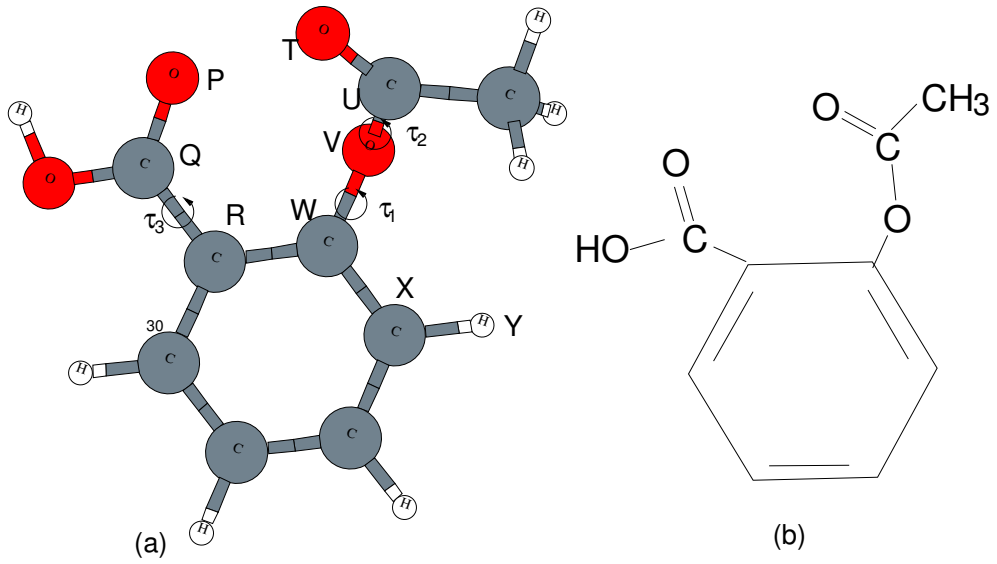

Figure 7.7: Molecular structure of aspirin. (a) and (b) are equivalent geometries. (b) is the skeletal structure of (a). Labels O, C and H denote oxygen, carbon and hydrogen atoms. Also, τ_1 represents the dihedral angle UVWX, τ_2, TUVW and τ_3, PQRS according to the label.

angles make possible the formation of this weak intramolecular hydrogen bond within the cavity of the BCD and hence adds to the extra stability of the complex. When the temperature is increased to 338 K, the initial structure is almost preserved as there is no change of hydrogen formation between the carboxylic group and the hydroxyl group of the carbon atom. This is because the τ_1, τ_2 and τ_3 bond rotations are restricted to the initial geometrical angles of 125°, 20° and 175°, respectively, as shown in Fig. 7.9(b), (c) and (d). The restriction of the angles by this temperature keeps the length OH in Fig. 7.9(a) fixed at the initial starting geometry at 0 fs.

Apart from these geometrical fluctuations of the length and the dihedral angles, we also analyse the radial distribution functions of this complex at 300 K as shown in Fig. 7.10. Figure 7.10(a) shows the RDF between the oxygen atoms of water molecules and all the oxygen atoms of the aspirin $g_{\mathrm{OW-Oasp}}$, together with this plot is, the RDF of the oxygen atoms of the water molecules ($g_{\mathrm{OW-OW}}$). The peak of $g_{\mathrm{OW-OW}}$ is around 2.82 Å which compares well to the values observed for bulk liquid water. The peak of $g_{\mathrm{OW-Oasp}}$ is narrower and a little bit shifted to the left to around 2.78Å. The O-O peaks of aspirin and water show the formation of hydrogen bonding which tends to add to further stabilization of aspirin in the hydrophobic cavity of β-cyclodextrin during the formation of the complex. Figure 7.10(b) shows the RDF of the carbon atoms of aspirin and the carbon atoms (C′) of BCD. The broad peak is around 5.5 Å. The range of distance distribution shows the formation of the complex with total encapsulation in the center of BCD. Figure 7.10(c) shows the RDF between the oxygen atoms of aspirin with the double bond (=O) and the hydroxyl group (OH') of BCD denoted by $g_{\mathrm{O=asp-OH'}}$, together with this also is the plot of RDF of glycosidic oxygen (OS) of BCD and the hydroxyl oxygen of aspirin denoted by $g_{\mathrm{OS-OH}}$. For each curve, the $g(r)$ exhibits a broad peak at distances $r \approx 4$ and 4.5

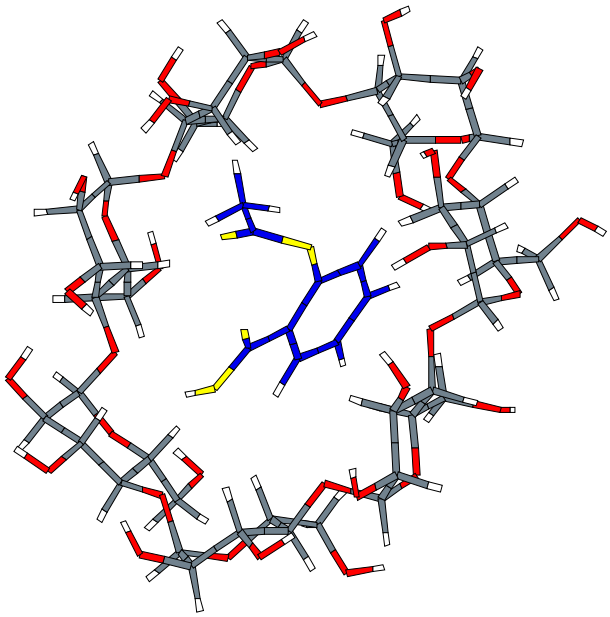

Figure 7.8: Relaxed geometry of the aspirin-β-cyclodextrin complex calculated using the conjugated gradient method relaxation of the DFTB code. Water molecules are not shown for clarity. There is slight puckering of the BCD ring due to its flexibility to allow proper encapsulation of the aspirin guest inside the ring of BCD. The carbon and oxygen atoms of aspirin are coloured differently for easy identification.

Å, respectively. The behaviour shows the formation of the adduct between the host and guest molecules.

7.3.3 Inclusion complex with organic dyes

Organic dyes are molecules with an extended π-electron system which interact with electromagnetic radiation in the UV/Vis range with absorption occurring when energy quanta correspond to the energy gap between the ground ($|0\rangle$) and one of the excited states ($|n\rangle$). The UV and visible absorption spectra of a variety of π-electron chromophores have been extensively studied and utilized for the acquisition of chemical information [204]. When dye dimers or oligomers are subject to electromagnetic radiation, the UV/Vis (and possibly CD) spectra show changes that may be interpreted as chromophore-chromophore interaction [204, 205]. The excitonic interaction between two chromophores a and b splits the excited state ($|n\rangle$) into two energy levels. The energy gap $2V_{ab}$ which corresponds to the energy absorbed, D^+ -D^-, is called Davydov splitting shown in Fig. 7.11. Dye monomer and dimer inclusion compounds in cyclodextrin cavities have been previously studied using molecular mechanics technique to investigate the stability of these complexes [206]. The chromophore of interest for our present study is pinacyanol chloride. This dye otherwise known as bis-(N-ethyl-2-quinolyl)-trimethinium chloride is shown in Fig. 7.12. The two identical quinolyl units are connected by a trimethine bridge, CH-CH-CH. This compound has received attention because of its application as a saturable absorber, mode-locker, and sensitizer in imaging technology [206]. In this study we present

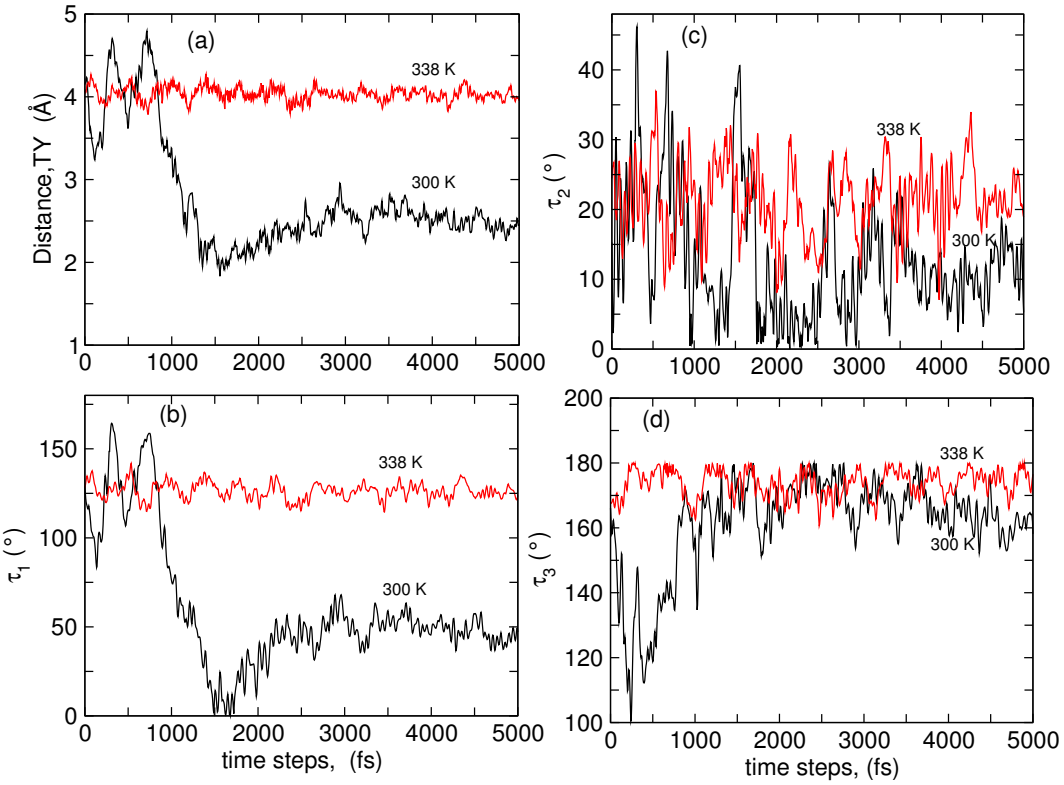

Figure 7.9: Evolution of (a) weak intramolecular hydrogen bond between carboxylic oxygen and the hydrogen of OH group of the neighbouring carbon atoms, (b) dihedral angle UVWX (τ_1), (c) dihedral angle TUVW (τ_2) and (d) dihedral angle (τ_3) PQRS according to the label in Fig 7.7 at two different temperatures.

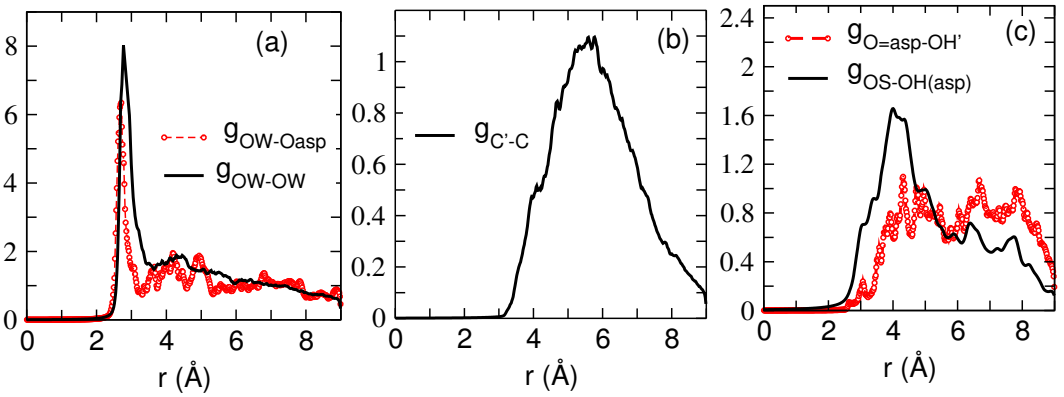

Figure 7.10: Radial distribution functions computed for the complexes of the BCD with aspirin at 338 K. (a) RDF between the oxygen atoms of water molecules and all the oxygen atoms of the aspirin $g_{\mathrm{OW-Oasp}}$, together with this plot is, the RDF of the oxygen atoms of the water molecules ($g_{\mathrm{OW-OW}}$). (b) RDF of the carbon atoms of aspirin and the carbon atoms (C′) of BCD. (c) RDF between the oxygen atoms of aspirin with the double bond (=O) and the hydroxyl group (OH$^{p}rime$) of BCD denoted by $g_{\mathrm{O=asp-OH'}}$; together with this also is shown the plot of RDF of glycosidic oxygen (OS) of BCD and the hydroxyl oxygen of aspirin denoted by $g_{\mathrm{OS-OH}}$.

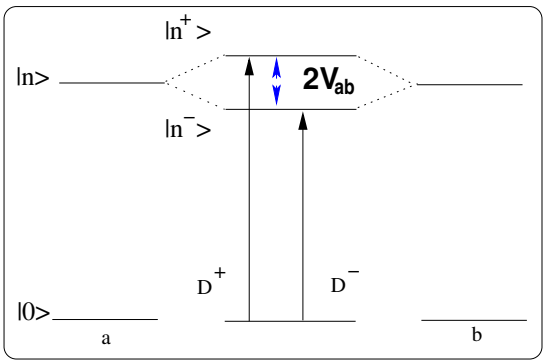

Figure 7.11: Schematic energy diagram of the excitonic (Davydov) splitting.

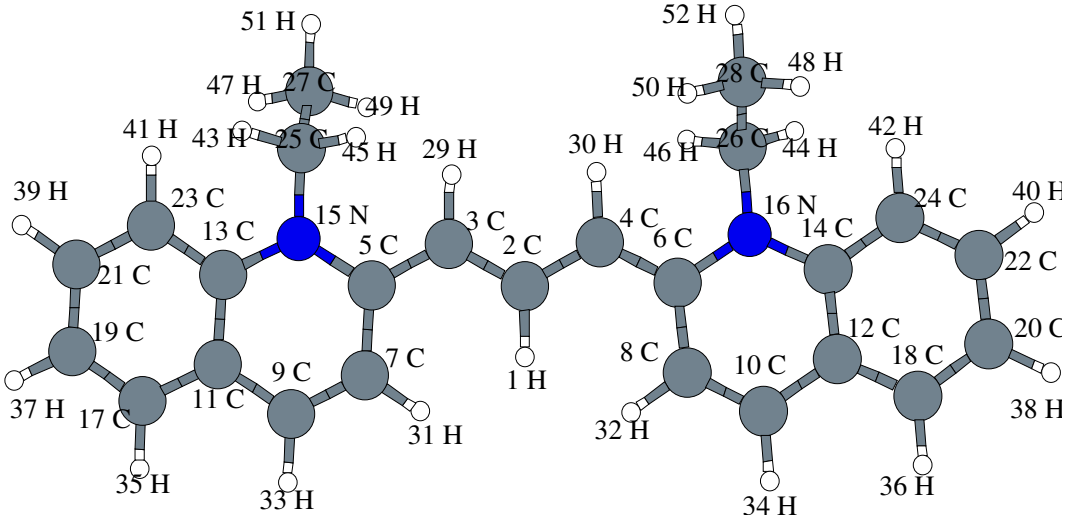

Figure 7.12: Pinacyanol chloride dye.

the results of structure optimization and molecular dynamics simulation for the pinacyanol dimers in water and γ-cyclodextrin-pinacyanol inclusion complexes.
The calculations in this work were performed in three steps by using the DFTB method:

i. Geometry optimization of the dye monomer.

ii. Optimization and dynamics of the complexed dye dimer in water.

iii. Optimization of the cyclodextrin-complexed dimer with some water droplets.

The starting geometry for γ-cyclodextrin, 'SIBJAO', was taken from the Crystallographic Database [207]. The optimization of the pinacyanol dye monomer was first carried out using the conjugate gradient (CG) mode of the DFTB code, with the background charge set to -1 so that the whole system charge was zero. After relaxation the pinacyanol monomer has a twisted geometry, (symmetry C_2) with both dihedral angles N15-C5-C3-C2 and N16-C6-C4-C2 equal to 173°. This twist confirms the non-planar geometry of the isolated unit of pinacyanol dye in its ground state as shown in Fig. 7.13. The calculated twist with DFT/B3LYB and a 6-31G** basis is 172° (K. Kolster, unpublished). The

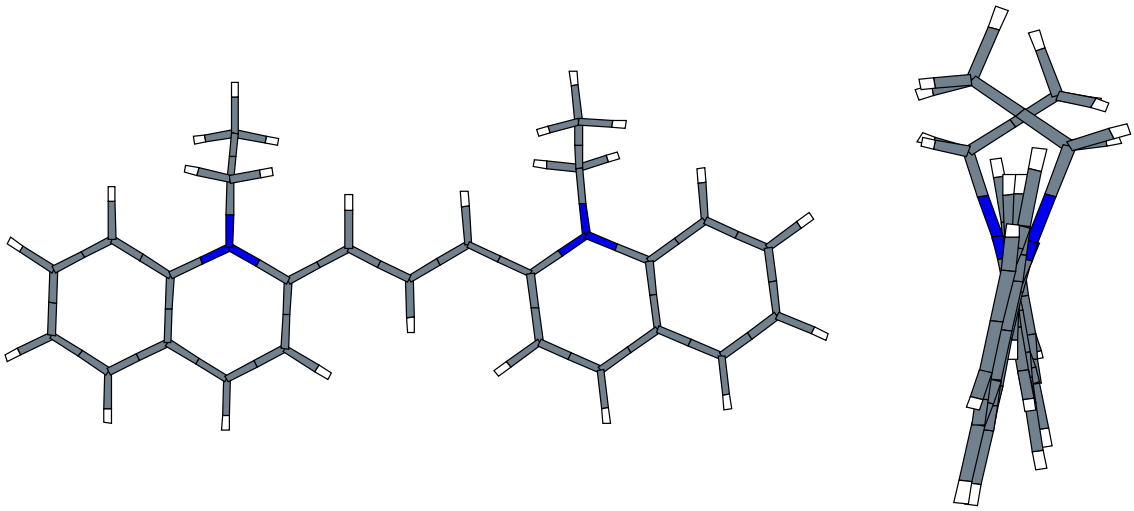

Figure 7.13: Geometry of the pinacyanol dye after optimization (Left: front view, right: side view).

pinacyanol dye dimer was constructed from the optimized monomer of Fig. 7.13. To choose the starting geometry of the dye dimer and the dye dimer-γ-cyclodextrin system, two alternatives for the relative orientation of the dye monomer are possible (although more are conceivable) [206]. These alternatives are schematically shown in Fig. 7.14. In

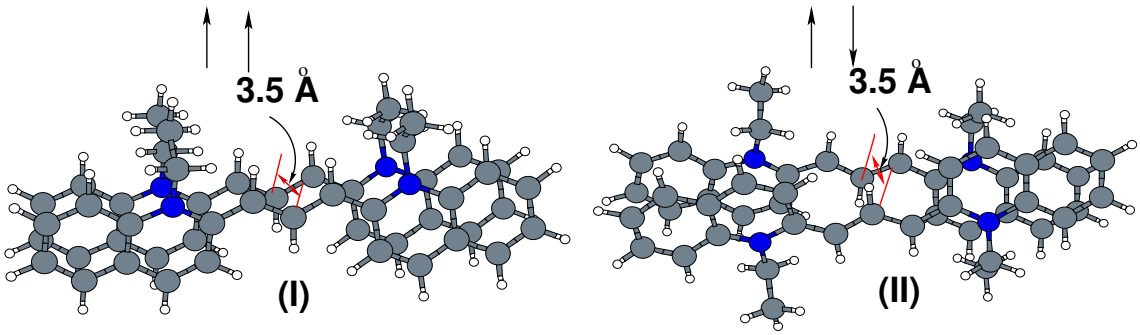

Figure 7.14: Dimers (I with diethyl groups placed parallel, II anti-parallel).

(I), the monomers are aligned parallel (highest possible symmetry C_{2v}), in (II) they are antiparallel (C_{2h}). In the latter, there is less steric repulsion of the ethyl groups since they are on opposite sides of the complex. The initial distance between the two monomer units was taken to be 3.5 Å, which is close to the distance between the neighbouring layers in graphite. The arrangements (I) and (II) were allowed to relax in a simulation box containing eighty molecules of water. For the complexed dimer the cyclodextrin ring was located at the central portion of the methine chain of the dye, and the total system was then optimized with a few droplets of water molecules. The variation of geometry and relative orientation of the two monomers in the uncomplexed dimer and the dimer included in cyclodextrin was followed during the calculation by measuring the dihedral angles N15-C5-C3-C2 and N16-C6-C4-C2 of each monomer unit and the angles between

the planes of the dimer which is the twist of the planes with dihedral angles (C21-C22-C22′-C21′) or (C19-C20-C20′-C19′) (the prime on the labelled atom indicates the second identical monomer unit; we make reference to Fig. 7.12 for labeling the atoms). This twist was set to zero at the start of the relaxation and changed in response to the CG relaxation as can be seen in Tables 7.3 and also for the changes in dihedral angles of individual monomer units of the dimer as shown in Table 7.4. Molecular dynamics

Table 7.3: The twist of the planes measured along planes between the line C21-C22 for the first monomer and C22′-C21′ for the second monomer. It is also repeated for C19-C20 and C20′-C19′ for comparison. Refer to Fig. 7.12 for labeling of the atoms. The results were taken after the CG relaxation.

	C21-C22-C22′-C21′	C21-C22-C22′-C21′
Uncomplexed dimer↑↑	-3.2	-2.9
Uncomplexed dimer↑↓	-6.3	-6.5
Dimer↑↑ in γ-CD	2.7	1.9
Dimer↑↓ in γ-CD	12.2	12.9

simulations were performed at a fixed temperature, 300 K, with a time step of 0.5 fs starting from the optimized geometry of step (iii) listed above to see the evolution of the twists of the planes of the dimers in the simulation box of water, since there are little noticeable changes in this structure after the CG relaxation as can be seen from Table 7.3, which corresponds to the starting structure for MD shown in Fig. 7.16 and 7.17. In the dimer, these dihedral angles change both in water and in the cavity of cyclodextrin

Table 7.4: The two major dihedral angles C15-C5-C3-C2 and C16-C6-C4-C2 for the first monomer unit of the dimer taken after CG relaxation. Refer to Fig. 7.12 for labeling of atoms.

	C15-C5-C3-C2	C16-C6-C4-C2
Uncomplexed dimer↑↑	175.8	171.2
Uncomplexed dimer↑↓	171.1	-179.5
Dimer↑↑ in γ-CD	169.2	166.6
Dimer↑↓ in γ-CD	165.0	162.4

with the anti-parallel arrangement in which there is less steric repulsion of ethyl groups, showing a larger change (from 180°) inside the cavity of cyclodextrin, as can be noticed in Tables 7.3 and 7.4 and in Fig. 7.15. The results which are reported in Tables 7.3 and 7.4 were taken after the CG relaxation. Table 7.4 shows the twist (change from zero degree) observed in the dimer. The CG relaxation data presented in these Tables serve as the starting structure for the MD simulation runs. Figures 7.16 and 7.17 show snapshots after a MD simulation time of 600 fs of the pinacyanol dyes for arrangements (I) and (II) in water with parallel and anti-parallel orientations of the monomers. The water molecules are omitted for clarity of view. The evolution of the distance between the monomers and the twist of the planes of the dimer against each other during the MD simulations

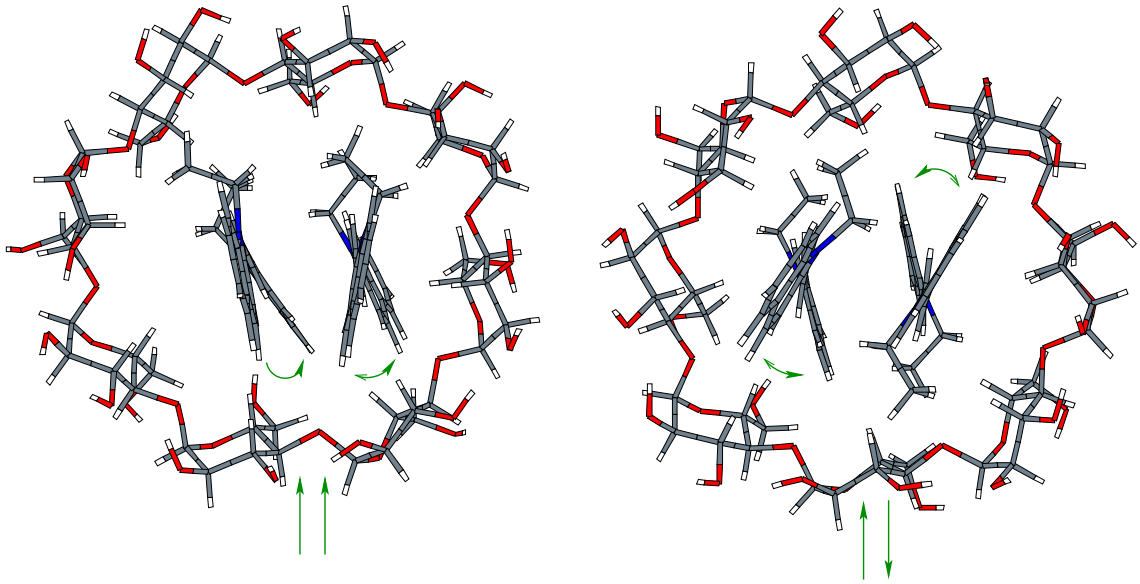

Figure 7.15: Geometry of the pinacyanol dimer-cyclodextrin complexes after relaxation, showing that the monomers in the anti-parallel dimer are distinctly more twisted than in parallel dimer. Water molecules are not shown.

are shown in Figs. 7.18 and 7.19 for both parallel and anti-parallel arrangement of the diethyl groups. The monomers in arrangement (I) move closer with an average distance of 3.25 Å and the distance between the two monomers centers (C2-C2′) of this arrangement fluctuates non-uniformly during the 600 fs MD simulations as shown in Fig. 7.18(a). The non-uniform fluctuation is due to the steric repulsion of the ethyl groups leading to an instability of the average distance. The monomers in arrangement (II) move apart non-uniformly at the beginning of the molecular dynamics simulation and equilibrate at a distance of about 4.45 Å as shown in Fig. 7.18(b). The twists (C21-C22-C22′-C21′ and C19-C20-C20′-C19′) in the planes of the dimer show an increase with MD time steps in both arrangements (I) and (II) as can be seen in Figs. 7.19(a) and (b). The geometry linked fluctuations suggest the specific mode of interaction between the monomer units of the pinacyanol dye. This interaction as measured by the twist between the planes of the monomer units, as calculated from C21-C22-C22′-C21′ and (C19-C20-C20′-C19′), can be related to the experimental observation of the UV/CD spectra of the chromophores in which there is a split of the excited states of the monomer units as previously described above.

7.3.4 Inclusion complex with binaphthyl compound

Binaphthyl (BNP) compounds are sources of the most important family of auxiliaries, ligands and catalysts employed in the enantioselective reactions. Optically pure binaphtols have been extensively used as chiral auxiliary reagents for a variety of asymmetric reactions [208]. The inclusion complex of these compounds with the three prominent cyclodextrins (α, β and γ) have been experimentally studied by absorption, induced

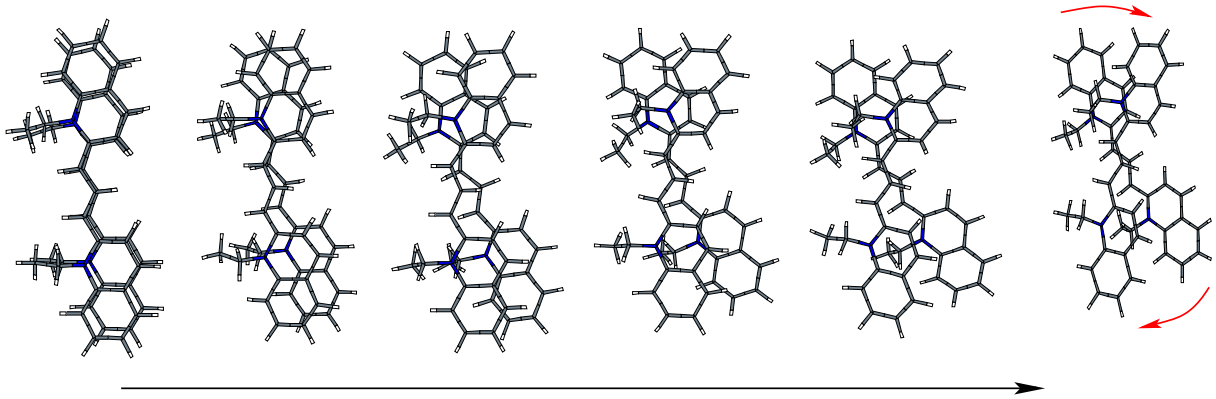

Figure 7.16: Snapshots of the 600 fs movie of the uncomplexed parallel pinacyanol dimer. Water molecules are omitted.

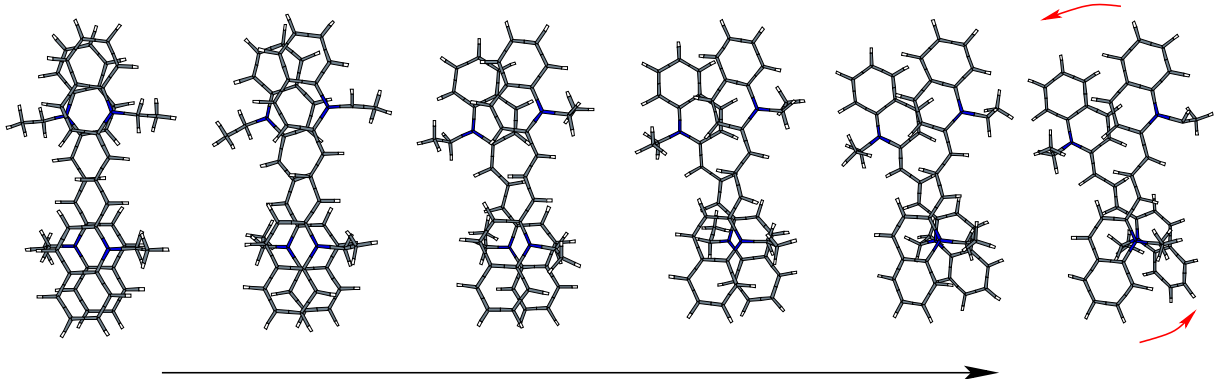

Figure 7.17: Snapshots of the 600 fs movie of the uncomplexed anti-parallel pinacyanol dimer. Water molecules are omitted.

circular dichroism (ICD), fluorescence spectroscopy and triplet-triplet absorption spectroscopy [209]. Our present study tends to interpret the ICD behaviour in the light of the complex structures obtained by *ab-initio* molecular dynamics approach in order to offer information on these complexes.

Of particular interest of these binaphthyl derivatives studied in our present work, is 2,2'-dihydroxy-1,1'-binaphthyl. This is a chiral molecule which exits in enantiomeric form as shown in Fig. 7.20. The second (S) enantiomer was obtained by simple reflection of the first one (R)· The conjugated gradient relaxation during the DFTB calculations shows that both the R- and S-BNP preferred a **twisted** geometry of the aromatic planes to perpendicular planes as shown in Fig. 7.20. The twisted geometry has the energy lowered by about 0.034 eV compared to the perpendicular geometry. The calculation was confirmed by performing investigations with VASP, which also show a lower energy difference in favour of the twisted geometry with dihedral angles Φ(C5-C8-C17-C21) equal to 67.3° and -67.3° for R- and S-BNP, respectively, while the DFTB method yields respective dihedral angles of 63.4° and -63.4°. Also measured from the DFTB calculations were the angle Φ(C21-C17-C8-C5) = $\Phi_{211'9'}$ and bond length C17-C8 (=C1-C1′) connecting the two bi-

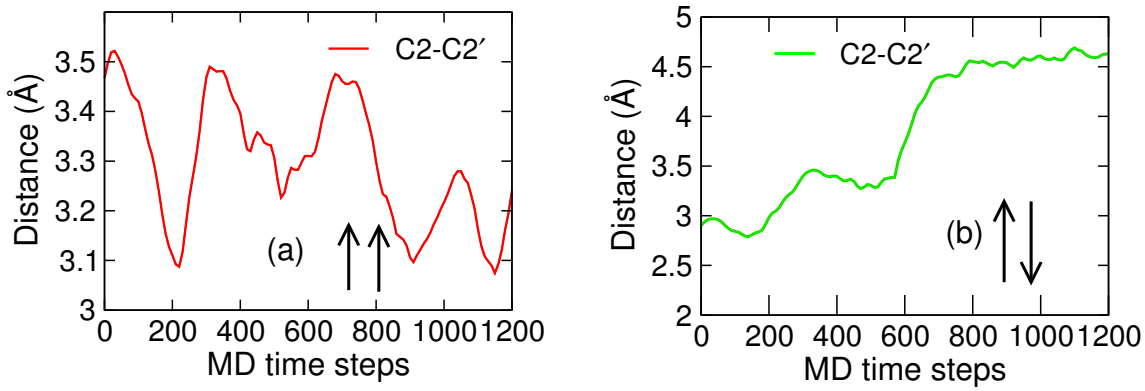

Figure 7.18: (a) Plot of the distance between the centers of the monomer units in the uncomplexed **parallel** dimer as a function of time. (b) Plot of the distance between the centers of the monomer units in the uncomplexed **anti-parallel** dimer as a function of time.

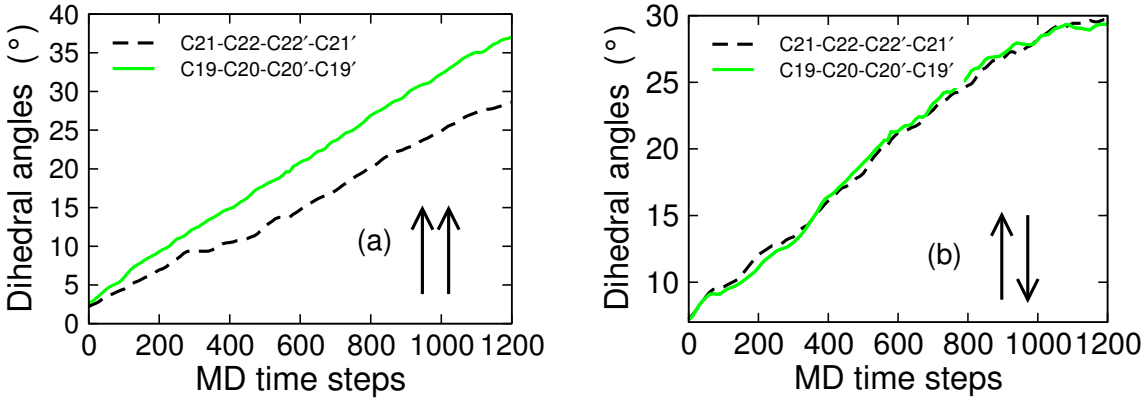

Figure 7.19: (a) Plot of the dihedral angles (C21-C22-C22′-C21′ and C19-C20-C20′-C19′) between the monomer units in the uncomplexed *parallel* dimer as a function of time. (b) Plot of the dihedral angles (C21-C22-C22′-C21′ and C19-C20-C20′-C19′) between the monomer units in the uncomplexed **anti-parallel** dimer as a function of time.

phenyl planes as 117.6° and 1.4869 Å, respectively, for the twisted (or bend) conformation (use Fig. 7.21 for reference labelling or Fig. 7.22) showing the relaxed twisted geometry of S-BNP. After this, the geometry optimization of S-BNP inside β-cyclodextrin was investigated. We considered the different topologies of entry of the guest molecules (S-BNP) inside the host (BCD) in order to search for the possible minima of the complex. The trial orientations of S-BNP inside BCD were done according to Fig. 7.23. S-BNP was inserted from both the primary wider end (shown) and the secondary narrower ends (not shown) in a longitudinal (axial) and transverse (equatorial) direction according to the same illustration diagram A and B of Fig. 7.23. We focused our attention first on the calculation of the inclusion complex of S-BNP using the DFTB method. The conjugate gradient relaxation of (A) and (B) according to Fig. 7.23 was carried out and the energy of both were compared. This is then followed by the MD simulation in vacuo without periodic boundary conditions at room temperature starting from the optimized geometry

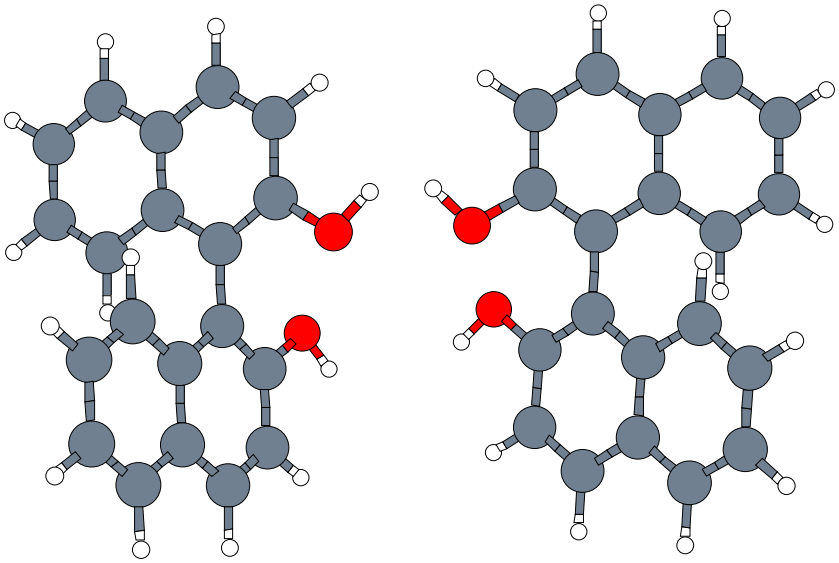

Figure 7.20: Enantiomeric pair of binaphthyl (R and S, R = “rectus”-right, S = “sinister”-left).

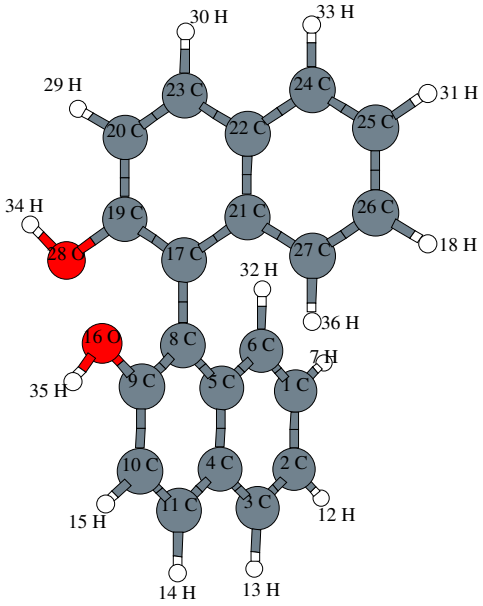

Figure 7.21: (R)-BNP for reference labelling.

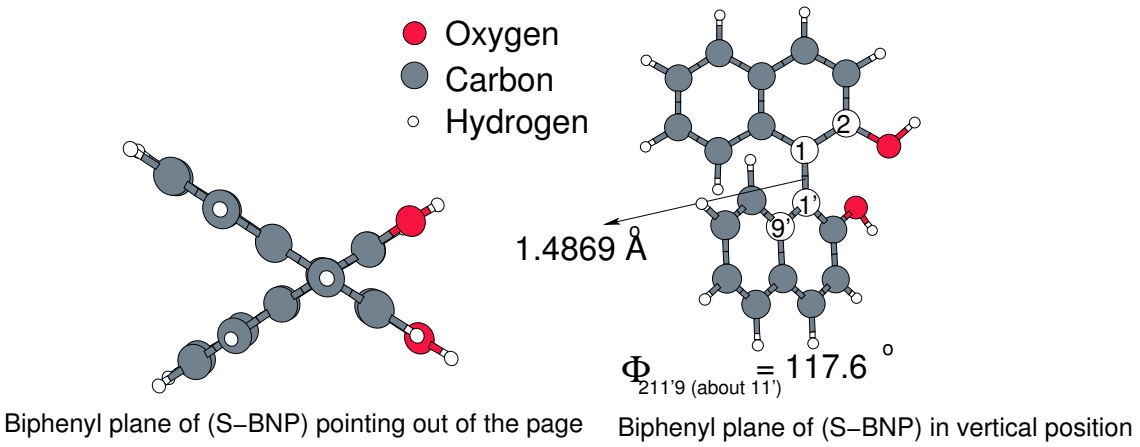

Figure 7.22: The relaxed geometry of S-BNP calculated with SCC-DFTB showing the twisted geometry from two different views. The measured dihedral angles $\Phi_{211'9'}$ between the two naphthalene planes and the pivotal bond C1-C1′ connecting the two ring systems are also shown.

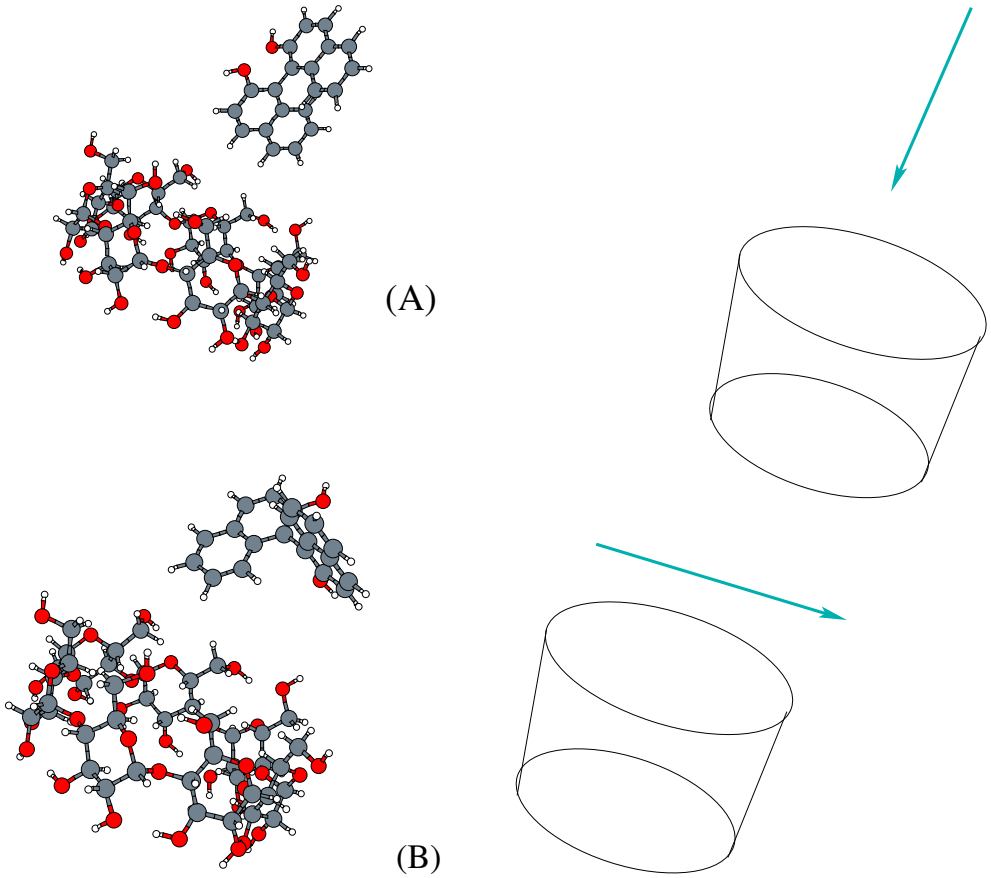

Figure 7.23: Sketch of the different topologies for the entry of the guest (S-BNP) molecule inside the host BCD through the wider end of the cavity. The vertical arrow illustrates the axial entry of BNP in (A). The horizontal arrow illustrates the equatorial entry of BNP in (B).

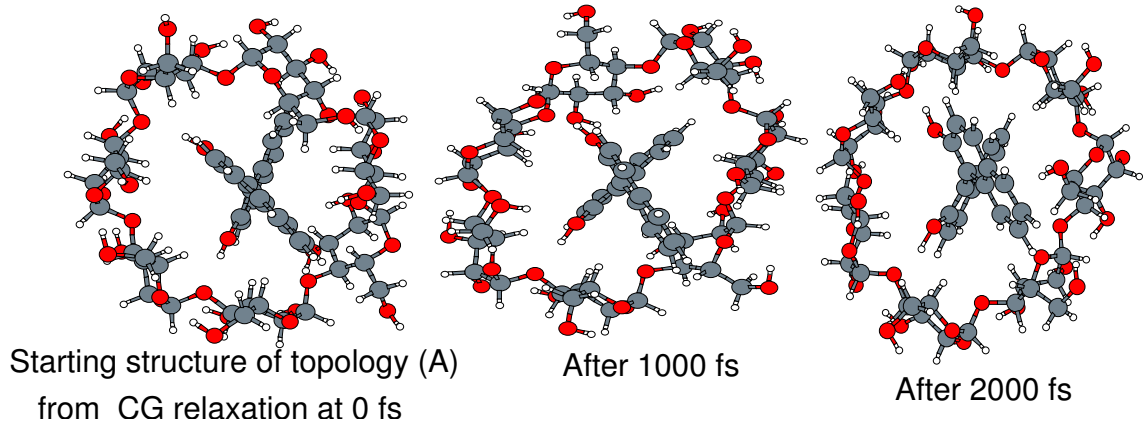

Figure 7.24: Time evolution of β-cyclodextrin-2,2'-dihydroxyl-1,1'-binaphthyl complex during the MD run at 300 K (from topology A).

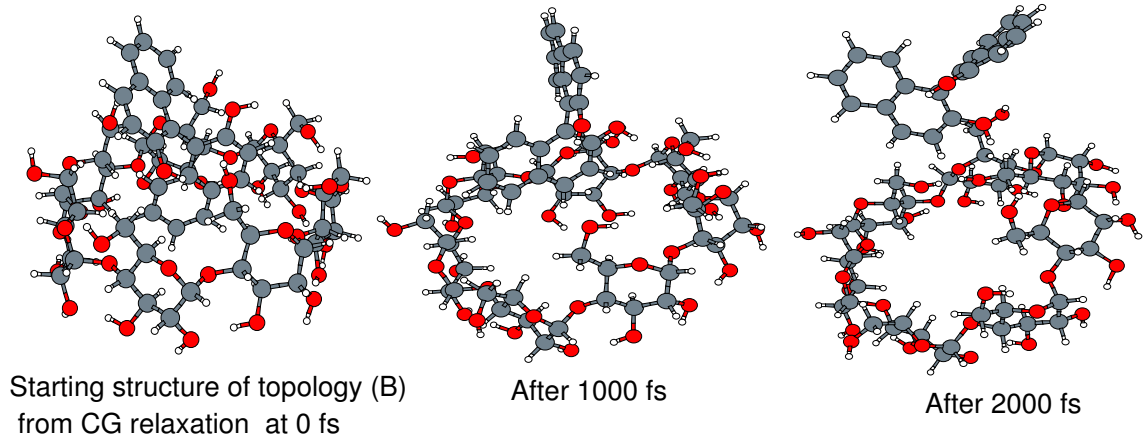

Figure 7.25: Time evolution of β-cyclodextrin-2,2'-Dihydroxyl-1,1'-binaphthyl complex during the MD run at 300 K (from topology B).

using an MD time step of 0.5 fs in order to monitor how the structure evolves in the complex. This provides useful information for which of these trial conformations is the preferred orientation before the final solvation of the complex is done in order to save computational time. The results of these simulations are shown in Fig. 7.24 and 7.25. The geometry fluctuations of these structures during the MD run were measured.
The preferred geometries for S-BNP complexed with BCD were then solvated with addition of 119 molecules of water in the cubic bounding box of dimension $25 \times 25 \times 25$ Å^3. The relaxed geometry of the host-guest-water is shown in Fig. 7.26. The conformation shown in Fig. 7.23 A with docking of the BNP along the axial of the wider cavity is found to be stable according to Figs. 7.24, 7.25 and 7.27 which show the results of the complex of S-BNP with BCD in vacuo. The snapshots from movies in Fig. 7.24 show the encapsulation of BNP in the hydrophobic cavity of BCD. There was deformation of the BCD structures after 1000 fs before returning to its doughnut shape with BNP always entrapped in the centre of the cavity. Figure 7.27 shows the instability in the geometry

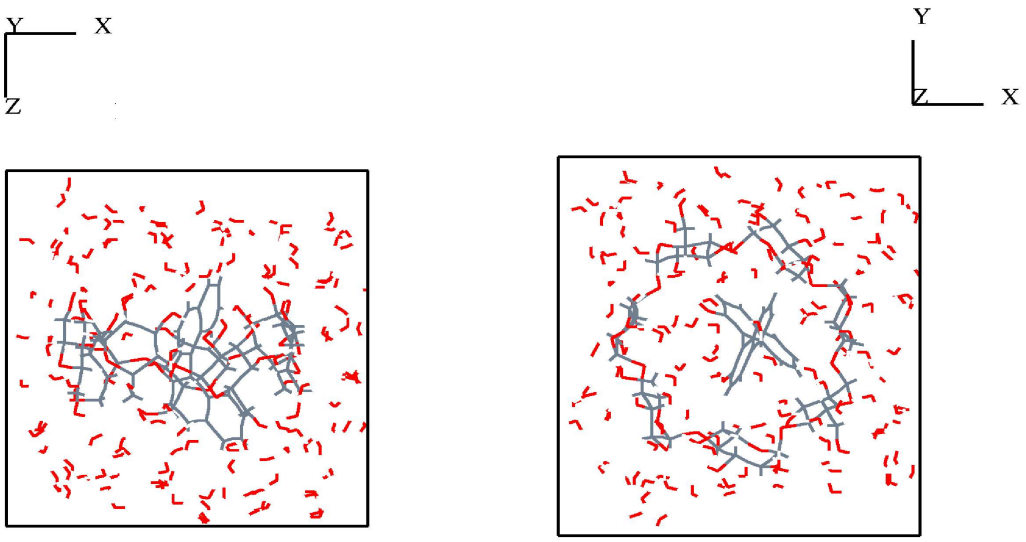

Figure 7.26: The relaxed geometry of β-cyclodextrin-binaphthyl in water.

as the BNP evolves from its relaxed complexation with BCD. BNP was totally out of the cavity of BCD which means that the complexation is not favoured in this equatorial direction. The diameter flexibility of BCD is not enough to entrap the BNP in this direction.

We investigated the structural properties of this system during the molecular dynamics simulation by calculating the radial distribution functions of pairs of atoms constituting the complex in the solution. Figure 7.28(a) shows the radial distribution functions between the water oxygen atoms (OW) and the BCD molecule hydroxyl (OH) and glycosidic (OS) oxygen atoms. The g_{OW-OW} function is almost equal to that computed for bulk water shown in Fig. 6.3. The RDF between the BCD hydroxyl oxygen atoms (OH) and the water atoms (OW) reveals the existence of two shells of water molecules around BCD at $r = 3.0$ (small sharp peak) and $r = 5.3$ Å (broad peak), respectively, as shown in Fig. 7.28(a) in agreement with the calculation done by Manuza *et. al.* [210] using the DLPOLY(2) program. There is a small peak of in RDF of OW-OS at 3.2 Å and a broad peak which becomes flat at 6.0 Å. Figure 7.28(b) shows the RDFs between BCD hydroxyl (OH) and glycosidic (OS) oxygen atoms. In the equilibrium conformation the hydroxyl groups of the BCD molecule link together with the glycosidic oxygens via the formation of hydrogen bonds, as evidenced by the peaks of $g_{OH-OS(BCD)}$ at 2.9 Å (large peak), 4.4 Å and 6.0 Å in Fig. 7.28(b). Also in this Figure, there are peaks of OS-OS at 4.3 Å, 7.8 Å and 9.8 Å, which show the relative positions of the glycosidic oxygen in BCD in equilibrium. Figure 7.28(c) shows the RDFs between the water oxygen atoms (OW) and the BCD carbons atoms. The first shell of water molecules is around 3.6 Å leading to the first broad peak of $g_{OW-C(BCD)}$. The position of the peak agrees with the report of about 3.6 Å for the methane-water system [211]. The other broad peak occurs at broad distance of 6.Å. The picture confirm the hydrophobicity of the inner cavity of BCD. No water molecules were found inside the BCD cavity due to the hydrophobicity of the cavity

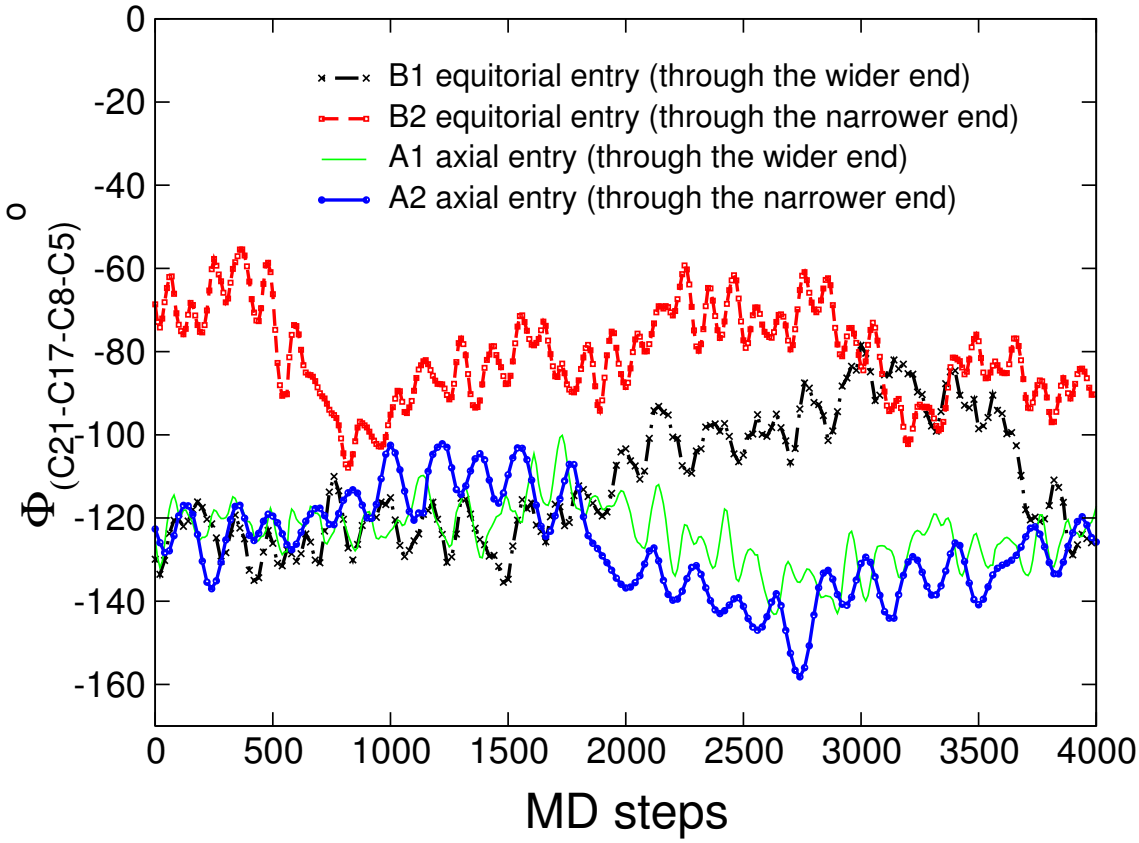

Figure 7.27: Evolution of the dihedral angle ϕ(C21-C17-C8-C5) for the trial conformations in A and B. A1 is the trial from the wider end of the cavity in the axial direction and A2 from the narrower direction. B1 is the equatorial trial from the wider open and B1 from the narrower in same axial direction. A1 and A2 shows some stability with regular fluctuations of the ϕ(C21-C17-C8-C5) while B1 and B2 show some irregular fluctuations. This can be compared with snapshots shown in Fig. 7.24 and 7.25.

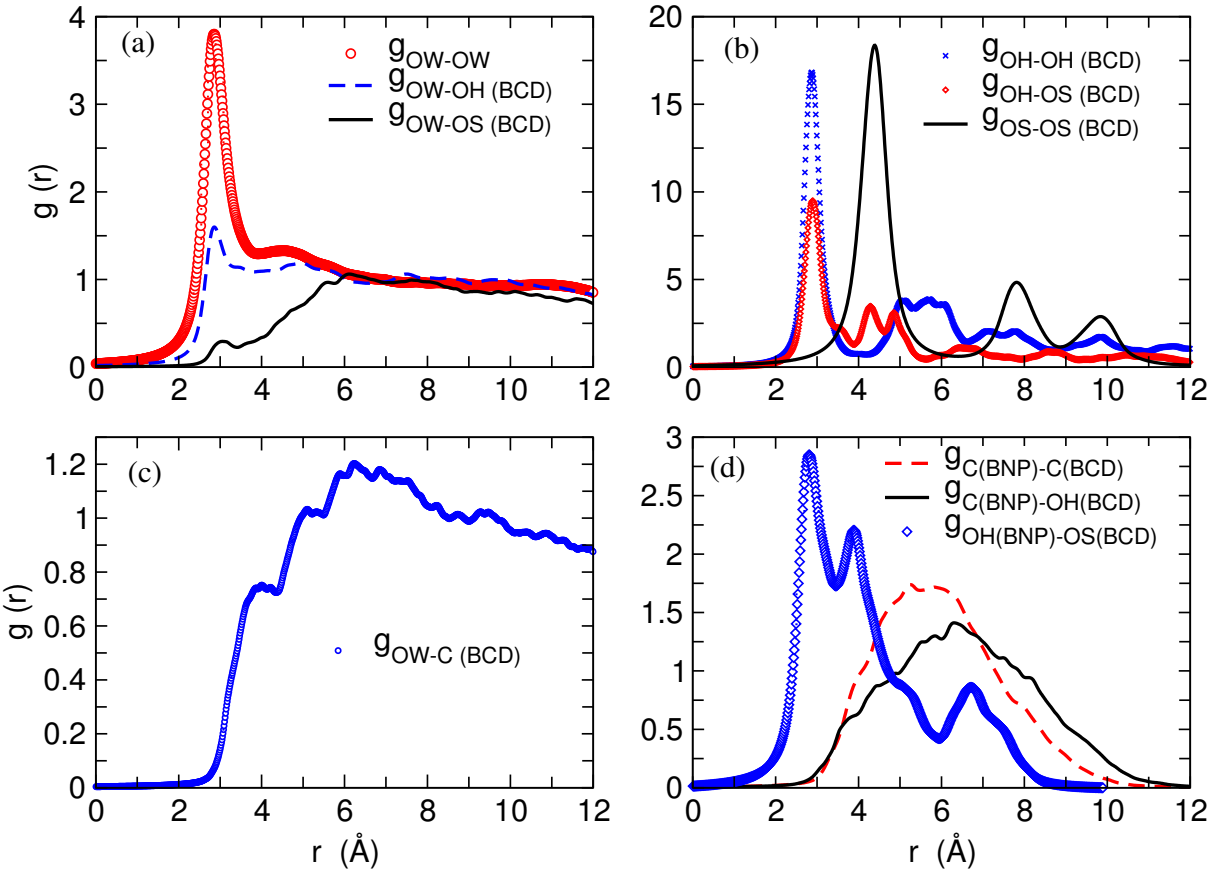

Figure 7.28: (a) Radial distribution functions between the water oxygen atoms (OW) and the BCD molecule hydroxyl (OH) and glycosidic (OS) oxygen atoms. (b) RDF between BCD hydroxyl (OH) oxygen atoms, the BCD hydroxyl oxygen (OH) and glycosidic (OS), and glycosidic oxygen oxygen atoms of (OS). (c) RDF between the water oxygen atom (OW) and the BCD carbons C atoms. (d) RDF of the hydroxyl group (OH) of BNP and glycosidic (OS) oxygen atoms of BCD. The first peak at 2.85 Å shows the formation of hydrogen bonding with OS atoms of BCD. There are other peaks at around 4.0 and 6.8 Å showing the relative positions of glycosidic oxygen atoms with respect to the other glycosidic oxygen atoms. Also shown in (c) is the RDF for carbon atoms of BNP with carbon atoms of BCD, and the RDF of the aromatic carbons of BNP and hydroxyl groups of BCD. All these pictures in (c) confirms the encapsulation of the guest (BNP) molecule inside the cavity of BCD.

and the presence of the guest BNP molecule occupying the central region. Figure 7.28(d) confirms the formation adduct of the host (BCD)-BNP complex with the formation of hydrogen bonding between the hydroxyl group of the BNP and the glycosidic oxygen atoms of BCD as indicated by the first peak in $g_{OH(BNP)-OS(BCD)}(r)$. The position of the peak is around 2.85 Å. This indicates the presence of biphenyl aromatic rings of binaphthyl inside the hydrophobic cavity of BCD. Water molecules form a network of hydrogen bonds with both the primary and secondary hydroxyl groups.

In conclusion to this analysis of the molecular dynamics simulations based on the results of tight-binding density functional theory, we have been able to highlight the interaction between the BCD (host) and the BNP (S enantiomers) guest. The structure of

the complexation correlates with the data obtained from UV/Vis and circular dichroism spectral study in which a family of BNP was encapsulated in the biopolymeric matrix of BCD [209]. The chiral separation ability of BCD on both R and S enantiomers of binaphthyl is of interest. Many experimental and theoretical studies have been carried out on varieties of guest compounds which are chiral [212]. The next Section is devoted to the study of chiral recognition of R- and S-BNP by β-cyclodextrins.

7.3.5 Chiral discrimination of binaphthyl by β-cyclodextrin

In this Section, we study the origin and the degree of chiral discrimination between β- cyclodextrin and the enantiomers of BNP. As mentioned in the previous Section, BNP exists in two enantiomeric forms shown in Fig. 7.20. A couple of these mirror images, which are not superimposable, constitute an enantiomeric pair. A pair of these compounds, which possess equal physical properties, such as density, boiling point, refractive index, etc., may be together present in a solution. They are distinguished by the prefixes R and S which refer to the relative spatial orientation of the two substituted rings with respect to each other. The rules for deriving these prefixes can be found in the literature [213]. These enantiomers, R- and S-2,2'-dihydroxy-1,1'-binaphthyl or R- and S-BNP, for short, can in principle interconvert by rotation about the pivotal C1-C1′-bond (see the labels in Fig. 7.22). However, due to the high energy of the planar geometry, the rotation is hindered and the enantiomers can be obtained separately. In order to effect the separation, or resolution, of such a mixture of enantiomers, a chiral reagent is needed which reacts differently with the two mirror image forms of a chiral compound, an effect which is called "chiral discrimination". For a critical discussion of this term see Ref. [214]. There exist several methods for enantiomer separation, *e.g.* resolution by enzymatic degradation, fractional crystallization [215], or capillary electrophoresis [216, 217]. Here we are concerned with the separation of enantiomers by formation of inclusion complexes with chiral hosts such as cyclodextrins [218]. Cyclodextrins have found widely useful as chiral selectors because they are readily available in enantiomerically pure form and lead to stable complexes with many different compounds, including chiral ones.
Separation of enantiomers is of immense practical importance in all areas where the interaction with living organisms is concerned, such as the food and drug industry. Of the enantiomers of a pharmaceutical agent only one may exhibit the desired effect; the other one might be ineffective or even harmful [219]. In order to compare the complex of both R- and S- enantiomers for chiral recognition of BCD, we started from a preferred direction of docking as discussed in the previous Section, where the preferred axis of complexation is axial. This is again followed by energy minimization of both complexes in vacuum. The complexes that were previously minimized in vacuum were now immersed in a separate cubic supercell with dimension $22 \times 22 \times 22$ Å^3 containing now 64 molecules of water. The positions and orientations of β-cyclodextrin and all the water molecules are the same for both complex systems. This means that the geometry of the two enantiomeric complexes are the same in the box except for the reflection of the R-BNP in the cavity of BCD inside the second simulation box containing S-BNP. We did this, because

the same number of water molecules has different hydrogen bonding network formation for different orientations and hence, different binding energy. Calculations done with some water clusters containing the same number of water molecules show that they have different energy minimum configurations because of different orientations of the protons of the water as fully discussed in the previous Chapter [130, 220]. Therefore, in accounting for the total energy of the cyclodextrin-guest complex, water molecules orientations with different binding energies may contribute and lead to wrong prediction of energy differences between the two enantiomers in complex solution. To avoid this effect, we started with the same geometrical orientation of all the molecules in the complexes. We minimized the energies of the two complexes in solution until the atomic forces became smaller than 10^{-3} eV/Å for VASP and the DFTB method. The final energies of the two complexes were then compared. Molecular dynamics simulation at 300 K, using a time step of 0.5 fs, was then carried out for 5 ps using the DFTB method in order to compare the structural behaviour of the chiral guests in the two complexes. In our simulation, there was no restriction on the atoms in the complex as all were allowed to move freely.

The relaxed geometries for both R- and S-enantiomers are shown in Figs. 7.29(a) and (b). The Figure shows that S-BNP is totally encapsulated in the hydrophobic centre of the BCD cavity with water molecules providing extra stability through the hydrogen bonding formation with the hydroxyl groups of the binaphtols. The result does not differ from the previous calculation of the S-BNP complex relaxed in 119 molecules of water as shown in Fig. 7.26. R-BNP on the other hand, in Fig. 7.29(b), shows partial inclusion in the cavity with the upper part of the biphenyl ring protruding from the cavity despite docking of the two chiral molecules through the same axis along the wide cavity of BCD.

According to the DFTB result, it is very difficult to notice the energy difference between the two complexes at the end of the relaxation despite the geometrical structural change of the complexes as shown in Fig. 7.30. The final structure obtained from this method was further investigated using VASP. Figure 7.31 shows the variation of the energy of the two complexes during the relaxation runs. Obviously, the relaxation with the DFTB method does not allow to distinguish the energetically favourable complex (this might be due to the approximations the DFTB algorithm is built on). The MD simulations carried out on these relaxed complexes show that S-BNP remains inside the cavity of BCD throughout the simulation period while R-BNP remains partially enclosed with one end of the biphenyl protruding out of the ring. The analysis of the RDF shown in Fig. 7.32 of the carbon atoms of the S-BNP and R-BNP molecules and the carbon atoms of the BCD confirms the relative inclusion of the two chiral molecules in the hydrophobic cavity of BCD. The Figure shows that the carbon-carbon distances of S-BNP-BCD atoms are broadly distributed over a wide range of distances from 2.3 Å to 11.0 Å with a broad peak at around 5.2 Å. The range of average distance of R-BNP-BCD carbon-carbon atoms is shifted from an average value of 3.3 Å to 11.0 Å and also broadly peaks at around 6 Å. The broad peaks of the two complexes occur at relatively different heights indicating the frequency of occurrence of these C-C distances of host and guest molecules. The relative heights of the peaks in $g_{CC'}(r)$ of the two complexes show that S-BNP is fully encapsulated in the cavity, while R-BNP is partially encapsulated as there are less closer carbon-carbon

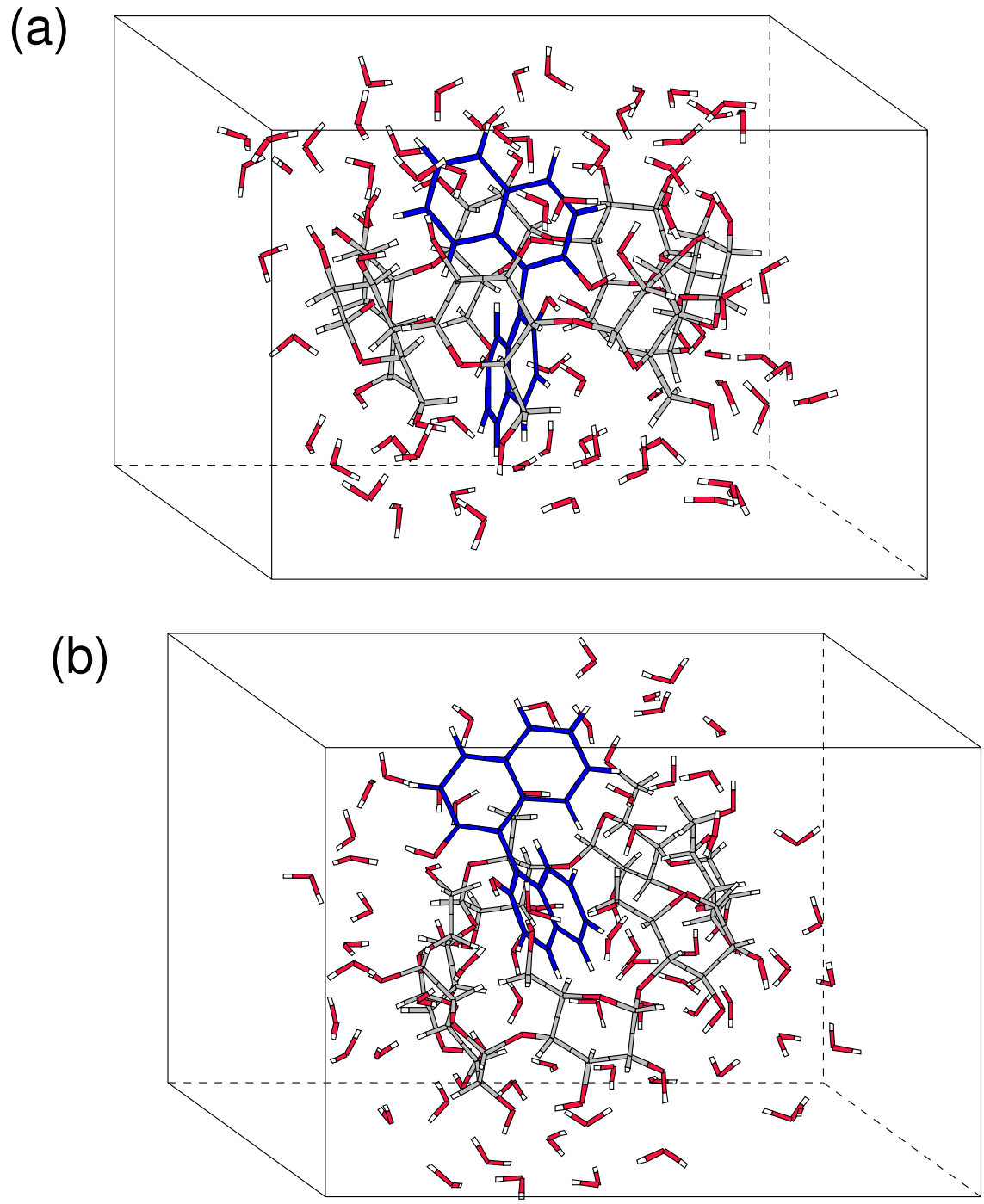

Figure 7.29: Simulation box of water containing the relaxed geometry of (a) S-BNP and (b) R-BNP in the hydrophobic cavity of β-cyclodextrin.

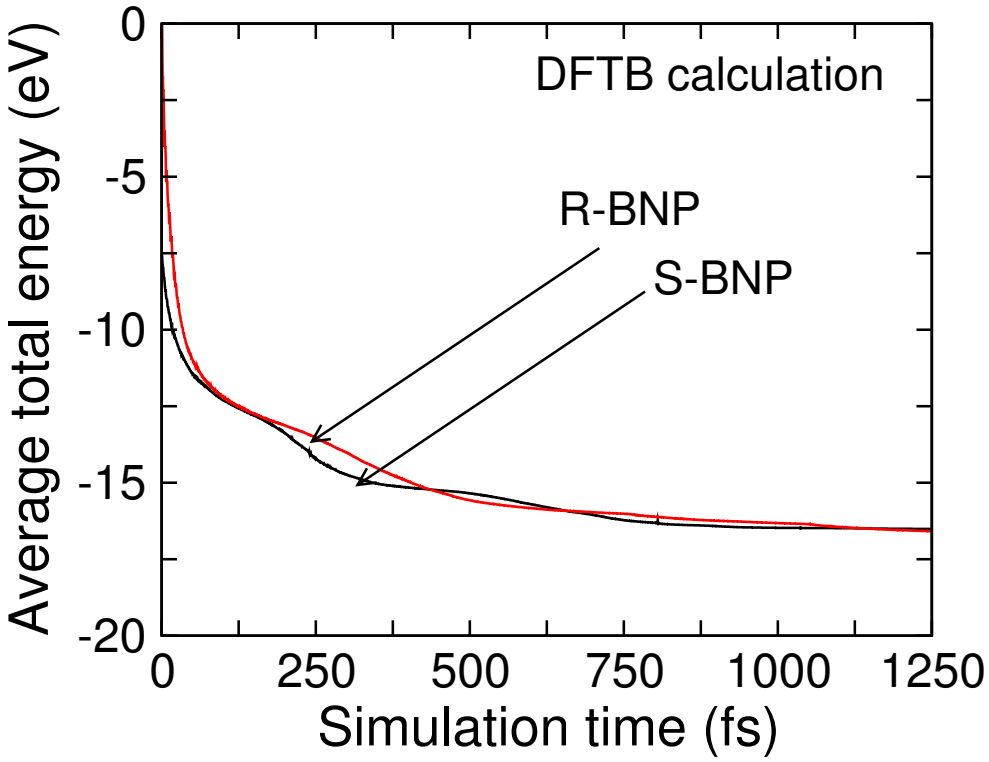

Figure 7.30: Average energies of 1:1 complexes between BCD and enantiomers calculated with DFTB.

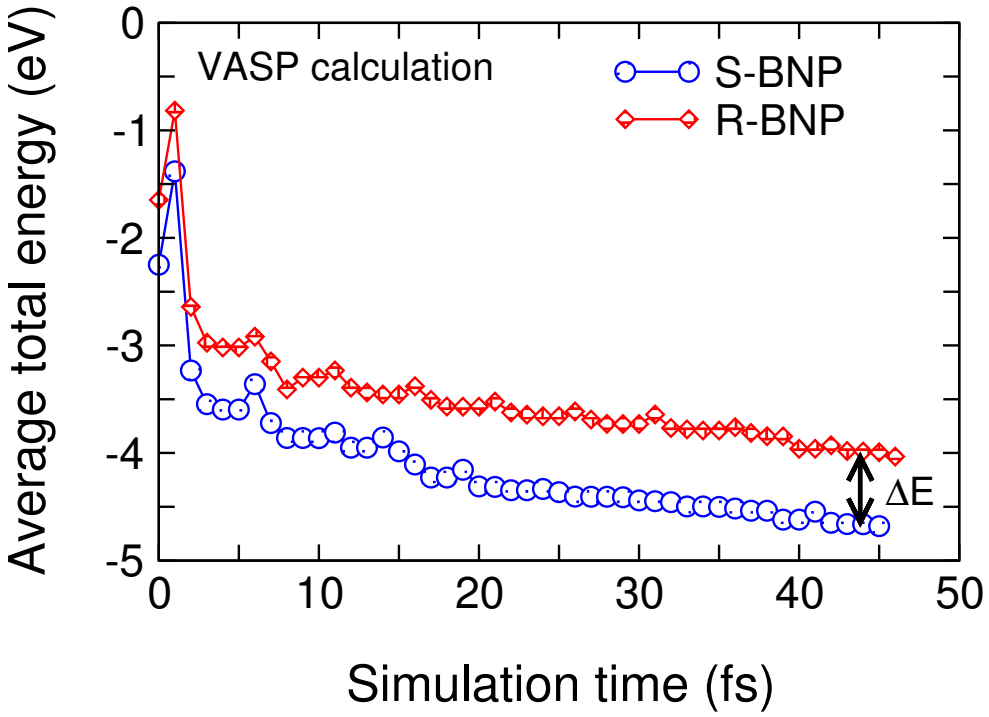

Figure 7.31: Average energies of 1:1 complexes between BCD and enantiomers calculated with VASP. The calculation was done on the relaxed geometry obtained with the DFTB method.

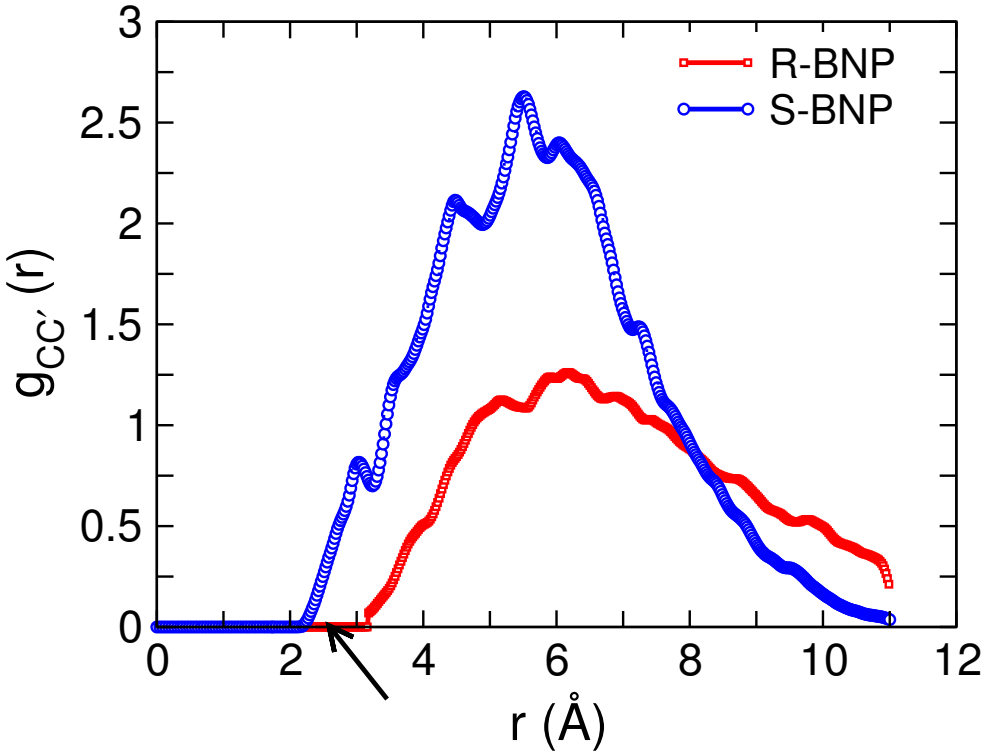

Figure 7.32: Radial distribution functions (RDF)for carbon atoms (C) of the two chiral compounds of BNP with carbon atoms C' of BCD. The picture shows partial inclusion of R-BNP while S-BNP is wholly included in the hydrophobic cavity of BCD.

distances in comparison to the S-BNP complex.

A similar calculation of the RDF for hydroxyl oxygen atoms of S-BNP and glycosidic oxygen atoms of BCD complexed in a simulation box containing 60 molecules of water using VASP can be compared with the results of DFTB method for the same RDF in Fig. 7.28(d). The peaks show the relative positions of the hydroxyl oxygens of S-BNP to the glycosidic oxygen atoms of BCD. They occur at 2.85 Å, 4.0Å, 6.15 Å and 7.5 Å for the VASP calculations in Fig. 7.33 and 2.85 Å, 4.0Å, 6.8 Å and 7.5 Å for the DFTB calculations in Fig. 7.28(d) . The fourth peak at 7.5 Å in DFTB calculations is hardly visible. The first peak of both methods shows the hydrogen bonding formation between the hydroxyl oxygen of S-BNP and glycosidic oxygen of BCD which enhances the stabilization of the complex. This first peak distance can be compared to the RDF of the first oxygen-oxygen atoms distance peak. The most important fact from results of these two methods of calculation is that they both illustrate the inclusion complex formed by BNP with BCD.

Based on our analysis of the molecular dynamics simulation on chiral complexes, we have been able to highlight the interaction between the BCD (host) and the (S,R)-BNP (both enantiomers). Judging from the energy difference obtained from the VASP calculations and from the structural analysis of the complexes based on the MD results, it is found that S-BNP forms a more stable complex than the corresponding R-BNP. This is

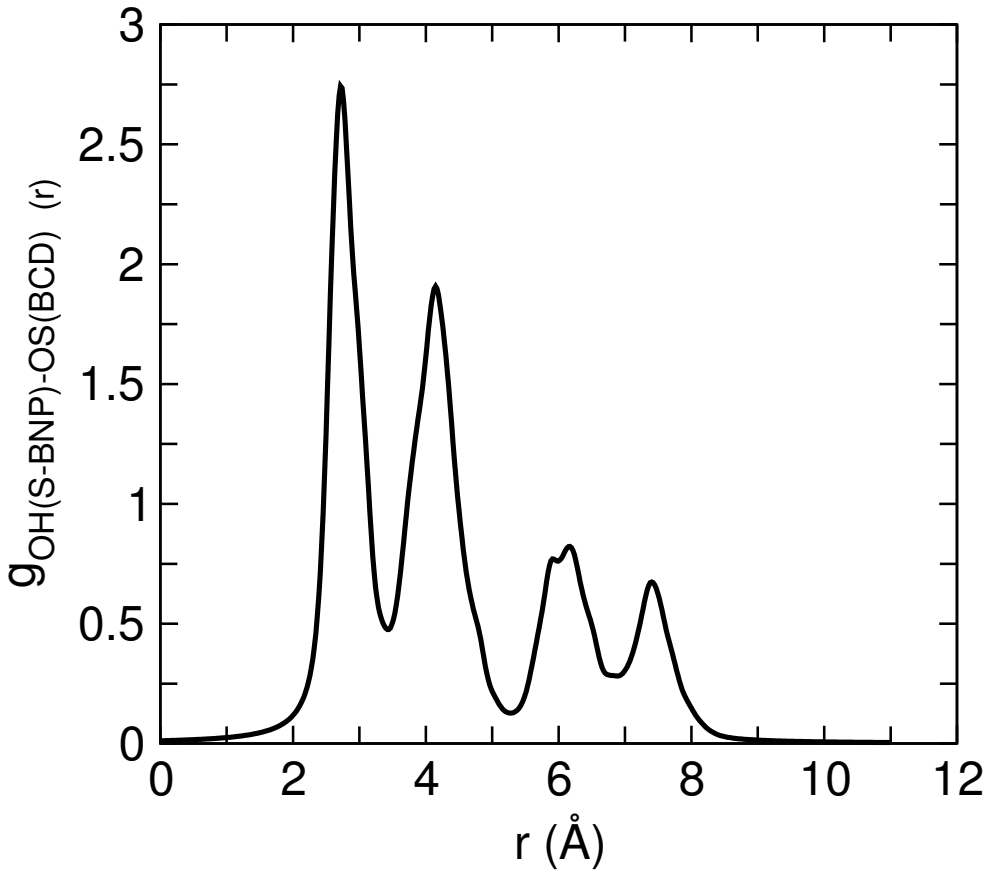

Figure 7.33: Radial distribution functions for hydroxyl oxygen atoms of S-BNP and glycosidic oxygen atoms of BCD complexed in a simulation box containing 60 molecules of water. This calculation done using VASP can be compared with the results of employing the DFTB method for the same RDF in Fig. 7.28 (d). The peaks show the relative positions of the hydroxyl oxygens of S-BNP to the glycosidic oxygen atoms of BCD.

one of the main reason why most of the experiments and analyses are based on S-BNP (rather than the R-BNP) because of its stability and its full encapsulation by the cavity of β-cyclodextrin. The preference for complexation of S-BNP has also been found by capillary electrophoresis with monosaccharides [216]; however, resolution of enantiomers was not accomplished. Koji *et al.* [221] have reported that the chiral separation of some binaphtol derivatives was achieved by capillary electrophoresis with linear α-1,4-linked oligosaccharides such as maltose and maltotriose as chiral selectors. Based on state of the art *ab-initio* calculations we have been able to confirm the chirally discriminating power of BCD by calculating and analyzing the complexes formed with S- and with R-BNP, respectively. We hope that the results of our calculations will give more directional clues for further experimental investigations.

Summary

We present in this work the first-principle investigation of the structural and dynamical properties of water and other hydrogen-bonded liquid methanol and the inclusion complexes of cyclodextrins. The main results are discussed mostly through the analysis of molecular dynamics simulation and in addition to the case of ice, in terms of lattice dynamical theory. The thesis consists of seven Chapters, a Summary, an Appendix and a list of References. Here is a brief summary of the seven Chapters.

- **Chapter 1** presents the overview of the whole thesis starting from the introduction to the topics of various works carried out in this research.

- **Chapter 2** presents the basic formalism of density functional theory and various features of the two packages used in the work.

- **Chapter 3** presents the discussion of the *tight-binding* model which explains some basic implementations of the self-consistence density functional *tight-binding* code applied in this work.

- **Chapter 4** presents the general features of molecular dynamics simulation and some of the important equations used in the analysis of the structural and dynamical data obtained from the MD runs.

- **Chapter 5** presents the calculations of binding energies and melting transitions of water clusters of n-mer with $n = 2, 3, \ldots, 36$. Two different configurations of water clusters prepared with two different methods from SCC-DFTB which consists of some local minimum configurations and the well known global minimum configurations obtained with the TIP4P classical pairwise additive potential were considered in our calculation. We used the VASP and DFTB methods to calculate the binding energies of the global minimum configurations and compared the results with the DFTB binding energies of the DFTB structures. We also compared the binding energies of water clusters containing the same number of water molecules obtained with the other classical model potentials with our *ab-initio* results. The calculated binding energies show the same behaviour when plotted against the cluster size except for the difference in the scale of energy for different potentials. The DFTB results show small energy differences between the calculated binding energies on the global minimum configurations and the DFTB structures containing the same number of water molecules. In all cases, the binding energy curves are almost parallel for clusters larger than the trimer, and there is no evidence of increased stability of a particular size relative to neighbouring ones in either case, though the minimum structures for the different potentials are not the same. We also observed that the binding energy per water molecule increases negatively in exponential sense as the size of the cluster grows and saturates with a sudden negative increase of binding energy at the value of $n = 8$. It is not clear whether there are some magic numbers

of water molecules, as was observed for some other clusters like argon and sodium. Our result shows with some temptation that $n = 8$ is the first magic number for water clusters as was also reported in the literature. We also reported that anomalous behaviour in the binding energy might be due to the complexity of water connected with the formation of the hydrogen bonding networks.
The result of melting transitions of these clusters using the abrupt change in the slope of energy versus temperature of the calorific curve along with Lindemann's criteria of melting reveals further, the anomalies in the behaviour as the calculated melting temperatures versus water cluster size shows non-linear behaviour. We also observed the effect of initial configuration on the melting transition temperature with global minimum configuration requiring more energy than the local one to raise its statistical entropy. The global minimum configurational structure therefore has a larger melting temperature than the local minimum structure.

- **Chapter 6** presents the results of structural and dynamical properties of liquid water and crystalline ice from molecular dynamics simulation. Also presented in this Chapter are the results of lattice dynamical properties of ice through the phonon calculation based on direct supercell force-constant method in [100] direction of the cubic unit cell used in th calculation. Our molecular dynamics results through the analysis of radial distribution functions correlate well with the neutron diffraction scattering experimental data at ambient temperatures up to the supercritical region. An attempt to cross-over from the supercool liquid to the ice structure could not be achieved because it is too computationally expensive. It is also sometimes very difficult to achieve the re-ordering of the hydrogen bond in the supercool liquid compared to that of ice structure without imposing an external constraint such as pressure or the application of electric field during cooling as it was done recently. Our calculated diffusion coefficient at room temperature also agrees well with the experimental data.
  For investigation of the ice crystal, a specially prepared ice structure following the Bernal Fowler ice rule was used to produce tetrahedrally arranged oxygen atoms in hexagonal-like ice packed in a tetragonal box according to our simulation. Molecular dynamics simulation carried out through the analysis of radial distribution functions of this ice crystal shows some agreement in the positions of peaks in comparison with neutron diffraction data.
  The phonon dispersion calculations in [100] direction shows a better result in comparison with a recent *ab-initio* calculation done in the same direction. Also the dispersion curves shows a reasonable comparison with other dispersions reported in the literature in [0001] direction of hexagonal ice. Our calculated longitudinal acoustic velocity agrees well with the longitudinal acoustic velocity from inelastic neutron scattering data. The vibrational density of states reproduces all the features in covalently O-H stretching region, intra-molecular bending region, molecular librational region as well as in the molecular translational region, when comparing our results to some infrared spectra, Rahman spectra as well as inelastic neutron

scattering results. The analysis of the vibrational density of states of ice in our calculation shows a boson peak, a characteristic common to amorphous systems, at low energy of translational region.
The results of another hydrogen bonding like liquid methanol briefly presented in this Chapter through the analysis of radial distribution functions from molecular dynamics calculations show the ability of both VASP and DFTB methods in reproducing the experimental results of the hydro-carbon organic solvents, which forms a benchmark for calculations of other organic compounds such as cyclodextrin and its complexes.

- **Chapter 7** presents results based on the application of density functional theory and *ab-initio* molecular dynamics to the inclusion complexes of cyclodextrins with the various guest molecules in as the solvent which provides the driving force for the complexation. The structural and geometrical analysis of the molecular dynamics simulation data shows the inclusion of phenol in β-cyclodexrin with phenol included with its molecular axis strongly inclined.
Our *ab-initio* investigation with the DFTB method on aspirin with β-cyclodextrin shows the formation of a stable complex in agreement with the predicted orientational geometry in the cavity of BCD. The temperature dependence of the geometry of aspirin in the complex, according to the DFTB simulation results on the aspirin complex, predicts a more stable complex at 300 K than the higher temperature simulation.
The results of structure optimization and molecular dynamics simulation of host-guest γ-cyclodextrin-pinacyanol dye inclusion complex are also reported. The results attempt to correlate UV/Vis and circular dichroism spectra data with calculated aggregate structures of the sandwich dimer, with the monomers twisted slightly against each other. The inclusion complex of a dimer of pinacyanol dye with some droplets of water inside γ-cyclodextrin shows structural properties which can be ascribed to the experimental observation of UV/CD spectra of the chromophores, in which there is a split of the excited states of the monomer units. The uncompexed dimers of these chromophores in water show a twisted geometry only when they are heated as revealed by our molecular dynamics simulation at room temperature. In both complexed and uncomplexed dimers, the twist of the dimers is more pronounced when the ethyl group of the monomers align parallel compared to the anti-parallel case, due to the steric repulsion of this ethyl functional groups. But in the complexed case, the twist readily takes place unlike in the uncomplexed dimers, in which case, they have to be heated, to yield the twist. The sense of the twist is usually predetermined by the chirality of the complexing host. The result of interaction between two monomers, which results in Davydov splitting of the two dimers states, was interpreted using the exciton model.
The last part of this Chapter presents the investigation of the interaction of the β-cyclodextrin-2,2′-dihydroxy-1,1′-binaphtyl complex by means of molecular dynamics simulation. The first part of the work focused in particular on the investiga-

tion of the most stable conformation of this complex by investigating some of the structural properties that change with time which includes the hydrogen bonding formation of the active agent guest molecule with the torus-like macro ring of the host β-cyclodextrin. This leads to the formation of a stable adduct in the lipophilic cavity of the biopolimeric matrix. The results obtained for this complex reveal the direction of encapsulation of the most probable orientation of the guest within the host cavity. This was obtained by studying the time-dependence of the complex formation.

The second part of this Section concentrates on the ability of the chiral host β-cyclodextrin to differentiate between the enantiomers of the binaphthyl guest. Our study shows that S-binaphtyl forms a more stable complex with β-cyclodextrin than the corresponding R-enantiomer judging from the binding energy difference of the two diastereo complexes and the significant structural differences of the two enantiomers in β-cyclodextrin.

A Appendix

A.1 Theory of lattice dynamics and phonon calculation

The formulation of this theory starts from the definition of an infinitely extended crystal. This theory is simplified by using lattice periodicity and space group symmetry which results from the absence of crystal surfaces [173, 222–225]. An arbitrary Bravais lattice is defined by lattice translational vectors

$$\mathbf{x}(l) = l_1\mathbf{a}_1 + l_2\mathbf{a}_2 + l_3\mathbf{a}_3, \tag{A.1}$$

where l_1, l_2 and l_3 are arbitrary integers labelled collectively by l. The three noncoplanar vectors $\mathbf{a}_{1,2,3}$ are primitive translational vectors of the lattice. If there are n atoms in the basis of the lattice, the positions of these n atoms in the unit cell, with respect to the origin of the unit cell, are given by the vectors $\mathbf{x}(k)$, where the index k distinguishes the different atoms in the basis, or equivalently, in the primitive unit cell, and takes the values $1, 2, \ldots n$. Thus, in general the position vectors of the kth atom in the lth primitive cell is given by

$$\mathbf{x}(lk) = \mathbf{x}(l) + \mathbf{x}(k). \tag{A.2}$$

The atomic positions in an infinitely crystal defined by the set of vectors $\{\mathbf{x}(lk)\}$ are referred to as the rest positions of the atoms. As a result of thermal fluctuations at nonzero temperature and zero-point motions at zero temperature the atoms in the crystal execute vibrations about their rest positions. If we denote by $p_\alpha(lk)$ the α Cartesian component of the momentum of the kth atom in the lth primitive unit cell, the total kinetic energy of the crystal can be written as

$$\mathcal{K} = \sum_{lk\alpha} \frac{p_\alpha^2(lk)}{2M_k}, \tag{A.3}$$

where M_k is the mass of the kth kind of atom.
We assume that the potential Φ of a crystal is a function of the instantaneous positions of the atoms. We denote by $u_\alpha(lk)$ the α Cartesian component of the displacement of the kth atom in the lth primitive unit cell from its rest position given by (A.2). The potential energy Φ can then be formally expressed as a power series of the components leading to

$$\Phi = \Phi_0 + \sum_{lk\alpha} \Phi_\alpha(lk)u_\alpha(lk) + \frac{1}{2}\sum_{lk\alpha}\sum_{l'k'\alpha'} \Phi_{\alpha\beta}(lk;l'k')u_\alpha(lk)u_\beta(l'k') + \frac{1}{6}\sum_{lk\alpha}\sum_{l'k'\alpha'}\sum_{l''k''\alpha''} \Phi_{\alpha\beta\gamma}(lk;l'k';l''k'')u_\alpha(lk)u_\beta(l'k')u_\gamma(l''k'') + \ldots \tag{A.4}$$

In this expression Φ_0 is the potential energy of the static lattice, i.e., when all atoms are in their rest positions, while the expansion coefficients are

$$\Phi_\alpha(lk) = \left.\frac{\partial\Phi}{\partial u_\alpha(lk)}\right|_0, \tag{A.5}$$

$$\Phi_\alpha(lk;l'k') = \left.\frac{\partial^2\Phi}{\partial u_\alpha(lk)}\partial u_\beta(l'k')\right|_0, \tag{A.6}$$

$$\Phi_\alpha(lk;l'k') = \left.\frac{\partial^3\Phi}{\partial u_\alpha(lk)}\partial u_\beta(l'k')\partial u_\gamma(l''k'')\right|_0, \quad \text{etc.}, \tag{A.7}$$

where the subscript 0 means that the derivatives are evaluated with all the atoms at their rest positions. The physical interpretation of the coefficient $\Phi_\alpha(lk)$ is that it is the negative of the force in the α direction acting on the atom (lk) when it and all other atoms in the crystal are at rest positions. Similar interpretation can be given to the higher order coefficients $\Phi_{\alpha\beta}(lk;l'k')$, $\Phi_{\alpha\beta\gamma}(lk;l'k';l''k'')$, ... Consequently, the coefficients $\Phi_\alpha(lk)$, $\Phi_{\alpha\beta}(lk;l'k')$, $\Phi_{\alpha\beta\gamma}(lk;l'k';l''k'')$, ..., are known as *atomic force constants* of the first, second, third,..., order, respectively. The first order atomic force constants distinguish the case of the atoms in their rest positions from the case when the rest positions are also equilibrium positions. In the latter case the configuration of the crystal corresponds to vanishing stress. While the rest positions imply only that there is no net force action on the atoms. For the equilibrium crystal, this is a more strict definition meaning the first order atomic force constants force must vanish. There are several problems of physical interest where it is necessary to consider atoms in their rest positions which are not equilibrium positions [225]. One example is the study of the dynamical properties of crystals being under external imposed stress. It is convenient to combine the terms linear in the atomic displacements with the terms of third and higher order and treat them as perturbation of the contributions to the vibrational part of the energy obtained from the quadratic terms in the atomic displacements. Then, the vibrational Hamiltonian for a crystal can be written as

$$H = H_0 + H_A, \tag{A.8}$$

where

$$H_0 = \sum_{lk\alpha}\frac{p_\alpha^2(lk)}{2M_k} + \frac{1}{2}\sum_{lk\alpha}\sum_{l'k'\alpha'}\Phi_{\alpha\beta}(lk;l'k')u_\alpha(lk)u_\beta(l'k'), \tag{A.9}$$

$$\begin{aligned} H_A = &\sum_{lk\alpha}\Phi_\alpha(lk)u_\alpha(lk) \\ &+ \frac{1}{6}\sum_{lk\alpha}\sum_{l'k'\alpha'}\sum_{l''k''\alpha''}\Phi_{\alpha\beta\gamma}(lk;l'k';l''k'')u_\alpha(lk)u_\beta(l'k')u_\gamma(l''k'') + \ldots \end{aligned} \tag{A.10}$$

The Hamiltonian H_0 is the vibrational Hamiltonian in the *harmonic approximation*. The Hamiltonian H_A is called *anharmonic* part of the vibrational Hamiltonian. In many crystals the anharmonic terms in the crystal are small and can be treated as a perturbation of the harmonic Hamiltonian; in some cases the anharmonic effects are negligibly small. A great advantage is that in the harmonic approximation the equations of motion of

atoms become simple and exactly solvable. From the Hamiltonian (A.9) and Hamiltonian's equation of motion (see Eq. (2.14)),

$$\dot{u}_\alpha = \frac{\partial H_0}{\partial p_\alpha(lk)} = \frac{P_\alpha}{M_k}, \tag{A.11}$$

$$\dot{P}_\alpha = \frac{\partial H_0}{\partial u_\alpha(lk)} = -\sum_{l'k'\beta} \Phi_{\alpha\beta}(lk;l'k')u_\beta(l'k'), \tag{A.12}$$

the equation of motion of a crystal reads

$$M_k\ddot{u}_\alpha(lk) = -\sum_{l'k'\beta} \Phi_{\alpha\beta}(lk;l'k')u_\beta(l'k'). \tag{A.13}$$

A solution of this set of coupled equations can be obtained in a lattice-periodic form, because, in this case it will satisfy the symmetry conditions [225], yielding

$$u_\alpha(lk) = M_k^{\frac{1}{2}} e_\alpha(k) exp(i\mathbf{k}\cdot\mathbf{x}(l) - i\omega t). \tag{A.14}$$

The coefficient function $e_\alpha(k)$ satisfies the equation

$$\omega^2 e_\alpha(k) = \sum_{k'\beta} D_{\alpha\beta}(kk';\mathbf{k})e_\beta(k'), \tag{A.15}$$

which is obtained by substituting the second derivative of (A.14) into the equation of motion (A.13). The dynamical matrix $D_{\alpha\beta}$ is defined by the equation

$$D_{\alpha\beta}(kk';\mathbf{k}) = (M_k M_{k'})^{\frac{1}{2}} \sum_{l'} \Phi_{\alpha\beta}(lk;l'k') exp(i\mathbf{k}\,[\mathbf{x}(l) - \mathbf{x}(l')]). \tag{A.16}$$

Equation (A.15) contains no dependence on the cell index l. Since the atomic force constants depend only on the relative distances between the atoms, the origin l does not play a role anymore and can be set equal to zero. The matrix $D_{\alpha\beta}(kk';\mathbf{k})$ is called the *dynamical matrix*. It is a $3n \times 3n$ Hermitian matrix (n is the number of atoms in the unit cell) with the properties,

$$D_{\alpha\beta}(kk';\mathbf{k}) = D_{\beta\alpha}(k'k;\mathbf{k}), \tag{A.17}$$

$$D_{\alpha\beta}(kk';-\mathbf{k}) = D^*_{\beta\alpha}(k'k;\mathbf{k}). \tag{A.18}$$

It follows from (A.15) that the allowed values of the squares of the frequency ω for a given value of $\mathbf{k}$ are the eigenvalues of the dynamical matrix $D_{\alpha\beta}(kk';\mathbf{k})$. Because the latter is a $3n \times 3n$ matrix, there are $3n$ solutions for ω^2 for each value of $\mathbf{k}$, i.e., the values $w_j^2(\mathbf{k})$, where $j = 1, 2, \ldots 3n$. The $3n$ functions $\omega_j^2(\mathbf{k})$ for each value of $\mathbf{k}$ can be regarded as the branches of the phonon dispersion. From the Hermiticity of of the dynamical matrix, it follows that $\omega^2(\mathbf{k})$ is real. Stability of the crystal implies that $\omega_j(\mathbf{k})$ must also be real. An imaginary frequency corresponds to atomic motions which are not harmonic having amplitudes given by (A.14) which grow exponentially with time. This means that the

stability requires that $\omega_j^2(\mathbf{k})$ is not only real but also positive. For each of the $3n$ values of $\omega^2(\mathbf{k})$ corresponding to a given value of $\mathbf{k}$ there exists a $3n$-component vector $\mathbf{e}_\alpha(k)$, whose components are solutions to the set of equations (A.15). To make clear that this vector depends on the given value of $\mathbf{k}$ and is associated with the particular phonon branch j, its components can be re-written as $e_\alpha(k;\mathbf{k}_j)$. The Eq. (A.15) then reads

$$\omega^2(\mathbf{k})e_\alpha(k;\mathbf{k}_j) = \sum_{k'\beta} D_{\alpha\beta}(kk';\mathbf{k})e_\beta(k';\mathbf{k}_j). \tag{A.19}$$

From the conditions imposed on the atomic force constants by the invariance of the potential energy and its derivatives against an infinitesimal rigid body displacement of the whole crystal, it follows that the frequencies of three branches of $w_j(\mathbf{k})$ $(j = 1, 2, 3)$ vanish with vanishing $\mathbf{k}$ and the corresponding eigenvectors have the property that $e_\alpha(k;\mathbf{k} = 0, j)/\sqrt{M_k}$ is independent of k, i.e., the same for all the atoms [225]. These three branches are called *acoustic* branches, because in the long wavelength limit they give the frequency of sound waves propagating through the crystal. The remaining $3n-3$ branches, whose frequencies approach non-zero values as $\mathbf{k}$ tends to zero, are called *optical* branches, because these branches are observed in infrared absorption and light scattering experiments in the limit $\mathbf{k} \approx 0$. The displacement vector pattern obtained by substituting into (A.14) a particular eigenvector $e_\alpha(\mathbf{k}_j)$ and the corresponding frequency $w_j(\mathbf{k}_j)$,

$$u_\alpha(lk) = \frac{1}{\sqrt{M_k}} e_\alpha(k;\mathbf{k}_j) exp\left[i\mathbf{k}\cdot\mathbf{x}(l) - i\omega(\mathbf{k})t\right], \tag{A.20}$$

is called a *normal mode* of the crystal described by the wave-vector $\mathbf{k}$ and branch index j.

There are several ways to calculate phonons by *ab-initio* methods. The *linear response* method allows to express the dynamical matrix in terms of the inverse of the dielectric matrix describing the response of the valence electron density to a periodic lattice perturbation. The *frozen phonons* method allows the calculation of the displacement amplitude in terms of the difference in energies of distorted and ideal lattices. This approach is restricted to phonons, whose wavelength is compatible with the periodic boundary conditions applied to the supercell used in the calculations. We have employed an alternative method of direct method approach using *ab-initio* force constants in the calculation of phonon dispersion of ice. The direct *ab-initio* force constant method was used by Parlinski [167], whereby the forces are calculated via the Hellmann-Feymann theorem in the total energy calculations. Usually, the calculations are done on a supercell with periodic boundary conditions. In such a supercell, a displacement $\mathbf{u}(0, k)$ of a single atom induces forces $\mathbf{F}(lk)$ acting on all other atoms

$$F_\alpha(lk) = \sum_{l'k'\beta} \Phi_{\alpha\beta}(lk;l'k').u_\beta(l'k'). \tag{A.21}$$

This expression allows to determine the force constant matrix directly from the calculated forces (see Parlinski *et al.*) [167]. The phonon dispersion branches calculated by the direct method are exact for discrete wave vectors defined by the equation

$$\exp\left(2\pi\imath\mathbf{k}_L\cdot\mathbf{L}\right) = 1, \tag{A.22}$$

where $\mathbf{L} = (L_a, L_b, L_c)$ are the lattice parameters of the supercell. Usually, the $\mathbf{k}_L$ wave vectors correspond to high-symmetry points of the Brillouin zone. Increase of the supercell size increases the density of the wave vector grid $\mathbf{k}_L$. In this case better accuracy of the phonon dispersion curves is achieved. The direct method implies that the dispersion curves between the exact points can be interpolated. The precision of such interpolation depends on how far the long range forces propagate in the crystal. If the forces converge to zero within a short distance (within the considered supercell), the precision of the phonons for $\mathbf{k} \neq \mathbf{k}_L$ is high. In the case of very long range interaction, the deviation from the correct solution can increase. From the equation of motion (A.15) one can deduce the influence of the supercell size. The greater the range of the interatomic forces are the greater are the number of terms in the Fourier series in (A.15) for $\omega^2(\mathbf{k})$. So, in order to obtain accurate phonon dispersion curves for a crystal, one has to take care about the size of the supercell and the quality of the calculated Hellmann-Feynman forces. Usually, in order to obtain precise phonons along a desired direction, the calculations are carried out with elongated supercells. After all necessary atoms k have been displaced, the corresponding Hellmann-Feynman forces $F_\alpha(lk)$, the force constant matrix $\Phi_{\alpha\beta}(lk; l'k')$ and the dynamical matrix can be obtained according to (A.16). The diagonalization of the dynamical matrix yields for every value of $\mathbf{k}$ a number of eigenvalues for $\omega^2(\mathbf{k}, j)$ and corresponding polarization vectors $\mathbf{e}(\mathbf{k}, j)$. A related technique has recently been used to obtain accurate full phonon dispersions in highly symmetric structures of Ni_2GaMn [169].

A.2 The many phases of ice

Ice, the frozen form of liquid water. It is one of the most common materials on earth and in outer space, and has important relevance to a large number of diverse fields such as astronomy, geophysics, chemical physics, life sciences, etc. Besides its environmental importance, ice is also special because of the interesting phenomena contained within its structure. The crystal structure of ice is very unusual because, while the molecules lie on a regular crystal lattice, there is disorder in their orientations. This property leads to many interesting characteristics in electrical polarization and conductivity. While ice is commonly seen everyday this is only one phase of ice known as ice Ih. What is generally not emphasized is that ice actually has at least thirteen other crystalline phases which exist at various temperatures and pressures. All the solid ice phases involve the water molecules being hydrogen bonded to four neighbouring water molecules. In all cases the two hydrogen atoms are equivalent, with the water molecules retaining their symmetry, and they all obey the "ice" rule: Two hydrogen atoms near each oxygen, one hydrogen atom on each O....O bond. The detailed of all different phases of ice known at the moment can be found in the reference [166]. A brief of discussion of some them are made here.

A.2.1 Ice Ih

Ice Ih phase is the normal form of ice obtained by freezing water at atmospheric pressure. The "h" following the "I" is used to designate that it is a normal hexagonal phase of

ice. The commonly seen phase diagram for Ice Ih, water, and vapour is depicted in Fig. A.1. From the Figure one can see that triple point, point where all three phases are

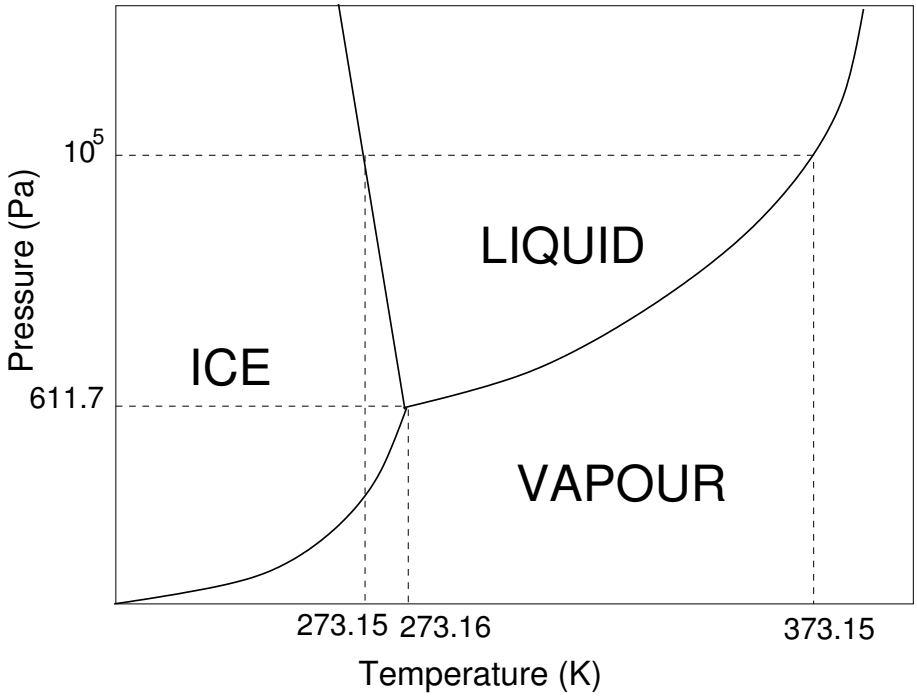

Figure A.1: Schematic phase diagram of water at low pressure (not to scale). The three phases are in equilibrium at triple point (273.16 K) and the corresponding pressure is 611.7 Pa.

in equilibrium, occurs at temperature 273.16 K and the corresponding pressure 611.7 Pa. Water is unusual in that the melting curve has a negative slope with the melting curve point at atmospheric pressure being at 273.15 K, and this value is taken as the zero point of the Celsius scale of temperature. The negative negative slope of the melting curve is, by Le Chatelier's principle, a consequence of the fact that water expands on freezing, breaking vessels, bursting pipes and causing icebergs to float. This expansion is not unique to ice; it occurs also in silicon and germanium which have similar low-density structures in the solid state as discussed in the next Section. In general we consider this type of ice to form at freezing temperatures above 150 K, with other phases of ice to form at lower temperatures. While there are many other phases of ice there are also some varieties of ice Ih phase. S1 ice occurs when ice forms platelets lying on the surface with the *c*-axis vertical forming columnar grains. This is then considered a vertically growing ice such as that found on the sides of containers. If the ice is formed more rapidly, we have randomly oriented grains which grow perpendicular to the *c*-axis. This represents a horizontally growing ice such as that formed on the top of lakes known as S2 ice. Polycrystalline ice then has randomly oriented grains in every direction and is known as T1 ice. This type of ice is very similar to glacier ice. These types of ice all have the hexagonal crystal structure as shown by the basic structure of ice in Fig. A.2 This is the model developed by Pauling in 1935 and later confirmed through neutron diffraction studies by Peterson and Levy in

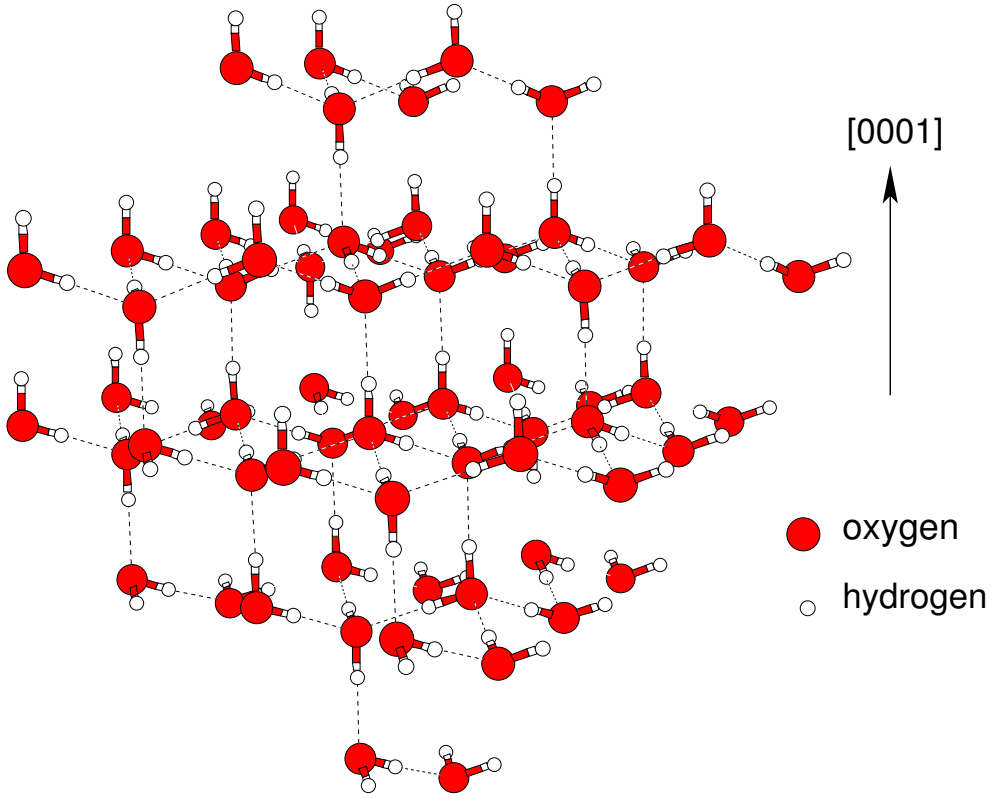

Figure A.2: Crystal structure of ice Ih.

1957. As can be seen in this Figure, each oxygen atom has four nearest neighbours at the corners of a regular tetrahedron. The hydrogen atoms are covalently bonded to the nearest oxygen atoms to form water molecules which are linked to each other through hydrogen bonds. The layers of this structure are then stacked in an ABAB... repeating pattern as shown in Fig. A.3(b). The main thing to note about this structure is that there is no long-range order in the orientation of the water molecules or hydrogen bonds.

A.2.2 Ice Ic

Cubic ice or "ice Ic" is a metastable variant of Ice Ih. It was discovered by Konig in 1943 using electron diffraction technique. Here the oxygen atoms are arranged in the cubic structure of diamond rather than on the hexagonal lattice of ice Ih. As in the case of ice Ih, the water molecules of ice Ic still form four hydrogen bonds to its neighbours. The sequence of stacking of this phase of ice is of the ABCABC... form according to Fig. A.3(a). Ice Ic is produced at freezing temperatures between 130 and 150 K with amorphous ice being produced at lower temperatures. While ice Ic is formed below 150 K, it is important to note that ice Ih does not become ice Ic at temperatures below 150 K. However, around 200 K cubic ice does transform to hexagonal ice. Ice Ic is a very popular structure for theoretical modelling of ice because its high symmetry simplifies calculations. Molecular dynamics simulations were carried out by Svishchev *et. al.* in

1994 in which the crystallization of ice from supercooled liquid water always produces Ic [226]. This never actually occurs in macroscopic experiments and shows how subtle the difference between ice Ic and Ice Ih is.

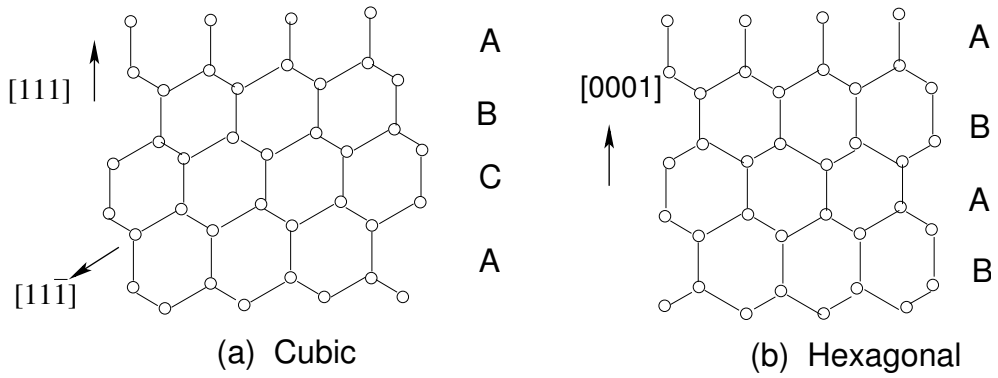

Figure A.3: Comparison of the structures of (a) cubic and (b) hexagonal, seen in projection onto a $\{11\bar{2}0\}$ plane of the hexagonal lattice.

A.2.3 Amorphous ice

There are two main forms of amorphous ice, low density and high density. Low density amorphous ice (LDA, not to be confused with local density approximation earlier seen in DFT) has a density at atmospheric pressure of about 0.94 gcm^{-3} while high density amorphous ice (HDA) is formed at high pressure but has an atmospheric density of 1.174 gcm^{-3}. If the entire region of phases is considered, there could be some transition, a so-called glass transition from one phase of the ice to another under controlled temperature and pressure. For example, theoretical simulations carried out by Okabe *et. al.* show that ice Ih transforms to HDA at 1.27 GPa and 77 K [227]. Also, the simulation tells us that LDA can be formed by heating HDA to 160 K under no applied pressure. While amorphous ice does exist, it has been shown by Schober *et. al.* that both LDA and HDA display many crystal like effects similar to those of ice Ic with LDA showing a higher degree of crystal like properties [228]. High frequency dynamics of both amorphous ices were measured using inelastic X-ray scattering and very narrow width phonon-like excitations were observed. These excitations were interpreted as a sign of local disorder. Also Finney has provided a proof using radial distribution functions derived by neutron diffraction to show the two phases of amorphous ice [229].

A.2.4 Higher phases of ice

The higher phases of ice as well as the intersection with the liquid phase can be seen in Fig. A.4 which summarizes the group of available phases of ice labelled with Roman numerals from ice I to XII. Each phase is stable over a certain temperature range and pressure, but many of the phases are metastable outside of this given range.

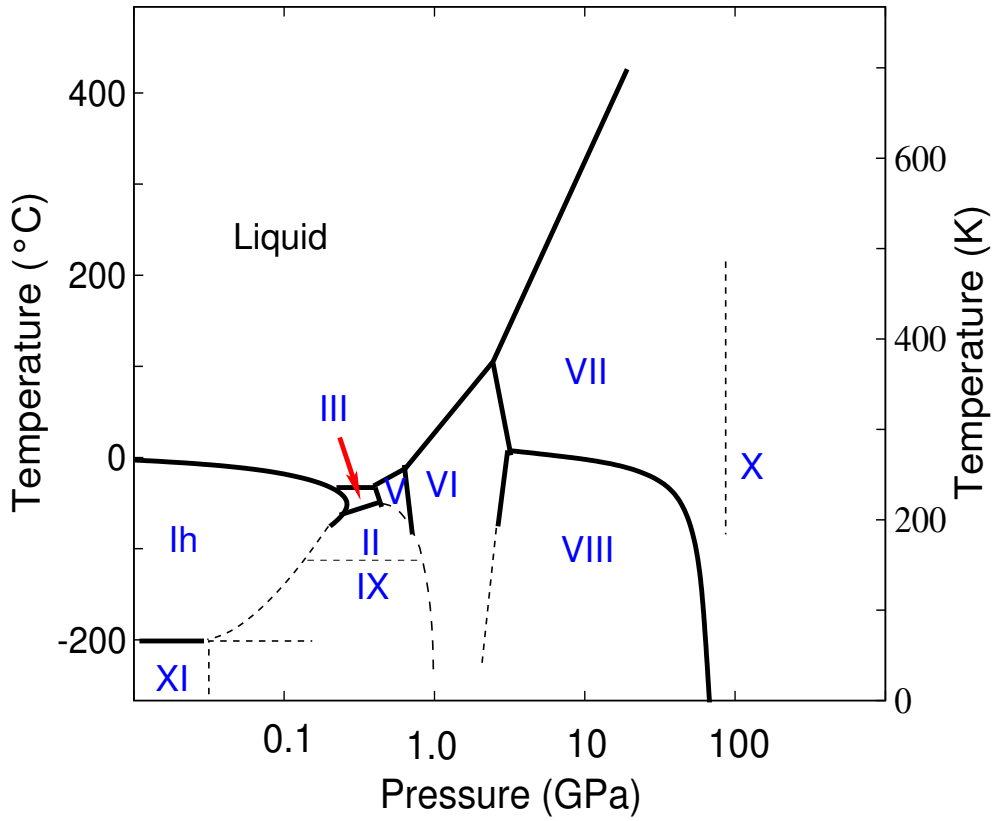

Figure A.4: The phase diagram of water and stable phases of ice.

- **Ice II**: Ice II has a truly ordered structure and is formed by compressing ice Ih at 190 to 210 K. If heated, ice II becomes ice III but the reverse process is not readily accomplished. The unit cell is rhombohedral but the structure can also be described in a larger hexagonal cell of 36 molecules. It contains hexagonal rings linked to one another in which ice II achieves a higher density than ice Ih.

- **Ice III**: Ice III is the least dense of the high-pressure phases of ice, but it is more dense than the liquid phase. Ice III is formed from water at 300 MPa by lowering its temperature to 250 K. Its unit cell forms tetragonal crystals. In the crystal, all water molecules are hydrogen bonded to four others, two as donors and two as acceptor. Ice III contains five membered rings joined as bicyclo-heptamers and possesses a density of 1.16 gcm^{-3} at 350 MPa. The hydrogen bonding is disordered and constantly changing as in hexagonal ice.

- **Ice IV**: Ice IV exists only as a metastable phase and it is not easily formed without the aid of a nucleating agent. The structure is rhombohedral with the three fold axis vertical. Almost planar six membered rings of molecules lie perpendicular to this axis. There is also a hydrogen bond between a pair of different molecules passing through the center of each ring.

- **Ice V**: Ice V has the most complicated structure of all the ice phase. It is formed from liquid water at 500 MPa by lowering its temperature to 253 K. Its unit cell forms monoclinic crystals with each unit cell containing 28 molecules. Ice V contains four-, five-, six- and eight-membered rings and groups of seven molecules at four different lattice sites with each experiencing a different molecular environment. All molecules form one connected lattice with a density of 1.24 gcm^{-3} at 350 MPa. The hydrogen bonding is disordered and also constantly changing as in hexagonal ice.

- **Ice VI**: The crystal structure of ice VI is tetragonal and the structure is formed from chains built up of hydrogen bonded molecules lying parallel to to the fourfold [001] axis. The chains centered on the corners of the unit cell are linked together by hydrogen bonds parallel to the a and b axes. The symmetry of this structure indicates that the hydrogen positions are disordered. Ice VI is formed from liquid water at 1.1 GPa by lowing its temperature to 270 K, and has a density of 1.31 gcm^{-3} at 0.6 GPa. It is also interesting to note that the permittivity of this phase exhibits Debye relaxation.

- **Ice VII**: Ice VII has a cubic arrangement of oxygen atoms. It also has a very simple high density packing of water molecules. Each oxygen atoms has eight nearest neighbours but is tetrahedrally linked by hydrogen bonds to only four of them. There are two interpenetrating but independent sub-lattices each with the structure of cubic ice. It has a density of about 1.65 gcm^{-3} at 2.5 GPa, which is less than twice the cubic ice density. Neutron diffraction data show that the hydrogen atoms are disordered. Because of this hydrogen disorder, the permittivity will exhibit a similar Debye relaxation to that of hexagonal ice.

- **Ice VIII**: Ice VIII is the ordered structure of ice VII. Ice VIII is formed from ice VII by lowering its temperature. The hydrogen bonding is ordered and fixed as ice VII undergoes a proton disordered-order transition to ice VIII when cooled at 5°C. Ice VII and ice VIII have identical structures apart from the proton ordering. Ice VIII forms a tetragonal crystal containing eight water molecules per unit cell, where all of the water molecules are hydrogen bonded to four others, two as donors and two as acceptors. Similarly to ice VII, ice VIII consists of two interpenetrating cubic ice lattices. It has a density of about 1.66 gcm^3 at 8.2 GPa and 223 K which is less than twice the cubic ice density.

- **Ice IX**: Ice IX is formed by cooling Ice III. As we cool ice III from -65 to -108 °C, there is a gradual fall in permittivity as ice IX is formed. Ice IX is very closely related to ice III having a similar crystal structure as well as other properties. The ordering of ice IX was determined by neutron diffraction to be anti-ferroelectric as is the case with ice III as well.

- **Ice X**: Ice X was initially observed in 1984 by Hirsch and Holzapfel using Raman scattering. They observed some features which looked like a phase change around 40-50 GPa and called it ice X. Ice X is also known as the proton ordered symmetric

ice. It is still under dispute whether ice X has indeed been verified experimentally. It is believed that ice VIII can be transformed into ice X but there is yet to be experimental proof. It is also predicted that ice VII should transform into ice X at about 70 GPa.

- **Ice XI**: Ice XI was initially observed by Kawada in 1972, however, it took until 1984 when Tajima performed high precision calometry experiments for ice XI to be accepted as a new phase. Ice XI is the low-temperature equilibrium structure of hexagonal ice prepared from dilute KOH (10 millimole) solution kept just below -201 °C for about a week. The hydroxide ions create defects in the hexagonal ice allowing protons to jump more freely between the oxygen atoms. A loss of entropy by proton ordering occurs to give a more stable structure. Ice XI is the thermodynamically favoured form of ice under atmospheric pressure at these low temperatures. It is a proton-ordered form of hexagonal ice forming orthorhombic crystals. All bonds are parallel to the c-axis and oriented in the same direction making ice XI a ferroelectric.

- **Ice XII**: Ice XII may be formed by heating high-density amorphous ice at a constant pressure of 0.81 GPa and from 77 K to $\sim$ 183 K and recovered at atmospheric pressure at 77 K. Ice XII is metastable within the ice-V and ice-VI phase space. It forms a tetragonal crystal. In the crystal, all water molecules are hydrogen bonded to four others, two as donors and two as acceptors. Ice XII contains a screw-type hydrogen bonded arrangement quite unlike that found in the other crystalline forms of ice, with the smallest ring size consisting of seven molecules. It has a density of 1.30 gcm^{-3} at 127 K and ambient pressure, somewhat greater than ice-V whose density is 1.23 gcm^{-3}. The hydrogen bonding is disordered and constantly changing as in hexagonal ice.

From these brief description, there are currently thirteen well defined ice phases. The majority of these phases can be transformed into other phases of ice but some are yet to be well defined such as ice X. While ice is one of the most easily recognised and common solid seen in life, it still remains one of the most complex solids to understand. While many phases have been identified it does not mean that there are *not* more phases of ice especially as we we look to higher and higher pressure.

A.3 Thermal properties of ice

Apart from the dynamical properties through the analysis of the phonon dispersions and the modes of vibration of the molecules in ice already discussed in the main text of the thesis, ice like other tetrahedrally co-ordinated bonded solid crystals such as Si, Ge, GaAs, ZnSe and GaP show some fascinating properties in their thermal behaviour, especially negative thermal expansion at low temperature. One of the examples of such tetrahedrally co-ordinated bonded solid crystal is α-SiO_2 shown in Fig. A.5. The Figure can be compared with ice Ih shown Fig. A.2. The liquid like silica possess local tetrahedral symmetry but do not have hydrogen bonds displaying the same property. The mean linear

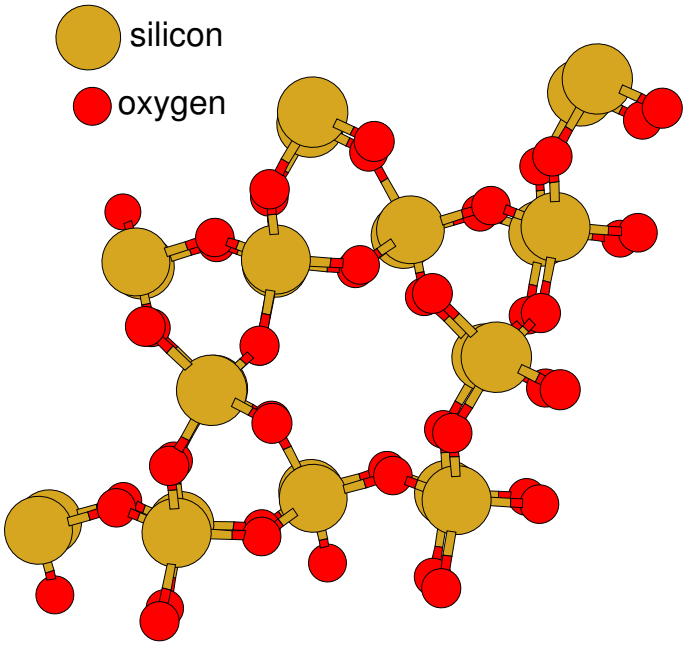

Figure A.5: Structure of α-SiO2 compared to ice Ih in Fig. A.2.

expansion $\alpha(T)$ coefficients derived from lattice parameters of H_2O and D_2O are shown in Fig.A.6 taken from Ref. [177]. In this Figure, $\alpha(T)$ is negative below 73 K which is a common property of tetrahedrally co-ordinated crystals. The interpretation of the thermal expansion of a crystalline material depends on the anharmonic nature of the inter-atomic forces, and this is discussed in terms of the translational modes of lattice vibrations using the Grüneisen parameter $\gamma(T)$ [45]. For a specific mode i the quantity γ_i is defined by

$$\gamma_i = -\frac{\partial \ln \nu_i}{\partial V}, \tag{A.23}$$

where ν_i is the mode frequency and V is the volume. For truly harmonic potential γ_i will be zero. For an isotopic crystals, general thermodynamic arguments show that the linear expansion coefficient α is related to the heat capacity C_v (per unit volume) and the bulk modulus B by

$$\alpha = \frac{\gamma(T) C_v}{3B} \tag{A.24}$$

in which $\gamma(T)$ is the thermal weighted average of the γ_i. For most modes γ_i is positive (i.e. the mode frequencies fall as the crystal expands) and $\gamma(T)$ is approximately constant and of order of unity. In such cases the crystal expands on heating and the temperature dependence of α is dominated by that of heat capacity. However, for some transverse acoustic modes it is possible for γ_i to be negative, and if these modes have low energy and dominate the average at low temperatures, $\gamma(T)$ and hence α can be negative. In the

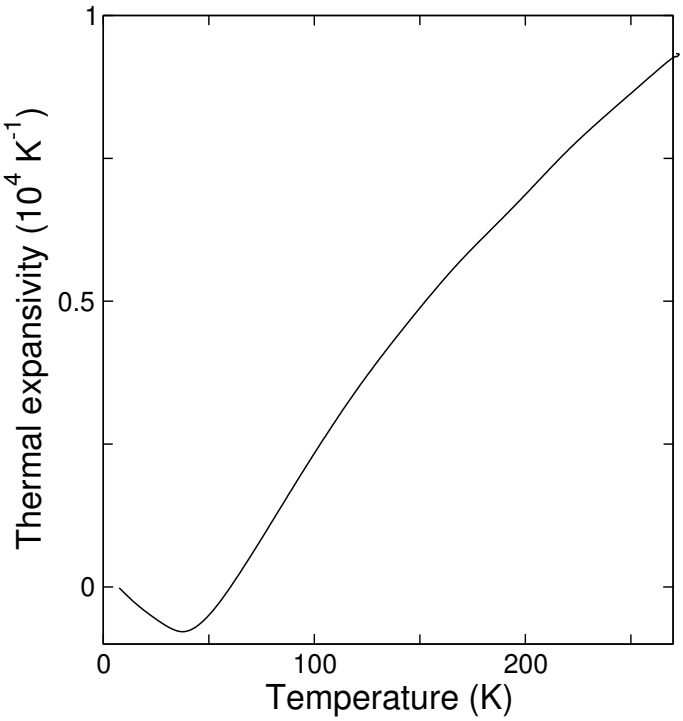

Figure A.6: Linear expansion of coefficients of H_2O and D_2O ice as calculated from the lattice parameter data (From Tanaka (1998) [177]).

lattice dynamical model of the structure of ice, Tanaka (1998) has identified hydrogen-bond bending modes which have this property, and he has derived negative expansion coefficients of approximately the observed magnitude [177]. The significance of negative α is that anharmonicity of the low energy modes is such that as they become excited the crystal shrinks. Another explanation given to the origin of this anomalous behaviour of expansion is that ice is a *permanent* tetrahedral network held together by hydrogen bonds while liquid water's tetrahedrality is local and transient [153]. Regions of local tetrahedral order possess a larger specific volume than the average unlike regions of, say, local close-packed order. The entropy, on the other hand, always decreases upon cooling, because the specific heat is, of necessity, positive. As temperature decreases, the local specific volume increases due to the progressive increase in tetrahedral order. Thus, the entropy and volume can become anticorrelated, and, α can become negative.

References

[1] K. T. Högskolan, *Computation Modelling of Biological Membrane and Interface Dynamics*, PhD thesis, Royal Institute of Technology, Department of Physics 2001.

[2] W. B. Bosma, L. E. Fried and S. Mukamel, *Simulation of the intermolecular vibration spectra of liquid water and water clusters*, J. Chem. Phys. **98**, 4413 (1993).

[3] W. B. Wayne and M. M. Rhodes, *Molecular dynamics simulations of structural transitions and phase coexistence in water pentamers*, J. Chem. Phys. **117**, 9286 (2002).

[4] I. R. McDonald and M. L. Klein, *Intermolecular potentials and the simulation of liquid water*, J. Chem. Phys. **68**, 4875 (1978).

[5] R. S. Taylor, L. X. Dang and B. C. Garrtet, *Molecular dynamics simulations of the liquid/vapor interface of SPC/E Water*, J. Chem. Phys. **100**, 11720 (1996).

[6] F. Franks, *Water Science Review 5: The Molecules of Life*, Cambridge University Press, Cambridge 1990.

[7] I. Ohmine, H. Tanaka and P. Wolynes, *Large local energy fluctuations in water. II. Cooperative motions and fluctuations*, J. Chem. Phys. **89**, 5852 (1988).

[8] C. L. Briant and J. J. Burton, *A molecular dynamics study of the structure and thermodynamic properties of argon microclusters*, J. Chem. Phys. **63**, 2045 (1975).

[9] M. Blackman and N. D. Lisgarten, *Elect diff of cubic & other struc forms of ice*, Adv. Phys. **7**, 189 (1958).

[10] I. M. Svishchev and P. G. Kusalik, *Crystallization of liquid water in a molecular dynamics simulation*, Phys. Rev. Lett. **73**, 975 (1994).

[11] A. S. Cote, I. Morrison, X. Cui, S. Jenkins and D. K. Ross, *Ab-initio density-functional lattice-dynamics studies of ice*, Can. J. Phys. **81**, 115 (2003).

[12] I. Morrison and S. Jenkins, *First-principles lattice dynamics studies of the vibrational spectra of ice*, Physica B **263**, 442 (1999).

[13] C. Lee, D. Vanderbilt, K. Laarsonen, R. Car and M. Parrinello, *Ab-initio studies on the structural and dynamical properties of ice*, Phys. Rev. B **47**, 4863 (1993).

[14] S. S. Xantheas and H. T. Dunning, *Ab initio studies of cyclic water clusters $(H_2O)_n$, n = 1-6. I. Optimal structures and vibrational spectra*, J. Chem. Phys. **99**, 8774 (1993).

[15] E. D. Sloan, *Clathrate hydrates of natural gases*, Dekker, USA 1998.

[16] E. D. Sloan, *Fundamental principles and applications of natural gas hydrates*, Nature **426**, 353 (2003).

[17] M. Ahmed, C. Hughes and J. C. Whitehead, *The adsorption of methanol on large water clusters*, Chem. Phys. Lett. **240**, 216 (1995).

[18] M. Ahmed, C. J. Apps, C. Hughes, N. E. Watt and J. C. Whitehead, *Adoption of organic molecules on large water clusters*, J. Phys. Chem. A **101**, 1250 (1997).

[19] J. L. Atwood, J. E. D. Davies, F. V. D. D. MacNicol and J. M. Lehn, *Comprehensive Supramolecular Chemistry*, Bd. 3, Elsevier Science Ltd, Oxford 1996.

[20] B. K. Lipkowitz, *Applications of computational chemistry to the study of cyclodextrin*, Chem. Rev. **98**, 1829 (1998).

[21] W. Saegner, J. Jacob, K. Steiner, D. Hoffman, H. Sanbe, K. Koizumi, S. M. Smith and T. Takaha, *Structures of the common cyclodextrins and their larger analogues-beyond the doughnut*, Chem. Rev. **98**, 1787 (1998).

[22] J. Szejtli, *Utilization of cyclodextrins in industrial products and process*, J. Mater. Chem. **7**, 575 (1997).

[23] F. Trotta, G. Cravotto and S. Rossignoli, *Asymmetric synthesis in the presence of cyclodextrins*, J. Inclus. Phenom. Macrocyclic Chem. **44**, 293 (2002).

[24] W. A. Adeagbo, V. Buss and P. Entel, *Inclusuion complexes of dyes and cyclodextrins: Modelling supermolecules by rigourous quantum mechanics*, J. Inclus. Phenom. Macrocyclic Chem. **44**, 203 (2002).

[25] T. Loftsson, B. Ólafsdóttir, H. Fridriksdottir and S. Jónsdottir, *Cyclodextrin complexation of NSAIDs: Physiochemical characteristics.*, Eur. J. Pharm. Sci. **1**, 95 (1993).

[26] N. Metropolis, A. Rosenbluth, M. Rosenbluth, A. Teller and E. Teller, *Equation of state calculation by fast computing machines*, J. Chem. Phys. **21**, 1087 (1953).

[27] B. J. Alder and T. E. Wainwright, *Phase transition for a hard sphere system*, J. Chem. Phys. **27**, 1208 (1957).

[28] W. W. Wood and J. D. Jacobsen, *Preliminary results from a recalculation of the Monte-Carlo equation of state of hard spheres*, J. Chem. Phys. **27**, 1207 (1957).

[29] M. E. Tuckerman, *Ab-initio molecular dynamics: Basic concepts, current trends and novel applications*, J. Phys.: Condens. Matter **14**, 1297 (2002).

[30] L. J. Lewis and N. Mousseau, *Tight-binding molecular dynamics studies of defects and disorder in covalently bonded materials*, Comput. Mater. Sci. **12**, 210 (1998).

[31] C. Goringe, D. Bowler and E. Hernandez, *Tight-binding modelling of materials*, Prog. Phys. **60**, 1447 (1997).

[32] M. Elstner, D. Porezag, G. Jungnickel, J. Elsner, M. Haugk and T. Frauenheim, *Self-consistent-charge density-functional tight-binding method for simulations of complex materials properties*, Phys. Rev. B **58**, 7260 (1998).

[33] P. Slater and G. Koster, *Simplified LCAO method for the periodic potential problem*, Phys. Rev. **94**, 1498 (1954).

[34] F. Bloch, *Elektron im periodischen Potential, Bändermodell des Festkörpers*, Z. Phys **52**, 555 (1928).

[35] D. J. Wales and I. Ohmine, *Structure, dynamics and thermodynamics of model $(H_2O)_8$, and $(H_2O)_20$ clusters*, J. Chem. Phys. **98**, 7245 (1993).

[36] G. Kresse and J. Futhmüller, *Efficient iterative schemes for ab initio total-energy calculations using a plane-wave basis set*, Phys. Rev. B **54**, 11169 (1996).

[37] W. Kohn and L. J. Sham, *Self-consistent equations including exchange and correlation effects*, Phys. Rev. **140**, A1133 (1965).

[38] P. Hohenberg and W. Kohn, *Inhomogeneous electron gas*, Phys. Rev. **136**, B864 (1964).

[39] R. M. Dreizler and E. K. U. Gross, *Density functional theory*, Springer, Berlin 1990.

[40] P. Fulde, *Electron Correlations in Molecules and Solid*, Springer, Berlin 1995.

[41] R. G. Parr and Y. Weitao, *Density functional Theory of Atoms and Molecules*, Oxford University Press, Oxford 1994.

[42] R. O. Jones and O. Gunnarsson, *The density functional formalism, its applications and prospects*, Rev. Mod. Phys. **61**, 689 (1989).

[43] P. W. Atkins and R. S. Friedman, *Molecular Quantum Mechanics*, Oxford University Press., New York 2001.

[44] M. Springborg, *Methods of Electronic-Structure Calculations From Molecules to Solids*, Wiley, New York 2000.

[45] N. W. Ashcroft and Mermin, *Solid State Physics*, Saunders College, Philadelphia 1976.

[46] D. Marx and J. Hutter, *Modern Methods and Algorithms of Quantum Chemistry*, Bd. 1, NIC series, J. Grotendorst (Forschungszentrum Jülich) 2000.

[47] M. Levy, *Universal variational functionals of electron densities, first-order density matrices, and natural spin-orbitals and solution of the v-representability problem*, Proc. Natl. Acad. Sci. **76**, 6062 (1979).

[48] R. G. Paar and W. Yang, *Density Functional Theory of Atoms and Molecules*, Oxford University Press, Oxford 1989.

[49] M. Levy, *Electron densities in search of Hamiltonians*, Phys. Rev. A **26**, 1200 (1982).

[50] O. Gunnarsson and B. I. Lundqvist, *Exchange and correlation in atoms, molecules, and solids by the spin-density-functional formalism*, Phys. Rev. B **13**, 4274 (1976).

[51] D. C. Langreth and J. P. Perdew, *The exchange correlation energy of a metallic surface*, Solid State Commun. **17**, 1425 (1975).

[52] J. Harris, *Adiabatic-connection approach to Kohn-Sham theory*, Phys. Rev. A **29**, 1648 (1974).

[53] J. Harris and R. O. Jones, *The surface energy of a bounded electron gas*, J. Phys. F.: Metal Physics **4**, 1170 (1974).

[54] J. P. Perdew and A. Zunger, *Self-interaction correction to density-functional approximations for many-electron systems*, Phys. Rev. B **23**, 5048 (1981).

[55] U. V. Barth and L. Hedin, *A local exchange-correlation potential for the spin polarized case: I*, J. Phys. C **5**, 1629 (1972).

[56] S. H. Vosko, L. Wilk and M. Nusair, *Accurate spin-dependent electron liquid correlation energies for local spin density calculations: A critical analysis*, Canad. J. Phys. **58**, 1200 (1980).

[57] J. P. Perdew and Y. Wang, *Accurate and simple analytic representation of the electron-gas correlation energy*, Phys. Rev. B **45**, 13244 (1992).

[58] P. R. Briddon and R. Jones, *LDA calculations using a basis of gaussian orbitals*, Phys. Stat. Solidi (B) **217**, 131 (2000).

[59] A. D. Becke, *Density-functional exchange-energy approximation with correct asymptotic behavior*, Phys. Rev. A **38**, 3098 (1988).

[60] W. Y. C. Lee and R. C. Paar, *Development of the Colle-Salvetti correlation-energy formula into a functional of the electron density*, Phys. Rev. B **37**, 785 (1988).

[61] J. P. Perdew, K. Burke and M. Ernzerhof, *Generalized gradient approximation made simple*, Phys. Rev. Lett. **77**, 3865 (1996).

[62] A. J. Cohen and N. C. Handy, *Dynamic correlation*, Mol. Phys. **99**, 607 (2001).

[63] N. C. Handy and A. J. Cohen, *Left-right correlation energy*, Mol. Phys. **99**, 403 (2001).

[64] N. C. Handy and A. J. Cohen, *A dynamical correlation functional*, J. Chem. Phys. **116**, 5411 (2002).

[65] Q. Wu and W. Yang, *Empirical correction to density functional theory for van der Waals interactions*, J. Chem. Phys. **116**, 515 (2002).

[66] A. D. Becke, *Density-functional thermochemistry. I. The effect of the exchange-only gradient correction*, J. Chem. Phys. **96**, 2155 (1992).

[67] A. D. Becke and M. R. Roussel, *Exchange holes in inhomogeneous systems: A coordinate-space model*, J. Phys. Rev. A **39**, 3761 (1989).

[68] A. D. Becke, *Simulation of delocalized exchange by local density functionals*, J. Chem. Phys. **112**, 4020 (2000).

[69] E. Proynov, H. Chermette and D. R. Salahub, *New τ-dependent correlation functional combined with a modified Becke exchange*, J. Chem.Phys. **113**, 10013 (2000).

[70] M. Ernzerhof, S. N. Maximoff and G. E. Scuseria, *Functionals of quantities other than the electron density: Approximations to the exchange energy*, J. Chem. Phys. **116**, 3980 (2002).

[71] Z. H. Liu and E. A. Carter, *Full Configuration Interaction Molecular Dynamics of Na_2 and Na_3*, J. Phys. Chem. **99**, 4355 (1995).

[72] J. A. White and D. M. Bird, *Implementation of gradient-corrected exchange-correlation potentials in Car-Parrinello total-energy calculations*, Phys. Rev. B. **50**, 4954 (1994).

[73] G. Bachelet, D. Hamann and M. Schluter, *Pseudopotentials that work: From H to Pu*, Phys. Rev. B **26**, 4199 (1982).

[74] N. Troullier and J. L. Martin, *Efficient pseudopotentials for plane-wave calculations*, Phys. Rev. B **43**, 1993 (1991).

[75] D. Vanderbilt, *Soft self-consistent pseudopotentials in a generalized eigenvalue formalism*, Phys. Rev. B **41**, 7892 (1990).

[76] P. E. Blöchl, *Projector augmented-wave method*, Phys. Rev. B **50**, 17953 (1994).

[77] J. Ihm, A. Zunger and M. L. Cohen, *Momentum-space formalism for the total energy of solids*, J. Phys. C: Solid State Phys. **12**, 4409 (1979).

[78] J. S. Lin, A. Qteish, M. C. Payne and V. Heine, *Optimized and transferable nonlocal separable ab initio pseudopotentials*, Phys. Rev. B **47**, 4147 (1993).

[79] D. R. Hamann, M. Schlüter and C. Chiang, *Norm-conserving pseudopotentials*, Phys. Rev. Lett. **43**, 1494 (1979).

[80] M. C. Payne, M. P. Teter, D. C. Allen, T. A. Arias and J. D. Joannopoulos, *Iterative minimization techniques for ab-initio total-energy calculations: Molecular dynamics and conjugate gradients*, Rev. Mod. Phys. **64**, 1045 (1992).

[81] W. E. Pickett, *Pseudopotential methods in condensed matter applications*, Comput. Phys. Rep. **9**, 115 (1989).

[82] L. Kleinman and D. M. Bylander, *Efficacious form for model pseudopotentials*, Phys. Rev. Lett. **48**, 1425 (1982).

[83] X. Gonze, P. Kaeckell and M. Scheffler, *Ghost states for separable, norm-conserving, ab- initio pseudopotentials*, Phys. Rev. B **41**, 12264 (1990).

[84] X. Gonze, R. Stumpf and M. Scheffler, *Analysis of separable potentials*, Phys. Rev. B **44**, 8503 (1991).

[85] R. W. Hockney, *Born-Oppenheimer molecular-dynamics simulations of finite systems: Structure and dynamics of* $(H_2O)_2$, Phys. Rev. B **48**, 2081 (1993).

[86] G. Martyna and M. Tuckerman, *A reciprocal space based method for treating long range interactions in ab initio and force-field-based calculations in clusters*, J. Chem. Phys. **110**, 2810 (1999).

[87] P. Mináry, M. E. Tuckerman, K. A. Pihakari and G. J. Martyna, *A new reciprocal space based treatment of long range interactions on surfaces*, J. Chem. Phys. **116**, 5351 (2002).

[88] M. E. Tuckerman, P. Minary, K. A. Pihakari and G. J. Martyna, *Computational Methods for Macromolecules: Challenges and Applications*, Springer, Berlin 2002.

[89] Grimsehl, *Lehrbuch der Physik,*, Bd. 4, edited by A. Lösche, Leipzig 1988.

[90] M. J. Frisch, G. W. Trucks, H. B. Schlengel, P. M. W. Gill, B. G. Johnson, M. A. Robb, J. R. Cheeseman, T. Kreith, G. A. Peterson, J. A. Montgomery, J. Cioslowski, B. B. Stefanov, A. Nanayakkara, M. Challacome, C. Y. Peng, P. Y. Ayala, W. Chen, M. W. Wong, J. L., Adres, E. S. Replogle, R. Gomperts, R. L. Martin, D. J. Fox, J. S. Binkley, D. J. Defrees, J. Baker, J. P. Stewart, M. Head-Gordon, C. Gonzalez and J. A. Pople, *Gaussian Inc.,*, Gaussian, Pittsburg PA 1998.

[91] J. M. Jancou, R. Scholz and F. Bassani, *Empirical spds* tight-binding calculation for cubic semiconductors: General method and material parameters*, Phys. Rev. B **57**, 6493 (1998).

[92] R. Scholz, J. M. Jancou, , F. Beltram and F. Bassani, *Tight-binding approach to computational materials science*, MRS Symp. Proc, Materials Research Society, Pittsburg **491**, 383 (1998).

[93] D. Carlo, *Tight-binding approach to computational materials science*, MRS Symp. Proc, Materials Research Society, Pittsburg **491**, 389 (1998).

[94] C. Z. Wang, K. M. Ho and C. T. Chan, *Tight-binding molecular-dynamics study of amorphous carbon*, Phys. Rev. Lett. **70**, 611 (1993).

[95] P. Ordejón, D. Lebedenko and M. Menon, *Improved nonorthogonal tight-binding Hamiltonian for molecular-dynamics simulations of silicon clusters*, Phys. Rev. B **50**, 5645 (1994).

[96] M. Menon and K. R. Subbaswamy, *Nonorthogonal tight-binding molecular-dynamics scheme for silicon with improved transferability*, Phys. Rev. B **55**, 9231 (1997).

[97] O. K. Andersen and O. Jepsen, *Explicit, first-principles tight-binding theory*, Phys. Rev. Lett. **53**, 2571 (1984).

[98] E. Artacho and F. Ynduráin, *Nonparametrized tight-binding method for local and extended defects in homopolar semiconductors*, Phys. Rev. B **44**, 6169 (1991).

[99] R. E. Cohen, M. J. Mehl and D. A. Papaconstantopoulos, *Tight-binding total-energy method for transition and noble metals*, Phys. Rev. B **50**, 14694 (1994).

[100] O. F. Sankey and D. J. Niklweski, *Ab-initio multicenter tight-binding model for molecular-dynamics simulations and other applications in covalent systems*, Phys. Rev. B **40**, 3979 (1989).

[101] D. Porezag, T. Frauenheim, T. Köhler, G. Seifert and R. Kaschner, *Construction of tight-binding-like potentials on the basis of density-functional theory: Application to carbon*, Phys. Rev. B **51**, 12947 (1995).

[102] W. M. C. Foulkes and R. Haydock, *Tight-binding models and density functional theory*, Phys. Rev. B **39**, 12520 (1989).

[103] J. Hubbard, *Electron correlations in narrow energy bands*, Proc. Roy. Soc. **276**, 238 (1963).

[104] H. Eschrig, *The Optimized LCAO Method and Electronic Structure of Extended Systems*, Akademieverlag, Berlin 1988.

[105] G. Seifert, H. Eschrig and W. Bieger, *An approximate variant of the LCAO-X.α. method*, Z. Phys. Chem. (Leipzig) **267**, 529 (1986).

[106] T. Frauenheim, F. Weich, T. Köhler, S. Uhlmann, D. Porezag and G. Seifert, *Density-functional-based construction of transferable nonorthogonal tight-binding potentials for Si and SiH*, Phys. Rev. B **52**, 11492 (1995).

[107] P. Sitch, T. Frauenheim and R. Jones, *A density functional tight-binding approach for modelling Ge and GeH structures*, J. Phys.: Condens. Matter **8**, 6873 (1996).

[108] J. Widany, F. Weich, T. Köhler, D. Porezag and T. Frauenheim, *Dynamic properties and structure formation of boron and carbon nitrides*, Diamond Relat. Matter **5**, 1031 (1996).

[109] F. Weich, J. Widany, F. Weich and T. Frauenheim, *Paracyanogenlike structures in high-density amorphous carbon nitride*, Phys. Rev. Lett. **78**, 3326 (1997).

[110] R. Gutierrez, T. Frauenheim, T. Köhler and G. Seifert, *Stability of silicon carbide structures: from clusters to solid surfaces*, J. Mater. Chem. **6**, 1657 (1996).

[111] M. Haugk, J. Elsner and T. Frauenheim, *A density-functional based tight-binding approach to GaAs surface reconstructions*, J. Phys.: Condens. Matter **9**, 7305 (1997).

[112] R. Pariser, *Theory of the electronic spectra and structure of the polyacenes and alternant hydrocarbons*, J. Chem. Phys. **24**, 250 (1956).

[113] K. Ohno, *Some remarks on thr Pariser-Parr-Pople method*, Theor. Chim. Acta **2**, 219 (1964).

[114] G. Klopman, *A semiempirical treatment of molecular Structures. II. Molecular terms and application to diatomic molecules*, J. Am. Chem. Soc. **86**, 4550 (1964).

[115] N. Mataga and K. Nishimoto, *Electronic structure and spectra of nitrogen heterocycles*, Z. Phys. Chem. (Frankfurt) **13**, 140 (1957).

[116] D. L. Beveridge and W. L. Jorgensen, *Computer Simulation of Chemical and Biomolecular Systems*, Bd. 482, Ann. NY Acad. Sci., New York Academy of Sciences, New York 1986.

[117] H. J. C. Berendsen, J. P. M. Postma, W. F. van Gunsteren, A. DiNola and J. R. Haak, *Molecular dynamics with coupling to an external bath*, J. Chem. Phys **81** (1984).

[118] W. G. Hoover, *Canonical dynamics: Equilibrium phase-space distribution*, Phys. Rev. A **31** (1985).

[119] J. M. Haile, *Molecular Dynamics Simulation. Elementary methods*, Wiley, New York 1997.

[120] M. P. Allen and D. J. Tildesley, *Computer Simulations of Liquids*, Oxford University Press, Oxford 1987.

[121] W. Saenger, *Principles of Nucleic Acid Structure*, Springer-Verlag, New York 1984.

[122] J. Caldwell, X. Dang and P. A. Kollman, *Implementation of nonadditive intermolecular potentials by use of molecular dynamics: Development of a water-water potential and water-ion cluster interactions*, J. Am. Chem. Soc. **112**, 9144 (1990).

[123] M. Sprik, *Hydrogen bonding and the static dielectric constant in liquid water*, J. Chem. Phys. **95**, 6762 (1991).

[124] U. Niesar, G. Corongiu, E. Clementi, G. R. Kneller and D. K. Bhatacharya, *Molecular dynamics simulations of liquid water using the NCC ab-initio potential*, J. Phys. Chem. **94**, 7949 (1990).

[125] R. Car and M. Parrinello, *Unified approach for molecular dynamics and density-functional theory*, Phys. Rev. Lett. **55**, 2471 (1985).

[126] D. A. Estrin, L. Paglieri, G. Corongiu and E. Clementi, *On small clusters of water molecules using density functional theory*, J. Phys. Chem. **100**, 8701 (1996).

[127] T. R. Dyke, K. M. Mack and J. S. Muenter, *The structure of water dimer from molecular beam electric resonance spectroscopy*, J. Chem. Phys. **66**, 498 (1977).

[128] E. Sakir and G. Emel, *Molecular-dynamics simulations of water clusters*, Physica E **8**, 40 (2000).

[129] H. L. Lemberg and F. H. Stillinger, *Central-force model for liquid water*, J. Chem. Phys. **62**, 1677 (1975).

[130] D. J. Wales and M. P. Hodges, *Global minima of water clusters* $(H_2O)_n$, $n \leq 21$, *described by an empirical potential*, Chem. Phys. Lett. **286**, 65 (1998).

[131] A. Vegiri and S. C. Farantos, *Classical dynamics of hydrogen bonded systems: Water clusters*, J. Chem. Phys. **98**, 4059 (1993).

[132] C. E. Dykstra, *Structures and vibrational frequencies of small water complexes from electrical molecular mechanics*, J. Chem. Phys. **91**, 6472 (1989).

[133] K. S. Kim, M. Dupuis, G. C. Lie and E. Clementi, *Revisiting small clusters of water molecules*, Chem. Phys. Lett. **131**, 451 (1986).

[134] R. Kusche, T. Hippler, M. Schmidt, B. von Issendorf and Haberland, *Melting of free sodium clusters*, Eur. Phys. J. D **9**, 1 (1999).

[135] R. D. Etters and J. Kaelberer, *Thermodynamics properties of small aggregates of rare-gas atoms*, Phys. Rev. A **11**, 1068 (1975).

[136] D. J. Wales and I. Ohmine, *Rearrangements of model $(H_2O)_8$, and H_2O_{20} clusters*, J. Chem. Phys. **98**, 7257 (1993).

[137] Robert and W. Cahn, *Melting from within*, Nature, **413**, 582 (2001).

[138] D. J. Wales and T. R. Walsh, *Theoretical study of the water pentamer*, J. Chem. Phys. **105**, 6957 (1996).

[139] P. L. Moore and T. S. Chen, *Investigation of structure and stability of small clusters: Molecular dynamics studies of water pentamers*, J. Chem. Phys. **86**, 7149 (1987).

[140] S. Clough, Y. Beers, G. Klein and L. Rothman, *Dipole moment of water from Stark measurements of (H_2O), HDO, and (D_2O)*, J. Chem. Phys. **59**, 2254 (1973).

[141] H. S. Frank and W. Y. Wen, *Structural aspects of ion-solvent interaction in aqueous solution: A suggested picture of water*, Disc. Faraday Soc. **24**, 133 (1957).

[142] K. E. van Holde, W. C. Johnson and P. S. Ho, *Physical Biochemistry*, Patience Hall, New Jersey 1998.

[143] A. K. Soper, *The radial distribution functions of water and ice from 220 to 673 K and at pressure up to 400 MPa*, Chem. Phys. Lett. **258**, 121 (2000).

[144] J. D. Bernal and R. H. Fowler, *A theory of water and ionic solution*, J. Chem. Phys. **1**, 515 (1933).

[145] P. Postorino, R. H. Tromp, M. A. Ricci, A. K. Soper and G. W. Neilson, *The interatomic structure of water at supercritical temperatures*, Nature **366**, 668 (1993).

[146] E. S. Fois, M. Sprik and M. Parinello, *Properties of supercritical water: An ab initio simulation*, Chem. Phys. Lett. **223**, 411 (1994).

[147] A. K. Soper, *Orientational correlation function for molecular liquids: The case of liquid water*, J. Chem. Phys. **101**, 6888 (1994).

[148] A. A. Chialvo and P. T. Cummings, *Hydrogen bonding in supercritical water*, J. Chem. Phys. **101**, 4466 (1994).

[149] Y. E. Gorbaty and A. G. Kalinichev, *The radial distribution functions of water and ice from 220 to 673 K and at pressure up to 400 MPa*, J. Phys. Phys. **99**, 5336 (1995).

[150] A. G. Kalinichev and J. D. Bass, *Hydrogen bonding in supercritical water: a Monte Carlo simulation*, Chem. Phys. Lett. **231**, 301 (1994).

[151] A. K. Soper, F. Bruni and M. A. Ricci, *Site-site pair correlation functions of water from 25 to 400 °C: Revised analysis of new and old diffraction data*, J. Chem. Phys. **106**, 247 (1997).

[152] K. Krynicki, C. D. Green and D. W. Sawyer, *Pressure and temperature dependence of self-diffusion in water*, Faraday Discuss. Chem. Soc. **66**, 199 (1978).

[153] P. G. Debenedetti and H. E. Stanle, *Supercooled and glassy water*, Physics Today p. 40, July (2003).

[154] K. Toukan, M. A. Ricci, S. H. Chen, C. K. M. Loong, D. L. Price and J. Teixeira, *Neutron-scattering measurements of wave-vector-dependent hydrogen density of states in liquid water*, Phys. Rev. A **37**, 2580 (1982).

[155] L. Pauling, *The structure and entropy of ice and of other crystals with some randomness of atomic arrangement*, J. Am. Chem. Soc. **57**, 2680 (1935).

[156] M. Marchi, J. S. Tse and M. Klein, *Lattice vibrations and infrared absorption on ice Ih*, J. Chem. Phys. **85**, 2414 (1986).

[157] E. Whalley and J. E. Bertie, *Optical spectra of orientationally disordered crystals. I. Theory of translational lattice vibrations*, J. Chem. Phys. **46**, 1264 (1967).

[158] D. D. Klug and E. Whalley, *Origin of the high-frequency translational bands of ice I*, J. Glaciology **21**, 55 (1978).

[159] B. Renker and P. Blanckenhagen, *Physics of Ice*, Plenum, New York 1969.

[160] H. J. Prask and S. F. Trevino, *Ice I-lattice dynamics and incoherent neutron scattering*, J. Chem. Phys. **56**, 3217 (1972).

[161] R. E. Shawyer and P. Dean, *Atomic vibrations in orientationally disordered systems. I. A two dimensional model*, J. Phys. C **5**, 1017 (1972).

[162] G. Nielsen, R. M. Townsend and S. A. Rice, *Model based calculations of the lattice mode spectra of ice Ih and amorphous solid water*, J. Chem. Phys. **81**, 5288 (1984).

[163] J. S. Tse, M. L. Klein and I. R. McDonald, *Lattice vibrations of ices Ih, VIII, and IX*, J. Chem. Phys. **81**, 6124 (1984).

[164] G. Nielson, R. M. Townsend and S. A. Rice, *Model based calculations of the lattice mode spectra of ice Ih and amorphous solid water*, J. Chem. Phys. **81**, 5288 (1984).

[165] K. Parlinskin, *Phonon*, Cracow, Poland, Software, Version 3.11 2002.

[166] V. F. Petrenko and R. W. Whitworth, *Physics of Ice*, Oxford University Press, Oxford 1999.

[167] K. Parlinskin, Z. Q. Li and Y. Kawazoe, *First-principles determination of the soft mode in cubic ZrO_2*, Phys. Rev. Lett. **78**, 4063 (1997).

[168] P. Gammon, H. Kiefte, M. Clouter and W. Denner, *Elastic constants of artificial and natural ice samples by Brillouin spectroscopy*, J. Glaciology **29**, 433 (1983).

[169] A. T. Zayak, P. Entel, J. Enkovaara, A. Ayuela and R. M. Nieminem, *A first-principles investigation of phonon softenings and lattice instabilities in the shape memory system Ni_2MnGa*, Phys. Rev. B **68**, 132402 (2003).

[170] B. Renker, *Physics and Chemistry of Ice*, (University of Toronto Press) p. 82, Toronto 1973.

[171] J. Li, *Inelastic neutron scattering studies of hydrogen bonding in ices*, J. Chem. Phys. **105**, 6733 (1996).

[172] P. P. Faure, *Étude d'un modéle dynamique du réseau cristallin de la glance*, J. Physique (France) **30**, 214 (1969).

[173] G. P. Srivastava, *The Physics of Phonons*, Adam Hilder, New York 1990.

[174] F. Sette, G. Ruocco, M. Krisch, C. Masciovecchio, R. Verbeni and U. Bergmann, *Transition from normal to fast sound in liquid water*, Phys. Rev. Lett. **77**, 83 (1996).

[175] W. S. Benedict, N. Gailar and E. K. Plyler, *Rotation-vibration spectra of deuterated water vapour*, J. Chem. Phys. **24**, 1139 (1956).

[176] J. E. Bertie and E. Whalley, *Optical spectra of orientationally disordered Crystals. II. Infrared spectrum of ice Ih and ice Ic from 360 to 50 cm^{-1}*, J. Chem. Phys. **46**, 1264 (1967).

[177] H. Tanaka, *Thermodynamic stability and negative thermal expansion of hexagonal and cubic ices*, J. Chem. Phys. **108**, 4887 (1998).

[178] P. Jund and R. Jullien, *Densification effects on the Boson peak in vitreous silica: A molecular-dynamics study*, J. Chem. Phys. **113**, 2768 (2002).

[179] S. Ciliberti, T. S. Grigera, V. Martín-Mayor and P. Verrocchio, *Brillouin and Boson peaks in glasses from vector Euclidean random matrix theory*, J. Chem. Phys. **119**, 8577 (2003).

[180] M. J. Harris, M. T. Dove and J. M. Parker, *Floppy modes and boson peak in crystalline and amorphous silicates: an inelastic neutron scattering study*, Mineralogical Magazine, **64**, 435 (2000).

[181] T. S. Grigera, V. Martin, G. Parisi and P. Verrocchio, *Phonon interpretation of the 'boson peak' in supercooled liquids*, Nature **422**, 289 (2003).

[182] T. Yamaguchi, K. Hidaka and A. K. Soper, *The structure of liquid methanol revisited: A neutron diffraction experiment at -80 °C and +25 °C*, Mol. Phys. **96**, 1159 (1999).

[183] S. Dixit, W. C. K. Poon and J. Crain, *Hydration of methanol in aqueous solutions: A Raman spectroscopic study*, J. Phys: Condens. Matt. **12**, L323 (2000).

[184] M. L. Bender and M. Komiyama, *Cyclodextrin Chemistry*, Spring-Verlag, Berlin 1978.

[185] J. Szejtli, *Cyclodextrins and Their Inclusion Complexes*, Akademia, Budapest 1982.

[186] P. Bortolus and S. Monti, *Advances in Photochemistry, Vol. 21*, John Wiley, New York 1996.

[187] T. Andersson, M. Sundahl, G. Westman and O. Wennerstoem, *Host-guest chemistry of fullerenes: A water-soluble complex between C_70 and γ-cyclodextrin*, Tetrahedron Lett. **35**, 7103 (1994).

[188] V. J. Schuri, *Separation of enantiomers by gas chromatography*, Chromatography A **906**, 275 (2001).

[189] M. T. Rojas, R. Koeniger, J. F. Stodart and A. E. Kaifer, *Supported monolayers containing preformed binding sites. Synthesis and interfacial binding properties of a thiolated β-cyclodextrin derivative*, J. Am. Chem. Soc. **117**, 336 (1995).

[190] W. Kroutil, A. Kleewein and K. Faber, *A computer program for analysis, simulation and optimization of asymmetric catalytic processes proceeding through two consecutive steps: Type 2: Sequential kinetic resolution.*, Tetrahedron Asymm. **8**, 3251 (1997).

[191] K. A. Connors, *The stability of cyclodextrin complexes in solution*, Chem. Rev. **97**, 1325 (1997).

[192] I. Bakó and L. Jicsinszky, *Semiempirical calculations on cyclodextrins*, J. Inclusion Phenom. Mol. Recognit. **18**, 275 (1994).

[193] M. Kitagawa, H. Hoshi and H. Sakurai, *The large dipole moment of cyclomaltohexaose and its role in determining the guest orientation in inclusion complexes*, Carbohyr. Res. **163**, c1 (1987).

[194] M. Sakura, M. Kitagawa, H. Hoshi, Y. Inoue and R. Chûjô, *A molecular orbital study of cyclodextrin (cyclomalto-oligosaccharide) inclusion complexes. III, dipole moments of cyclodextrins in various types of inclusion complex*, Carbohyr. Res. **198**, 181 (1990).

[195] A. Botsi, K. Yannakopoulou, E. Hadjoudis and J. Waite, *AM1 calculations on inclusion complexes of cyclomaltoheptaose (β-cyclodextrin) with 1,7-dioxaspiro[5.5] undecane and nonanal, and comparison with experimental results*, J. Carbohydr. Res. **283**, 1 (1996).

[196] P. C. Manor and W. Saenger, *Topography of cyclodextrin inclusion complexes. III. Crystal and molecular structure of cyclohexaamylose hexahydrate, the water dimer inclusion complex*, J. Am. Chem. Soc. **96**, 3630 (1974).

[197] K. Lindner and W. Saenger, *Topography of cyclodextrin inclusion complexes. XVI. Cyclic system of hydrogen bonds: structure of α-cyclodextrin hexahydrate, form (II): comparison with form (I)*, Acta Crystallogr. B **38**, 203 (1982).

[198] G. L. Bertrand, J. R. Faulkner, S. M. J. Han and D. W. Armstrong, *Substituent effects of the binding of phenols to cyclodextrins in aqueous solution*, J. Phys. Chem. **93**, 6863 (1989).

[199] A. Buvari and L. Barcza, *Complex formation of phenol, aniline, and their nitro derivatives with β-cyclodextrin.*, J. Chem. Soc. Perkin Trans. **2**, 543 (1988).

[200] M. Kamiya, S. Mitsuhashi, M. Makino and H. Yoshioka, *Analysis of inducded rotational strength of mono- and di-substituted benzenes included in β-cyclodextrin.*, J. Phys. Chem. **96**, 95 (1992).

[201] S. Jourdier, *A miracle drug*, Chemistry Britain **35**, 33 (1999).

[202] W. C. Evans, *In Trease and Evans' Pharmacognosy, Vol. 3*, Sauders, 14th edition, Philadelphia 1996.

[203] R. S. Payne, R. C. Rowe, R. J. Roberts, M. H. Chalton and R. Docherty, *Potential polymorphs of aspirin*, J. of Comp. Chem. **20**, 262 (1999).

[204] M. Legend and M. J. Rougier, *Stereochemistry Fundamentals and Methods, Vol. 2*, Kagan, Stuttgart 1977.

[205] N. Harada and K. Nakanishi, *Circular Dichroic Spectroscopy Exciton Coupling in Organic Stereochemistry*, University Science Books, Mill Valley, CA 1983.

[206] M. Ohashi, K. Kasatani, H. Shinohara, and H. Sato, *Molecular mechanics studies on inclusion compounds of cyanine dye monomers and dimers in cyclodextrin cavities*, J. Am. Chem. Soc. **112**, 5284 (1990).

[207] J. Ding, T. Steiner and W. Saenger, *Structure of the γ-cyclodextrin-1-propanol-17H_2O inclusion complex*, Acta Crystallogr. B **47**, 731 (1991).

[208] Z. Pakulski and A. Zamojski, *Separation of racemic binaphtol into enantiomers. Synthesis of neomenthylthioacetic acid chloride- A new chiral resolving agent*, Tetrahedron Asymm. **6**, 111 (1995).

[209] P. Bortolus, G. Marconi, S. Monti, G. Grabnaer and B. Meyer, *Structures and excited state properties of 2- and 3-hydroxybiphenyl complexed with cyclodextrins*, Phys. Chem. Chem. Phys. **2**, 2943 (2000).

[210] B. Manunza, S. Deiana, M. Pintore and C. Gessa, *Structure and internal motion of solvated beta-cyclodextrin: molecular dynamics study*, J. Molec. Struct. (Theochem) **419**, 133 (1997).

[211] K. B. Lipkowitz and G. A. Anderson, *Computational Approaches in Supramolecular Chemistry*, Kluwer, Dordrecht 1994.

[212] K. Kano, Y. Kato and M. Kodera, *Mechanism for chiral recognition of binaphtyl derivatives by cycoldextrin*, J. Chem. Soc. Perkin Trans. **2**, 1211 (1996).

[213] R. S. Cahn, C. K. Ingold and V. Prelog, *Specification of molecular chirality*, Angew. Chem. **78**, 413 (1966).

[214] E. L. Eliel and S. H. Wilen, *Stereochemistry of Organic Compounds, p. 155*, Wiley, New York 1994.

[215] S. Miyano, K. kawahara, Y. Inoue and H. Hashimoto, *A Convenient preparation of optically active 1,1'-binaphthyl-2,2'-diol via enzymatic hydrolysis of the racemic diester*, Chem. Lett., p. 355 (1987).

[216] H. Nakamura, A. Sano and H. Sumi, *Chiral separation of (R,S)-1-*1′*-binaphyl-2,*2′*-dihyl hydrogen-phosphate by capillary electrophoresis using monosaccharides as chiral Selectors*, Analyt. Sci. **14**, 375 (1998).

[217] H. Nakamura, A. Sano and H. Sumi, *Recent progress in chiral separation principles in capillary electrophoresis*, Electrophoresis **21**, 4112 (2000).

[218] F. Toda, K. Tanaka, Z. Stein and I. Goldberg, *Optical resolution of binaphthyl and biphenanthryl diols by Inclusion crystallization with N-alkylcinchonidium halides. structural characterization of the resolved materials*, J. Org. Chem. **59**, 5748 (1994).

[219] H. Dodziuk, *Modern conformational analysis: Elucidating novel exciting molecular structures*, VCH, New York 1995.

[220] H. Kabrede and R. Hentschke, *Global minima of water clusters* $(H_2O)_N$, $N \leq 25$, *described by three empirical potentials*, J. Phys. Chem. B **107**, 3914 (2003).

[221] K. Kano, K. Minami, K. Horiguchi, T. Ishimura and M. Kodera, *Ability of non-cyclic oligosaccharides to form molecular complexes and its use for chiral separation by capillary zone electrophoresis*, J. Chromatogr. A **694**, 307 (1995).

[222] M. Born and H. Kun, *Dynamical Theory of Crystal Lattices.*, Clarendon Press, Oxford 1988.

[223] M. T. Dove, *Introduction to Lattice Dynamics*, Cambridge University Press, Cambridge 1993.

[224] W. Cochran, *Dynamics of Atoms in Crystals.*, Arnold, London 1973.

[225] G. K. Horton and A. A. Maradudin, *Dynamical Properties of Solids*, North-Holland Publishing Company, Amsterdam 1974.

[226] I. M. Svishchev and P. G. Kusalik, *Crystallization of liquid water in a molecular dynamics simulation*, Phys. Rev. Lett. **73**, 975 (1994).

[227] I. Okabe, T. Hideki and K. Nakanishi, *Structure and phase transitions of amorphous ice*, Phys. Rev. E **53**, 2638 (1996).

[228] H. Schober, *Crystal-like high and low density amorphous ice by neutron diffraction*, Phys. Rev. Lett. **85**, 4100 (2000).

[229] J. L. Finney, *Structures of high and low density amorphous ice by neutron diffraction*, Phys. Rev. Lett. **88**, 225503 (2002).

Acknowledgements

I give glory to the Almighty God for his protection and for seeing me through in this research work. I would like to thank my thesis supervisor, Prof. Dr. Peter Entel, for the greatest opportunity offered me to do my Ph.D work in his group at the University of Duisburg-Essen. I am quite grateful for his unrelented efforts, kindness, understanding, unflinching assistance and encouragement shown throughout my work. His useful discussions guides me through in my research work.
I must also show my gratefulness to Prof. Dr. Volker Buss for his untiring efforts, kindness and patience in assisting me in all the helpful discussions and full support needed in order to progress through my research work in the area of organic molecules.
I am very much thankful to my colleagues in the group for the pleasant atmosphere in the whole department. I am particularly grateful to Dr. Minoru Sugihara, for his assistance with my calculations at the beginning of my work. I must also thank Egbert Hoffmann for some useful assistance concerning the use of our codes. I thank Dr. Ralf Meyer for his patience for some useful discussions in the area of molecular dynamics simulation.
With respect to the computer facilities I always got a full support from the system administrator of our group, Dr. Fred Hucht and Markus Grunner for his help in rescuing me whenever I had trouble with my computer.
I must thank my closest colleague and friend, Alexei Zayak for his kindest assistance in the use of some softwares and also for the kind interest shown in my work. His friendship relationship makes life enjoyable in Duisburg. I must not forget Georg Rollman and his wife for their ever kindness and painstaken whenever it comes to some administrative work in the Graduate College despite their own task. Also I am indebted to Carsten Holfort for his initial assistance on my first arrival in Germany.
I must remember Dr. Andrei Postnikov for his great friendship and for introducing and explaining the theoretical aspects of electronic structure calculations during his lecture courses. His useful discussion is highly appreciated.
I must thank our colleague Dr. Heike Herper for providing nice and lively atmospheres when it comes to any get together in the department. I thank all my other colleagues whose names I could not mention here for making life adaptable for me in the department and Duisburg at large.
I must express my gratitude to Oliver Weingert despite his tight schedule in his own research in the chemistry group he always spared his time to help in printing my posters for the conferences.
I will like to give special thanks to Melanie Meurer and other members of Jehovah's withness organisation Duisburg for the love and kindness they showed me throughout my staying in Duisburg.
On behalf of our group I thank Prof. Keith Ross for allowing us to use one of their phonon dispersions for comparison with our results. Also, I acknowledge Prof. Soper for providing us the neutron diffraction data of radial distribution functions of liquid water and ice for fitting our *ab-initio* simulation results.

Lastly, I must acknowledge the financial support of the Deutsche Forschungsgemeinschaft (Graduiertenkolleg 277) which allowed me to stay in Germany during three years and work under optimal conditions.

Curriculum Vitae

Personal data

Name:	**Waheed Adeniyi Adeagbo**
Date of birth:	July 16, 1971
Place of birth:	Ibadan, Oyo State, Nigeria
Nationality:	Nigeria
Marital status:	Unmarried
Present position:	Ph.D student in the group of Prof. Dr. P. Entel at the University Duisburg-Essen, Germany
Present e-mail address:	**adeagbo@thp.uni-duisburg.de**
Permanent e-mail address:	**wadeagbo@mail.skannet.com**

Graduate program

1989-1994:	Enrolement at the University of Ibadan, Nigeria. (B.Sc. Physics) B.Sc-Thesis: *Analytic orbitals of copper and beryllium*, supervised by Prof. Dr. Awele Maduemezia
1995-1997:	Master of Science (M.Sc): Physics, University of Ibadan, Ibadan, Nigeria (Speciality: Solid state physics) Master-Thesis: *Gap equation in superconductivity with generalized BCS pairing*, supervised by Prof. Dr. Awele Maduemezia
1999-2000:	Condensed Matter Diploma: Physics, Abdus-Salam International Center for Theoretical Physics, Trieste, Italy (Speciality: Condensed matter physics) Diploma-Thesis: *Iterative solution of integral equation of fluid*, supervised by Prof. Dr. Pastore
Since February 2001:	Ph.D work in the theoretical Low-Temperature Physics section at the University of Duisburg-Essen, Germany (Supervisor: Prof. Dr. P. Entel)

Professional experience

- Analytic orbitals of copper and beryllium. Using numerical computational method of differential correction algorithm of curve fitting to obtain the analytic orbitals of copper and beryllium (B.Sc. research project at the University of Ibadan, Nigeria).
- Gap equation of superconductivity with generalized BCS pairing. Deriving the integral equations for the gap of superconductivity using the G'orkov approach and also

using numerical computational method to solve these equations. (Master Thesis at the University of Ibadan, Nigeria).

- Iterative solution of integral equation of fluids. Investigation of stability and phase freezing criteria of the iterative solutions of integral equations of Ornstein-Zernike with some pair potentials. (Diploma Thesis at Abdus-Salam International Center for Theoretical Physics, Trieste, Italy)

- *Ab-initio* density functional simulations of water and Inclusion complex molecules: Electronic structure calculations, molecular dynamics simulation of organic molecules like cyclodextrins and its inclusion complexes, structural and dynamical properties of cyclodextrins and their complexes from molecular dynamics investigations, melting transition of water clusters $(H_2O)_n$, $n = 1, 2, \ldots, 36$ from molecular dynamics investigation, molecular dynamics simulation of liquid water, ice, and other hydrogen bonding liquids, lattice dynamical properties of ice.

- Development of scientific software in UNIX environments using programming languages Fortran and C.

- Practical work on different kinds of computers: PCs, work-stations, massive-parallel super-computers (CRAY, IBM, HP).

Teaching Experience

1994-1995:	Muslim High School Babanloma, Kwara State, Nigeria (Teaching physics and mathematics during the National Youth Service Corps in semi and final year classes)
1995-1997:	Ikolaba High School, Agodi, Ibadan (Teaching physics and mathematics in semi and final year classes)
1997-2000:	University of Ibadan, Ibadan, Nigeria (Teaching solid state physics in 3rd and 4th year classes, teaching 2nd year students of medical departments applications of physics in biology, and teaching first year elementary physics)

List of publications

- W. A. Adeagbo, V. Buss and P. Entel. Inclusion Complexes of Dyes and Cyclodextrins: Modelling Supermolecules by rigorous Quantum Mechanics. J. Inclusion Phenomena Macrocyclic Chem. **44**, 203, 2002.
- W. A. Adeagbo and P. Entel. Determination of Melting of Water Clusters using Density Functional Theory. Phase Transitions, **77**, 63, 2004.
- W. A. Adeagbo, V. Buss and P. Entel. Calculation of Inclusion Complex of a Binaphtyl Derivative and Beta-Cyclodextrin using the density functional theory. Phase Transitions, **77**, 53, 2004.
- P. Entel, K. Kadau, W. A. Adeagbo, M. Sugihara, G. Rollmann, A. T. Zayak, and M. Kreth: Molecular Dynamics Simulation in Biology, Chemistry and Physics. In: Heraeus Summer School (2002) Proceedings, edited by W. Hergert (Springer, Berlin, 2003), LNP, in print.
- P. Entel, R. Meyer, W. A. Adeagbo and K. Kadau. Modellrechnung bei nichtmetallischen und metallischen Nanoclustern Published by the University of Duisburg-Essen, Forum Forschung, pg. 28, 2003/2004.
- W. A. Adeagbo, V. Buss and P. Entel. A first-principles study of the chiral recognition capability of β-cyclodextrin on binaphtyl compound. Phys. Chem. Chem Phys., submitted.
- P. Entel, W. A. Adeagbo, M. Kreth, R. Meyer and K. Kadau. Computer Simulation of Structural Transformations in Nanoparticles. 3rd International Conference, Computational Modelling and Simulation of Materials From the Atomistic to the Engineering Scales; special symposium "Modelling Simulating Materials Nanoworld", Acireale (Catania), Sicily, Italy, May 30 June 4, 2004.
- W. A. Adeagbo, A. Zayak and P. Entel. Ab-initio study of structure and dynamical properties of crystalline ice. Phase Transitions, submitted.
- A. Zayak, W. A. Adeagbo and P. Entel. Crystal structures of Ni_2MnGa from density functional calculations. Phase Transitions, submitted.

Attended conferences with posters

- W. A. Adeagbo, P. Entel and V. Buss. *Ab-initio* calculation of β-cyclodextrin host complexation with guest binaphtyl derivatives. Frühjahrstagung des Arbeitskreises Atome, Moleküle, Quantenoptik und Plasmen (AMOP) der Deutsche Physikalische Gesellschaft e. V. (DPG), (mit Physik- und Buchausstellung), Osnabrück, Germany. March 4-8, 2002.

- W. A. Adeagbo, V. Buss and P. Entel. Inclusion Complexes of Dyes and Cyclodextrins: Modelling Supermolecules by rigorous Quantum Mechanics. 11^{th} International Cyclodextrin Symposium, May 5^{th}-8^{th} 2002 Reykjavik Iceland.

- W. A. Adeagbo and P. Entel. Melting of water clusters from *ab-initio* point of view. International Symposium on Structure and dynamics of Heterogeneous Systems-SDHS'02, November 28-29, 2002, University of Duisburg-Essen, Gerhard-Mercator Haus, Duisburg, Germany.

- W. A. Adeagbo, V. Buss and P. Entel. A first-principles study of the chiral recognition capability of β-cyclodextrin on binaphtyl compound. 17 European Colloid and interface Society (ECIS) Conference Firenze, 21-26 September 2003, Convitto della Calza Italy.

- W. A. Adeagbo and P. Entel. Molecular dynamics and lattice dynamical study of crystalline ice structure from first-principles. International Symposium on Structure and dynamics of Heterogeneous Systems-SDHS'03, November 20-21, 2003, University of Duisburg-Essen, Gerhard-Mercator Haus, Duisburg, Germany.

- Waheed Adeniyi Adeagbo, Alexei Zayak, Peter Entel and Jürgen Hafner. First-principle investigations of phonon spectra of crystalline ice. Frühjahrstagung des Arbeitskreises Festkörperphysik der Deutsche Physikalische Gesellschaft e. V. (DPG), (mit Physik- und Buchausstellung), Regensburg, Germany. March 8-12, 2004.

- P. Entel, W. A. Adeagbo, M. Kreth, R. Meyer and K. Kadau. Melting and Freezing of non-metallic and metallic clusters by molecular dynamics simulations. 7th International Conference on Nanostructured Materials. Wiesbaden, Germany. June 20-24, 2004.